

Gregory I. Mashanov
Christopher Batters *Editors*



Single Molecule Enzymology

Methods and Protocols

METHODS IN MOLECULAR BIOLOGY™

Series Editor
John M. Walker
School of Life Sciences
University of Hertfordshire
Hatfield, Hertfordshire, AL10 9AB, UK

For further volumes:
<http://www.springer.com/series/7651>

Single Molecule Enzymology

Methods and Protocols

Edited by

Gregory I. Mashanov

Division of Physical Biochemistry, National Institute for Medical Research, London, UK

Christopher Batters

*Physiologisches Institute, Zelluläre Physiologie,
Ludwig-Maximilians-Universität München, Munich, Germany*



Editors

Gregory I. Mashanov
Division of Physical Biochemistry
National Institute for Medical Research
London, UK
gmashan@nimr.mrc.ac.uk

Christopher Batters
Physiologisches Institute
Zelluläre Physiologie
Ludwig-Maximilians-Universität München
Munich, Germany
Chris.Batters@med.uni-muenchen.de

ISSN 1064-3745
ISBN 978-1-61779-260-1
DOI 10.1007/978-1-61779-261-8
Springer New York Dordrecht Heidelberg London

e-ISSN 1940-6029
e-ISBN 978-1-61779-261-8

Library of Congress Control Number: 2011932986

© Springer Science+Business Media, LLC 2011

All rights reserved. This work may not be translated or copied in whole or in part without the written permission of the publisher (Humana Press, c/o Springer Science+Business Media, LLC, 233 Spring Street, New York, NY 10013, USA), except for brief excerpts in connection with reviews or scholarly analysis. Use in connection with any form of information storage and retrieval, electronic adaptation, computer software, or by similar or dissimilar methodology now known or hereafter developed is forbidden.

The use in this publication of trade names, trademarks, service marks, and similar terms, even if they are not identified as such, is not to be taken as an expression of opinion as to whether or not they are subject to proprietary rights.

Printed on acid-free paper

Humana Press is part of Springer Science+Business Media (www.springer.com)

Preface

Studies of single molecules have risen exponentially during the last 15 years. We have witnessed the birth and maturation of many original methods and the development of protocols specific to single-molecule measurements and their analysis. A variety of new techniques have emerged, including optical imaging, electron microscopy, optical and magnetic trapping, and developments in atomic force microscopy.

Of the thousands of biologically important molecules, enzymes are the most exciting and yet most complicated proteins. These biomolecular “machines” dramatically increase the speed of chemical reactions. They are also involved in signaling and are capable of converting one form of energy into another. The investigation of these “machines” at the single-molecule level enables the extraction of detailed information about their work cycles, their static and kinetic properties, and provides information about their location and activity within cells.

Written by experts from Europe, America, and Japan, this book focuses on single-molecule investigations of enzymes. It is intended for use within the diverse community of molecular biologists, biochemists, and biophysicists studying enzymes in detail and can be used by researchers planning their first single-molecule study or to aid more experienced researchers in further developing their existing studies. It gives practical advice on many aspects of single-molecule enzymology and provides strategic overviews of interconnected methods involved in sample preparation, single-molecule measurements, and data analysis.

*London, UK
Munich, Germany*

*Gregory I. Mashanov
Christopher Batters*

Contents

<i>Preface</i>	v
<i>Contributors</i>	ix
1 Single Enzyme Studies: A Historical Perspective	1
<i>Alex E. Knight</i>	
2 Functional Surface Attachment in a Sandwich Geometry of GFP-Labeled Motor Proteins	11
<i>Volker Bormuth, Felix Zörgibel, Erik Schäffer, and Jonathon Howard</i>	
3 Studying Kinesin's Enzymatic Cycle Using a Single-Motor Confocal Motility Assay, Employing Förster Resonance Energy Transfer	19
<i>Zdenek Lansky and Erwin J.G. Peterman</i>	
4 Fluorescence Imaging with One Nanometer Accuracy: In Vitro and In Vivo Studies of Molecular Motors	33
<i>Melinda Tonks Hoffman, Janet Sheung, and Paul R. Selvin</i>	
5 Snapshots of Kinesin Motors on Microtubule Tracks	57
<i>Franck J. Fourniol and Carolyn A. Moores</i>	
6 Structural and Dynamic Characterization of Biochemical Processes by Atomic Force Microscopy	71
<i>Frédéric Eghiaian and Iwan A.T. Schaap</i>	
7 Using Optical Tweezers to Study the Fine Details of Myosin ATPase Mechanochemical Cycle	97
<i>Christopher Batters and Claudia Veigel</i>	
8 Quantum Dot Labeling Strategies to Characterize Single-Molecular Motors	111
<i>Shane R. Nelson, M. Yusuf Ali, and David M. Warshaw</i>	
9 Imaging Individual Myosin Molecules Within Living Cells	123
<i>Tatiana A. Nenasheva, Gregory I. Mashanov, Michelle Peckham, and Justin E. Molloy</i>	
10 Single-Molecule Measurements Using Microneedles	143
<i>Toshio Yanagida, Yoshiharu Ishii, and Akihiko Ishijima</i>	
11 Fluorescent Nucleoside Triphosphates for Single-Molecule Enzymology	161
<i>Christopher P. Toseland and Martin R. Webb</i>	
12 Probing the Mechanics of the Complete DNA Transcription Cycle in Real-Time Using Optical Tweezers	175
<i>Christoph G. Baumann and Stephen J. Cross</i>	
13 A Single-Molecule Approach to Visualize the Unwinding Activity of DNA Helicases	193
<i>Natalia Fili, Christopher P. Toseland, Mark S. Dillingham, Martin R. Webb, and Justin E. Molloy</i>	

14	Real-Time Single-Molecule Observation of Green Fluorescent Protein Synthesis by Immobilized Ribosomes	215
	<i>Ryo Iizuka, Takashi Funatsu, and Sotaro Uemura</i>	
15	Single-Molecule Measurements of Topoisomerase Activity with Magnetic Tweezers	229
	<i>Yeonhee Seol and Keir C. Neuman</i>	
16	Assembly of Recombinant Nucleosomes on Nanofabricated DNA Curtains for Single-Molecule Imaging	243
	<i>Ja Yil Lee and Eric C. Greene</i>	
17	Simultaneous Observation of Chemomechanical Coupling of a Molecular Motor	259
	<i>Takayuki Nishizaka, Yuh Hasimoto, and Tomoko Masaike</i>	
18	Microsecond Resolution of Single-Molecule Rotation Catalyzed by Molecular Motors	273
	<i>Tassilo Hornung, James Martin, David Spetzler, Robert Ishmukhametov, and Wayne D. Frasch</i>	
	<i>Index</i>	291

Contributors

- M. YUSUF ALI • *Department of Molecular Physiology and Biophysics,
University of Vermont College of Medicine, Burlington, VT, USA*
- CHRISTOPHER BATTERS • *Physiologisches Institut, Zelluläre Physiologie,
Ludwig-Maximilians-Universität München, Munich, Germany*
- CHRISTOPH G. BAUMANN • *Department of Biology, University of York, York, UK*
- VOLKER BORMUTH • *Max Planck Institute of Molecular Cell Biology and Genetics,
Dresden, Germany*
- STEPHEN J. CROSS • *Department of Biology, University of York, York, UK*
- MARK S. DILLINGHAM • *DNA–Protein Interactions Unit, Department of Biochemistry,
School of Medical Sciences, University of Bristol, Bristol, UK*
- FRÉDÉRIC EGHLIAIAN • *Drittes Physikalisches Institut, Georg August Universität,
Göttingen, Germany*
- NATALIA FILI • *MRC National Institute for Medical Research, London, UK;
École Polytechnique Fédérale de Lausanne, Lausanne, Switzerland*
- FRANCK J. FOURNIOL • *Institute of Structural Molecular Biology, Birkbeck College,
London, UK*
- WAYNE D. FRASCH • *Faculty of Biomedicine and Biotechnology, School of Life Sciences,
Arizona State University, Tempe, AZ, USA*
- TAKASHI FUNATSU • *Graduate School of Pharmaceutical Sciences, University of Tokyo,
Bunkyo-ku, Tokyo, Japan*
- ERIC C. GREENE • *Department of Biochemistry and Molecular Biophysics,
Columbia University, New York, NY, USA*
- YUH HASIMOTO • *Department of Physics, Gakushuin University, Tokyo, Japan*
- MELINDA TONKS HOFFMAN • *Physics Department, University of Illinois at Urbana-Champaign, Urbana, IL, USA*
- TASSILO HORNUNG • *Faculty of Biomedicine and Biotechnology, School of Life Sciences,
Arizona State University, Tempe, AZ, USA*
- JONATHON HOWARD • *Max Planck Institute of Molecular Cell Biology and Genetics,
Dresden, Germany*
- RYO IIZUKA • *Graduate School of Pharmaceutical Sciences, University of Tokyo,
Bunkyo-ku, Tokyo, Japan*
- YOSHIHARU ISHII • *CREST JST Department of Frontier Biosciences, Osaka University,
Suita, Osaka, Japan*
- AKIHIKO ISHIJIMA • *Institute of Multidisciplinary Research for Advanced Materials,
Tohoku University, Sendai, Miyagi, Japan*
- ROBERT ISHMUKHAMETOV • *Faculty of Biomedicine and Biotechnology, School of Life
Sciences, Arizona State University, Tempe, AZ, USA*

- ALEX E. KNIGHT • *Analytical Science Division, National Physical Laboratory, Teddington, Middlesex, UK*
- ZDENEK LANSKY • *Laboratory of Plant Cell Biology, Wageningen University, Wageningen, The Netherlands*
- JA YIL LEE • *Department of Biochemistry and Molecular Biophysics, Columbia University, New York, NY, USA*
- JAMES MARTIN • *Faculty of Biomedicine and Biotechnology, School of Life Sciences, Arizona State University, Tempe, AZ, USA*
- TOMOKO MASAIKE • *Department of Physics, Gakushuin University, Tokyo, Japan*
- GREGORY I. MASHANOV • *Division of Physical Biochemistry, National Institute for Medical Research, London, UK*
- JUSTIN E. MOLLOY • *MRC National Institute for Medical Research, London, UK*
- CAROLYN A. MOORES • *Institute of Structural Molecular Biology, Birkbeck College, London, UK*
- SHANE R. NELSON • *Department of Molecular Physiology and Biophysics, University of Vermont College of Medicine, Burlington, VT, USA*
- TATIANA A. NENASHEVA • *MRC National Institute for Medical Research, London, UK*
- KEIR C. NEUMAN • *Laboratory of Molecular Biophysics, National Heart, Lung, and Blood Institute, National Institutes of Health, Bethesda, MD, USA*
- TAKAYUKI NISHIZAKA • *Department of Physics, Gakushuin University, Tokyo, Japan*
- MICHELLE PECKHAM • *School of Biomedical Science, Leeds University, Leeds, UK*
- ERWIN J.G. PETERMAN • *Department of Physics and Astronomy and Laser Centre, VU University Amsterdam, Amsterdam, The Netherlands*
- IWAN A.T. SCHAAP • *Drittes Physikalisches Institut, Georg August Universität, Göttingen, Germany*
- ERIK SCHÄFFER • *Nanomechanics Group, Biotechnology Center, TU-Dresden, Dresden, Germany*
- PAUL R. SELVIN • *Physics Department, University of Illinois at Urbana-Champaign, Urbana, IL, USA*
- YEONEE SEOL • *Laboratory of Molecular Biophysics, National Heart, Lung, and Blood Institute, National Institutes of Health, Bethesda, MD, USA*
- JANET SHEUNG • *Physics Department, University of Illinois at Urbana-Champaign, Urbana, IL, USA*
- DAVID SPETZLER • *Faculty of Biomedicine and Biotechnology, School of Life Sciences, Arizona State University, Tempe, AZ, USA*
- CHRISTOPHER P. TOSELAND • *MRC National Institute for Medical Research, London, UK; Institut für Zelluläre Physiologie, Physiologisches Institut, Ludwig Maximilians Universität, Munich, Germany*
- SOTARO UEMURA • *Oomics Science Center, RIKEN Yokohama Institute, Tsurumi-ku, Yokohama, Japan*
- CLAUDIA VEIGEL • *Physiologisches Institute, Zelluläre Physiologie, Ludwig-Maximilians-Universität München, Munich, Germany*
- DAVID M. WARSHAW • *Department of Molecular Physiology and Biophysics, University of Vermont College of Medicine, Burlington, VT, USA*

MARTIN R. WEBB • *MRC National Institute for Medical Research, London, UK*
TOSHIO YANAGIDA • *Department of Frontier Biosciences, Osaka University, Suita,
Osaka, Japan*

FELIX ZÖRGIBEL • *Institute for Materials Science, Max Bergmann Center
of Biomaterials, TU-Dresden, Dresden, Germany*

Chapter 1

Single Enzyme Studies: A Historical Perspective

Alex E. Knight

Abstract

Single-molecule enzymology has a longer history than is often supposed, with the first measurements being made as early as 1961. However, the development of new technologies has meant that most of the progress has been made in the last two decades. I review the development of single-molecule enzymology, focussing on five key papers which are milestones in the field. In particular, I discuss the 1961 paper by Boris Rotman, which made inventive use of what now seems like primitive technology, and continues to be influential to this day.

Key words: Single-molecule enzymology, Static heterogeneity, Dynamic heterogeneity, Single turnovers

This chapter presents a personal view of the chief milestones in the application of single-molecule methodologies to enzymes. It begins with the first measurement of the activity of single enzyme molecules in 1961, before considering more recent developments, such as the first measurements of single enzyme turnovers and the first mechanical measurements of proteins, as well as discussing the theoretical progress that has been made.

Although recent years have seen rapid progress in the application of single-molecule techniques to the study of enzymes, the field has a relatively long history. In fact, the first paper describing the detection and measurement of the catalytic activity of a single enzyme molecule was published in 1961 by Boris Rotman ([1](#)). This ground-breaking paper is remarkable in many ways; its methodological inventiveness, and the way in which it prefigures so many later studies, are remarkable. Indeed, this paper is the origin not only of the field of single-molecule enzymology, but also of much subsequent single-molecule research. In this review, I discuss this paper in some detail before moving on to discuss some of the subsequent highlights in the development of single-molecule enzymology (see Table [1](#)).

Table 1
Chronology of key papers in single-molecule enzymology

Year	Paper	Enzyme	References
1961	First measurement of the catalytic activity of single enzyme molecules	β -Galactosidase	(1)
1995	First demonstration of static heterogeneity in native enzyme molecules	LDH	(8)
1995	Visualisation of single substrate turnovers	Myosin	(9)
1998	Measurement of dynamic heterogeneity and observation of “memory” effects	Cholesterol oxidase	(13)
2006	Reconciliation of single molecule and Michaelis–Menten kinetics	β -Galactosidase	(14)

It is fascinating to me that this paper was written before I was born, and yet that the detection of single molecules has really only become common currency in molecular biology since I began my PhD studies in 1990. In some part, this shows that although the Rotman paper was a remarkable conceptual breakthrough, technological developments in subsequent years have been necessary for this potential to be realised. For example, lasers were first developed in 1960, but improvements in laser technology, including power output, stability, efficiency, choice of wavelengths and reduction in cost have all played a role in the capacity of researchers to measure single molecules – for example by fluorescence or by optical tweezers measurements. Computers have enabled the acquisition and analysis of vast volumes of data. New detector technologies, together with the accompanying electronics, like electron multiplying CCD cameras and avalanche photodiodes, have enabled the detection and accurate measurement of tiny signals.

The advantages of single-molecule techniques when studying biological molecules have been rehearsed too many times for me to repeat them here (2–5). But it is quite striking that the Rotman paper encompasses so many of them. Although he was not able to measure the heterogeneity of rates in native enzyme molecules, and (because of his amplification-based approach) he was unable to measure dynamic heterogeneity, he was still able to demonstrate a form of static heterogeneity by showing that thermal inactivation of the enzymes was an all-or-nothing process.

A feature of enzymes that makes single-molecule detection more tractable is the intrinsic amplification that results from the accumulation of products from many turnovers of the enzyme.

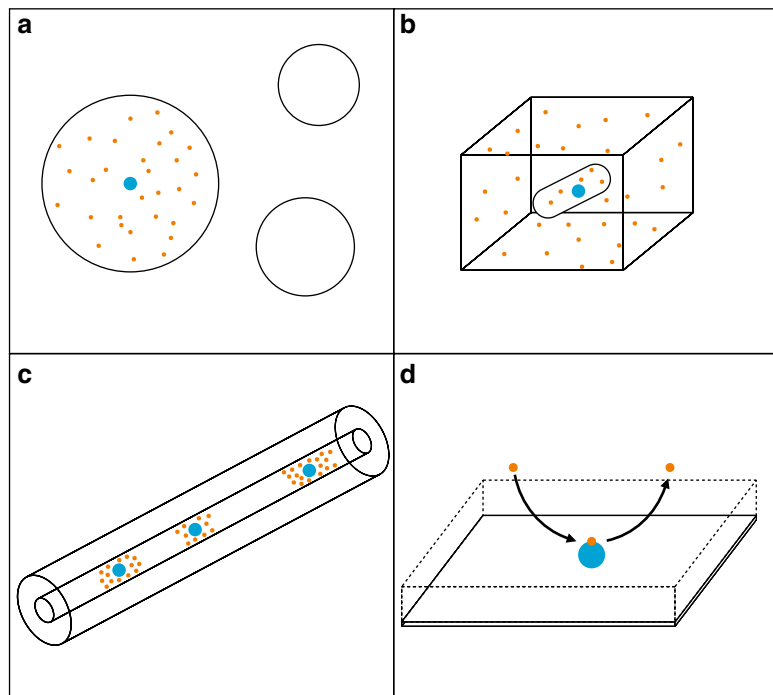


Fig. 1. Experimental designs for single-molecule enzymology. In panels (a–d), enzyme molecules are represented by *large dots* and fluorescent product or substrate molecules are represented by *small dots*. In (a–c), the substrate is a fluorogenic molecule (not shown). In (d), the substrate is also fluorescent. Panel (a) shows Rotman's droplet method (1). Aqueous droplets containing extremely dilute enzyme and excess substrate are dispersed in silicon oil. Droplets containing enzyme molecules accumulate fluorescent product. In (b), *E. coli* or yeast cells expressing low levels of enzyme are captured in microfluidic chambers. The fluorescent products accumulate in the chamber. In (c), the products are confined in two dimensions by a capillary and in a third by diffusion. They can then be “read out” by electrophoresis. In (d), single turnovers are detected. Fluorescent substrate or product molecules are detected when they bind to enzyme molecules immobilised on a surface within an evanescent wave (represented schematically by *dashed lines*).

This is the approach that was used in several early studies. To achieve this, enzyme molecules must be in some way distributed into separate “containers” where their products can accumulate (see Fig. 1 for examples). Rotman achieved this – in a kind of biochemical echo of Millikan’s famous oil-drop experiment (6) – by spraying a dilute solution of the enzyme onto silicon oil and placing a cover-slip on top. The droplets were 0.1 μm to 40 μm in diameter and Rotman took care to check that this process did not significantly denature the enzymes, and included BSA and yeast extract to limit the denaturation. Of course, in such an approach the enzyme molecules are randomly distributed, and the number of molecules in the droplets follows a Poisson distribution. If the right concentration is chosen, many of the droplets will contain 0 enzyme molecules, some will contain 1, and a few will contain 2 or 3, or more. In fact, this is exactly what Rotman observed (see Fig. 2).

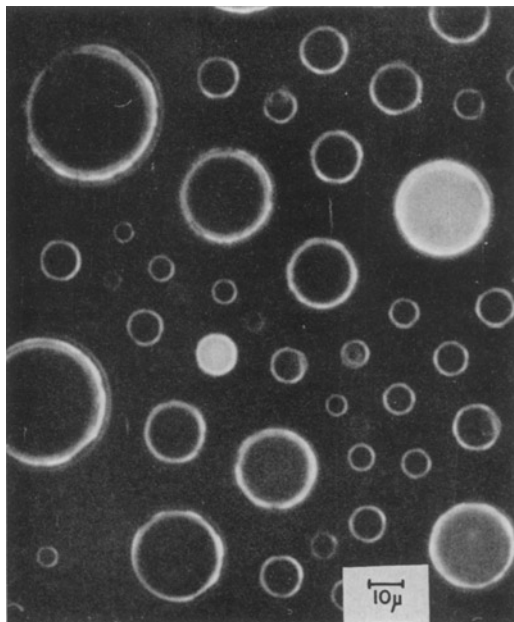


Fig. 2. Rotman's droplet confinement experiment. This photomicrograph is from Rotman's 1961 paper (1). It shows aqueous droplets dispersed in silicon oil; the *scale bar* indicates 10 μm . Dark field illumination with a blue filter was used. Droplets exhibiting green fluorescence appear as *white circles*. In this particular experiment, the fluorescent droplets contained *E. coli* cells, prefiguring the work of Cai et al. 45 years later (7).

Another critical innovation in this paper was the development of a fluorogenic substrate for the enzyme under study, which in this instance was β -galactosidase. (The chromogenic substrate O-nitrophenyl- β -D-galactopyranoside (ONPG) was already known, but fluorogenic substrates permit greater sensitivity.) In fact, the new substrate, 6-hydroxyfluoran- β -D-galactopyranoside (6HFG), has been widely used since, and is the reason for many of the citations of this paper. Rotman was able to show that this product accumulated in the droplets, and to use its fluorescence to measure the enzyme activity in the droplets after incubation at 36°C. When compared to modern fluorescence microscopes and detectors, his system was primitive; however, he estimated that he could detect two million molecules (or three attomoles) of the 6-hydroxyfluoran product, and therefore he calculated that he should be able to detect the activity of a single enzyme in 10 h.

With his new technique, Rotman was able to make a number of ground-breaking measurements. One was to directly measure the molar concentration of the enzyme by counting the number of fluorescent and non-fluorescent droplets (and inferring the average number, and thus the concentration, from the Poisson distribution). Knowing the mass concentration, he was then able to back-calculate the molecular weight of the enzyme. More significantly still, by making repeated observations of droplets, he was able to

measure the kinetics of the enzyme, and make a direct determination of the enzyme's turnover number (115 s^{-1}) – bulk approaches require knowledge of the specific activity and molecular weight of the enzyme, and highly purified enzyme of known concentration. This measurement demonstrated the benefits of direct measurements of single molecules for the first time.

Two more observations took this further yet. Using a mutant form of the enzyme with a 57-fold lower activity, Rotman investigated whether this reduced activity was a uniform property of the mutant enzyme, or whether it consisted of a mix of wild-type and mutant proteins. He reasoned that if the latter were true, a solution of enzyme with the same activity as the wild-type solution would give the same frequency of fluorescent droplets in his experiment. In fact, no fluorescent droplets were seen, indicating that the mutation affected all molecules of the enzyme equally. In contrast, he found that when he performed an experiment with a partially heat-inactivated preparation of the enzyme, there was again a Poissonian distribution of activity in the droplets, indicating that individual molecules were either active or inactive, and that heat inactivation worked by completely inactivating some of the molecules while a few remained fully active. To put it another way, he had demonstrated an extreme case of static heterogeneity.

Towards the end of his paper, Rotman notes,

The method described here has general applications to problems concerning molecular homogeneity and, at the cellular or sub-cellular level, determination of the enzymatic activity of cells or biological particles.

Indeed.

Although perhaps not as well known as it should be, the Rotman paper has had a significant influence on subsequent workers. A much more recent paper which adopts some of the principles of Rotman's work was published by Cai et al. in 2006 (7). They note that a principal limitation of Rotman's approach when studying cells is that they tend to pump the fluorescent products out across the membrane so that cells cannot be used as "containers" to accumulate the signal from enzyme activity. Their solution to this problem was to perform their experiments in microfluidic compartments, which performed the same role as Rotman's droplets (see Fig. 1b). The goal of their experiments was to investigate the stochastic nature of gene expression; they used the *lacZ* gene of *E. coli* as their model, the product of which is of course β -galactosidase. They also used a fluorogenic substrate, in this case fluorescein-di- β -D-galactopyranoside (FDG), which is hydrolysed to fluorescein and galactose. By making repeated measurements of the fluorescence from the compartments, they were able to monitor the rate of accumulation of fluorescence; by differentiating this rate, they were able to work out how many enzyme molecules were present. Inflections in the line indicated

the synthesis of a new enzyme molecule, and allowed them to infer the parameters of the transcription and translation of the *lacZ* gene under repressed conditions.

After the 1961 paper, the next major developments had to wait for 34 years. In 1995, two different, but very influential, papers were published. Xue and Yeung (8) were the first to demonstrate static heterogeneity in the activities of native enzyme molecules. They also relied upon the amplification of the signal of enzyme activity through the accumulation of fluorescent products, but instead of confining their enzymes in physical containers, they relied upon slow diffusion in capillaries to create “zones” around each enzyme molecule, as shown in Fig. 1c. They then used electrophoresis and fluorescence to “read out” the activity of their enzymes. They studied lactate dehydrogenase (LDH) which catalyses the conversion of NAD⁺ and lactate to NADH, which is fluorescent. As the product zones were electrophoresed through the detection volume, peaks were recorded with a width commensurate with that expected from the diffusion of NADH during the incubation period. The area of each peak then indicated the activity of the corresponding enzyme molecule; they found that different molecules showed different rates of activity. They also performed a dual incubation experiment, where after the first incubation a brief electrophoresis was used to separate the enzyme from its products, followed by a second incubation. This resulted in paired peaks, and they found that for a given enzyme, the peak areas were very similar. They concluded that individual enzyme molecules showed intrinsically different rates, and these did not change over time; in other words, they observed static heterogeneity.

To observe enzyme behaviour at shorter timescales – and thereby permit the observation of phenomena such as dynamic heterogeneity – required the detection not just of the activity of single enzymes, but of single turnovers. This was also first achieved in 1995, by Funatsu et al. (9). This paper is also a milestone in research on motor proteins. Many motor proteins are also enzymes – they hydrolyse ATP and use the resulting free energy to do mechanical work (others are driven by ion gradients across membranes – for example, the bacterial flagellar motor and the F_o motor of the F_oF₁ ATPase). The first single-molecule mechanical measurements on motor proteins were made in 1993 (for kinesin) and 1994 (for myosin) using optical tweezers (10, 11). The central question in molecular motor research is how a chemical reaction (hydrolysis) is coupled to a mechanical process (force and displacement) – and this was the motivation for Funatsu’s work.

To detect single turnovers requires the direct detection of individual substrate or product molecules. To achieve this detection, they exploited two different effects. Firstly, to detect fluorescence from a single molecule requires an excellent signal-to-noise ratio. A popular method for achieving this is Total Internal Reflection

Fluorescence Microscopy (12), where an evanescent wave is generated at the interface between a microscope slide and a solution. (Another popular approach is to use a focussed laser spot to restrict excitation to a very small volume). This evanescent wave can excite fluorescence, but decays exponentially away from the interface so that only molecules in a very thin layer near the surface are excited. By immobilising their myosin molecules at this interface, they were also able to exploit a second effect. Small molecules, such as ATP and ADP diffuse extremely rapidly in solution, and hence cannot be imaged by a microscope at video rates because the fluorescence is “smeared out.” However, molecules bound to the enzyme are immobilised and can be imaged provided that their dwell times are longer than the exposure time of the camera (Fig. 1d).

Rather than using a fluorogenic substrate as in the previous work, Funatsu used a Cy3-labelled analogue of ATP. The hydrolysis product Cy3-ADP was also fluorescent, meaning that the substrate and product molecules could not be distinguished. However, myosin is an unusual enzyme in that the release of product (ADP and phosphate) from the active site is the rate-limiting step. This means that by recording the dwell times of the molecules, the rate of product release could be determined. Funatsu et al. measured a rate of 0.059 s^{-1} , consistent with the rate determined in bulk solution (0.045 s^{-1}). This type of approach has been adopted by many experimentalists since.

A slightly different approach to observing single turnovers was taken by Lu et al. in 1998 (13) who investigated cholesterol oxidase. Rather than using fluorescently labelled or fluorogenic substrates, they exploited the native fluorescence of an enzyme cofactor, FAD. In its oxidised form, its fluorescence can be excited with a 442 nm laser, whereas the reduced form, FADH_2 , is non-fluorescent. They showed that in the presence of excess cholesterol and oxygen, the fluorescence from single enzyme molecules blinked as the enzyme cycled through these states. Because the FAD group was found to be very photostable, they were able to make very long observations of individual molecules with more than 500 turnovers, and so calculate very detailed statistics. They observed static disorder when average rates were calculated over these long trajectories, with k_2 (the rate-limiting step) varying from $\sim 3\text{ s}^{-1}$ to $\sim 14\text{ s}^{-1}$. They suggested that this could be due to “damage” to the enzyme molecule in the form of proteolysis or side-chain oxidation. They also found that autocorrelation function of fluorescence traces from single molecules was not a single exponential, suggesting that the rate of catalysis was fluctuating; the enzymes were exhibiting dynamic heterogeneity. They also showed that there was a correlation between the duration of adjacent “on” events. This was a startling result. Conventional kinetics treats reactions as Markovian processes – in other words, it assumes that they are stochastic processes with no “memory” – their state now does not depend on

their state in the past. Clearly, this is not always the case, at least for complex molecules, such as enzymes. Remarkably, they were also able to provide an explanation for this phenomenon, by providing evidence for conformation fluctuations in the enzyme molecule, which occurred on the same time scale as the rate fluctuations.

The exquisite dissection of enzyme mechanism that was now possible raised a potential conflict between the “conventional” macroscopic kinetics that we are all taught as undergraduates and the microscopic behaviours observed in single-molecule experiments. This conflict was directly addressed by English et al. in 2006 (14) who came full circle and studied β -galactosidase using a fluorogenic substrate, this time resorufin- β -D-galactopyranoside (RGP), which is cleaved to yield fluorescent resorufin. Unlike myosin, product release is not rate-limiting, and so only a brief “burst” of fluorescence was detected before the resorufin diffused out of the detection volume. Because the fluorophore was regenerated with every turnover, they were able to record very long traces – up to 2×10^4 turnovers on one enzyme molecule, and thus to obtain yet more detail of molecular behaviour over several orders of magnitude in timescale. They were able to confirm the results seen by other workers, including the observation of a considerable degree of dynamic heterogeneity, and to show that there must in fact be many slowly inter-converting forms of the enzyme with different reaction rates. They were also able to show how the microscopic single-molecule observations – including dynamic heterogeneity – could be reconciled with the macroscopic Michaelis–Menten kinetics with which we are more familiar.

We have covered in some detail the methods that can be used to make passive observations of the behaviour of enzymes, mainly by fluorescence but also (for motors) with optical tweezers. By applying feedback to optical tweezers, more active investigations of molecular behaviour can be achieved (11, 15). A recent paper has shown how mechanical interventions can probe the details of enzyme regulation – at least in the case of enzymes that are regulated by force, such as the titin kinase (16). Puchner and colleagues applied atomic force spectroscopy to show how this enzyme – which is believed to regulate gene expression in skeletal and cardiac muscle in response to the load they experience – was regulated by force. They were able to show that low forces removed an inhibitory domain from the active site of the kinase, which permitted ATP to bind. This then allowed the kinase to autophosphorylate an inhibitory tyrosine residue, activating the kinase.

This is just one example of the many ways in which the paradigm of single-molecule enzymology is being extended as the field matures – and many more examples are found within the pages of this volume. Given the acceleration of progress in recent years, the continual emergence of new and improved experimental tools, and the application of this paradigm to many new systems, it looks as though exciting times lie ahead.

Acknowledgment

I would like to acknowledge support from the Chemical and Biological Metrology programme of the National Measurement Office.

References

1. Rotman, B. (1961) Measurement of activity of single molecules of β -D-galactosidase. *Proc. Natl. Acad. Sci. USA* **47**, 1981–1991.
2. Weiss, S. (1999) Fluorescence Spectroscopy of Single Biomolecules, *Science* **283**, 1676–1683.
3. Knight, A. E., (Ed.) (2009) *Single Molecule Biology* Academic Press.
4. Bustamante, C. (2008) In singulo Biochemistry: When Less Is More. *Annu. Rev. Biochem.* **77**, 45–50.
5. Moerner, W. E. (2007) New directions in single-molecule imaging and analysis. *Proc. Natl. Acad. Sci. USA* **104**, 12596–12602.
6. Millikan, R. A. (1913) On the Elementary Electrical Charge and the Avogadro Constant. *Phys. Rev.* **2**, 109.
7. Cai, L., Friedman, N., and Xie, X. S. (2006) Stochastic protein expression in individual cells at the single molecule level. *Nature* **440**, 358–362.
8. Xue, Q., and Yeung, E. S. (1995) Differences in the chemical reactivity of individual molecules of an enzyme. *Nature* **373**, 681–683.
9. Funatsu, T., Harada, Y., Tokunaga, M., Saito, K., and Yanagida, T. (1995) Imaging of Single Fluorescent Molecules and Individual ATP Turnovers by Single Myosin Molecules in Aqueous Solution. *Nature* **374**, 555–559.
10. Svoboda, K., Schmidt, C. F., Schnapp, B. J., and Block, S. M. (1993) Direct observation of kinesin stepping by optical trapping interferometry. *Nature* **365**, 721–727.
11. Finer, J. T., Simmons, R. M., and Spudich, J. A. (1994) Single Myosin Molecule Mechanics – Piconewton Forces and Nanometer Steps. *Nature* **368**, 113–119.
12. Knight, A., Mashanov, G., and Molloy, J. (2005) Single molecule measurements and biological motors. *Eur. Biophys. J.* **35**, 89.
13. Lu, H. P., Xun, L., and Xie, X. S. (1998) Single-Molecule Enzymatic Dynamics. *Science* **282**, 1877–1882.
14. English, B. P., Min, W., van Oijen, A. M., Lee, K. T., Luo, G., Sun, H., Cherayil, B. J., Kou, S. C., and Xie, X. S. (2006) Ever-fluctuating single enzyme molecules: Michaelis-Menten equation revisited. *Nat. Chem. Biol.* **2**, 87.
15. Visscher, K., Schnitzer, M., and Block, S. (1999) Single kinesin molecules studied with a molecular force clamp. *Nature* **400**, 184–189.
16. Puchner, E. M., Alexandrovich, A., Kho, A. L., Hensen, U., Schäfer, L., Brandmeier, B., Gräter, F., Grubmüller, H., Gaub, H., and Gautel, M. (2008) Mechanoenzymatics of titin kinase. *Proc. Natl. Acad. Sci. USA* **105**, 13385–13390.

Chapter 2

Functional Surface Attachment in a Sandwich Geometry of GFP-Labeled Motor Proteins

Volker Bormuth, Felix Zörgibel, Erik Schäffer, and Jonathon Howard

Abstract

Molecular motors perform work in cells by moving in an ATP-dependent manner along filamentous tracks. In vitro, the mechanical action of such motor proteins can be investigated by attaching the molecules to surfaces in the so-called gliding or bead assays. Surface attachment protocols have to be used that do not interfere with the function of the molecule. Here, we describe a sandwich protocol that preserves functionality. The protocol can be used for a large variety of proteins, in particular kinesin motor proteins that are GFP-tagged.

Key words: Motor protein, Surface attachment, Kinesin, Kip3p, Gliding assay, Bead assay

1. Introduction

The success of in vitro motility assays depends critically on the attachment of the motor proteins to surfaces, such as plastic or glass beads and glass coverslips or microscope slides. Early success with kinesin-1 was due to its fortuitous attachment to glass surfaces such that some of the motors remained functional and allowed microtubule sliding (1). This probably explains why it was kinesin-1, rather than other kinesins, that was first isolated (2). Later success with protein-coated surfaces (3) and specifically casein-coated surfaces (4) facilitated the development of single-motor assays. However, it turned out that other kinesins were not so easy to reconstitute in vitro, probably because success relies on attachment to surfaces of non-motor domains, which are highly divergent within the kinesin superfamily (5).

The development of new surface-coating protocols tailored for individual motor proteins is very labour-intensive – about

1 person-year per protocol, in our experience. Thus, the development of a generic protocol is highly advantageous. This chapter describes such a protocol for GFP-tagged proteins ([6](#), [7](#)).

2. Materials

2.1. Flow Cell

1. Coverslip 22×22 mm and 18×18 mm (Corning, No. 1.5).
2. Parafilm.
3. Hot plate (150°C).
4. Polystyrene (Fluka, Munich, Germany) 1 wt% dissolved in toluene.
5. Spin coater (S.P.S. Vertriebs GmbH, Ingolstadt, Germany).

2.2. Gliding and Bead Assay

1. NeutrAvidin (Pierce, Rockford, USA) 1 mg/ml in PBS.
2. Biotinylated monoclonal antiGFP (use EZ-Link NHS-PEO Solid Phase).
3. Biotinylation kit (Perbio GmbH, Bonn, Germany).
4. BRB80: 80 mM PIPES/KOH pH 6.9, 1 mM MgCl₂, 1 mM EGTA.
5. Motility buffer: BRB 80 with 1 mM ATP, 0.16 mg/ml casein and varying salt concentration depending on the kind of protein under investigation – use 112 mM KCl for the kinesin-8 Kip3p.
6. Microtubules ([8](#), [9](#)).
7. His6-Kip3p-EGFP (expressed in our lab).
8. Phosphate-buffered saline (PBS), pH 7.4.
9. Pluronic F-127 (Invitrogen).

2.3. Bead Assay

1. Polystyrene microspheres: 500 nm in diameter with a concentration of 2.61 wt% (Polyscience, Warrington, USA).
2. Streptavidin-coated microspheres (Sperotech, Lake Forest, USA).
3. Low protein binding tubes (nerbe plus, Winsen/Luhe, Germany).
4. Wash buffer A: PBS with 5 mg/ml biotin-free BSA and 0.1% Tween20.
5. Wash buffer B: PBS with 5 mg/ml biotin-free BSA and 0.1% Tween20 and 0.2 nM biotin.
6. Sonication bath.
7. Thermomixer comfort.
8. Tubulin antibody (SAP.4G5, Sigma Aldrich).

3. Methods

3.1. Flow Cell

1. Before building the flow cell, the cover glasses are rendered hydrophobic either by silanization (9) or by spin-coating a teflon (10) or polystyrene film (several tens of nanometres thick) onto a glass surface (hold the cover glass with vacuum on the rotating stamp of the spin coater, add 50 µl of dissolved polystyrene or Teflon on the cover glass, rotate cover glass for 10 s at 2,000 rpm and an acceleration of 10,000 rpm, to stabilize the polystyrene coating on the cover glass you can bake them for 30 min to 1 h at 150°C in an oven).
2. The flow cell is constructed out of one 22 × 22 mm and another 18 × 18 mm cover glass separated by two parafilm strips placed next to each other to form channels 100 µm thick, 2 mm wide, and 18 mm long. The parafilm is shortly melted on a hot plate to seal the channel walls.

3.2. Gliding Assay

3.2.1. Surface

Functionalization (8, 9)

Use filter paper or vacuum to flow given volumes through the channel of the flow cell while always keeping solution in the channel.

1. 20 µl NeutrAvidin (0.1 mg/ml in PBS); incubate 10 min.
2. 20 µl PBS (to wash out unbound NeutrAvidin).
3. 20 µl F-127 (1% in PBS); incubate 10 min.
4. 5 × 20 µl PBS (to wash out unbound F-127).
5. 20 µl biotinylated antiGFP diluted in PBS (the degree of dilution will determine the density of bound GFP-tagged motor proteins in the next steps); incubate 10 min.
6. 3 × 20 µl BRB80 (to wash out unbound antibodies).

3.2.2. Motility Experiment

1. 20 µl motility buffer (equilibration).
2. 20 µl of motility buffer with the GFP-tagged motor protein; incubate 5 min.
3. 3 × 20 µl motility buffer (to wash out unbound motor protein).
4. 20 µl motility buffer with microtubules.
5. The movement of fluorescently labelled microtubules propelled by GFP-labelled proteins can be observed by fluorescence (see Fig. 1) or LED-illuminated video-enhanced differential interference contrast (DIC) microscopy (11).

3.3. Bead Assay

Overview

1. Prepare or purchase (see Notes 1–5) microspheres functionalized with biotin-binding proteins.
2. Bind biotinylated antibodies via the biotin-tag to the functionalized microspheres.

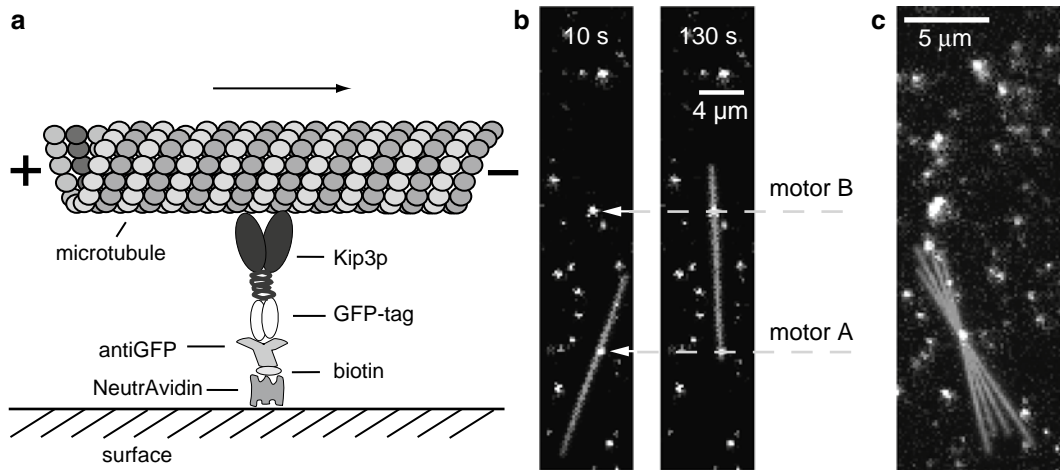


Fig. 1. Sandwich geometry of motor surface attachment for single-molecule gliding assay. **(a)** Schematic of the experiment. **(b)** A single surface attached Kip3p (budding yeast kinesin-8, motor A, *white*) transports a microtubule (grey). At a later time point (130 s), the microtubule binds to a second surface attached motor (motor B) and is transported by both motors. **(c)** Maximum projection of all frames while the microtubule was transported by a single molecule. The microtubule swivelled around a single attachment point which coincides with a single GFP-tagged Kip3p molecule.

3. Bind microtubules to the surface of the flow cell channel.
4. Bind protein of interest via the antibodies onto microspheres for motility experiment.

3.3.1. Coat Microspheres Passively with NeutrAvidin

1. Clean 10 μl of microspheres (Polysciences, USA, diameter ≈ 0.5 μm, 2.6 wt%) three times by centrifugation in 1 ml water (2 min, 16,000×*g*).
2. After the last centrifugation step, resuspend pellet in 100 μl PBS followed by a short sonication step.
3. Add while sonicating 500 μl of 0.2 mg/ml NeutrAvidin in PBS (see Note 6) to the microsphere solution.
4. Incubate for 4 h at 4°C while shaking in a thermomixer at 700 rpm.
5. Fill microspheres up to a volume of 1.5 ml with wash buffer A, split the volume into three times 500 μl.
6. Centrifuge at 5,300×*g* for 10 min with a bench top centrifuge (cooled to 4°C optional).
7. Resuspend pellets in 500 μl wash buffer A (dissolve the pellets by sucking the solution in and out with a pipette, squirting the solution onto the pellet followed by 5 s sonication).
8. Repeat steps 6 and 7 four times.
9. Centrifuge again, remove supernatant and keep 20 μl in the tube. Resuspend the pellets in these 20 μl (see step 7).
10. Collect the three bead solutions in a new tube and fill up to a final volume of 100 μl with wash buffer A.

11. Check if microspheres are clustered!
12. Cleaned NeutrAvidin-coated microspheres can be stored for several months at 4°C.

3.3.2. Bind Biotinylated AntiGFP to Functionalized Microspheres (see Notes 6–9)

1. Add 40 µl of wash buffer A to 10 µl of cleaned, biotin-binding protein-functionalized microspheres (diameter ≈ 0.5 µm, 0.25 wt% (see Note 5) or use purchased microspheres).
2. Add 50 µl of 0.1 mg/ml biotinylated antiGFP (see Note 6) to the diluted microspheres from step 1 (mix while sonicating!).
3. Incubate at 4°C for 4 h while shaking in a thermoshaker with 700 rpm.
4. Fill microsphere solution up to a volume of 1.5 ml with wash buffer B (see Note 8).
5. Incubate 30 min.
6. Centrifuge at 5,300 × g for 10 min with bench top centrifuge (cooled to 4°C, optional).
7. Resuspend pellets in 500 µl wash buffer A (dissolve the pellets by sucking the solution in and out with a pipette, squirting the solution onto the pellet followed by 5 s sonication).
8. Repeat steps 6 and 7 four times.
9. Centrifuge again, remove supernatant, and keep 20 µl in the tube. Resuspend the pellets in these 20 µl each (see step 7).
10. Collect the three bead solutions in a new tube.
11. Check if beads are clustered (see Note 10).

3.3.3. Bind Microtubules to the Surface of the Flow Cell Channel

Use filter paper or vacuum to flow given volumes through the channel of the flow cell while always keeping solution in the channel.

1. 20 µl tubulin antibody (diluted in PBS); incubate 10 min.
2. 20 µl PBS (to wash out unbound antibodies).
3. 20 µl F-127 (1% in PBS); incubate 10 min.
4. 5 × 20 µl BRB80.
5. 20 µl microtubules; incubate 10 min.
6. 20 µl motility buffer (to equilibrate channel).

3.3.4. Motility Experiment

1. Mix microspheres with GFP-tagged motor protein; incubate for 5–10 min.
2. Dilute microspheres in motility buffer and flow the solution into the channel with the microtubules.
3. The motility of microspheres along microtubules can be visualized by LED-illuminated video-enhanced DIC (Fig. 2) (11) (see Note 11).

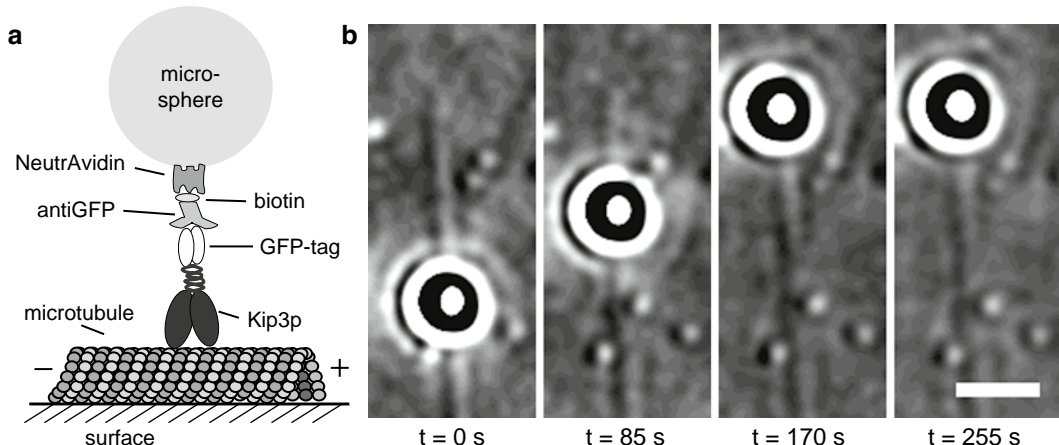


Fig. 2. Sandwich attachment for single-molecule microsphere assay. **(a)** Schematic of the experiment. **(b)** Time series of Kip3p-EGFP transporting an attached microsphere along a microtubule. The microsphere and microtubule are imaged using our video-enhanced LED-DIC (11). The microsphere stops at the microtubule end without detaching from the microtubule, which is characteristic for Kip3p (2). The scale bar corresponds to 2 μm .

4. Notes

1. Avidin, streptavidin, or NeutrAvidin can be used as biotin-binding protein. Note that they have different isoelectric points and thus a different net charge in your buffer of choice.
2. Streptavidin-coated microspheres can be purchased, for example from Bangs Laboratories (Fishers, USA), Polysciences (Warrington, USA), or Spherotech (Lake Forest, USA). Spherotech also sells functionalized microspheres of diameter $< 0.5 \mu\text{m}$.
3. Problems with purchased microspheres: First, purchased beads, especially with diameter $< 1 \mu\text{m}$ are often strongly clustered. Break clusters by sonicating the microspheres with a tip sonicator for 30 s in ice (a bath sonicator is often not powerful enough to break the clusters) or by creating shear forces by passing many times through a $27\frac{3}{4}\text{g}$ needle. Second, often the microsphere suspension still contains free biotin-binding proteins and the biotin-binding capacity varies strongly. Wash the beads before use and test their functionality by binding them, for example, to biotinylated microtubules in kinesin-gliding assays (8). Microspheres should bind easily by diffusion exclusively to biotinylated microtubules and not to the surface.
4. We worked with polystyrene microspheres purchased from Spherotech and with polystyrene microspheres that we functionalized by passive adsorption of NeutrAvidin. A detailed protocol for the passive adsorption is given in the main text.

5. Problems with passive adsorbed NeutrAvidin: First, proteins are not covalently bound to the microsphere surface but can unbind slowly especially when changing the buffer conditions. Second, the strength of the adsorption depends on the surfactants used by the supplier. Third, if the protein detaches slowly from the surface, it is difficult to separate the microspheres from the biotin-binding protein (see Note 10).
6. Use five to ten times more protein than necessary to form a protein monolayer on the microsphere surface (see Bangslabs TechNote 204 for surface-binding capacity of various proteins <http://www.bangslabs.com/literature/technotes>).
7. You can upscale the amount of beads used in this protocol according to the amount of available antibody. It is easier to work with larger amounts due to loss of microspheres on the tube surface during the washing steps.
8. The biotin in the wash buffer B saturates the remaining free biotin-binding sites of the NeutrAvidin. If concentrations of biotin are too high, biotin will compete the biotinylated antibodies off the microsphere!
9. We used a monoclonal antibody against GFP produced in our institute that we biotinylated with the EZ-Link NHS-PEO Solid Phase Biotinylation kit. Commercially available biotin-conjugated antibodies can also be used, for example the Penta-His Biotin-conjugated antibody from Qiagen.
10. Free biotin-binding proteins in the microsphere suspension lead to the formation of protein aggregates and microsphere clusters after the addition of biotinylated antibodies to the microsphere suspension (biotin-binding proteins have four biotin-binding sites, and the antibodies are biotinylated at multiple sites).
11. Functional attachment is controlled by comparing *in vivo* speeds and, in the case of the bead and gliding assays, we checked speeds against single-molecule TIRF data.

Acknowledgments

The authors acknowledge the input of members of the Howard, Schäffer, and Diez labs in the development of these protocols.

References

1. Allen, R. D., Weiss, D. G., Hayden, J. H., Brown, D. T., Fujiwake, H., and Simpson, M. (1985) Gliding movement of and bidirectional transport along single native microtubules from squid axoplasm – Evidence for an active role of microtubules in cytoplasmic transport. *Journal of Cell Biology* 100, 1736–1752.

2. Vale, R. D., Schnapp, B. J., Reese, T. S., and Sheetz, M. P. (1985) Organelle, bead, and microtubule translocations promoted by soluble factors from the squid giant-axon. *Cell* **40**, 559–569.
3. Howard, J., Hudspeth, A. J., and Vale, R. D. (1989) Movement of microtubules by single kinesin molecules. *Nature* **342**, 154–158.
4. Block, S. M., Goldstein, L. S. B., and Schnapp, B. J. (1990) Bead movement by single kinesin molecules studied with optical tweezers. *Nature* **348**, 348–352.
5. Lawrence, C. J., Dawe, R. K., Christie, K. R., Cleveland, D. W., Dawson, S. C., Endow, S. A., et al. (2004) A standardized kinesin nomenclature. *Journal of Cell Biology* **167**, 19–22.
6. Bormuth, V., Varga, V., Howard, J., and Schäffer, E. (2009) Protein Friction Limits Diffusive and Directed Movements of Kinesin Motors on Microtubules. *Science* **325**, 870–873.
7. Varga, V., Leduc, C., Bormuth, V., Diez, S., and Howard, J. (2009) Kinesin-8 Motors Act Cooperatively to Mediate Length-Dependent Microtubule Depolymerization. *Cell* **138**, 1174–1183.
8. Nitzsche, B., Bormuth, V., Brauer, C., Howard, J., Ionov, L., Kerssemakers, J., Korten, T., Leduc, C., Ruhnow, F., and Diez, S. Studying Kinesin Motors by Optical 3D-Nanometry in Gliding Motility Assays. *Methods in Cell Biology* **95**, 247–271.
9. Gell, C., Bormuth, V., Brouhard, G. J., Cohen, D. N., Diez, S., Friel, C. T., Helenius, J., Nitzsche, B., Petzold, H., Ribbe, J., Schäffer, E., Stear, J. H., Trushko, A., Varga, V., Widlund, P. O., Zanic, M., and Howard, J. Microtubule Dynamics Reconstituted In Vitro and Imaged by Single-Molecule Fluorescence Microscopy. *Methods in Cell Biology* **95**, 221–245.
10. Schäffer, E., Norrelykke, S. F., and Howard, J. (2007) Surface forces and drag coefficients of microspheres near a plane surface measured with optical tweezers. *Langmuir* **23**, 3654–3665.
11. Bormuth, V., Howard, J., and Schäffer, E. (2007) LED illumination for video-enhanced DIC imaging of single microtubules. *Journal of Microscopy-Oxford* **226**, 1–5.

Chapter 3

Studying Kinesin's Enzymatic Cycle Using a Single-Motor Confocal Motility Assay, Employing Förster Resonance Energy Transfer

Zdenek Lansky and Erwin J.G. Peterman

Abstract

Kinesin is an essential eukaryotic protein that drives intracellular transport of cargo, such as vesicles and organelles. It is the smallest motor protein known that converts free energy obtained from ATP hydrolysis into mechanical work, by stepping along microtubules. The enzymatic cycle of kinesin is tightly coupled to mechanical action. How kinesin's two identical motor domains (that both bind and hydrolyze ATP and bind to a microtubule) bring about motility has been the subject of much research. Recently, we have developed and applied a single-motor motility assay based on confocal fluorescence microscopy to measure changes in distance and orientation of the two motor domains during processive walking using Förster resonance energy transfer. The key benefit of this approach is its unprecedented time resolution of about 0.1 ms. In this chapter, we explain our approach in detailed protocols.

Key words: Kinesin, FRET, Single-molecule fluorescence, Correlation analysis, Motility assays

1. Introduction

Kinesin-1 (hereafter called kinesin) is the founding member of a large superfamily of proteins involved in intracellular transport, microtubule (MT) maintenance, and cell division (1). Kinesin is a key driver of intracellular transport of cargo, such as vesicles and organelles along the microtubules. It effectively converts the free energy released by the hydrolysis of ATP into mechanical work. Kinesin is processive: it makes hundreds of 8 nm steps along a microtubule, in the plus-end direction, before releasing (2, 3). The minimal unit that can step processively is homodimeric, consisting of a long tail with two motor domains on one end containing the

catalytic centers for ATP hydrolysis and microtubule binding. Kinesin's stepping velocity depends on ATP concentration and can be described with Michaelis–Menten kinetics (4). At cellular, saturating ATP concentrations, the velocity is on the order of 0.8 $\mu\text{m/s}$, corresponding to a stepping cycle duration of ~ 10 ms. The mechanical action of the motor is tightly coupled to the enzymatic cycle. Different states in the chemical cycle with distinct affinity for the microtubule and distinct conformation can be discerned (4). It has been the subject of many research efforts to uncover the exact mechanism by which the two motor domains work together to bring about processive motility. Much progress has been made using a wide variety of methods, e.g., steady-state and pre-steady-state enzyme kinetics, mutation analysis, X-ray crystallography, and motility assays. Particularly revealing have been single-molecule motor assays, the development of which has gone hand-in-hand with the discovery and characterization of kinesin (5). Two key approaches can be discerned. First, optical trapping assays, in which a microsphere that can be held in the trap is attached to a kinesin molecule (6). Stepping and force generation (due to movement out of the center of the harmonic potential well formed by the trap) by kinesin can be measured with nm and pN accuracy, with a time resolution down to approximately milliseconds (7). Many important results have been obtained in this way, but the approach has an important limitation: it only reports on the position of the attachment point of the microsphere to the motor, which is in most cases the long tail of the motor, the center of mass of kinesin. Thus, optical trapping experiments are not very well suited to unravel how the individual motor domains cooperate in kinesin action. A second approach is single-molecule fluorescence microscopy, which, in principle, stands a better chance; probes can be attached to the motor domains (8), their orientation can be measured using fluorescence polarization (9), and the distance between the motor domains with Förster resonance energy transfer (FRET) (10). In most applications, however, wide-field fluorescence methods employing CCD cameras have been used, with intrinsically limited time resolution (maximal frame rates of about 100/s, about equal to the stepping rate of kinesin). In order to decipher what is exactly going on during a single stepping cycle a much better time resolution is required. We have recently developed a different single-molecule fluorescence approach with a time resolution of about 0.1 ms (11–13). In this approach, we do not employ a CCD camera, but we use an avalanche photodiode as a single-point detector using a confocal fluorescence microscope. The assay we employ is depicted in Fig. 1a. The confocal spot is aimed at a microtubule; fluorescently labeled kinesins walking over this microtubule will walk through the spot and emit fluorescence, which can be detected with high time resolution. In order to measure changes in distance

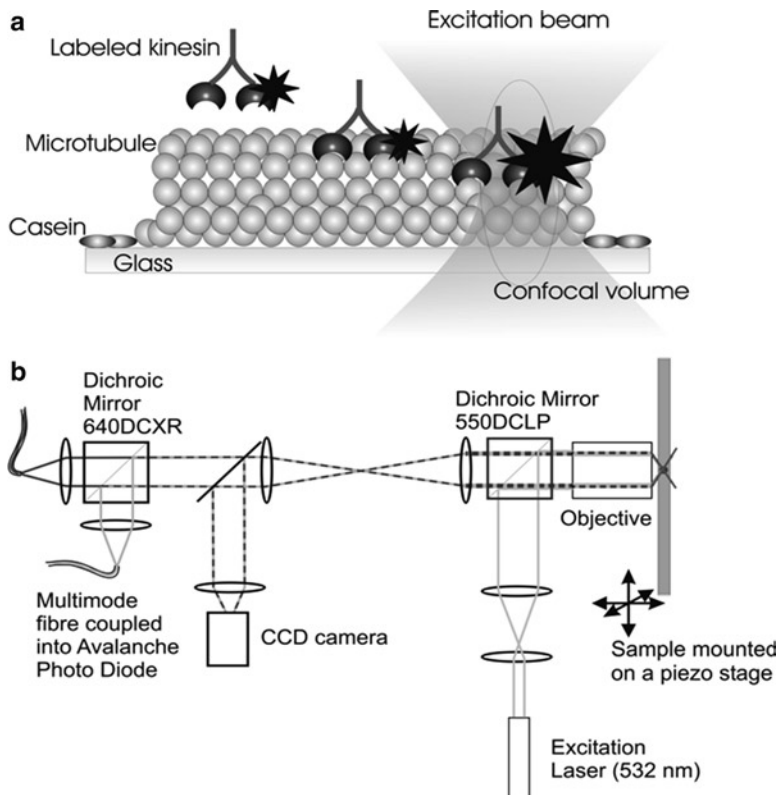


Fig. 1. Schematic representation of the single-molecule assay and setup. (a) Confocal spot is positioned on an MT, labeled kinesin binds to the MT and emits fluorescence as it walks through the confocal spot (drawing not to scale). (b) Sample is excited with 532 nm laser light, emission signal is filtered by 550DCLP dichroic and either imaged on a CCD camera or split into donor and acceptor channels by a dichroic mirror and focused onto the cores of two multimode optical fibers connected to the detectors.

and relative orientation of the two motor domains during processive stepping, we have employed FRET between a donor fluorophore attached to one motor domain and an acceptor on the other (12). Using this approach, we have resolved an intermediate in the stepping process; the stepping motor domain appears to wait for 3 ms, before passing the other motor domain. In the rest of this chapter, we explain in detail our approach. We focus on protein expression, purification and labeling, the experimental assay, the instrumentation used and data analysis. For these experiments, a modified and inducible kinesin gene on a bacterial vector is required. For specific cysteine-reactive labeling, it is necessary that all surface-exposed cysteins are modified for non-reactive residues and that a reactive cysteine is introduced in a proper location on the motor domain. For details, we refer to published protocols (12).

2. Materials

2.1. Kinesin Expression and Purification

1. LB plates: 10 g Bacto-Tryptone, 5 g yeast extract, 10 g NaCl, 15 g Bacto-agar for 1 L H₂O (see Note 1) supplemented with 25 µg/ml ampicillin.
2. LB liquid medium: 10 g Bacto-Tryptone, 5 g yeast extract, 10 g NaCl for 1 L H₂O supplemented with 25 µg/ml ampicillin.
3. 1 M isopropyl β-D-1-thiogalactopyranoside (IPTG), store at -20°C.
4. Lysis buffer: 20 mM pipes, 150 mM NaCl, 4 mM MgSO₄, pH 7.0, keep at room temperature. Before use, dissolve one tablet of Complete® (Roche) protease inhibitors in 50 ml lysis buffer.
5. Wash buffer: 20 mM pipes, 150 mM NaCl, 4 mM MgSO₄, 80 mM imidazole, pH 7.0 (adjust after addition of imidazole), keep on ice.
6. Elution buffer: 80 mM pipes, 4 mM MgSO₄, 50 mM NaATP, 300 mM imidazole, pH 7.0 (adjust after addition of imidazole), keep on ice.
7. PEM80: 80 mM pipes, 1 mM EGTA, 2 mM MgCl₂, pH 7.0, keep on ice.

2.2. Kinesin Labeling

1. Fluorescent dyes (donor and acceptor) as for example Alexa555 and Alexa647 (Invitrogen) dissolved in dimethyl sulfoxide (DMSO).
2. 100 mM ATP in H₂O, pH 7.0.
3. PEM80: 80 mM pipes, 1 mM EGTA, 2 mM MgCl₂, pH 7.0.
4. 100% sucrose solution: 0.1 g of sucrose, 100 µl of H₂O.
5. Tubulin (Cytoskeleton, Denver, CO).
6. 10 mM GTP in H₂O.
7. 10 mM taxol (paclitaxel) (Sigma-Aldrich) in DMSO, store in -20°C. 1 mM taxol in DMSO mix directly before use and keep at room temperature.
8. 100 mM solution of non-hydrolyzable ATP analog Adenosine 5'--(β,γ-imido)triphosphate tetrolithium salt (AMP-PNP) (Jena Bioscience, Jena, Germany).
9. 100 mM dithiothreitol (DTT).
10. Zeba protein desalting spin column (Thermo-Fisher, Rockport, IL).
11. Cushion solution: PEM80, 10 µM Taxol, 50% Glycerol, keep at room temperature.
12. Release buffer: 0.5 mM ATP, 200 mM KCl, 10 µM Taxol in PEM80, keep on ice.

2.3. Sample Preparation

1. 10 mM taxol in DMSO store in -20°C. 1 mM taxol in DMSO mix directly before use and keep at room temperature.
2. PEM12-taxol: 12 mM pipes, 1 mM EGTA, 2 mM MgCl₂, pH 7.0, 10 µM Taxol.
3. PEM80-Taxol: 80 mM pipes, 1 mM EGTA, 2 mM MgCl₂, pH 7.0, 10 µM taxol, keep at room temperature.
4. 100 mM GTP in H₂O.
5. Caseine solution 0.3 mg/ml in PEM12.
6. 50 mM TROLOX (Sigma-Aldrich) in water.
7. 10× oxygen scavenging mix: 200 mM glucose, 3 mg/ml glucose oxidase, 1 mg/ml catalase in PEM12, pH 7.0, mix just before use – keep on ice.
8. 10× ATP regeneration system: 10 mM phosphocreatine, 50 µg/ml creatine kinase, mix just before use – keep on ice.

2.4. Single-Molecule Confocal Fluorescence Setup (Fig. 1)

1. Excitation source is attenuated 532-nm laser beam of a Verdi V10 (Coherent, Santa Clara, CA).
2. Laser beam is circularly polarized with a quarter-λ plate and expanded six times using a beamexpander to fill the back aperture of the objective.
3. A lens (focal length 600 mm) on a flip mount is used to switch between wide-field (lens in the light path – laser beam focused in the back focal plane of the objective) and confocal (lens out of the light path – laser beam parallel) illumination.
4. Laser light is coupled into an inverted microscope (TE-2000-U Nikon, Tokyo, Japan), directed toward the 100× oil immersion objective with numerical aperture 1.3 (Nikon Plan Fluor) using a 550DCLP dichroic mirror (Chroma, Rockingham, VT).
5. In wide-field mode, emission is filtered by a HQ575/50 emission filter (Chroma, Rockingham, VT) and imaged on a 902H camera (Watec, Orangeburg, NY).
6. In confocal mode, the emission is split in two wavelength channels by a second dichroic mirror 645DCXR (Chroma, Rockingham, VT), filtered by emission filters HQ575/50 or HQ675/50 (Chroma, Rockingham, VT) and focused onto a multimode optical fiber (100-µm core diameter), serving as a pinhole ([14](#)), connected to an avalanche photodiode (APD) (SPQM-AQR-14, PerkinElmer, Vaudreuil, Quebec, Canada), resulting in digital pulses that are recorded and time tagged by an electronic counter-board (6602, National Instruments, Austin, TX) with 12.5-ns time resolution. Arrival times of detected photons are stored on a computer using custom-built Labview software (Labview 7.1, National Instruments).

7. Accurate positioning of the confocal spot within the sample and scanning of the sample is achieved using a feedback-controlled piezo translation stage (P-561, PI, Karlsruhe, Germany) with a custom-built sample holder mounted on top of the stage (see Note 2).

3. Methods

3.1. Kinesin Expression and Purification

1. Grow *E. coli* on plates. Streak LB plate containing 25 µg/ml ampicillin with -80°C stock of *E. coli* BL21 cells containing the kinesin-pET23b vector and grow overnight at 37°C.
2. Grow a small-volume liquid culture. Inoculate 10 ml liquid LB containing 25 µg/ml ampicillin with one colony, grow for several hours at 37°C while shaking (225 rpm) until the optical density (OD) of the culture (at 600 nm) is ~2.
3. Grow a large-volume liquid culture. Decant the small volume culture into a large flask with 500 ml LB containing 25 µg/ml ampicillin. Grow for 2–3 h at 37°C while shaking (225 rpm) to OD₆₀₀ = 0.5. Induce kinesin expression by addition of IPTG to a final concentration of 0.4 mM. Grow the culture overnight at room temperature while shaking (225 rpm).
4. Collect the cells. Spin the culture at 4,000×*g* for 20 min at 4°C, discard the supernatant.
5. Disrupt the cells. Resuspend the pellet in lysis buffer (4 ml of buffer per 1 g of pellet)+0.1 mg/ml lysozyme. Incubate for 15 min at room temperature and then 15 min on ice. The suspension should become viscous. Add 1 Unit of DNase per 1 ml of cell lysate. Disrupt the cells by a tip sonicator. Sonicate in ~10 s pulses (~1 min of sonication per 10 ml of lysate) on ice (see Note 3).
6. Collect proteins. Spin the cell lysate at 20,000×*g* for 20 min at 4°C. Keep the supernatant. Add imidazole to the supernatant to a final concentration of 20 mM.
7. Equilibrate Ni-NTA agarose beads. Fill an empty column with Ni-NTA Agarose beads. Use 1 ml of Ni-NTA (=2 ml 50% slurry) per 5 ml of the cell free extract. Wash the column with 2×1 Ni-NTA beads volume (BV) of lysis buffer. Wash the column with 1 BV of lysis buffer containing 20 mM imidazole (see Note 4).
8. Bind His-tagged kinesin to Ni-NTA beads. Incubate the supernatant from step 6 with equilibrated Ni-NTA agarose beads for 30–60 min at 4°C while slowly rotating (see Note 5).

9. Purify kinesin. Load the supernatant with Ni-NTA agarose beads onto a column and discard the flow-through. Wash the column with 2×1 BV of lysis buffer and discard the flow-through. Wash the column with 2×1 BV of wash buffer and discard the flow-through. Let the column almost run dry, then wash the column with 4×0.5 BV + 1×1 BV of elution buffer and collect the flow-through fractions. Keep the collected samples on ice.
10. Removal of low molecular weight contaminants. Equilibrate a PD-10 desalting column (GE Healthcare, Hoevelaken, Netherlands) with 25 ml of PEM80. Load sample on the column in total volume of 2.5 ml and let run dry (see Note 6). Load 3.5 ml of PEM80 and collect the flow-through in 0.5 ml fractions. Add glycerol to a final concentration of 20%. Aliquot and flash-freeze in liquid nitrogen. Store at -80°C .
11. Estimate the quantity and purity of kinesin. Run a SDS-PAGE gel using a 7.5% Tris-HCl Gel. Estimate the kinesin concentration from the SDS-PAGE gel using a protein of known concentration.

3.2. Kinesin Labeling

1. Dilute Alexa555 and Alexa647 in DMSO with H_2O to the required final concentration (see Note 7).
2. Label kinesin. Mix kinesin, Alexa555, Alexa647 and ATP to a final concentration of 40 μM . Incubate this mix for 3 h at 4°C in dark (see Note 8).
3. Polymerize and stabilize MTs. Incubate 2 mg/ml tubulin with 1 mM GTP in PEM80 at 36°C for 30 min (see Note 9). Add 1 mM taxol to a final concentration of 10 μM . Add 100 mM AMP-PNP to a final concentration of 0.5 mM. Mix gently and let cool down for a minute to room temperature.
4. Stop labeling reaction. Add 100 mM DTT to the kinesin-dye mix to a final concentration of 1 mM. Filter the sample using Zeba Protein Desalting Spin Column at 4°C .
5. MT-affinity purification of kinesin: Part 1 – binding kinesin to MTs. Add the labeled kinesin sample to the polymerized MTs and incubate on (not in) ice for 15 min. Load the sample into an ultracentrifuge tube, add 80 μl of cushion solution (see Note 10) underneath the sample using a very thin pipette point and spin for 10 min at $140,000 \times g$ at 4°C (see Note 11).
6. MT-affinity purification of kinesin: Part 2 – releasing kinesin from MTs. Remove supernatant and wash pellet twice with ~50 μl of PEM80 (see Notes 12 and 10). Resuspend the pellet in 50 μl of release buffer (pipette the solution slowly up and down, prevent foam formation) (see Note 10). Incubate the

solution in ice for 15 min to allow kinesin to release from the MTs. Add 80 μ l of cushion solution underneath the sample. Spin the sample for 10 min at 140,000 $\times g$ at 4°C (see Note 13). Take the supernatant, which contains labeled kinesin, add sucrose to a final concentration of 20%, aliquot and flash-freeze in liquid nitrogen, store at -80°C.

3.3. Sample Chamber Preparation

1. Cleaning coverslips and slides. Rinse coverslips (No. 1.5) and slides with H₂O. Put them in a 1 M KOH bath for 15 min while sonicating. Rinse them again with H₂O. Sonicate in an H₂O bath for 15 min. Rinse them with H₂O. Repeat the H₂O sonication and rinse steps two more times. Slides are stored in H₂O, blow them dry with nitrogen, before use.
2. Coating of coverslips with DETA (N1-[3-(trimethoxysilyl)-propyl]diethylenetriamine, Sigma-Aldrich). Use clean coverslips from step 1. Put coverslips in 1,000 \times diluted DETA solution in H₂O and sonicate for 15 min. Rinse with H₂O. Sonicate the coverslips in H₂O for 10 min. Rinse them with H₂O. Repeat the H₂O sonication and rinse steps two more times. Place slips in a holder into an oven at ~130°C till they are dry. Store the DETA-coated coverslips on filter paper in a Petri dish.
3. Create the sample chamber. Cut a couple of stripes out of double-sticky Scotch 3 M tape. Stick them side-by-side on a clean slide leaving ~2 mm space between two adjacent stripes. Stick a DETA-coated coverslip on top to create several ~10 μ l sample chambers on the same slide.

3.4. Sample Preparation

1. Polymerize and stabilize MTs. Incubate unlabeled tubulin, rhodamine-labeled tubulin (unlabeled:labeled tubulin ~15:1, final concentration of tubulin ~2 mg/ml) with 1 mM GTP in PEM80 at 36°C for 30 min. After polymerization, stabilize MTs with ~20 μ l of PEM80-taxol. Taxol-stabilized MTs can be stored at room temperature (in dark) for up to a week.
2. Dilute the stabilized MTs with PEM80-taxol and flush them into the sample chamber (see Note 14).
3. Passivate the glass surface. Flush 0.3 mg/ml caseine solution in the sample chamber and incubate it for 10 min at room temperature (see Note 15). Flush the sample chamber with ~20 μ l of PEM12-Taxol to remove casein that did not adhere to the surface.
4. Add kinesin to MTs. Dilute 10 \times oxygen scavenging system and 10 \times ATP regeneration system to the 1 \times concentration with PEM12-taxol, add labeled kinesin diluted with PEM12-taxol, add ATP to a final concentration of 1 mM, MgCl₂ to a final concentration of 1 mM and TROLOX to a final concentration of 5 mM. Seal the chamber with vacuum grease.

3.5. Single-Molecule Confocal Imaging of Kinesin

1. Wide field. Using the wide-field illumination and the CCD camera, locate a labeled MT in the sample.
2. Confocal scanning. Translate the sample to position the MT within 1 μm from the confocal spot. Switch to confocal illumination and APD signal acquisition. Scan a $\sim 1 \times 1 \mu\text{m}$ area of the sample around the current position of the confocal spot.
3. Find the center of an MT cross-section. Fit a Gaussian to the scanned cross-section of the MT and position the confocal spot to the maximum of the Gaussian. MT is now positioned within $\sim 20 \text{ nm}$ of the center of the confocal spot.
4. Bleach the fluorophores on the MT by applying a higher laser power for a while and then start measuring the fluorescent signal of labeled kinesins walking through the confocal spot.

3.6. Data Analysis

1. Time-bin the recorded photon arrival times. To browse through the data and localize events (a kinesin passing through the confocal spot), it is convenient to create intensity time traces using relatively large bins ($\sim 10 \text{ ms}$) (Fig. 2a). For further calculation of the correlation curves, use a bin size as small as allowed by the signal-to-noise ratio of the experiments ($\sim 0.1 \text{ ms}$ in most of our measurements).
2. Select events for further analysis. Only events that (a) are Gaussian, (b) show emission both in the donor and acceptor channel (and thus contain both donor and acceptor fluorophores), and (c) do not photo bleach before moving half-way through the confocal spot are selected for further analysis. Events, including $\sim 100 \text{ ms}$ of background signal on both sides are fitted with a Gaussian function. The fitted offset (dark counts and background fluorescence) is used for background correction during the calculation of correlation curves. The width of the fitted Gaussian is used for the estimation of kinesin's velocity, and the amplitude of the Gaussian is used to verify that only one donor and one acceptor fluorophore are attached to the kinesin.
3. Calculate correlation curves (Fig. 2b, c). Background-corrected fluorescence intensity traces of the donor, x_i , and the acceptor, x_j , binned at $\Delta t = 0.1 \text{ ms}$ are cross- ($i \neq j$) and autocorrelated ($i = j$) using:

$$G_{ij}(n\Delta t) = \sum_{k=0}^{2N-2} x_i(k\Delta t)x_j(n\Delta t + k\Delta t) \quad (1)$$

with N the total number of time bins of an event. Note that the cross- and autocorrelations obtained using Eq. 1 are not normalized.

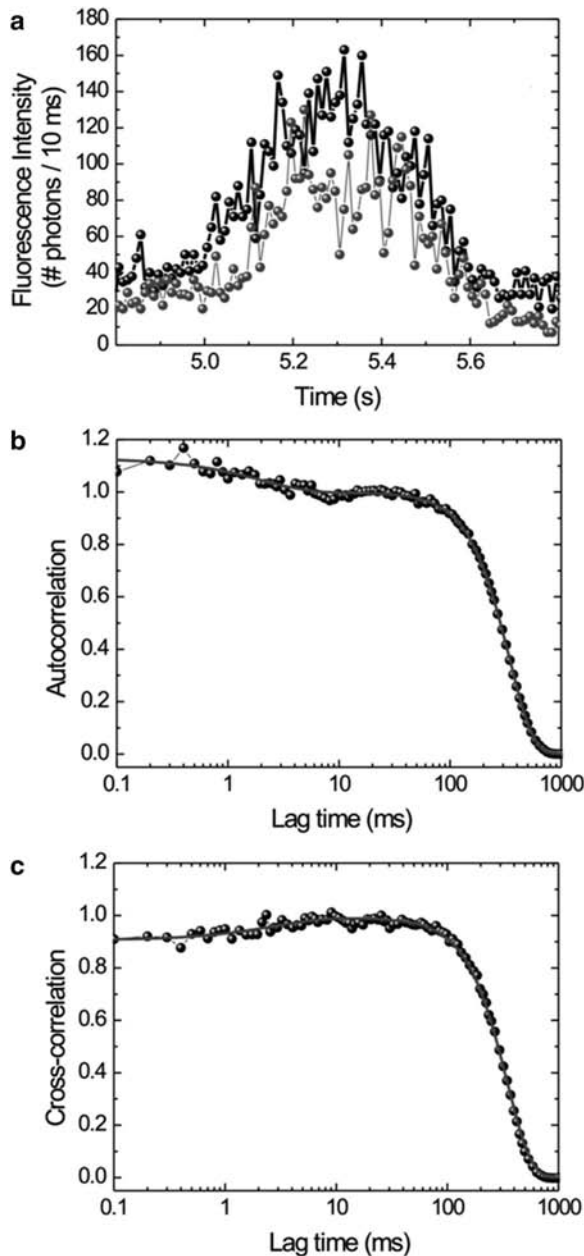


Fig. 2. Time traces and correlation curves of a single kinesin walking through the confocal spot. (a) Typical event due to a kinesin labeled with both a donor and an acceptor fluorophore. Donor signal is depicted in *black*, acceptor in *gray*. (b) Autocorrelation of the donor signal from panel (a). Short time-scale increase in autocorrelation reflects the fluctuations in fluorescence intensity due to switching between different FRET states. (c) Cross-correlation of donor and acceptor signals from panel (a). Note that the short time-scale part of the curve has now negative amplitude – a clear indication of FRET (donor and acceptor are anticorrelated). Both, auto and cross-correlation are fitted with Eq. 2.

4. Interpret the correlation curves. Auto and cross-correlation curves G of a donor and acceptor-labeled kinesin, for which the FRET efficiency switches between two states during the stepping cycle have two main components (Fig. 2b, c). (a) A short time-scale exponential component G_1 that is caused by intensity fluctuations due to switching between different FRET states and (b) a longer time-scale component G_2 that is caused by the fluorescence intensity change due to kinesin moving in, through and out of the confocal spot:

$$G(\tau) = G_1(\tau)G_2(\tau) \quad (2)$$

with:

$$G_1(\tau) = \left(1 + A \exp\left(-\frac{\tau}{T_{\text{FRET}}}\right) \right)$$

and

$$G_2(\tau) = N \left(1 + \frac{\tau}{T_T} \right)^{-1} \exp\left(-\frac{\tau^2}{\alpha T_{\text{step}}^2}\right) \quad (3)$$

T_{FRET} and A are the correlation decay constant and amplitude caused by switching between states with different intensity (caused by FRET). N is the amplitude of the correlation, α is a factor that describes the width of the confocal volume, and T_{step} is the average step time. The term involving T_T is empirical and corrects for distortions of time traces from ideal Gaussian shape. These can be due to various reasons, such as photo bleaching, landing of kinesin into the confocal spot, detachment of kinesin from the confocal spot, and the stochastic nature of stepping (11). For further calculations, only the autocorrelation of the donor fluorescence intensity is used, since the donor-signal fluctuations are a direct measure of the FRET efficiency changes and are not affected by cross talk between donor and acceptor channels (15). Cross-correlation curves are used as an additional qualitative measure as the FRET events cross-correlations have $A < 0$ (Fig. 2c).

3.7. Quantitative Interpretation of the Autocorrelation Data

For further interpretation of the donor autocorrelation, a kinetic model needs to be assumed. Depending on the level of complexity of the model different approaches can be taken. A model involving two states, one (F) with FRET, the other one (NF) without, can be readily solved analytically (adapted from ref. 16).

$$A = \frac{k_{\text{NF}}k_F E_F^2}{(k_F + k_{\text{NF}}(1 - E_F))^2} \quad (4)$$

$$T_{\text{FRET}} = \frac{1}{(k_{\text{NF}} + k_{\text{F}})} \quad (5)$$

$$T_{\text{step}} = \frac{1}{k_{\text{F}}} + \frac{1}{k_{\text{NF}}} = \frac{1}{k_{\text{step}}} \quad (6)$$

With k_{NF} and k_{F} the rates out of the NF and F state, respectively, E_{F} is the FRET efficiency of the F state, k_{step} is the step rate, and T_{step} is the average step time of the walking kinesin. Here, the FRET efficiency of the NF state, E_{NF} , is set to 0. These equations are exponential and can be used to calculate model parameters directly from exponential fits to the data.

Autocorrelations resulting from more complex models (involving three or more states) are nonexponential. Already a three-state model is rather cumbersome to solve analytically; and in general, the data is not of good enough quality to allow direct fitting of these complex functions involving many parameters. We have chosen to use another approach, stochastic modeling of time traces, assuming three-state or more complex models. We fit the obtained autocorrelation curves from modeled time traces with an exponential and compare the fitting parameters with those obtained from the experimental autocorrelation curves (12, 13). In this analysis, we take into account the ATP-concentration dependence (following Michaelis–Menten kinetics) of the kinesin step time. For this modeling, we have written a LabView program that allows testing of different kinetic models, assuming different ATP-dependent states and different FRET efficiencies.

4. Notes

1. All solutions should be prepared with demineralized water with a resistivity of at least 18.2 MΩ cm.
2. The thermal and mechanical stability of the setup is essential. This can be achieved by use of an air-damped optical table. It is preferable to use a CCD camera that does not use forced convection cooling or produce a substantial amount of heat.
3. Check the temperature of the lysate regularly during sonication. Do not allow the lysate to heat up.
4. Make sure that the column never runs dry.
5. Do not allow the Ni-NTA beads to sediment.
6. In case the sample has a volume of less than 2.5 ml, add buffer up to a total volume of 2.5 ml.

7. The final concentration of dye in the labeling mix (step 2) should be ~5× more than the concentration of kinesin. The dye concentration can be determined using a spectrophotometer.
8. Start incubation of the tubulin mix needed in step 3 after 2.5 h.
9. The final concentration of tubulin in the MT-affinity purification (steps 5 and 6) should be approximately 1.5× the concentration of kinesin.
10. The volumes of cushion solution and buffer for washing and resuspension of pellet (step 6) are dependent on the amount of sample and on the volume of centrifuge tubes and can be scaled accordingly. We generally use ~80 µl of sample in 5 × 20 mm polyallomer Ultrafuge tubes (Beckman-Coulter, Brea, CA).
11. In some cases, the pellet can be visibly colored, due to labeled kinesin attached to MTs. This depends, however, strongly on concentration. Absence of color should not be taken as a sign that no labeled kinesin is present in the sample.
12. Great care should be taken not to disrupt the pellet.
13. If a pellet was visible at the end of the step 5, it should now have lost most of its color, since it should no longer contain kinesin, only MTs.
14. Check the MTs under a microscope and adjust the concentration (or labeled tubulin fraction) if required. It is desirable to have ~10 MTs in a field of view.
15. Use stripes of filter paper to suck the liquid out from the sample chamber while flushing in the casein from the other side of the chamber. Be careful not to introduce air bubbles. The sample should always be immersed in buffer.

References

1. Vale, R. D. (2003) The Molecular Motor Toolbox for Intracellular Transport. *Cell* **112**, 467–480.
2. Block, S. M. (2007) Kinesin motor mechanics: Binding, stepping, tracking, gating, and limping. *Biophys. J.* **92**, 2986–2995.
3. Gengerich, A., and Vale, R. D. (2009) Walking the walk: how kinesin and dynein coordinate their steps. *Curr. Opin. Cell Biol.* **21**, 59–67.
4. Cross, R. A. (2004) The kinetic mechanism of kinesin. *Trends Biochem. Sci.* **29**, 301–309.
5. Kapitein, L. C., and Peterman, E. J. G. (2009) Single Molecule Experiments and the Kinesin Motor Protein Superfamily: Walking Hand in Hand, in *Single Molecule Biology*. pp 35–60, Academic Press, New York.
6. Visscher, K., Schnitzer, M. J., and Block, S. M. (1999) Single kinesin molecules studied with a molecular force clamp. *Nature* **400**, 184–189.
7. Carter, N. J., and Cross, R. A. (2005) Mechanics of the kinesin step. *Nature* **435**, 308–312.
8. Yildiz, A., Tomishige, M., Vale, R. D., and Selvin, P. R. (2004) Kinesin walks hand-over-hand. *Science* **303**, 676–678.
9. Asenjo, A. B., and Sosa, H. (2009) A mobile kinesin-head intermediate during the ATP-waiting state. *Proc. Natl. Acad. Sci. USA* **106**, 5657–5662.
10. Mori, T., Vale, R. D., and Tomishige, M. (2007) How kinesin waits between steps. *Nature* **450**, 750–U715.

11. Verbrugge, S., Kapitein, L. C., and Peterman, E. J. G. (2007) Kinesin moving through the spotlight: Single-motor fluorescence microscopy with submillisecond time resolution. *Biophys. J.* **92**, 2536–2545.
12. Verbrugge, S., Lansky, Z., and Peterman, E. J. G. (2009) Kinesin’s step dissected with single-motor FRET. *Proc. Natl. Acad. Sci. USA* **106**, 17741–17746.
13. Verbrugge, S., Lechner, B., Woehlke, G., and Peterman, E. J. G. (2009) Alternating-Site Mechanism of Kinesin-1 Characterized by Single-Molecule FRET Using Fluorescent ATP Analogues. *Biophys. J.* **97**, 173–182.
14. Haustein, E., and Schwille, P. (2003) Ultrasensitive investigations of biological systems by fluorescence correlation spectroscopy. *Methods* **29**, 153–166.
15. Ha, T., Enderle, T., Ogletree, D. F., Chemla, D. S., Selvin, P. R., and Weiss, S. (1996) Probing the interaction between two single molecules: Fluorescence resonance energy transfer between a single donor and a single acceptor. *Proc. Natl. Acad. Sci. USA* **93**, 6264–6268.
16. Torres, T., and Levitus, M. (2007) Measuring conformational dynamics: A new FCS-FRET approach. *J. Phys. Chem. B* **111**, 7392–7400.

Chapter 4

Fluorescence Imaging with One Nanometer Accuracy: In Vitro and In Vivo Studies of Molecular Motors

Melinda Tonks Hoffman, Janet Sheung, and Paul R. Selvin

Abstract

Traditional microscopy techniques are limited by the wave-like characteristics of light, which dictate that about 250 nm (or roughly half the wavelength of the light) is the smallest distance by which two identical objects can be separated while still being able to distinguish between them. Since most biological molecules are much smaller than this limit, traditional light microscopes are generally not sufficient for single-molecule biological studies. *Fluorescence Imaging with One Nanometer Accuracy* (FIONA) is a technique that makes possible localization of an object to approximately one nanometer. The FIONA technique is simple in concept; it is built upon the idea that, if enough photons are collected, one can find the exact center of a fluorophore's emission to within a single nanometer and track its motion with a very high level of precision. The center can be localized to approximately $(\lambda/2)/\sqrt{N}$, where λ is the wavelength of the light and N is the number of photons collected. When $N=10,000$, FIONA achieves an accuracy of 1–2 nm, assuming the background is sufficiently low. FIONA, thus, works best with the use of high-quality dyes and fluorescence stabilization buffers, sensitive detection methods, and special microscopy techniques to reduce background fluorescence. FIONA is particularly well suited to the study of molecular motors, which are enzymes that couple ATP hydrolysis to conformational change and motion. In this chapter, we discuss the practical application of FIONA to molecular motors or other enzymes in biological systems.

Key words: FIONA, Molecular motors, Single-molecule tracking, TIRF microscopy

1. Introduction

In order to conduct single-molecule studies, researchers are confronted with the diffraction limit of light. For visible optical microscopy, this limit is $\lambda/(2 \times NA)$, where λ (the wavelength of the light) is approximately 500 nm and NA (the numerical aperture of the microscope objective) is about 1.4. Diffraction-limited spots in a traditional light microscope are, therefore, generally larger

than 200 nm in diameter – much bigger than the molecules of interest. This resolution limit means that two identical fluorophores in close proximity can, therefore, not be distinguished using traditional light microscopy unless they are greater than ~250 nm apart. In recent years, some modern techniques, often called “super-resolution” techniques, have to varying degrees bypassed this limit (1, 2). Although extremely useful for some applications, most of these techniques require relatively slow timescales, multiple lasers, the use of photoswitchable dyes, and extensive postprocessing. In this chapter, we discuss *Fluorescence Imaging with One Nanometer Accuracy* (FIONA), a simpler but versatile technique for achieving nanometer precision at biologically relevant timescales. Unlike the superresolution techniques mentioned above, FIONA does not improve the resolution of fluorophores in close proximity but instead improves the localization accuracy of a single fluorophore.

We have shown that FIONA enables the localization of a single molecule to within 1.5 nm (3) and with 1–500 ms temporal resolution (4). Data can be taken inside or outside of live cells at a timescale that is physiologically relevant, making FIONA an extremely valuable tool in the toolbox of single-molecule research techniques. The principle behind FIONA is simple. In a typical FIONA measurement, a fluorophore is attached to some biological molecule of interest. As the biological molecule (and the attached fluorophore) moves through space, the center of its emission is continuously localized, making it possible to track single biomolecules with great precision. At the core of the technique is the ability to collect a large number of photons emitted by a single fluorophore. When we plot the number of photons emitted by a fluorophore versus its position in the x - y plane (Fig. 1), we can localize the center of the resulting Airy function much more accurately than the width of the function. (A 2D Gaussian function is often used to approximate the Airy function, with little error). Theoretically, the accuracy with which it is possible to locate the center is the standard error of the mean, i.e., the standard deviation divided by the square root of the total number of counts (5). Thus, the accuracy of FIONA depends on the collection of large numbers of photons. For 10,000 photons collected, for example, one obtains an accuracy of approximately $250/100 = 2.5$ nm.

To be slightly more quantitative, in practice, the accuracy depends on three factors, as shown in Eq. 1: the number of photons (N), the effective pixel size of the detector, a , which is the pixel size divided by magnification, and the standard deviation of the background, b .

$$\sigma = \sqrt{\left(\frac{s_i^2}{N} + \frac{a^2 / 12}{N} + \frac{8\pi s_i^4 b^2}{a^2 N^2} \right)} \quad (1)$$

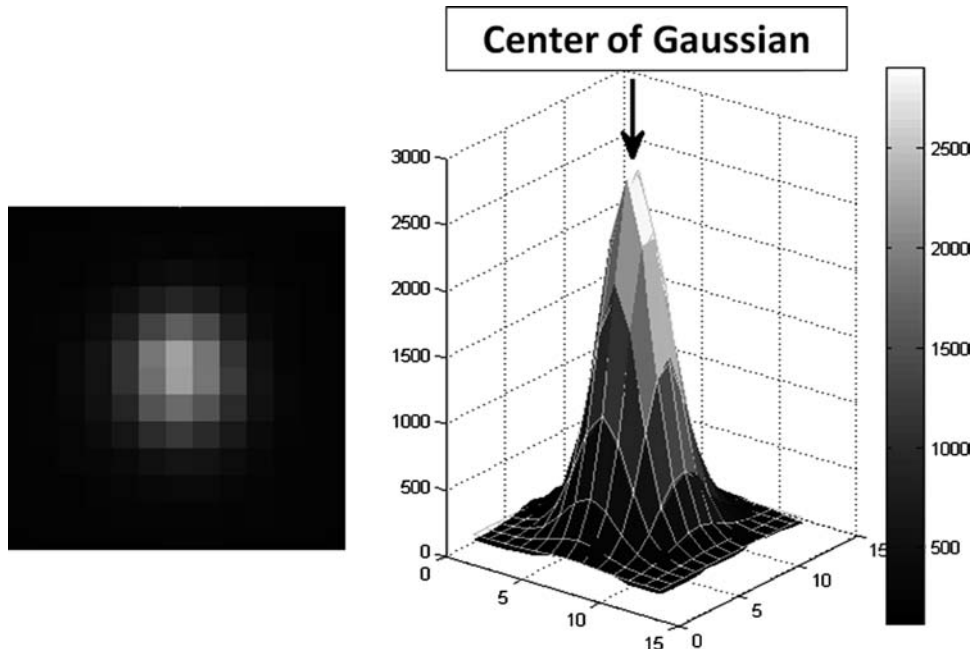


Fig. 1. Sample of a cropped fluorophore PSF captured with a CCD camera (**left**), and the same PSF plotted in three dimensions, intensity as a function of (x, y) . Note that a good PSF should be circularly symmetric and the peak should be significantly higher than the background. A Gaussian function is fitted to the PSF, shown as a mesh overlay in the plot.

σ is the uncertainty or standard error of the mean, a is the effective pixel size of the detector (pixel size divided by magnification), b includes both the background fluorescence and the detector noise, and s_i is the width of the distribution (which is approximately 250 nm for a diffraction limited spot of visible light) in direction i , where $i=x$ or y . The first term ($\frac{s_i^2}{N}$) is due to photon noise, the second term is the effect of the finite pixel size of the detector, and the third term is the effect of background. Assuming an appropriate effective pixel size (of 80–120 nm, or 16 μm divided by the magnification, e.g., 160 \times) is used, the second term does not contribute significantly. When appropriate techniques are used to minimize background noise (as discussed below), the first term (photon noise) is the limiting factor in a FIONA measurement.

Thus, it is crucial to both decrease the background and collect as many photons as possible from the single fluorophores to obtain the greatest precision of localization possible. Several considerations must be made: first, an appropriate fluorophore must be chosen – for accurate FIONA measurements to be made, the fluorophore must be sufficiently bright and highly photostable. Oxygen scavenging systems and other chemicals are generally needed to increase the lifetime and stability.

Second, background fluorescence must be minimized. This is typically achieved by the use of a Total Internal Reflection (TIR)

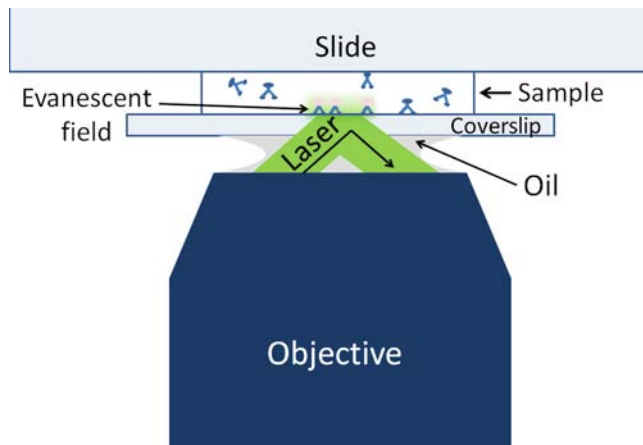


Fig. 2. When the incoming laser is at the correct critical angle for its wavelength, it is totally reflected by at the glass–water interface, and only an evanescent field penetrates into the sample. This evanescent field loses half of its intensity every ~50 nm into the sample, so effectively only fluorophores within ~100 m of the coverslip will be excited. This greatly minimizes background signal and will not photobleach dyes in the bulk of the sample. The oil between the sample chamber and the objective has the same index of refraction as the glass and eliminates refraction of the laser, which would occur if the laser traveled through air.

microscope, which allows the imaging of molecules that are attached to a surface while excluding fluorescence in the solution above the surface. With traditional epifluorescence microscopy, a laser beam is used to excite fluorophores in a sample; however, many fluorophores in solution above or below the focus plane are also excited, leading to high levels of background fluorescence and, therefore, a poor signal-to-noise ratio. Total Internal Reflection (TIR) microscopy solves this problem by sending the laser beam in to the glass–water interface at such a steep angle that TIR is achieved. With TIR, only a thin layer of light (of exponentially decreasing magnitude) called the evanescent wave penetrates into the sample. This evanescent wave excites fluorophores close to the surface of the slide, but will not excite any fluorophores more than about 100 nm away from the surface. Hence, the excellent signal-to-noise ratio and high levels of photon collection required for the FIONA technique are achieved (see Fig. 2). Careful cleaning of sample chambers and efficient surface blocking to avoid nonspecific binding of fluorescent molecules must also be employed to minimize background fluorescence, since impurities on the surface are within the evanescent wave and can decrease the signal-to-noise ratio, even when using TIR microscopy.

Third, sensitive photon detection is required, usually in the form of an electron multiplied charge-coupled device (EMCCD) camera. Back-thinning of EMCCD cameras allows a quantum efficiency of ~90%. In addition, electronic cooling to ~−70°C virtually eliminates dark current, while electron multiplying enables very sensitive detection of photons.

Once a sufficient number of photons can be collected, a researcher can use FIONA data analysis techniques to localize and track the particles in the images that have been recorded. A localization measurement with a standard error of 1–2 nm can be achieved using a laser in the visible spectrum, an effective pixel size of 80–120 nm (see Subheading 3.2), a TIR microscope and an EMCCD camera to minimize background, and a sufficiently bright fluorophore to obtain ~10,000 photons per frame (6). Finally, additional statistical analysis techniques such as Student's *t*-test or Hidden Markov Models can be used to find the steps in the trajectories (if applicable) to determine step size, dwell times, and so forth. These tools allow single-molecule tracking of molecular motors or other proteins *in vivo* or *in vitro* excellent spatial and temporal precision.

Although a number of different enzymes can be studied using FIONA, the technique is particularly well suited to the study of molecular motors, which are enzymes that couple ATP hydrolysis into conformational change and motion. Using the techniques described in this chapter, they can be precisely tracked as they move in a cell or in an artificial cell-like environment. For instance, a myosin or kinesin molecule can be tracked as it walks on actin or microtubules inside a living cell, or laid down on a prepared coverslip. The spatial and temporal precision gained by applying the FIONA technique reveals valuable information about the motors, such as the distance traveled with each step, the pause times between steps, or even details such as whether the monomers pass each other with each step (3) – information that cannot be determined using traditional microscopy-based measurements. The study of molecular motors and other types of enzymes can be greatly enriched by the precise localization measurements that FIONA makes possible.

2. Materials

2.1. TIR Setup

TIR microscopes are commercially available from a number of companies (Leica Microsystems, Olympus, Zeiss, and TIRF Technologies). However, for greatest versatility and to minimize cost, a custom-built TIR microscope can be constructed using an inverted microscope on an optical table (see (7)). We list the major components needed here and give a discussion of the major considerations involved in Subheading 3.1.

1. High-gain EMCCD camera: iXon EM+, DV-897E-CS0 (Andor).
2. Inverted microscope: Olympus IX70 or IX71 (Olympus).
3. Laser of desired wavelength (>10 mW power output): 633 nm, He–Ne laser, 35 mW, model #35-LHP-928-249 (Melles Griot) or a 532-nm diode laser, NdYAG, 75 mW, model #GCL-075-L (CrystaLaser).

4. High numerical aperture objective lens: PlanApo 100 \times , 1.45 NA ∞ /0.17 (Olympus) or ApoTIR 100 \times , 1.49 NA (Nikon).
5. TIR lens: plano-convex lens, AR coated, 30 cm focal length (ThorLabs).
6. Dichroic mirrors and filters: Cy3 – Q565LP dichroic (Chroma) with HQ585/70 M band-pass emission filter (Chroma), Cy5 – Q660LP dichroic (Chroma) with HQ690/90 M band-pass emission filter (Chroma), GFP – Q505LP dichroic (Chroma) with HQ525/50 M band-pass emission filter (Chroma).
7. General purpose optics and mechanics: mirrors, lenses, beam expanders, optical table, etc. (ThorLabs and Newport are good resources).
8. All parts should be set up on an optical table with pneumatically isolated legs: RS4000TM table and I-2000 Lab LegsTM (Newport Corp.).
9. Bead slide to check alignment: prepare a sample with some beads stuck to the surface and some floating in solution. Choose beads that have spectra similar to that of your fluorophore – for instance, if in the experiment Cy3 dye will be imaged, use Nile Red beads (#F-8784, Invitrogen). See Subheading 3.1 for instructions on how to prepare a bead slide. Once prepared, the openings of the sample chamber can be epoxied over, and the bead sample can be stored at room temperature in the dark for about a month (or until fluid evaporates).

2.2. Slides and Coverslips

1. Glass slides: 30103X1, 0.93–1.05 mm (Gold Seal Microslides).
2. Coverslips: 12-544-A 22X30-1.5 (Fisherbrand). It has the right thickness for 1.45 NA objective lenses.
3. Glass slide holder: 900570 (Wheaton Scientific).
4. Teflon coverslip holder: C-14784 (Invitrogen).
5. 1 M KOH. Store at room temperature.

2.3. PEGylation of Slides and Coverslips

1. Aminosilane: CAS 1760-24-3 (United Chem. Tech.). This should be stored at -20°C and brought to room temperature before opening.
2. mPEG-Succinimidyl Valerate: # MPEG-SVA-5000-1g, MW 5,000 (Laysan Bio, Inc.). Should be stored under nitrogen or argon at -20°C and brought to room temperature before opening.
3. Biotin-PEG-SC: Biotin-PEG-SC-5000-1g, MW 5,000 (Laysan Bio, Inc.,) – see storage note for item 2 above. Biotin PEG is used if immobilization of avidin-conjugated biomolecules is desired.
4. 1 M KOH. Store at room temperature.

5. 10 mM Sodium bicarbonate buffer (prepared in distilled water). This must be made fresh for each PEGylation preparation.
6. Acetic acid (glacial).

2.4. Sample Chamber

1. Cleaned slides and coverslips (see above).
2. Double-sided permanent adhesive tape.
3. Electric drill and $\frac{3}{4}$ mm diamond drill bit (Optional).
4. Quick-drying epoxy resin (such as “5-min” variety) (Optional).

2.5. Preparing a Sample Chamber and Acquiring Data

1. Labeled biological molecule of interest (see Note 1).
2. Axonemes (8) (or other molecular “track” appropriate to the specific experiment).
3. 20 mg/mL casein. Prepare stock by dissolving in motility buffer overnight, centrifuging at $245,000 \times g$ for 30 min, and filtering through 0.22- μm syringe filters to remove insoluble components. Measure protein concentration and dilute as necessary to give 20 mg/mL final concentration. Flash-freeze in liquid nitrogen and store at -80°C for 1 year (9).
4. BSA: Bovine Serum albumin. Dissolve at 10 mg/mL BSA in motility buffer and filter with a 0.22 μm syringe filter. Store at 4°C for up to 3 months.
5. Mg-ATP: Adenosine 5'-triphosphate magnesium salt. Prepare 100 mM ATP stock in motility buffer. Aliquot and flash-freeze in liquid nitrogen and store at -20°C or -80°C . Use each aliquot only once (do not refreeze).
6. Motility buffer BRB80: 80 mM PIPES, 1 mM EGTA and 1 mM MgCl_2 . Prepare 5 \times solution and filter with a 0.22- μm filter. Store at room temperature for a few months. see Note 2.
7. ATP regenerating system: Creatine kinase (#127566, Roche). Prepare 200 U/mL solution in motility buffer. Aliquot and flash-freeze in liquid nitrogen and store at -20°C for up to a year. Use each aliquot only once (do not refreeze). Creatine phosphate (Sodium creatine phosphate dibasic tetrahydrate, #27920, Sigma). Prepare 200 mM solution in motility buffer. Aliquot and flash-freeze in liquid nitrogen and store at -20°C for up to a year. Use each aliquot only once (do not refreeze).
8. Deoxygenation system – PCA and PCD (10): PCA (3,4-Dihydroxybenzoic acid, #37580, Fluka). Prepare 50 mg/mL solution in distilled water, adding 1 M NaOH as needed to dissolve PCA. Adjust pH to 7.4 with NaOH. Aliquot and flash-freeze in liquid nitrogen and store at -20°C for 6 months. Thaw aliquots as needed. Aliquots can be stored at 4°C for about a week. PCD (Protocatechuate 3,4-dioxygenase, #P8279, Sigma). Prepare 5 μM solution in 50% glycerol, 50 mM NaCl, 100 mM Tris, pH 8.3. Store at -20°C for up to several months.

9. DTT: Dissolve 1 M DDT stock in BRB80 buffer, make 10 μ L aliquots, and flash-freeze in liquid nitrogen. Store aliquots at -20°C or -80°C for no more than 6 months.
10. Final imaging solution: 2.5 mM PCA, 50 nM PCD, 1 mM DTT, 1 mM MgATP (pH 7.0), 2 U/mL creatine kinase (optional, see Note 11), 2 mM creatine phosphate (optional, see Note 11), 10 mg/mL BSA, desired concentration of labeled molecular motor, all in motility buffer, such as BRB80. This imaging solution CANNOT be made in advance but must be mixed during the protocol. See Subheading 3.5 step 1 for the proper timing. All the components of this imaging solution (with preparation and storage instructions) are listed above.

2.6. Data Analysis

1. Image viewing and manipulation program such as ImageJ.
2. Software program to fit a 2D Gaussian to each frame of movie: It can be custom written software, or commercial software. Another option is the free program called Video Spot Tracker, which can be downloaded at http://www.cs.unc.edu/Research/nano/cismm/download/spottracker/video_spot_tracker.html.
3. Step analysis program: Student's *t*-test or HMM custom-written, or contact selvin@illinois.edu for programs (11, 12).

3. Methods

See Note 3, applicable to all methods in this chapter.

3.1. Building a TIR Setup

While the details of building and aligning a TIR microscope are beyond the scope of this chapter, we list the essential components in such a setup and highlight the most important considerations involved. See Figs. 3 and 4 for a basic schematic of an objective-type TIR setup. For detailed instructions on how to align a TIR microscope, please see (7).

1. While using a commercial inverted microscope as a starting point is not strictly necessary, it does make the process much easier. We recommend either the Olympus IX70 or IX71, or a Nikon Eclipse TE2000-U.
2. A high numerical aperture objective is critical to getting good TIR images because it allows for the collection of more photons. An objective with 1.4 NA or higher is required to achieve TIR, such as the PlanApo 100 \times 1.45 NA $\infty/0.17$ (Olympus) or the ApoTIR 100 \times (1.49 NA) (Nikon).
3. A light source with which to illuminate the sample is obviously a critical piece of equipment. This must be matched to the absorption spectra of the fluorophore in question. It is best to

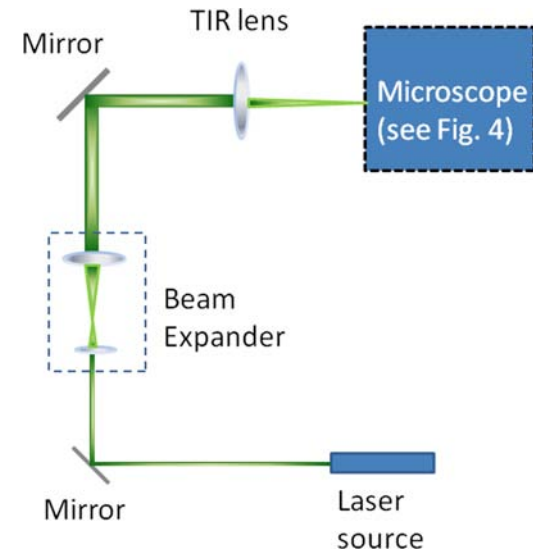


Fig. 3. Schematic of a minimalist TIRF microscopy setup. The laser beam is first expanded and collimated through a beam-expander, then passed through a plano-convex lens, which adjusts the angle with which the beam enters the microscope.

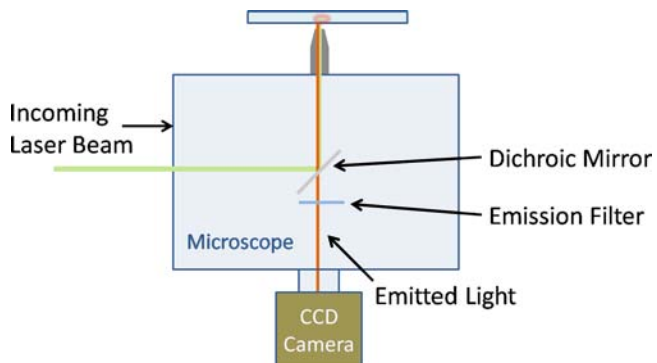


Fig. 4. Schematic of laser path inside the microscope. The incoming excitation laser is depicted (***lighter beam***) as is the outgoing emission signal (***darker beam***). Once inside the microscope, the laser reflects off a dichroic mirror and then through the objective, exciting the fluorophores in the sample. The signal initially travels back down the same path as the laser, but passes through the dichroic mirror chosen to reflect the laser but pass the signal. The signal then passes through an emission filter, which filters out any traces of the laser light that passed through the dichroic. The signal is then sent toward the CCD camera.

use a single mode, TEM_{00} laser. Generally, at least 10 mW of power is required. 532-nm diode lasers and 633-nm He-Ne lasers are perhaps the most common, but the specific type of laser needed will depend on the application. A clean Gaussian laser profile is also an important requirement to consider. See Note 4 for more information on choosing an appropriate laser.

4. A dichroic mirror and emission filter set will be needed inside the microscope. The type of dichroic and filter set

needed will depend on the fluorophores being used. Chroma and Semrock make high-quality filter sets for virtually any fluorophore desired.

5. A highly sensitive camera is absolutely critical for obtaining adequate data for FIONA measurements. Typically, this is a high-gain EMCCD camera, such as the iXon EM+ (DV-897E-CS0), Andor. The effective pixel size (once magnification of the objective and microscope are considered) should be 100–150 nm for optimal resolution (6).
6. Other standard optics parts, such as mirrors, lenses, beam expanders, and translation stages will also be needed. At least two mirrors are always required for proper laser alignment to give enough degrees of freedom to get the laser path to be perfectly straight into the microscope. Also, the laser beam generally needs to be expanded about ten times to create a large enough excitation area. This can be achieved using two lenses or by purchasing a commercial beam expander.
7. A large (50 mm diameter) lens of focal length ~30 cm is required to create TIR illumination. The lens must be placed such that the distance between the lens and the back focal plane of the objective equals the focal length of the lens. In other words, the lens focuses the laser down to a point at the back focal plane of the objective, creating a collimated beam that comes out the other end of the objective. We have found 30 cm focal length lenses to be ideal, as it is not possible to position the lens much closer than 30 cm from the objective, and because larger focal lengths create smaller illumination areas. Translating the lens in *x* and *y* changes the angle that the beam exits the objective (and thus allows for total internal reflection). The lens should be mounted on a 3D micrometer stage to allow for these adjustments. The large diameter of the lens is required because the TIR lens is translated when changing the angle of incidence, meaning the beam (which has been expanded to around 20 mm at this point) will be offset from the center of the lens. Smaller lenses might clip the beam. In addition, the larger diameter decreases the curvature of the lens in the area which the beam passes through, thereby reducing any possible spherical aberrations.
8. After the TIR setup is built and aligned (see Note 5), check the TIR alignment with a bead slide. To prepare a bead slide with carboxylate-modified 0.02-μm Nile Red beads (2% solids), first dilute beads by 1:1,000,000 in distilled water. Pipette 100 μL into each of two 0.5-mL tubes. To one tube, add 1 μL of 0.1 M HCl. Flow the HCl-bead solution through the sample chamber and incubate for 5 min. Then, wash the sample chamber with 100 μL water or buffer. Flow in the second aliquot of beads (without HCl) to provide some beads in solution. Epoxy over

openings if future reuse of bead slide is desired. Place the bead sample on the microscope stage and focus on the surface. Adjust the TIR lens position in either *x* or *y* until the beads on the surface fluoresce brightly, but no beads in solution are excited. Check that the excitation area is centered and has a roughly Gaussian intensity profile.

3.2. Microscope Slide and Coverslip Cleaning

In order to avoid background fluorescence from dust and organic debris, slides and coverslips must be carefully cleaned prior to use. We present a basic protocol for doing so below, but also see Note 6 for additional options.

1. Prerinse a slide holder, Teflon coverslip holder, and glass beaker with distilled water.
2. Place slides in a slide holder and place coverslips in a Teflon holder.
3. Fill slide holder and beaker with acetone. Place the Teflon holder in the beaker.
4. Sonicate for 20 min.
5. Remove Teflon holder from beaker. Carefully pour out acetone from slide holder and beaker and discard.
6. Refill slide holder and beaker with distilled water. Place the Teflon holder in the beaker.
7. Remove Teflon holder from beaker and pour out water from both slide holder and beaker.
8. Repeat steps 6 and 7 for a total of three rinse steps.
9. Fill slide holder and beaker with 1 M KOH. Place Teflon holder in beaker.
10. Sonicate for 20 min.
11. Remove Teflon holder from beaker. Carefully pour out KOH from slide holder and beaker and discard.
12. Refill slide holder and beaker with distilled water. Place the Teflon holder in the beaker.
13. Remove slides one by one from the slide holder with tweezers, rinsing with copious amounts of distilled water and drying carefully with nitrogen. Repeat with coverslips (see Note 7).
14. Proceed directly to assembling the sample chambers (see below), or store the slides and coverslips carefully covered for a few days before assembling.

3.3. PEGylation of Slides and Coverslips

Some biomolecules are especially “sticky” and require extra blocking to prevent them from binding nonspecifically to the glass surface. In general, a surface blocking agent such as BSA or casein can be used (see Subheading 3.4 for details), but in some cases more rigorous surface passivation is needed. Although much more time-intensive,

PEGylation yields a surface much more resistant to sticking of proteins (13). A mixture of biotinylated PEG and regular PEG can be used to immobilize avidin-conjugated molecules to the surface while blocking nonspecific adsorption of other molecules. If PEGylation is necessary, skip the slide cleaning protocol listed above and proceed straight to the PEGylation technique described below:

1. Clean coverslips in a glass holder by covering with 1 M KOH and sonicating 20 min.
2. Meanwhile, equilibrate aminosilane and PEG – to room temperature.
3. Rinse coverslips at least three times with distilled water.
4. Cover the coverslips with aminosilane solution (see Note 8): 2 mL aminosilane, 5 mL acetic acid (glacial), and 100 mL methanol.
5. Let coverslips sit in aminosilane solution for 20 min, sonicating briefly (1 min) halfway through.
6. Pour off aminosilane solution and rinse with distilled water.
7. Rinse each coverslip with water and dry with nitrogen (see Note 7).
8. Dissolve 80 mg PEG in 320 μ L of 10 mM sodium bicarbonate buffer. When using biotinylated PEG, a mixture of mPEG-SV and biotin-PEG-SC should be used. Depending on the application, 10–40% biotin-PEG-SC (by weight) is generally appropriate.
9. Vortex and centrifuge 1 min at $7,200 \times g$.
10. Carefully pipette 50 μ L of PEG solution onto the top of one coverslip. Spread out the liquid with pipette tip, then carefully flip over a second coverslip and place it on top of the first to make a “sandwich.”
11. Eliminate any air bubbles by tapping with a pipette tip or pressing gently.
12. Repeat with remaining coverslips.
13. Place in sealed container (see Note 9), and place in a dark place protected from light for 3 h.
14. Take each “sandwich” apart and rinse with copious amounts of distilled water, making sure to remember which side was exposed to the PEG solution. Blow dry with nitrogen and place in a container, with PEG-side up.
15. Store at -20°C or -80°C , protected from light, and in a sealed container (face up) until ready to use. Equilibrate to room temperature before opening the container.
16. Proceed to use PEGylated coverslip to build a sample chamber (see Subheading 3.4 below).

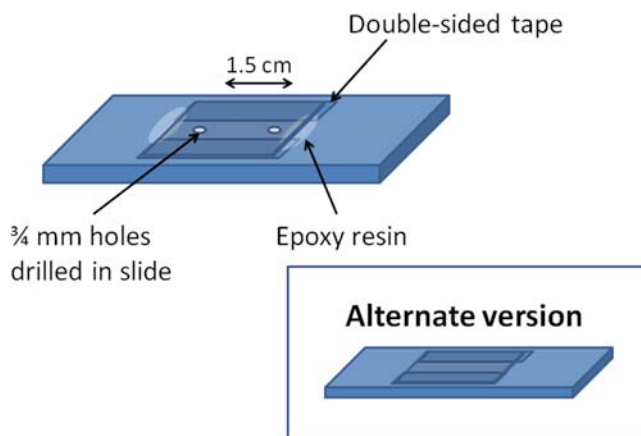


Fig. 5. Schematic of double-sided tape, drilled-hole sample chamber and alternative capillary flow chamber (*inset*). Two holes approximately 1.5 cm apart are drilled halfway between the two long edges of a microscope slide with an electric drill. After cleaning off both the drilled slide and coverslip, the coverslip is attached using double-sided tape. The openings at each end are sealed off with 5-min epoxy. *Inset*: Alternative chamber with no drilled holes and the openings left unsealed.

3.4. Building the Sample Chamber

1. If pipette holes in slide are desired (see Note 10), use a $\frac{3}{4}$ mm diamond drill bit to drill two holes about 1.5 cm apart as shown in Fig. 5. Wash the slide with water.
2. Clean the slide and coverslip as described in Subheading 3.2.
3. Place cleaned slide on a kimwipe (clean side up).
4. Cut two pieces of double-sided adhesive tape and place on the long edges of the slide, just above and below the holes. The tape pieces should be a few millimeters apart, leaving a long thin channel of untaped glass in between.
5. Place coverslip on top of tape, cleaned side down (or PEGylated side down, if applicable). Use a pipette tip to gently press the coverslip down, removing any air bubbles between the glass and the tape.
6. Seal the ends of the coverslip using epoxy resin and allow to dry for at least 15 min.
7. Remove excess tape with a razor blade, leaving only the tape beneath the coverslip.
8. The sample chamber volume should be approximately 20 μ L. Fluid can be flowed through the chamber by placing the pipette tip in one hole and gently expelling the liquid from the pipette through the chamber and out the other hole.

3.5. Preparing the Sample Chamber and Acquiring Data

The specific steps and parameters for this section will vary drastically depending on the biomolecule being studied and the goals of the experiment. Although many of these parameters might be different for other specific applications, we feel the clearest way to

explain this step would be to present a sample experimental protocol here, from which changes can be made as needed for your desired experiment. Below, we present a protocol for a single-molecule tracking of kinesin on axonemes.

1. Get a container of ice to put chemicals in as you are using them at the lab bench.
2. Mix in a small eppendorf 1 μL stock axonemes and 29 μL BRB80. Pipette up and down slowly to mix so that axonemes are not damaged. Flow this mixture into your sample chamber. Wipe off excess fluid that emerges from the opposite end and then store coverslip-side down at 4°C for half an hour so that the axonemes will stick to the surface of the coverslip.
3. (Optional) While you wait for the axonemes, you can do an axoneme affinity purification on the kinesin to select for the active protein. Set centrifuge to 4°C and mix in the tube the following components: 20 μL kinesin (~10 μM stock), 1 μL 100 mM MgATP, 5 μL axonemes, and 24 μL BRB80. Depending on how much of your protein is inactive, the final protein concentration will change after the affinity purification. Also, depending on how concentrated your protein was to start with, this purification might work better if the protein is diluted more with BRB80. Let mixture sit on ice for 10 min. Then spin at 4°C, 15,000 $\times g$ for 30 min. When it finishes spinning, there should be a visible milky white pellet at the bottom of the tube. This is the axonemes, along with any kinesin that bound to the axonemes but were inactive and, therefore, got stuck rather than walking off the axoneme. Pipette off the top 20 μL , being careful not to disturb the pellet. Proceed through the rest of the sample prep with kinesin taken from this tube.
4. Flow into your sample chamber a 1:10 dilution of 20 mg/mL casein or undiluted 20 mg/mL BSA to block the glass surface that is uncovered by axonemes. Wait for 10 min with coverslip-side down.
5. In a clean eppendorf tube, mix 1 μL kinesin with 1 μL anti-histidine conjugated Quantum dot 655 or other fluorophore of your choice (see Note 1). Mix thoroughly by pipetting up and down and then leave on ice for 20 min.
6. Meanwhile, mix final imaging buffer (see Subheading 2.5 item 11): 2.5 mM PCA; 50 nM PCD; 1 mM DTT; 1 mM MgATP (pH 7.0); 2 U/mL creatine kinase (optional, see Note 11); 2 mM creatine phosphate (optional, see Note 11); labeled kinesin from step 5. All chemicals mixed in BRB80 with 10 mg/mL BSA.
7. Plug in camera and turn on laser. Wait 5–10 min for laser to stabilize and camera to cool down.

8. Use a bead sample to optimize TIR lens position (thereby changing the TIR angle) for TIR imaging of the plane of the coverslip just inside the sample chamber (see Subheading 3.1 step 8 for how to make a bead slide; see the troubleshooting section in Note 16 if you cannot see the beads after placing a bead sample on the microscope).
9. Adjust ND filters in front of your laser to obtain the desired laser intensity. Generally with a bright dye like Alexa or quantum dots, an ND of 1.5 in front of a 75 mW laser is sufficient. Dyes that are less bright may require a higher laser power – this must be optimized for each set of experimental conditions (see Note 18).
10. Set camera software to acquire 500 frames at 100 ms exposure, with EM gain of 200. (These settings can be adjusted to suit the needs of the experiment).
11. Flow the imaging buffer into the sample chamber and clip the sample chamber securely onto the microscope stage. Turn off room lights and other lights.
12. Unshutter the laser and check that the signal is not saturating the camera (see Note 19). Adjust EM gain, Pre-amp gain, and/or the ND filter in front of the laser so that the brightest part of the image is close to but less than saturation. Move to a new location in the sample with a large number of fluorophores and reshutter laser.
13. Wait for 2 min for the stage to stabilize (see Note 20). When ready, unshutter the laser and quickly start the acquisition on the camera.
14. When the acquisition is done, make sure that file is saved, open it in a program such as ImageJ, and scroll through to see if there is movement. You may need to try a few different areas in the sample before finding a place where you see motility, as it is not uncommon for some of the motors to be inactive. If there is still no motion, see troubleshooting in Note 17.

3.6. Data Analysis

1. To apply FIONA to single-molecule tracking data, one must first select a spot and fit a two-dimensional Gaussian function to the point-spread function of the photons emitted (see Note 12). Using an Andor EMCCD camera, export data in TIF format, which is then easily viewed using the freely available program ImageJ, which can be downloaded at <http://rsb.info.nih.gov/ij/>. Using this program, select a fluorophore exhibiting motility and crop the movie images to exclude other fluorophores.
2. Fit a 2D Gaussian function to each frame of the movie. We use a custom program written in IDL for this step, but many other programming platforms can be used. See Note 13 for more options. The center of the 2D Gaussian gives the localization of the fluorophore (once pixels are converted to nanometers), which, along with the frame number (once converted to seconds), provides the trajectory of the fluorophore over time.

3. Use Eq. 1 to determine the uncertainty of each localization measurement: convert the number of counts measured by the camera to photons (this conversion will vary for each camera and the settings used for that camera during this particular movie). The number of photons emitted by the fluorophore for this frame is N . Also, measure the standard deviation of the background of the image (an area not including the spot), which is b . To determine α , calculate the effective pixel size of the detector (actual pixel size divided by magnification). Finally, the width of the Gaussian function (in the x or y direction) that was used to fit the frame is s_x or s_y , respectively.
4. Once the trajectory and fitting error have been found, the step size of the trajectory can be determined (if desired). Several different methods can be used to determine this. Steps can often be seen simply by eye, but it is best to use an analytical method to determine the step locations to avoid error due to human bias. The two most common methods used in our lab are the application of Student's t -test (see Fig. 6) or the use of a Hidden Markov model method (HMM). see Note 14 for a discussion about the circumstances in which each of these methods would be more appropriate (11, 12). Contact selvin@illinois.edu to obtain these program packages.

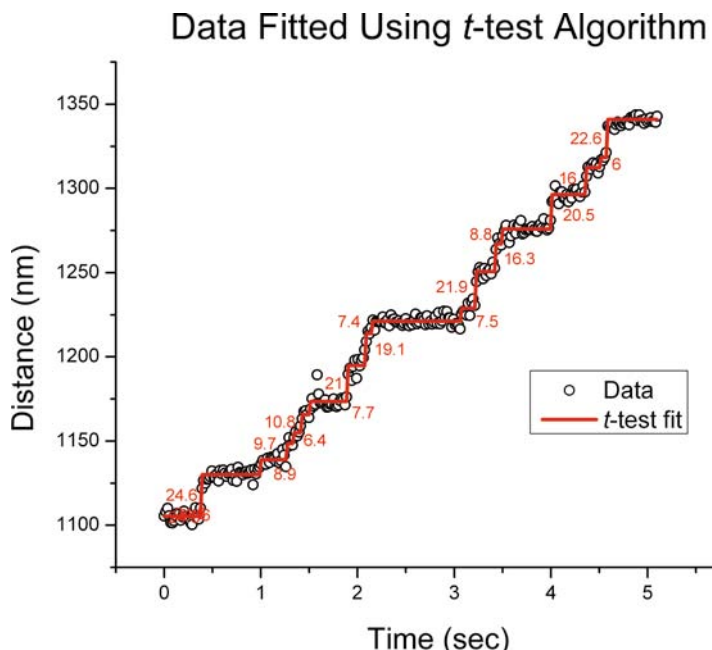


Fig. 6. An example of FIONA stepping data of kinesin motors attached to a fluorescent bead, walking on axonemes in sample chamber. **Open circles** represent the center of the Gaussian functions fitted to the PSF of the bead's emission for each frame. The **solid line** represents a Student's t -test fit to the trajectory, showing where steps occurred. The average of the step size distribution for the full trace as determined by the t -test fit is $8.7 \pm 0.5\text{nm}$.

3.7. In Vivo Considerations

In general, the same FIONA techniques can be used to image motors or other biomolecules inside live cells (see Note 15). This poses extra challenges, however. We list some examples of such challenges and solutions we have used successfully in our lab:

1. Challenge 1: Cells have a huge amount of autofluorescence. This can be reduced by using a fluorophore that can be excited with a red laser. Generally, increases in the excitation wavelength towards the red end of the spectrum result in less auto-fluorescence. This can also be improved by using cells that tend to be flatter (the smaller thickness means less autofluorescence per surface area). We have used cells such as HEK, HeLa, or Cos7 successfully, for instance.
2. Challenge 2: The areas of interest inside the cell are greater than 300 nm from the coverslip surface, meaning the evanescent wave does not penetrate far enough into the sample. Sometimes (when imaging proteins in the cell membrane, for instance) this can be addressed by adjusting the TIR lens slightly out of TIR so that more of the sample above the surface is excited. The laser should largely be reflected, just not completely. In other cases, the use of TIR is not possible. If the fluorophore is bright enough, achieving a good fit with FIONA may still be possible, but the background will be higher, since the volume above and below the region of interest is also exposed to laser light.
3. Challenge 3: The signal-to-noise ratio is still not high enough, even after following the suggestions in step 1. This can sometimes be solved by attaching multiple dyes to a motor or choosing a better fluorophore (a Qdot, for instance).
4. Challenge 4: In some cases, the photobleaching of the fluorophores can damage the cell that is being imaged due to the formation of reactive oxygen species. Using the smallest laser power possible to achieve the desired results can lessen the photobleaching, as can the use of oxygen scavenging systems. Also, in some cases it is desirable to illuminate the cell in pulses – for instance, taking one frame every 10 s. The laser can be shuttered in between frame acquisitions, thus reducing the amount of time the laser must hit the specimen.
5. Challenge 5: Getting the protein labeled or getting the labeled protein inside the cell. This is a very difficult problem, the solution to which will depend on the type of biomolecule being studied. The easiest solution is to create a fluorescent protein fusion with the protein of interest. However, as discussed earlier, fluorescent proteins are in general not photostable nor bright enough to be practical for FIONA imaging. It is sometimes possible to use multiple fluorescent proteins attached to the molecule of interest to get a brighter signal. For instance, we have successfully imaged large numbers of GFP inside

peroxisomes being transported inside a cell (4). Pigmented organelles such as melanosomes can be imaged in bright-field and successfully analyzed with FIONA (14). Various other strategies have been and continue to be explored to specifically label a biological molecule with a bright fluorophore inside a cell. Attempts to solve the problem of transporting a Q-dot or other fluorophore across the cell membrane include the use of hydrophobic counterions and cell-penetrating peptides (15), endocytosis (16), pinocytosis (17), and microinjection (18). The issue of specific labeling of a protein once the fluorophore has crossed the membrane must also be addressed (unless one is able to successfully transport an already-labeled purified protein in the cell). This can be done using covalent binding of site-specific small molecule probes, for instance (19). Other techniques include ligand–receptor interactions, intein-mediated processes, and enzyme-catalyzed protein modifications (20, 22).

4. Notes

1. Many different fluorophores can be attached to the molecule of interest to track it using FIONA. Qdots or even polystyrene beads are good choices, as they are extremely bright and, therefore, give very good signal-to-noise ratios. Our lab has used a variety of fluorophores for this experiment, two of which are Penta-His Alexa Fluor 532 Conjugate (Qiagen 35330) and Quantum dot 655 conjugated to anti-his with invitrogen's Qdot cconjugation kit (Cat. No. Q22021MP). If Qdots or polystyrene beads are used, make certain to use enough of the fluorophore such that there are more fluorophores than kinesin by at least 2 to 1. This makes it unlikely for multiple kinesin to be attached to the same fluorophore, which is critical if single-molecule traces are desired. Alternatively, organic dyes or even fluorescent proteins can be attached to the molecule using cysteine–maleimide linkages, Halo-tags, His-tags, or other specific labeling methods (or, in the case of fluorescent proteins, by creating a fusion protein). In general, fluorescent proteins do not give sufficient numbers of photons nor have long enough lifetimes before photobleaching to make it feasible to track them using FIONA. If using an organic dye, be certain to choose one that is as bright as possible while still absorbing and emitting at the wavelengths required for the experiment. Dyes that our lab have found especially useful include Cyanine dyes (especially Cy3), Alexa series dyes (Invitrogen), and Atto647 (ATTO-TEC GmbH). An excellent resource for viewing the spectra of dyes and choosing

appropriate filter sets is Invitrogen's Fluorescence Spectra Viewer, found at <http://www.invitrogen.com/site/us/en/home/support/Research-Tools/Fluorescence-SpectraViewer.html>.

2. Note that for some molecular motors, such as kinesin, the concentration of salt in the buffer can have a significant effect on motility and run length. Thus, it is important to be careful to choose product forms that eliminate any extra sources of salt. For instance, purchase regular PIPES (such as Fluka #80635) rather than PIPES sesquisodium salt. The exact buffer conditions used will, however, greatly depend on the type of biomolecule being studied and the specific demands of the experiment.
3. All methods in this chapter should be done wearing appropriate personal protective equipment – in most cases, nitrile gloves and safety glasses. Additional precautions for some steps are noted below.
4. Prices for a 100 mW laser range from several hundred dollars (USD) for a cheap red diode laser (633 nm) to over 10,000 for a very nice green or blue laser (532 nm or 488 nm). It is not necessary to buy a top-of-the line laser, as long as the laser profile is Gaussian. Cheaper lasers tend to output a larger wavelength range, for example emitting 633 ± 10 nm for a red laser. In most situations, this wider range will not affect your data, but if you are using multiple fluorophores with different absorption/emission spectra and are exciting the wrong ones because of the laser, the problem can be solved by simply placing an appropriate excitation filter in front of the laser to block off the unwanted wavelengths.
5. Laser alignment should be done while wearing laser safety goggles appropriate for the wavelength of the light, and while observing general laser safety practices.
6. Instead of using KOH and sonication to clean slides, plasma cleaning can also be used. We have used both techniques successfully, although plasma cleaning is faster. To use this method, rinse slides and coverslips briefly with isopropanol, dry with nitrogen, and place in plasma cleaner for 5 min under argon plasma.
7. In all steps that involve rinsing a slide (or coverslip), care must be taken to always use tweezers to hold the slide at the bottom edge. Apply rinsing fluid (water, isopropanol, etc.) using a squirt bottle by squirting the liquid as a stream on the top of the slide, allowing the liquid to run down the length of the slide, with the tweezers being the last thing the fluid touches before dripping off. Otherwise, the dirt or residue on the tweezers will flow onto the slide and it will not be left clean. This is also true when blowing dry a slide or coverslip with nitrogen – the tweezers should always be the last thing the liquid touches as it drips or is blown off the slide or coverslip.

8. Aminosilane and acetic acid are both harmful by inhalation, ingestion, or skin absorption. The steps involving these chemicals should be performed in a fume hood and while wearing appropriate gloves and goggles.
9. We prefer to use a plastic box designed to hold 1.5-mL plastic tubes to hold the coverslips during the incubation steps. We squirt distilled water into the bottom of the box so that each hole in the grid is about half full of water. We then place the coverslips on the top of the grid and close the box. This ensures that the box remains humid enough to not dry out the PEG solution as it incubates.
10. In many cases, it is actually more desirable to use capillary action to pull fluid through the sample chamber rather than forcing the liquid through with a pipette. In this case, the slides can be assembled similarly to what is described here, but with slides that do not have any drilled holes, and omitting the epoxy step. Then, rather than flowing the liquid through by placing the pipette tip in the hole, simply expel a small volume of fluid at the edge of the coverslip. As it is pulled through the chamber by capillary action, gradually add more fluid to that end, while applying a kimwipe to the other side to absorb the fluid. We have found this technique to be more reproducible in certain cases, as the rate of flow is not dependent upon the amount of pressure applied to the pipette.
11. Creatine kinase and creatine phosphate together function as an ATP recycling system, which is necessary for sustaining a low, unsaturated ATP concentration. If a low ATP concentration is not required, such as saturated levels of ATP, i.e., >1 mM, omit the creatine kinase and creatine phosphate.
12. The programs used to achieve this can vary depending on the equipment used to acquire images and the desired programming platform. We present the steps of analysis based on the software generally used in our lab; however, other software can be used to achieve the same goals.
13. A free NIH-sponsored program called Video Spot Tracker (which can be downloaded at http://www.cs.unc.edu/Research/nano/cismm/download/spottracker/video_spot_tracker.html) can be used instead of a custom program. Instructions for this program can be found at the same URL. The program provides the *x-y* position of the molecule being tracked (in pixels) at every frame. If nanometer precision is desired using this program, make sure to reduce the tracking pointer so that it is as small as possible (radius = 1), reduce the precision to the minimum value (0.0001 pixel), and choose the interpolate option. Several commercial programs are also available that

are capable of performing these tasks. Some of these include Andor iQ (Andor Technology), MetaMorph (Universal Imaging Corporation), Image Pro (Media Cybernetics), and 3I's Workbench (Intelligent Imaging Innovations).

14. The Hidden Markov Model technique is very robust and can accurately find steps even with data that is quite noisy. However, it is somewhat model-dependent, requiring the input of some parameters that may not be known a priori. It also tends to be computationally more expensive for long traces. For data with minimal noise, the Student's *t*-test method finds steps accurately but is model-independent. Therefore, for reasonably "clean" data, a Student's *t*-test should be tried first. If the fitting is not satisfactory, the HMM method should then be tried.
15. Working with live cells requires additional safety precautions. Follow the local governmental and institutional biosafety regulations that apply to the type of cells being used.
16. Troubleshooting Problem 1: there is no signal (besides background noise)
 - (a) Make certain that you have chosen a dichroic mirror and emission filter appropriate to the emission spectra of the fluorophore and the wavelength of the laser.
 - (b) Put a bead calibration slide on the microscope. Do you see a signal with your bead slide? If not, skip to step (f).
 - (c) Does your fluorophore emit in the same wavelength range as the beads you used to calibrate? If not, make a bead slide with a more appropriate wavelength of beads and check that you see a signal with those beads (if you see no signal with the new bead slide, skip to step (f)).
 - (d) Does turning up the gain on the camera/increasing exposure time/increasing laser intensity fix the problem?
 - (e) Does your laser wavelength correspond to the peak (or close to it) of the excitation curve of the fluorophore? If not, your fluorophore will not be efficiently excited by this laser.
 - (f) Focus upward into the middle of your chamber. Do you see a lot of fluorophores diffusing in solution? If yes, then the motors did not attach to the surface. This could indicate a problem with the motors or the "track." If the motors are walking on axonemes, look for the axonemes with bright-field illumination to confirm that they are stuck on the coverslip. If not using axonemes, label your track with dye, preferably of different emission spectra from the tag of the motor (e.g., rhodamine on actin or microtubules) and check that the filaments are adhering to

the slide's surface. A different surface attachment scheme may be necessary (perhaps using biotin-conjugated tubulin monomers, for instance).

- (g) Check that you are focused on the right plane. If you were using exposure time higher than 100 ms, try decreasing exposure time to ~100 ms and changing the focus to find the correct plane again. If exposure is too long it is easy to completely miss the correct plane while scanning for it.
- (h) Do you see some laser light coming out of the objective at all? If not, the laser is misaligned. See step (i).
- (i) The laser may be misaligned. Check the laser path going backward from the microscope to the laser itself. Does it look like the beam is clipped somewhere, or strangely shaped? This indicates that the laser needs realignment.

17. Troubleshooting Problem 2: The motors are not walking

- (a) First, try a bulk assay such as a gliding assay, to make certain the motor proteins are still active. Over time (even when stored at -80°C) the proteins can degrade and lose activity. A fresh protein prep may be required.
- (b) Check that all chemicals are fresh and that the pH of the motility buffer is appropriate for the protein (generally around pH 7).
- (c) Make sure that the salt concentration is appropriate for the motor. Some motors are quite sensitive to salt concentrations – for instance, full-length kinesin requires a sufficient level of salt to avoid folding over, which prohibits motility.
- (d) Check that there is no nonspecific binding of the proteins to the glass surface. If you have fluorescently labeled the “tracks” (which we recommend) or are using axonemes (which are large enough to with bright-field illumination), check that the motors colocalize with the tracks. If a significant number do not, you will need to take steps to prevent this nonspecific adsorption onto the surface. This can be achieved using PEGylation or other coating techniques.

18. Troubleshooting Problem 3: The dyes photobleach too quickly

- (a) First try decreasing the laser power and increasing the gain of the camera. The higher the laser power, the more quickly the dyes will photobleach. Always use the smallest laser intensity possible to obtain sufficient signal-to-noise ratios.
- (b) Make sure that you are using an efficient deoxygenation system (see Subheading 3.5). Also, the emission of some dyes

can be improved by including reducing agents (for instance, Cy5 is greatly enhanced by including Trolox (21)).

- (c) Be sure that the motors are not simply detaching from the tracks (which sometimes can be confused with dye photobleaching). Adjusting salt concentrations can often affect run lengths of motors. With very small run lengths, the motors may detach from the track too frequently to obtain adequate traces.
- (d) Try a different dye. Some fluorophores, especially fluorescent proteins, simply do not last long enough to yield satisfactory FIONA data.

19. Troubleshooting Problem 4: There is too much background fluorescence

- (a) Make sure that the slides and coverslips are carefully cleaned according to the directions in Subheading 3.2.
- (b) Check that you are imaging the correct surface. It is sometimes possible to focus on the bottom of the glass slide rather than the top of the coverslip. Check that this is not occurring. One trick that is useful is to translate the sample chamber until the double-sided tape is over the objective. Focus on the bottom edge of the tape and then move the chamber back into position to image the sample.
- (c) Fluorophores could be binding nonspecifically to the surface (see step (d) of Note 17 above). This can be reduced by changing the surface blocking technique – using PEG coverslips, for instance.
- (d) Check that the immersion oil on the objective is not dirty and that there are no air bubbles in the oil. If in doubt, clean the oil off the objective and apply new.

20. Troubleshooting Problem 5: Drift

- (a) It is normal to see drift up to 1 nm/s on a microscope. Check to see if the measured location of a stationary fluorophore drifts only in one direction or randomly oscillates in all directions. Drift in one direction can be minimized by upgrading stage (to a micrometer controlled precision stage), clamping down microscope (for example, by removing the legs of the microscope and custom-fitting legs that can be clamped down onto the optics table as is done with optics table posts), or simply waiting longer before taking data for the stage to stabilize after moving it. Random oscillations can be due to an unstable laser (long path lengths traveled by laser before going into microscope, thus magnifying the instability) or air currents in the room, which can be minimized by putting a box around the setup.

Acknowledgments

The authors acknowledge the NIH and NSF for financial support.

References

1. Huang, B., Bates, M., Huang, X. (2009) Super resolution fluorescence microscopy. *Ann. Rev. Biochem.* **78**, 993–1016.
2. Hell, S.W. (2007) Far-Field Optical Nanoscopy. *Science* **316**, 1153–1158.
3. Yildiz, A., Forkey, J. N., McKinney, S. A., Ha, T., Goldman, Y. E., Selvin, P. R. (2003) Myosin V walks hand-over-hand: Single fluorophore imaging with 1.5 nm localization. *Science* **300**, 2061–2065.
4. Kural, C., Kim, H., Syed, S., Goshima, G., Gelfand, V. I., Selvin, P. R. (2005) Kinesin & Dynein Move a Peroxisome In Vivo: A Tug-of-War or Coordinated Movement? *Science* **308**, 1469–1472.
5. Thomson, R. E., Larson, D. R., Webb, W. W. (2002) Precise nanometer localization analysis for individual fluorescent probes. *Biophys. J.* **82**, 2775–2783.
6. Enderlein, J., Toprak, E., Selvin, P. R. (2006) Polarization effect on position accuracy of fluorophore localization. *Opt. Express* **14**, 8111–8120.
7. Selvin, P. R., Lougheed, T., Hoffman, M. T., Park, H., Balci, H., Blehm, B. H., Toprak, E. (2008) In vitro and in vivo FIONA and other acronyms for watching molecular motors walk. In Selvin PR, H. T., ed.: *Single-Molecule Techniques*. Cold Spring Harbor Laboratory Press, Cold Spring Harbor 37–71.
8. Pierce, D. W., Vale, R. D. (1998) Assaying Processive Movement of Kinesin by Fluorescence Microscopy. *Methods Enzymol.* **298**, 154–171.
9. Ozeki, T., Verma, V., Uppalapati, M., Suzuki, Y., Nakamura, M., Catchmark, J., Hancock, W. O. (2009) Surface-bound casein modulates the adsorption and activity of kinesin on SiO₂ Surfaces. *Biophys. J.* **96**, 3305–3318.
10. Aitken, C. E., Marshall, R. A., Puglisi, J. D. (2008) An oxygen scavenging system for improvement of dye stability in single-molecule fluorescence experiments. *Biophys. J.* **94**, 1826–1835.
11. Müllner, F. E., Syed, S., Selvin, P. R., Sigworth, F. J. (2010) Improved hidden Markov models for molecular motors. I. Basic theory. *Biophys. J.*
12. Syed, S., Müllner, F., Selvin, P. R., Sigworth, F. J. (2010) Improved hidden Markov models for molecular motors. 2. Extensions and application to experimental data. *Biophys. J.*
13. Rasnik, I., McKinney, S. A., Ha, T. (2005) Surfaces and Orientations: Much to FRET about? *Acc. Chem. Res.* **38**, 542–548.
14. Kural, C., Serpinskaya, A. S., Chou, Y. H., Goldman, R. D., Gelfand, V. I. (2007) Tracking melanosomes inside a cell to study molecular motors and their interaction. *PNAS* **104**, 5378–5382.
15. Jablonski, A. E., Humphries, W. H., Payne, C. K. (2009) Pyrenebutyrate-Mediated Delivery of Quantum Dots across the Plasma Membrane of Living Cells. *J. Phys. Chem. B*, 405–408.
16. Nan, X., Sims, P. A., Chen, P., Xie, X. S. (2005) Observation of Individual Microtubule Motor Steps in Living Cells with Endocytosed Quantum Dots. *J. Phys. Chem. Lett.* **109**, 24220–24224.
17. Courty, S., Luccardini, C., Bellaiche, Y. (2006) Tracking Individual Kinesin Motors in Living Cells Using Single Quantum-Dot Imaging. *Nano Lett* **6**, 1491–1495.
18. Derfus, A. M., Chan, W. C., Bhatia, S. N. (2004) Intracellular Delivery of Quantum Dots for Live Cell Labeling and Organelle Tracking. *Adv Mater* **16**, 961–966.
19. Chattopadhyaya, S., Srinivasan, R., Yeo, D. S., Chen, G., Yao, S. Q. (2009) Site-specific covalent labeling of proteins inside live cells using small molecule probes. *Bioorg. Med. Chem. Lett.* 981–989.
20. Miller, L. W., Cornish, V. W. (2005) Selective chemical labeling of proteins in living cells. *Curr. Opin. Chem. Biol.* **9**, 56–61.
21. Rasnik, I., McKinney, S. M., Ha, T. (2006) Nonblinking and long-lasting single-molecule fluorescence imaging. *Nature Methods* **3**, 891–893.
22. Chattopadhyaya, S., Srinivasan, R., Yeo, D., Chen, G., Yao, S. (2009) Site-specific covalent labeling of proteins inside live cells using small molecule probes. *Bioorg. Med. Chem.* **17**, 981–989.

Chapter 5

Snapshots of Kinesin Motors on Microtubule Tracks

Franck J. Fourniol and Carolyn A. Moores

Abstract

Kinesin motors couple ATP hydrolysis to movement along microtubules, which act both as tracks and as activators of kinesin ATPase activity. Cryo-electron microscopy and image processing enables generation of three-dimensional snapshots of kinesin motors on their tracks at different stages of their ATPase cycle, and can reveal their motor mechanisms at secondary structure resolution. Here, we describe in detail the methods and conditions employed in our lab to prepare high-quality frozen-hydrated samples, which yield structural insights into kinesin motor mechanisms.

Key words: Kinesin, Microtubules, Co-sedimentation assay, Negative stain electron microscopy, Cryo-electron microscopy

1. Introduction

Members of the diverse kinesin superfamily of microtubule-based motors fulfil many functions in cells, particularly in intracellular traffic, cell migration, and cell division (see for example (1, 2)). All kinesin motors possess a homologous ~40-kDa microtubule-binding motor domain, comprising a conserved core fold, which converts the chemical energy of ATP into mechanical force (3). Transmission of this force to family-specific structural elements will produce different effects, e.g. movement in one or the other direction along the tracks, anchoring or depolymerising microtubules (MTs).

MTs are essential for the activation of kinesin (4). X-ray crystallography has provided invaluable atomic-resolution descriptions of the motor domain on its own, but crystallisation conditions can induce conformational artefacts in the motor. Heterogeneous polymers such as MTs are impossible to study by X-ray crystallography, whereas cryo-electron microscopy (cryo-EM) allows visualisation of large macromolecular assemblies in near-physiological

conditions (5). The combination of cryo-EM and image processing can generate 3D reconstructions of kinesin-MT complexes captured at different stages in their ATPase cycle with sub-nanometer resolution. This has allowed visualisation of regular secondary structures and of the conformation of loops essential for the function of various kinesins (6–10).

The theoretical background and some practical aspects of the application to MTs of molecular and cellular EM techniques have been covered elsewhere (11, 12). Careful sample preparation and image acquisition is critical to generate high-quality cryo-EM data. Several good reviews have described the detailed procedures to prepare standard vitrified samples and to collect high-quality TEM images of globular macromolecules (see for example (13–15)). While many aspects of these procedures apply to MTs bound with kinesin motors, each sample requires specific considerations.

The aim of this chapter is to describe in detail methods used in our lab, with an emphasis on variations specific to MTs and their motor proteins.

First, a co-sedimentation assay and negative stain EM allow determination of the buffer conditions and concentration of protein required to fully bind microtubules. These conditions are then adapted to prepare samples for cryo-EM. Accurate microscope settings allow the acquisition of high-quality 2D images. These images are screened to select microtubules with the same architecture. Finally, EM-specific software enables the combination of a large number of images to generate a high-resolution 3D structure of the complex.

2. Materials

2.1. Polymerisation and Stabilisation of Microtubules

1. Glycerol-free bovine brain tubulin (Cytoskeleton, Inc., catalogue # T238). Store in single-use aliquots at –80°C (flash-frozen in liquid nitrogen).
2. MT polymerisation buffer (2×): 80 mM PIPES, pH 6.8, 10 mM MgCl₂. Store at room temperature.
3. GTP: 100 mM GTP in BRB80 buffer. Store in single-use aliquots at –20°C (see Subheading 2.2).
4. Paclitaxel: 100 mM Paclitaxel in DMSO (Calbiochem, catalogue # 580555). Store at –20°C.

2.2. Preparation of Kinesin Motor Domain

1. BRB80 buffer: 80 mM PIPES, pH 6.8, 1 mM EGTA, 1 mM MgCl₂ (suggested buffer, widely used in MT studies). Store at 4°C.
2. BRB20 buffer: 20 mM PIPES, pH 6.8, 1 mM EGTA, 1 mM MgCl₂. Store at 4°C.

3. AMPPNP: 100 mM AMPPNP in BRB80. Store in single-use aliquots at -20°C.
4. ADP: 100 mM ADP in BRB80. Store at -20°C.
5. Apyrase: 100 units/mL apyrase. Store at -80°C in single-use aliquots.
6. TCEP: (tris(2-carboxyethyl)phosphine), or DTT, or β-mercaptoethanol 20 mM in BRB80, adjust pH to 6.8. Store in single-use aliquots at -20°C.

2.3. Co-sedimentation

Assay

1. Ultracentrifuge and rotor (Beckman, TLA-100).
2. 230-μL thickwall polycarbonate tubes (fill with 200 μL max, 30 μL min).
3. Precast SDS-PAGE gels (NuPAGE 4–12% Bis-Tris, Invitrogen).
4. 20× MOPS running buffer (Invitrogen).

2.4. Sample Preparation for Negative Stain EM

1. Continuous carbon TEM grids, 400 mesh Cu (Pacific Grid-Tech. <http://www.grid-tech.com/catalog.htm#film>).
2. Glow-discharge unit (EMS 100×, Electron Microscopy Sciences).
3. Stainless-steel tweezers. An O-ring can be used to close them.
4. Filter paper (Whatman no. 1).
5. Uranyl acetate (UrAc) 1% solution. UrAc can be stored as a solution at room temperature (RT) wrapped in foil, since it is light-sensitive. It is advisable to re-filter it through 0.22 μm regularly. UrAc is toxic and mildly radioactive, so it must be disposed of according to local protocols, along with any contaminated material.

2.5. Sample Preparation for Cryo-EM

1. Holey carbon TEM grids (C-flats CF-2/2–4°C, Protochips <http://www.protochips.com/products/c-flat.html>, or Lacey 300 mesh Cu, Agar <http://www.agarscientific.com>).
2. Storage boxes and dewars for cryo grids.
3. Vitrobot (FEI Company).
4. Ethane gas bottle. Ethane is highly flammable; manipulate the gas in a fume hood. Once liquefied, ethane is a very efficient cryogenic agent and can cause severe burns. Wear protective goggles.

2.6. Micrograph Collection (Low Dose)

1. Negative-stain holder and cryo-holder.
2. Tecnai F20 FEG microscope (FEI Company), or equivalent transmission electron microscope (TEM) equipped with a field emission gun (FEG) operating at 200 kV or higher voltage.

2.7. Getting Started with Image Processing

1. SCAI scanner (Carl Zeiss).
2. Platforms: 32 or 64 bit AMD or Intel running Linux (SUSE) or OS X. The use of multi-CPU processors or clusters of computers speeds up processing considerably. RAM > 256 Mb. Hard drive > 500 Gb.
3. Software (free): RUBY-HELIX (16) (<http://structure.m.u-tokyo.ac.jp/English/software/Installation/Installation.html>) for helical reconstruction; SPIDER (17) (http://www.wadsworth.org/spider_doc/spider/docs/spider.html) and FREALIGN (18) (<http://emlab.rose2.brandeis.edu/software>) for single particle.

3. Methods

3.1. Polymerisation and Stabilisation of Microtubules

1. Thaw 20 µL tubulin rapidly by warming between fingers and immediately put it on ice (see Notes 1–3).
2. On ice, mix 1 µL 100 mM GTP with 20 µL 2× MT polymerisation buffer, to a final GTP concentration of ~5 mM.
3. Add the 20 µL tubulin and vortex well.
4. Incubate for 90 min at 37°C.
5. Add 0.4 µL paclitaxel (1 mM final) to stabilise the MTs.
6. Incubate for 1 h at 37°C.
7. Allow to sit for 24 h at RT for polymerisation to complete prior to use. Keep for a week at RT (not 4°C).

3.2. Preparation of Kinesin Motor Domain

1. Depending on the initial buffer and concentration of the kinesin protein, the buffer composition (see Notes 4–6) can be corrected by dilution or dialysis. We use BRB80 or BRB20 where possible. Addition of 2 mM TCEP (or another reducing agent, e.g. DTT or β-mercaptoethanol) prevents aggregation through disulphide bridges.
2. To get rid of potential aggregates centrifuge the kinesin sample in a benchtop centrifuge at 16,100 × g at 4°C for 20 min, or if possible in an ultracentrifuge at 392,000 × g at 4°C for 10 min.
3. Incubate kinesin with the desired nucleotide or analog at 5 mM, for 15 min on ice. Keep the concentration of nucleotide at 5 mM in subsequent buffers.
4. To study kinesin in its nucleotide-free state, use apyrase diluted 1:10 in the kinesin solution, for 15 min on ice. Apyrase hydrolyses ATP and ADP into AMP + Pi and is used here to degrade potential remnants of nucleotides associated with kinesin during expression/purification.

3.3. Co-sedimentation Assay

1. Work out the dilutions of MTs and kinesin for a range of kinesin concentrations (typically from 0.5 to 20 μM), with a fixed MT concentration (e.g. 2 μM).
2. For each concentration of kinesin, at RT, prepare the protein mix in a labelled thick-wall tube, using BRB80 + 2 mM TCEP to a final volume of 30 μL .
3. During the incubation, cover the tubes with parafilm to prevent evaporation.
4. Place the tubes in the rotor, with the label facing outside to keep track of the pellets later (pellets are not always visible).
5. Centrifuge at $392,000 \times g$ for 15 min at RT.
6. Label eppendorfs to collect the supernatant and pellets of each centrifuge tube. Fill each eppendorf labelled supernatant with 25 μL 2 \times loading buffer.
7. Add 25 μL of supernatant from each centrifuge tube to the corresponding eppendorf. Then, using a gel-loading fine pipette tip, pipette away all of the remaining supernatant, without resuspending the pellet.
8. Cover each pellet with 30 μL 2 \times loading buffer. Vortex well.
9. To help fully detach the pellet, leave the solution to freeze for 15 min at -20°C . Then thaw, vortex and scrape the tube with a pipette tip. Pipette the 30 μL 2 \times solution into the corresponding labelled eppendorf. Wash the centrifuge tube with 30 μL BRB80 that you then add to the same eppendorf.
10. Prepare for gel electrophoresis and load 10 μL of the supernatant and pellet of each kinesin-MT mix on the gel.
11. Run for 75 min at 200 V in 1 \times MOPS running buffer.
12. Stain the gel using standard procedures. An example of co-sedimentation assay results is shown in Fig. 1.

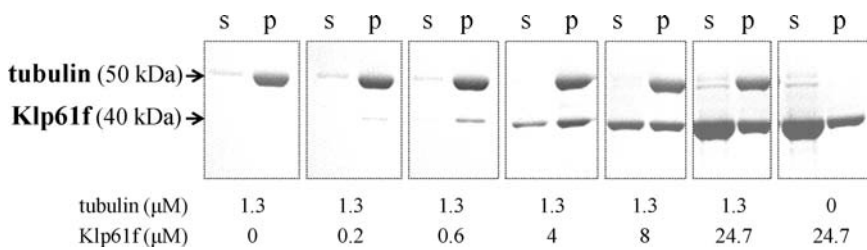


Fig. 1. Co-sedimentation assay of Klp61f (kinesin-5) motor domain with microtubules analysed by SDS-PAGE. Increasing amounts of *Drosophila* kinesin 5 (Klp61f) motor domain (recombinantly expressed in *E. coli*) with AMPPNP were incubated with paclitaxel-stabilised microtubules at a fixed concentration. Reaction mixes were centrifuged at high speed ($392,000 \times g$), supernatant and pellets were separated and visualised by gel electrophoresis. Two important controls were performed: a kinesin-free control (first two lanes) and a microtubule-free control (last two lanes). The latter allows an assessment of aggregation of Klp61f when it is highly concentrated. Note that α - and β -tubulin run as a single 50-kDa band, since the 100-kDa heterodimer dissociates under denaturing conditions.

3.4. Sample Preparation for Negative Stain EM

1. Apply a 40 mA negative glow-discharge in air for 40 s to continuous carbon grids (see Note 7).
2. Take two layers of filter paper.
3. Hold a grid with the tweezers so that they cover ~1/5 of the diameter of the grid. Slide the O-ring to keep the tweezers tight.
4. Dilute paclitaxel-stabilised MTs in BRB80, to 1–5 μM polymerised tubulin (see Note 1). Dilute kinesin motor domain to the concentration necessary to saturate MTs, determined by co-sedimentation assay and also by trial and error.
5. Vortex the MTs and spread 4 μL on the carbon surface. Leave on grid for 30 s.
6. Blot the solution by touching the rim of the grid on the filter paper (see Fig. 2).
7. Immediately add 4 μL kinesin solution (see Note 8). Incubate on grid for 30 s.
8. Blot and add 4 μL BRB80 to wash the excess protein off the grid.
9. Blot and stain with 4 μL UrAc. Blot immediately (see Notes 9 and 10). Examples of MTs stained with UrAc are shown Fig. 3.



Fig. 2. Negative stain EM grid preparation. In one hand, tweezers hold a glow-discharged EM grid, with its carbon side covered with solution A. In the other hand, 4 μL of solution B is ready to be pipetted onto the grid. As soon as solution A is blotted off from the rim of the grid, solution B is applied so that the sample does not dry out until the negative stain solution is applied.

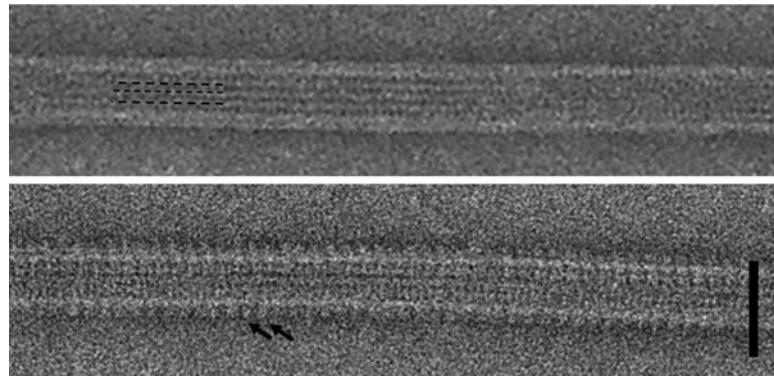


Fig. 3. Images of microtubules negatively stained with the heavy metal salt uranyl acetate. The contrast in negative stain images is high because it results from strong electron scattering by heavy atoms surrounding the macromolecules. Effectively, the structures visualised are not from the macromolecules themselves, but from the negative imprint formed by the dried stain (protein appears white). Microtubule sub-structures can be readily visualised. The top panel shows a paclitaxel-stabilised microtubule in which protofilaments are clearly visible, as emphasised by the *dashed lines*. The bottom panel shows a paclitaxel-stabilised microtubule bound with kinesin motor domain where extra densities are bound every 8 nm along the microtubule (*arrows*). Microtubules appear squashed and, therefore, wider than they are in solution, a major artefact induced by negative stain. Scale bar, 50 nm.

3.5. Sample Preparation for Cryo-EM

1. Start the Vitrobot (13) and set it at 37°C and 100% humidity (see Note 11). Allow at least 30 min for the filter papers to equilibrate in the humid chamber.
2. Prepare all the material needed to plunge-freeze grids: pipettes, grid boxes, screwdriver, fine tweezers, and large tweezers.
3. Dilute paclitaxel-stabilised MTs in BRB80, to ~10 µM polymerised tubulin. Note that the preparation of a cryo-sample requires higher protein concentration. Dilute kinesin motor domain to the concentration necessary to saturate MTs; this may also need to be tested by trial and error – usually the higher the better, e.g. for high affinity states, ~100 µM is ideal.
4. Glow-discharge the holey carbon grids as described in Subheading 3.4.
5. Fill the nitrogen holder (see Note 12). Wait 5 min for it to cool down. Then, fill the ethane holder.
6. Prepare a holey carbon grid following Subheading 3.4, steps 4–8.
7. Place the tweezers on the Vitrobot arm.
8. Run the Vitrobot plunging process with a blotting time of 2 s. When working out the conditions for a new sample, vary the blotting time until you get the right ice thickness (as defined in Subheading 3.6, step 7; see Note 6). Examples of cryo-EM images of MTs are shown Fig. 4.

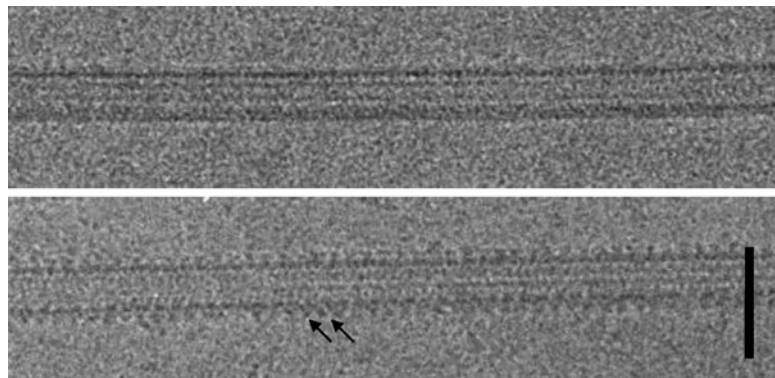


Fig. 4. Images of microtubules in vitreous ice. The contrast in cryo-EM images is low because it results from the protein atoms scattering electrons only slightly more than the atoms in the surrounding buffer. However, unlike in negative stain, the macromolecules themselves are directly visualised in a hydrated, near-physiological state (protein appears black). Based on optical properties of the TEM, images are recorded slightly under focus (in this figure – 2 μm) to enhance the contrast for subsequent image processing. This results in a loss of information, which has to be corrected to generate meaningful 3D reconstructions. The top panel shows a paclitaxel-stabilised microtubule. The *stripes* along the microtubule do not correspond to individual protofilaments but to the interference pattern (see Fig. 5) created by the scattering of protofilaments from the top (“near-side”) and bottom (“far-side”) of the microtubule. In the bottom panel, kinesin motor domains are bound every 8 nm along the microtubule (*arrows*). Scale bar, 50 nm.

3.6. Micrograph Collection (Low Dose)

1. To preserve the vitreous ice, it is essential to keep the sample below -140°C at all times (14).
2. For data collection on negatives, the emulsion should be set to 2.0 in Technai user interface. The “measured exposure time” read on the small screen depends on this emulsion value.
3. Make sure the microscope is properly aligned:
 - (a) Correct z height for the sample holder,
 - (b) Find the rotation centre,
 - (c) Align the condenser lens and correct astigmatism,
 - (d) Insert and centre the objective lens (aperture advised: 40 μm),
 - (e) Find focus,
 - (f) Correct the objective astigmatism.
4. Individual MTs appear as fine grey filaments at magnification 2,000 \times in negative stain. In cryo, when defocus is set to $-120\ \mu\text{m}$ and magnification set to 3,500 \times , MTs embedded in a layer of ice of the right thickness can be distinguished on CCD (binning 4, 0.5 s/frame, zoom 2 \times). If the ice looks patchy around the filaments, it is probably too thin over that hole.

5. Align the image centre in search mode to the image centre in exposure mode.
6. Select an empty hole, go to exposure mode (50,000 \times) and spread the beam so that the “measured exposure time” reads 1.8 s. The exposure dose can be checked at this stage (see Note 13).
7. Select an ice-covered hole and go to exposure mode. Do not change the beam intensity. The “measured exposure time” should now read ~2.0 s if the ice is of the right thickness.
8. For data collection:
 - (a) In search mode (3,500 \times), find an area with as many non-overlapping MTs as possible,
 - (b) In focus mode (150,000 \times), find focus, correct objective astigmatism, set the defocus to a value between 0.8 and 3.5 μm (pictures taken at a range of defocus values are needed for 3D reconstruction) and check that there is no image drift,
 - (c) Expose films/CCD for 1 s (see Note 14).

3.7. Basics of Image Processing

1. Negatives are scanned at a 7 μm step so that the final sampling is 1.4 $\text{\AA}/\text{pix}$ (see Note 15). Images can be binned 2 \times in the subsequent processing steps so that the sampling is 2.8 $\text{\AA}/\text{pix}$. This still allows generation of high-resolution (~8 \AA) reconstructions.
2. Determine the architecture of each microtubule. Microtubules display distinct moiré patterns in cryo-electron micrographs, corresponding to distinct architectures (19) (see Fig. 5; see Note 16).
3. Compute the power spectra of the microtubules to check for the presence and intensity of an 80 \AA layer line (see Fig. 6).
4. Helical microtubules can be processed to generate high-resolution reconstructions using the helical reconstruction script system Ruby-Helix ((16), and User’s Guide by Andrew Bodey: <http://structure.m.u-tokyo.ac.jp/software/guide.pdf>) (see Figs. 7a and 8).
5. 13-pf microtubules can be processed to generate high-resolution reconstructions using custom scripts based on single-particle software packages (8, 17, 18, 20) (see Fig. 7b).

4. Notes

1. Tubulin is unstable in its heterodimeric form and should be polymerised soon after being defrosted. However, measurement of tubulin concentration by Bradford assay should be performed prior to polymerisation.

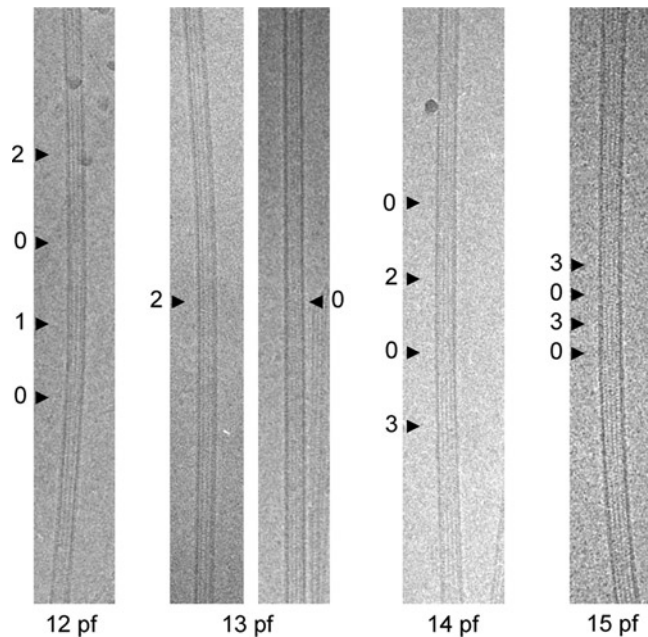


Fig. 5. Determination of the microtubule architectures most commonly observed in vitro. Cryo-EM images of microtubules present distinct moiré patterns corresponding to the protofilament (pf) numbers found in microtubules polymerised in vitro. The number of dark fringes (*arrowheads*, best viewed by looking along the microtubule at an angle) varies periodically along each microtubule, although for the 13-protofilament microtubule it is practically constant. The 13-protofilament architecture is observed in microtubules *in vivo* (23, 24), it is not helical but can be used for 3D reconstruction by single particle methods (8, 10, 18). Helical reconstruction can be applied to helical microtubules, essentially those with 15 or 16 protofilaments, which are scarce in paclitaxel microtubules (6, 7, 9).

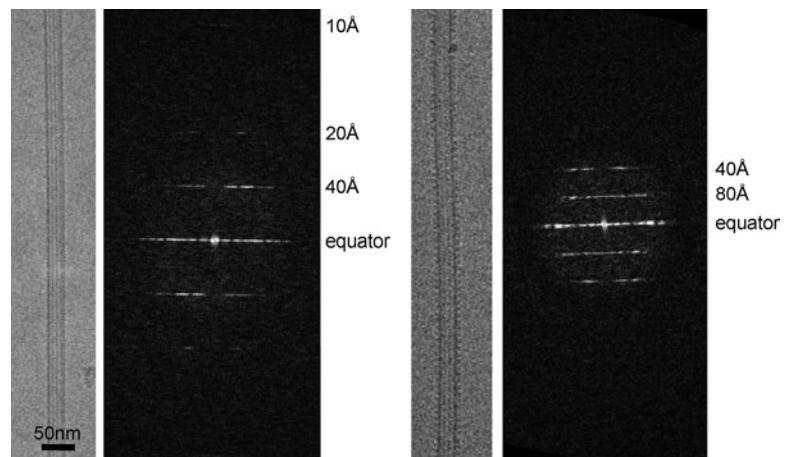


Fig. 6. Power spectra computed from cryo-EM images of microtubules. Power spectra of microtubules display lines of strong intensities, so-called layer lines. The height of the layer lines, i.e. the distance to the equator, reflects the axial periodicity in the microtubule structure. The power spectra of microtubules bound with a kinesin motor domain show a clear 80 \AA^{-1} layer line (*right panels*), corresponding to the 80 \AA axial repeat of kinesin. No 80 \AA^{-1} layer line is seen in power spectra of unbound microtubules (*left panel*).

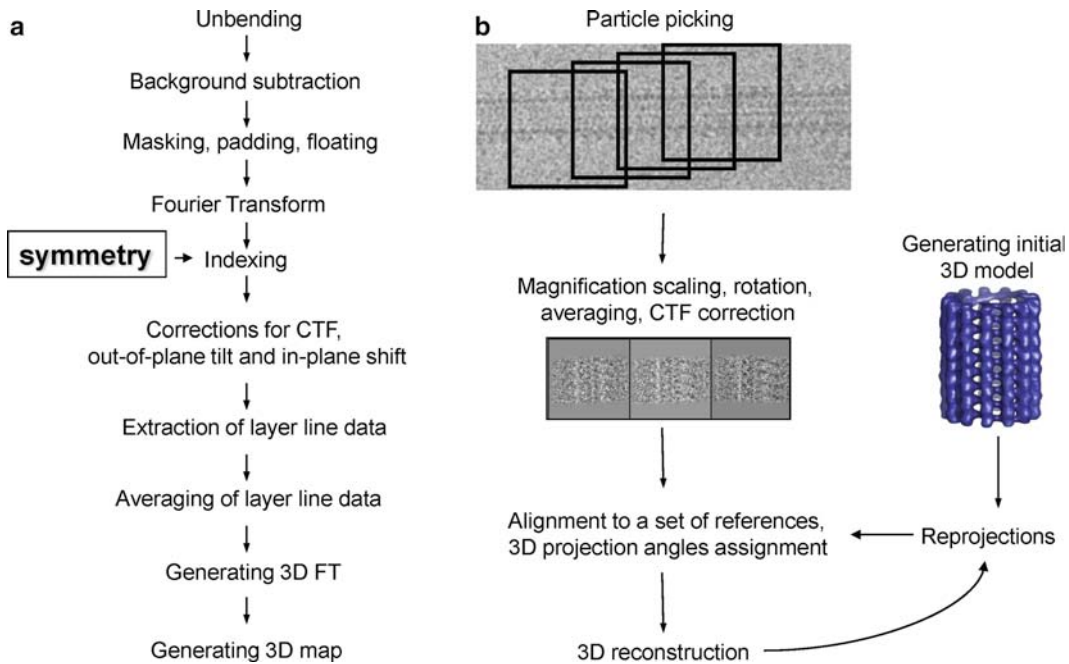


Fig. 7. Flowchart of the main processing steps involved in 3D reconstruction from cryo-EM images of microtubules. Depending on the microtubule architecture, two general approaches based on two different theories can be distinguished: helical reconstruction (a), and single particle reconstruction (b). In both cases, the goal of the computation is to align multiple 2D views of the microtubule-motor complex to enable calculation of the 3D structure. Because raw cryo-EM images have a poor signal/noise ratio, large numbers of images have to be combined to increase the signal and reveal high-resolution details. Whether helical or not, microtubules are 2D lattices of tubulin dimers and 3D reconstruction methods take advantage of this to average the signal of all the asymmetric units of the lattice (1 asymmetric unit = 1 tubulin dimer + 1 motor domain). Microtubules are not perfect lattices and e.g. curvature has to be dealt with by either unbending a long stretch of microtubule (a) or segmenting a microtubule into small particles that can be rotated individually (b). In the case of helical microtubules, a single 2D view contains enough information to generate a (very low-resolution) 3D structure assuming helical symmetry. On the contrary, multiple views of non-helical microtubules in different orientations have to be combined to calculate a 3D reconstruction. These orientations, defined by 3D projection angles, are not known *a priori* and can be assigned by comparison to 2D reprojections of an initial model. *CTF* contrast transfer function, *FT* Fourier transform.

2. The distribution of MT architectures depends on buffer condition and incubation time prior to adding paclitaxel. Polymerisation of helical MTs is favoured by a short incubation time and lower Mg^{2+} concentration (21), by adding DMSO (8% final), and/or by polymerising at 34°C instead of 37°C.
3. Neuronal tubulin contains a mixture of isoforms and post-translational modifications that can alter the affinity of some kinesins for MTs (22).
4. Kinesin affinity for MTs relies partly on electrostatic interactions. It is, therefore, of critical importance to keep ionic strength as low as possible ($[NaCl] < 100\text{ mM}$).
5. Cryoprotectants (for example glycerol) are detrimental to negative stain and to the vitrification of the sample (keep $[glycerol] < 5\%$).

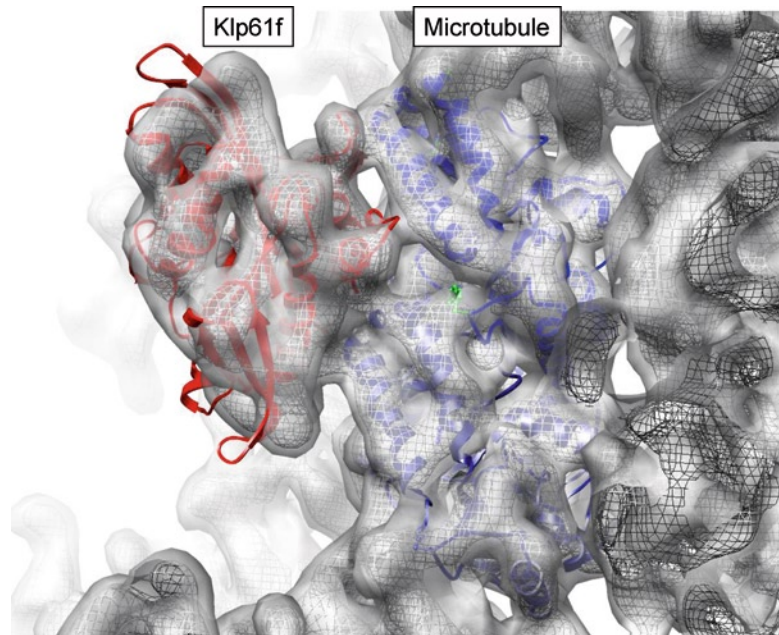


Fig. 8. Snapshot of the structure of kinesin 5 motor domain bound to AMPPNP and microtubule. 24 microtubules were carefully selected and ~40,000 asymmetric units averaged to calculate the 9 Å-resolution 3D reconstruction of the Klp61f-microtubule complex (9). Crystal structures (ribbons) of tubulin and Klp61f were fitted into the cryo-EM density map (surface and mesh). Secondary structures appear as distinct shapes in the cryo-EM map: in particular alpha-helices appear as rods of density.

6. In cryoEM, image contrast depends on the density of bound protein being higher than the density of the buffer. Avoid phosphate buffer and use the minimal concentration of kinesin to fully occupy MTs. Keep the layer of vitreous ice thin (but thick enough so that MTs are not squashed).
7. Glow-discharging makes the carbon hydrophilic and enhances adsorption of MTs (the surface of MTs is negatively charged). Unused carbon becomes hydrophobic again over time, so you should repeat the glow-discharging step for grids that have not been used within an hour.
8. MTs can be incubated with kinesin prior to application on the grid. However, this can cause bundling, so it is preferable to first adsorb the MTs on the carbon surface and then add the kinesin, as described in Subheading 3.4.
9. In negative stain, MTs get squashed on the grid, making it hard to use these images for 3D reconstruction. A slightly thicker stain, obtained by blotting the grid only partially, might reduce this squashing effect.
10. UrAc is acidic (pH 4.2). However, it gives the best staining for MTs, whereas other neutral stains, e.g. methylamine tungstate, seem to disrupt the structure of MTs. UrAc also appears to be tolerated by a number of kinesin motor domain constructs,

but such low pH can cause denaturation/aggregation of some proteins.

11. During the process of blotting and plunging the sample, the solution layer gets very thin and considerable evaporation can occur. This might cause an increase in ionic strength and potentially result in the protein complex falling apart. However, this problem can be overcome by a high humidity environment.
12. Ice contamination is one of the problems in obtaining a high-quality sample for cryo-EM. Humidity of the ambient air and of the user's breath tends to form ice crystals that accumulate in the liquid nitrogen and on the sample itself. To reduce ice contamination, keep liquid nitrogen covered whenever possible, avoid breathing near the sample and be as quick as possible.
13. A substantial fraction of the electrons cause radiation damage to biological samples in ice. This is dependent on the voltage at which the microscope is operated. At 200 kV, to preserve high-resolution information, the total electron dose must be limited to $15\text{--}20 \text{ e}^-/\text{\AA}^2$. The exposure dose can be readily measured on the microscope phosphorus screen or on the CCD using the respective user interfaces (the objective aperture stops part of the beam after it is scattered by the specimen and should, therefore, be out when measuring the electron dose effectively seen by the sample). When looking at the grid at low magnification, limit the area exposed to a minimum, keep the beam intensity low (the "measured exposure time" should read 3 s or higher), and use the beam blank whenever possible.
14. Digital micrographs collected on CCD images are increasingly employed instead of emulsion films to collect data for high-resolution reconstructions. To date, CCDs cover a smaller area than films; this is not a problem for single-particle reconstruction, but makes helical reconstruction difficult because long stretches of filaments are required.
15. It is recommended to scan the films at the smallest step size ($7 \mu\text{m}$ on a Zeiss SCAI scanner) because larger step sizes omit some information (e.g. with a $14 \mu\text{m}$ step size, only every other data point along the film is recorded compared to $7 \mu\text{m}$).
16. It has been shown that protofilament number can vary along a single MT polymerised *in vitro* (21), so the moiré pattern should be checked all along the MT.

Acknowledgments

The authors would like to thank past and present members of the Moores Lab (Andy Bodey, Carsten Peters, Christina Hoey, and Kanwal Zehra) for helpful discussions. We are grateful to Kanwal

Zehra and Natasha Lukyanova for providing us with constructive comments on the manuscript. We thank the Wellcome Trust, the Birth Defects Foundation, the Ecole Normale Supérieure, and the French Ministère de la Recherche for funding.

References

- Hirokawa, N. (1998) Kinesin and dynein superfamily proteins and the mechanism of organelle transport. *Science* **279**, 519–526
- Wittmann, T., Hyman, A., and Desai, A. (2001) The spindle: A dynamic assembly of microtubules and motors. *Nat. Cell Biol.* **3**, 28–34
- Vale, R.D., and Milligan, R.A. (2000) The way things move: looking under the hood of molecular motor proteins. *Science* **288**, 88–95
- Cross, R.A. (2004) The kinetic mechanism of kinesin. *TRENDS in Biochem. Sci.* **29**, 301–309
- Dubochet, J., Adrian, M., Chang, J.J., Homo, L.C., Lepault, J., McDowall, A.W., and Schultz, P. (1988) Cryo-electron microscopy of vitrified specimens. *Q Rev. Biophys.* **21**, 129–228
- Kikkawa, M., and Hirokawa, N. (2006) High-resolution cryo-EM maps show the nucleotide binding pocket of KIF1A in open and closed conformations. *EMBO J.* **25**, 4187–4197
- Hirose, K., Akimura, E., Akiba, T., Endow, S.A., and Amos, L.A. (2006) Large conformational changes in a kinesin motor catalyzed by interaction with microtubules. *Mol. Cell* **23**, 913–923
- Sindelar, C.V., and Downing, K.H. (2007) The beginning of kinesin's force-generating cycle visualized at 9-Å resolution. *J. Cell Biol.* **177**, 377–385
- Bodey, A.J., Kikkawa, M., and Moores, C.A. (2009) 9 Å structure of a microtubule-bound mitotic motor. *J. Mol. Biol.* **388**, 218–224
- Sindelar, C.V., and Downing, K.H. (2010) An atomic-level mechanism for activation of the kinesin molecular motors. *PNAS* **107**, 4111–4116.
- Amos, L.A., and Hirose, K. (2007) Studying the structure of microtubules by electron microscopy. *Methods Mol. Med.* **137**, 65–91
- Moores, C. (2008) Studying Microtubules by Electron Microscopy. *Methods in Cell Biol.* **88**, 299–317
- Iancu, C.V., Tivol, W.F., Schooler, J.B., Dias, D.P., Henderson, G.P., Murphy, G.E., Wright, E.R., Li, Z., Yu, Z., Briegel, A., Gan, L., He, Y., and Jensen, G.J. (2006) Electron cryotomography sample preparation using the Vitrobot. *Nat. Protoc.* **1**, 2813–2819
- Grassucci, R.A., Taylor, D.J., and Frank, J. (2007) Preparation of macromolecular complexes for cryo-electron microscopy. *Nat. Protoc.* **2**, 3239–3246
- Grassucci, R.A., Taylor, D.J., and Frank, J. (2008) Visualization of macromolecular complexes using cryo-electron microscopy with FEI Tecnai transmission electron microscopes. *Nat. Protoc.* **3**, 330–339
- Metlagel, Z., Kikkawa, Y.S., and Kikkawa, M. (2007) Ruby-Helix: An implementation of helical image processing based on object-oriented scripting language. *J. Struc. Biol.* **157**, 95–105
- Shaikh, T.R., Gao, H., Baxter, W.T., Asturias, F.J., Boisset, N., Leith, A., and Frank, J. (2008) SPIDER image processing for single-particle reconstruction of biological macromolecules from electron micrographs. *Nat. Protoc.* **3**, 1941–1974
- Grigorieff, N. (2007) FREALIGN: high-resolution refinement of single particle structures. *J. Struct. Biol.* **157**, 117–125
- Ray, S., Meyhofer, E., Milligan, R.A., and Howard, J. (1993) Kinesin follows the microtubule's protofilament axis. *J. Cell Biol.* **121**, 1083–1093
- Li, H., DeRosier, D.J., Nicholson, W.V., Nogales, E., and Downing, K.H. (2002) Microtubule structure at 8 Å resolution. *Structure* **10**, 1317–1328
- Chretien, D., Metoz, F., Verde, F., Karsenti, E., and Wade, R.H. (1992) Lattice defects in microtubules: Protofilament numbers vary within individual microtubules. *J. Cell Biol.* **117**, 1031–1040
- Konishi, Y., and Setou, M. (2009) Tubulin tyrosination navigates the kinesin-1 motor domain to axons. *Nat. Neurosci.* **12**, 559–567
- Tilney, L.G., Bryan, J., Bush, D.J., Fujiwara, K., Mooseker, M.S., Murphy, D.B., and Snyder, D.H. (1973) Microtubules: evidence for 13 protofilaments. *J. Cell Biol.* **59**, 267–275
- McIntosh, J.R., Morphew, M.K., Grissom, P.M., Gilbert, S.P., and Hoenger, A. (2009) Lattice structure of cytoplasmic microtubules in a cultured Mammalian cell. *J. Mol. Biol.* **394**, 177–182

Chapter 6

Structural and Dynamic Characterization of Biochemical Processes by Atomic Force Microscopy

Frédéric Eghiaian and Iwan A.T. Schaap

Abstract

Atomic Force Microscopy (AFM) has gained increasing popularity over the years among biophysicists due to its ability to image and to measure pN to nN forces on biologically relevant scales (nm to μm). Continuous technical developments have made AFM capable of nondisruptive, subsecond imaging of fragile biological samples in a liquid environment, making this method a potent alternative to light microscopy. In this chapter, we discuss the basics of AFM, its theoretical limitations, and we describe how this technique can be used to get single protein resolution in liquids at room temperature. Provided imaging is done at low-enough forces to avoid sample disruption and conformational changes, AFM allows obtaining unique insights into enzyme dynamics.

Key words: Atomic force microscopy, Cantilever, Thermal noise, Silane, Virus, Microtubule, Kinesin

1. Introduction

1.1. How It Works

1.1.1. Imaging

The principle of Atomic Force Microscopy (AFM) (1) draws similarities with that of a gramophone: Both employ a sharp probe located at the extremity of a lever and detect height variations on a surface. In the case of AFM, the cantilever is up to a few 100 micrometers-long, and the probe is a very sharp tip with a radius in the order of 10 nm (Fig. 1). When the tip contacts the surface, the bending of the cantilever provides us with a measure of the applied force. This bending is commonly measured by focusing a laser on the cantilever and collecting the reflected beam with a segmented photodiode, which gives an electrical signal proportional to the bending. Piezoelectric actuators control the position of the AFM cantilever with respect to the sample in all three dimensions with subnanometer precision. For applications where

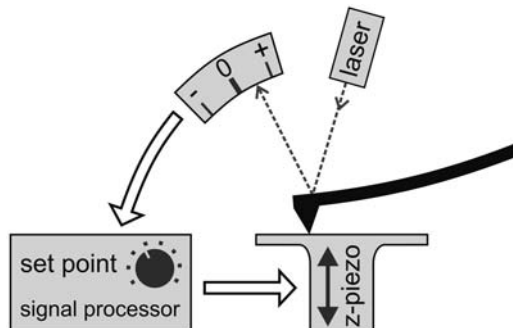


Fig. 1. The AFM feedback loop. The tip is positioned at the end of a flexible cantilever that is connected to a larger chip at its other end. The bending of the cantilever is measured, reflecting a laser beam shone on the back of the cantilever toward a segmented photodiode. The resulting electrical signal that is proportional to the bending is fed into a fast signal processor and compared with the desired bending (the set point). When a correction is needed the voltage to the z-piezo is changed to correct the height of the cantilever with respect to the sample. When the AFM is operated in tapping mode, the principle remains the same, and only now the amplitude of the oscillating cantilever is used as feedback parameter.

force is critical, a feedback loop acts on the z-piezo to keep the cantilever deflection constant, by adjusting the z-distance between the tip and the sample. The amount of force is determined by the “set point” (i.e., the desired amount of cantilever bending), and the settings of the feedback loop (controlled by the feedback parameters). For imaging the tip is scanned in x - and y -direction along the surface while keeping the force constant: When the tip meets a surface-bound object, this leads to an increase in cantilever bending, to which the feedback loop responds by moving away the scanner until the set point is reached. Thus, the topography of the sample can be reconstructed from the x - y - z signals that are used to control the scanner. For soft or weakly attached samples (such as single proteins or DNA, but also larger complexes such as microtubules or viruses), the scanning motion of the tip will result in high lateral forces applied to the samples that are not detected by the cantilever bending (see Note 1). To be able to image soft samples without wiping them away, tapping (or dynamic) mode ([2](#), [3](#)) is most often employed. In this mode, a small additional piezoelectric element drives the cantilever at frequencies from single to hundreds of kHz. When the oscillating tip is brought closer to the surface, the amplitude of the oscillation will reduce as a result of tip–surface interactions. Hence, in tapping mode the set point becomes the desired amplitude of oscillation of the cantilever, which will be kept constant by the action of the feedback loop on the scanner z -position. Lateral forces applied to the sample are greatly reduced because the oscillating tip is actually touching the sample only for about 10% of each oscillation cycle when operating in liquid ([4](#)).

1.1.2. Force Spectroscopy

AFM is also used to measure the mechanical properties of biological samples. The tip is placed on top of a structure (that can be located and identified by AFM imaging) and then used to indent it. The stiffness of the deformed object can be obtained by measuring the slope of the force versus distance (or FZ) curve (i.e., the measured force as function of the z-piezo displacement). In addition, the elasticity or fracture limits can be measured by looking at the reversibility of the deformation. Mechanical properties of biomolecular complexes such as microtubules (5), viruses (6), man-designed 3D DNA structures (7) and whole cells (8) have been studied using this technique. Alternatively, AFM can be used to pull on the molecules to measure their mechanics. In such experiments, the AFM tip is first brought in contact and attached to the molecule of interest. Often, specific cross-linking chemistry (biotin-streptavidin or thiols) is used to connect the surface-adsorbed molecule to the tip. Once the tip fishes a molecule of interest, the probe is moved upward to pull the sample. By this way, the forces involved in protein folding/unfolding (9, 10) and receptor–ligand interactions (11, 12) have been measured. The effects of an externally applied force on the enzymatic activity have also been measured by AFM pulling on single molecules (13).

1.2. Insights into the Structural Dynamics of Biomolecules

AFM can be operated in liquid at room temperature: Many solutions can be used in general, from physiological buffers to organic solvents (14), providing that the molecular structure or enzyme activity is preserved. Therefore, in these conditions, AFM has the potential to image biomolecules at high resolution in liquid and to follow their dynamics. The resolution, which lies in the single nanometer range (see also (15)), is mainly determined by the dimensions of the tip, the thermal noise and the softness of the sample itself. Obviously, AFM has its own pitfalls, mostly in terms of dynamic studies, as we see below.

1.2.1. Fast Imaging

Most of the commercially available AFMs can record nanometer-resolution images (i.e., 200×200 nm at 128×128 pixels) within tens of seconds. In comparison, fluorescence microscopy now achieves positional detection of fluorophores with nm precision or FRET detection at video rates (16) (≈ 40 ms/frame), with a field of view on the micrometer length scales. Despite its limited frame rate, standard AFM setups have been successfully used to study conformational changes of nanometer-sized macromolecules (17–19). Pioneering work by Ando and colleagues has led to the development of AFM instrumentation that is capable to image biological samples on the millisecond timescale (20) (see also (21–23)). Using very small cantilevers that combine a high resonance frequency with a low spring constant, fast piezo scanners and controlling electronics are essential for such fast scanning. Fast AFM provides an exciting view on subsecond dynamics of single molecules, such as molecular motors on their own (20), or on their “polymer” tracks (24), restriction enzymes (25), and chaperone proteins (26).

Alternatively, to access fast events with fast AFM, one can sacrifice the spatial resolution of images to the benefit of time resolution. In 1994, Radmacher et al. observed conformational changes of single Lysozyme molecules that were presumably associated with their enzymatic activity (27) by simply pressing the AFM tip on an individual enzyme at low force. Height fluctuations of the tip were recorded at kHz rate for a few seconds, which reflect the movements of the species sitting underneath. This technique is now rather easily accessible by most standard AFMs without any particular modification. An intermediate method is to reduce the image size to a single line (28), which permits to visualize the two-dimensional height profile of the molecule of interest and follow its variation with time. Single lines can be scanned at a maximal rate of about 20 Hz with a standard AFM setup. Viani et al. used single-line scanning to detect fast, 1 nm height fluctuations in GroEL/GroES “chaperone” complexes (29), which were attributed to the conformational dynamics of the assembly. With the new fast-speed AFM, Yokokawa et al. repeated single-line scanning of surface-bound GroEL/GroES at a 1,000 Hz scan rate, and determined that the lifetime of the height fluctuations was at least 10 ms (26).

1.2.2. Low Force Imaging

Most biological samples are fragile and will be easily destroyed during AFM imaging as a result of imaging forces: What is the maximum force to be applied to biological samples? By performing force versus distance curves on top of samples we and others have determined that the maximum force that can be applied on various biological structures is generally between 0.1 and 1 nN (summarized in Table 1, see Note 2). Similar forces are sufficient to disrupt ligand–receptor bonds and to unfold proteins (9, 11). During imaging, the forces have to be well below these limits. Figure 2 shows a microtubule (a relatively stiff filament of 25 nm diameter that is part of the cytoskeleton) that could only be scanned without destroying it using forces limited to \approx 100 pN. Pulling experiments with optical

Table 1
Force response of various biological structures

	Max. force (nN)	Spring constant (N/m)	References
Microtubules	0.35	0.074	(5)
Microtubules + tau	0.44	0.08	(41)
DNA tetrahedra	\approx 0.1	0.18	(7)
Alpha lactalbumin tubes	\approx 0.4	0.058	(45)
CCMV	>0.2	0.05–0.2	(46)
Liposomes	\approx 1	0.025	(47)

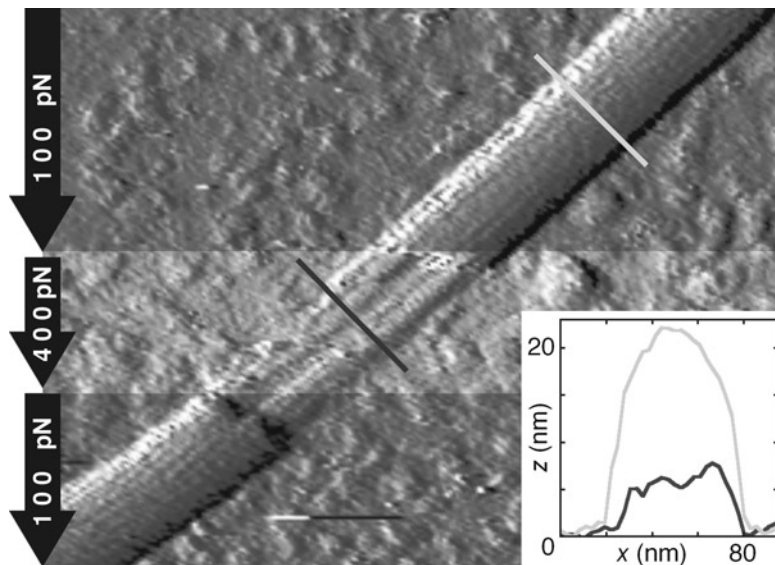


Fig. 2. Sample destruction at high scan forces. “Jumping mode” was used to record the exact forces applied during scanning, where for each image pixel a force versus distance curve is performed from which the exact maximum force and height of that pixel can be measured. The scanning direction was downward with horizontal scan lines. The image shows a microtubule; halfway, the scan force was increased from 100 to 400 pN. The region where 400 pN was used is rendered in a brighter color for clarity. At 100 pN the microtubule is intact and the protofilaments can be seen as lines running parallel to the microtubule axis. At a scan force of 400 pN, the microtubule got immediately destroyed, and only a layer of tubulin proteins was left on the surface. The inserted profiles clearly show the 20 nm height difference between the intact and destroyed parts of the microtubule. This figure is reprinted with kind permission from Springer Science + Business Media (43).

tweezers showed that forces as low as 10 pN are sufficient to pull kinesins off a microtubule (30), which implies that measurements of biomolecular dynamics require even more stringent control of forces (see Note 3). One biological molecule that is fairly insensitive to the scanning force is DNA, which withstands nN forces, and can even be scanned in air. Nevertheless, when the DNA sample forms 3D structures (7) or when its dynamic interactions with enzymes are investigated (18), the same low-force constraints apply.

2. Materials

2.1. AFM, Cantilevers, and Software

1. Nanotec Dulcinea (Nanotec, Madrid, Spain), Asylum Research MFP3D (Asylum Research, Santa Barbara, CA, US) atomic force microscopes (see Notes 4 and 5).
2. Rectangular RC800 ($20 \times 200 \mu\text{m}$, 0.05 N/m), BL150 ($30 \times 50 \mu\text{m}$, 0.03 N/m) or AC40 ($16 \times 38 \mu\text{m}$, 0.1 N/m) cantilevers, (Olympus, Japan) (see Notes 6–9).

3. The AFMs were operated with the default software (WSxM for Nanotec, IgorPro based for Asylum Research).
4. All image processing and analysis were carried out using the free WSxM software (Nanotec, Madrid, Spain) (31).
5. Processing of force versus distance curves and noise recordings was done with ORIGIN (ORIGINLAB) or IgorPro (WAVEMETRICS).
6. Conversion of PDB files to an AFM height image was done in a custom-written routine in LabVIEW (National Instruments).

2.2. Samples

1. “HPLC-grade” water or 0.22 μm filtered, deionized water with an $18.2 \text{ M}\Omega$ resistance for AFM imaging in water or for the preparation of aqueous buffers (see Notes 10 and 11).
2. Microscope coverslips (any source) as glass substrates, cleaned before use (see Subheading 3).
3. Muscovite mica was always of V-1 grade.
4. Hexamethyldisilazane (HMDS, *purum*, Fluka) and N'-(3-[Trimethoxysilyl]-propyl)diethylenetriamine (DETA, technical, Aldrich) were used to make glass hydrophobic or positively charged, namely. Store the silane stock at room temperature and away from light up to 2 months.
5. KOH pellets and glacial acetic acid used for silanization were >99% pure.
6. A 2-L sonication bath with an effective HF power of 80 W was used for all sonication steps.
7. The ribosomal 50S subunits were provided by A. Konevega and M. Rodnina, Max Planck Institut for biophysical chemistry, Göttingen, Germany. Microtubules were isolated from pig brain as described in (32). DNA and nucleosomes were provided by S. Sörös and W. Fischle, Max Planck Institut for biophysical chemistry, Göttingen, Germany. Kinesin motor proteins were provided by G. Wöhlke, Technical University Munich, Garching, Germany.

3. Methods

3.1. Surface Chemistry

How much a given sample binds to a surface depends on both the extent of the surface–sample contact area and the chemical nature of both the sample and surface. Many substrates are available that provide solutions for most of the biological AFM experiments. The most commonly used substrate is mica. Although mica does not bear a strong charge, one can easily bind biological samples to it using divalent ions such as Ni^{2+} or Mg^{2+} . Microtubules could be bound to mica and imaged with 40 mM of Mg^{2+} added to the

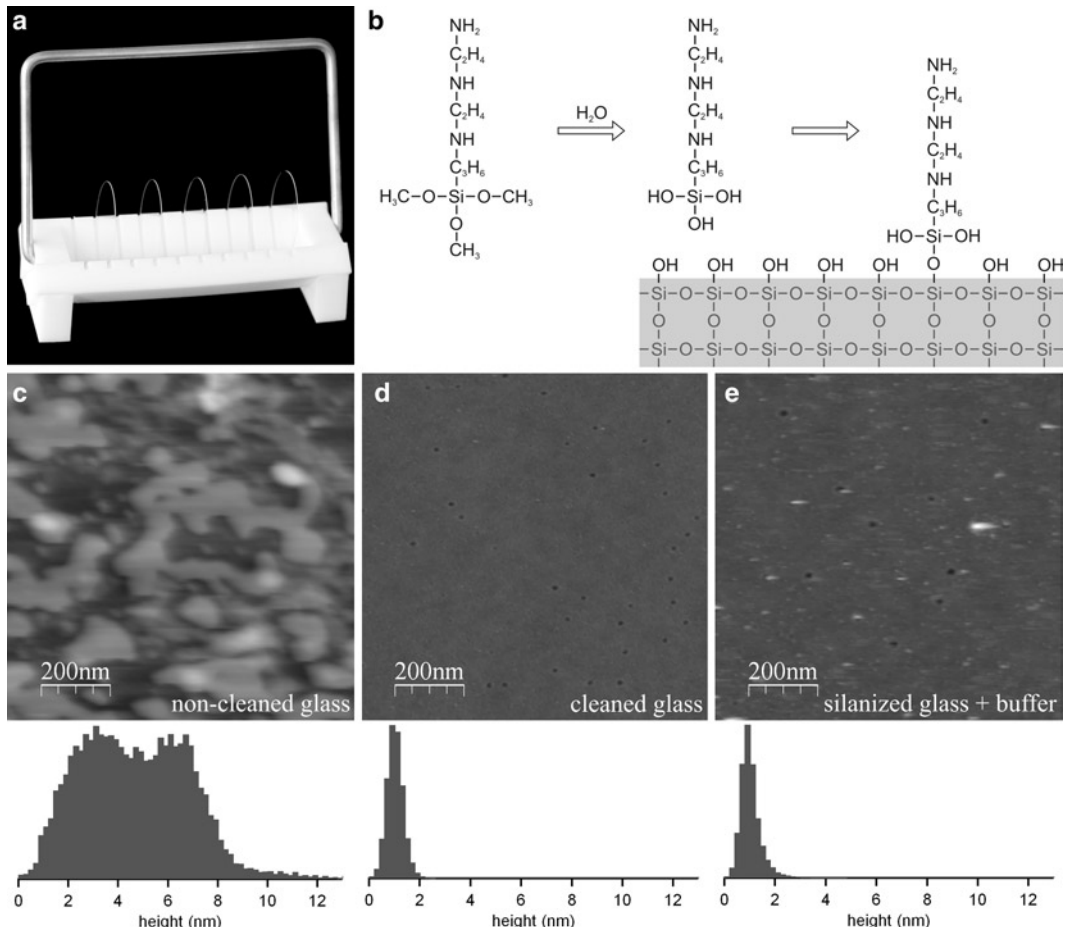


Fig. 3. Cleaning and functionalization of glass microscope coverslips. (a) Photograph of the custom-made Teflon coverslip holder that is used to immerse the coverslips into the cleaning and silanization solutions. (b) The reaction scheme between the amino-silane molecule and the glass surface. (c) AFM scan of a noncleaned coverslip, the histogram of pixel heights shows that the surface has a roughness of about 7 nm. (d) AFM scan of a cleaned coverslip, the roughness is about 1 nm. (e) AFM scan of a silanized coverslip imaged in buffer shows only a small increase of roughness and noise.

normal buffer. However, the kinetics of some enzymatic reactions may of course be affected at these concentrations.

Hydrophobic coating of glass is possible using the HMDS silane and was used with success to bind protein viruses (6, 33). Incubate clean glass into a container containing a few drops of HMDS for one or multiple hours. In all experiments presented in this chapter, we functionalized the glass surfaces with amino silanes (Fig. 3). As cleanliness is crucial for AFM, all glass substrates were first thoroughly cleaned, using the “KOH etching method” (see Note 12):

1. Dissolve ≈ 10 g of KOH in ≈ 10 ml water and supplement with ≈ 200 ml ethanol. Microscope coverslips are placed in a custom-made Teflon rack, which is placed in the glass container with the KOH solution.

2. Sonicate the container in a bath sonicator for 5 min. Subsequently, both the container and rack are rinsed and sonicated again in filtered and deionized water for 5 min. This washing step is repeated two more times. This cleaning procedure yields very flat surfaces (see Note 13).
3. For the silanization step, sonicate the coverslips again in a container filled with fresh water supplemented with 200 μ l of DETA and 20 μ l of acetic acid (the latter to avoid a too high pH resulting from the prior KOH etching steps, which would prevent the hydrolysis of the silane methyl groups). Next, sonicate the coverslips for 5 min in clean water, three times.
4. Place the Teflon rack in an oven until the coverslips are completely dry (\approx 20 min at 100°C). The silanized surfaces are usually stored in Petri dishes (see Note 14).

3.2. Choice of Cantilever, Low Force Imaging and Maximum Scan Speed

With the sample diluted to the right concentration (see Note 15) and bound onto the appropriate substrate, one has to choose a cantilever for its imaging (see Note 16). Both the maximum scan speed and the minimum force to be used during an AFM experiment directly depend on the type of cantilever used. First, the sensitivity of the bending detection and the spring constant of the used cantilever should be calibrated:

1. Align the AFM detector: With the cantilever immersed in liquid and the tip away from the surface, the laser beam is focused onto the cantilever and reflected onto a segmented photodiode (see Note 17). The photodiode is positioned such that the laser spot hits it in the center. The detector signal is in V and shows the deflection of the cantilever.
2. Do a force versus distance curve to convert the detector signal from V into a signal that describes the deflection of the cantilever in nanometers. The tip is brought down using the z-piezo against a hard surface (such as the glass background) and the bending of the cantilever (in V) is recorded. Because the displacement of the z-piezo is known (assuming this has been calibrated by the manufacturer or user), the slope of the contact part of the curve will give the calibration in m/V of the detector response (see Note 18).
3. If the applied forces are to be quantified for force spectroscopy, then record a thermal noise time series (using the detector signal, see Note 19), later to be used to find the resonance frequency and to calibrate the spring constant of the cantilever.
4. Convert the noise signal into a power spectrum. Figure 4a shows 5 s of a time series of noise obtained with a BL150 cantilever. Figure 4b shows the power spectrum of the same noise recording, obtained via a Fourier transformation (basically the square of the amplitude (i.e., the power) is plotted for

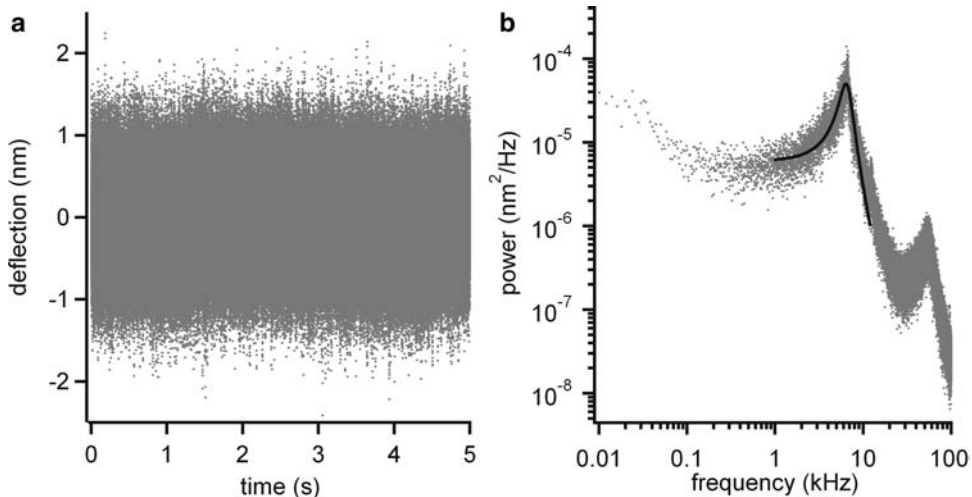


Fig. 4. Thermal fluctuations of the cantilever shown in the time and frequency domain. (a) The time series of the BL150 cantilever noise in nanometers sampled at 200 kHz, the amplitude is about 1 nm. (b) The same data shown as frequency spectrum. The first and second resonance frequencies of ≈ 6 and 40 kHz show up as peaks. The cantilever spring constant can be calculated by fitting a simple harmonic oscillator (Eq. 3) to the first resonance peak (black curve), which gives $S_0 = 4.8 \times 10^{-23} \text{ m}^2$, $f_0 = 6.6 \text{ kHz}$, $Q = 2.9$ (A and B were kept 0). Using these values in Eq. 4 results in a spring constant of 0.024 N/m .

each frequency). The large peak shows the fundamental resonance frequency, and the surface area under the plot gives the total amount of noise. In Fig. 5, the frequency response of three cantilevers is compared, the integrated force noise clearly shows that the total noise depends strongly on the type of cantilever and can be significantly reduced by decreasing the bandwidth of the data acquisition, although at the cost of temporal resolution (34, 35). Smaller cantilevers with the higher resonance frequency clearly show a superior performance.

5. Calibrate the spring constant of the cantilever when it is used in force experiments. The spring constant k of a cantilever describes its stiffness, i.e., how much force is needed to cause a certain amount of bending. AFM cantilevers are available with spring constants that range from 0.01 to 100 N/m. By detecting and adjusting the deflection, the applied force on the sample can be monitored and controlled. The spring constant is given by Eq. 1 (a one-sided clamped cantilever):

$$k = \frac{Ewt^3}{4l^3} \quad (1)$$

where E is the Young's (elastic) modulus of the material, w the width, t the thickness and l the length of the cantilever. The spring constant is given by the manufacturer but in practice the values can vary with almost a factor of 2 (Fig. 6). An easy

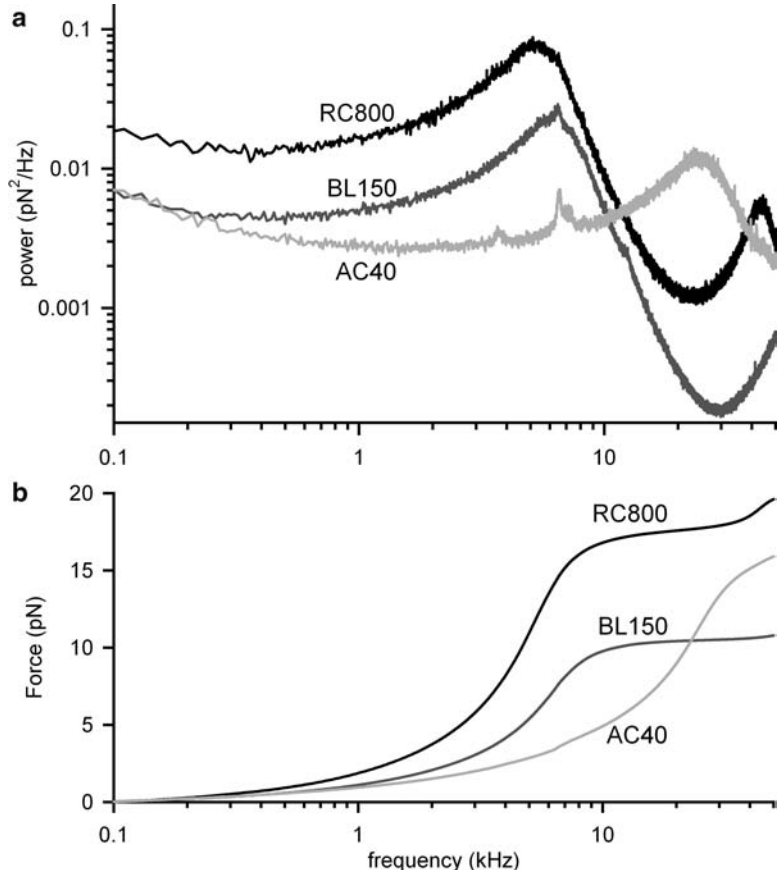


Fig. 5. Comparing the frequency response of three different cantilevers. (a) Power spectral density of the thermal noise (in pN²/Hz) for RC800, BL150, and AC40 cantilevers. To be able to quantitatively compare the noise of the different cantilevers, the signal was converted to force (pN) by multiplying the noise (in nm) with the spring constant (N/m) of the cantilever. (b) The integrated noise spectra for all three cantilevers shown up to 50 kHz. The smaller cantilevers clearly have the advantage of the lower noise, allowing the detection of smaller signals. The smallest cantilever (AC40) had superior performance up to 20 kHz. If the cantilever is to be used for force spectroscopy, it is beneficial to choose the recording bandwidth below its resonance frequency to reduce the noise.

calibration method that can be performed in liquid just before or after the measurements is to record the power spectrum of the noise (Fig. 4b) and use the equipartition theorem to calculate the spring constant (36). The equipartition theorem states that the average energy present in thermal motion of the spring is given by the product of the Boltzmann constant K_B and the absolute temperature T :

$$k \int S_x(f) = K_B T \quad (2)$$

where $\int S_x(f)$ is the integral of the power spectrum.

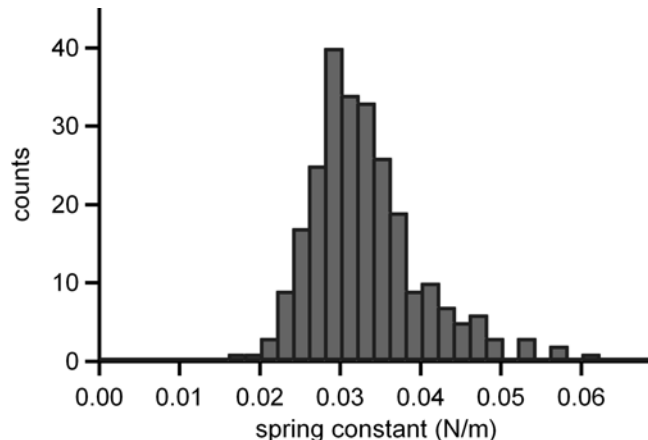


Fig. 6. Histogram of spring constants of 254 Olympus BL150 cantilevers used in our experiments between 2007 and 2010. The spring constants were calibrated using the Burnham method (38). The spring constant is $0.033 \text{ N/m} \pm 21\%$ (avg \pm s.d.).

6. Calibration routine: Use the thermal noise recording of the cantilever deflection (at least 10 s) and convert the detector signal into m as described before. The real deflection of the cantilever will be slightly underestimated because the cantilever is mounted under an angle α of about 15° with respect to the surface, which means that the reference frame of the detection is rotated by this angle with respect to the reference frame of the cantilever. Correct for this by multiplying the measured deflection by $1/\cos \alpha$. A second correction factor that typically ranges between 1.05 and 1.09 depends on the spot size of the laser and its position on the cantilever (37).

Convert the corrected deflection versus time recording into a power spectrum $S_x(f)$ (which has m^2/Hz as units) which is the squared frequency spectrum that is obtained by a Fourier transformation. For calculation of the spring constant, perform a fit using a simple harmonic oscillator (Eq. 3) to the first resonance peak visible in the power spectrum (38) (Fig. 4b), (see Note 20).

$$S_x(f) = \frac{A}{f} + B + \frac{S_0 f_0^4}{Q^2 (f_0^2 - f^2)^2 + (f_0 f)^2} \quad (3)$$

f is the frequency, A and B the pink and white noise respectively (see Note 21). S_0 the amplitude at the resonance frequency f_0 , and Q gives the quality factor of the resonance peak. The spring constant of the cantilever k is obtained by inserting the fit parameters of Eq. 3 into:

$$k = \frac{2K_B T Q}{\pi S_0 f_0} \quad (4)$$

Most AFMs have such calibration routines built in and if not, the cantilever deflection should be recorded at a high enough sampling frequency (at least four times the expected resonance frequency) for about 10 s and processed with a data processing program like ORIGIN or IgorPro following the aforementioned steps.

7. Set the cantilever drive frequency and amplitude. When using tapping mode, drive the piezo at the resonance frequency of the cantilever to obtain the maximum amplitude at the minimal drive energy (see Note 22). The resonance frequency in vacuum is given by:

$$f_{0\text{vacuum}} = \sqrt{\frac{k}{m}} / 2\pi = \frac{t}{4\pi l^2} \sqrt{\frac{E}{\rho_{\text{cantilever}}}}, \quad (5)$$

where m is the mass and $\rho_{\text{cantilever}}$ the density of the cantilever. In liquid, the resonance frequency will be lower than that calculated by Eq. 5 because of the viscous drag on the cantilever. The relation is given in Eq. 6, where ρ_{fluid} is the density of the surrounding fluid (for more details see ref. 39),

$$\frac{f_{0\text{vacuum}}}{f_{0\text{fluid}}} = \sqrt{1 + \frac{\pi w \rho_{\text{fluid}}}{4t \rho_{\text{cantilever}}}}. \quad (6)$$

The amplitude of oscillation can be set as low as a few nm; we mostly use values between 3 and 10 nm (see Note 23).

8. Use smaller cantilevers for fast imaging. The resonance frequency of the cantilever should exceed that of the z-piezo by a factor of ≈ 10 . For most current AFM scanners this requires > 10 kHz. Equations 1 and 5 show that the spring constant and resonance frequency of the cantilever depend on its dimensions. A proportional reduction of t and l , will not affect the spring constant, whereas Eq. 5 shows that a twofold reduction of t and l will lead to a doubling of the resonance frequency. Reducing w in Eq. 1 will further lower the spring constant but will not affect the resonance frequency. In conclusion, by making the cantilevers smaller in all three dimensions a low spring constant can be combined with a high resonance frequency. In addition Fig. 5 shows that the smaller cantilevers also have the lower noise levels as result of their reduced surface area. Limits on the minimal dimension arise from the fabrication process and the size of the laser spot (which is limited by diffraction) that is used to measure the deflection.

3.3. Image Analysis

AFM images are mostly displayed using a color or gray scale, in which dark is used for low parts and bright for the high parts. The unprocessed AFM images will be affected by drift, tilt of the surface and noise from various sources. The quality of the images can

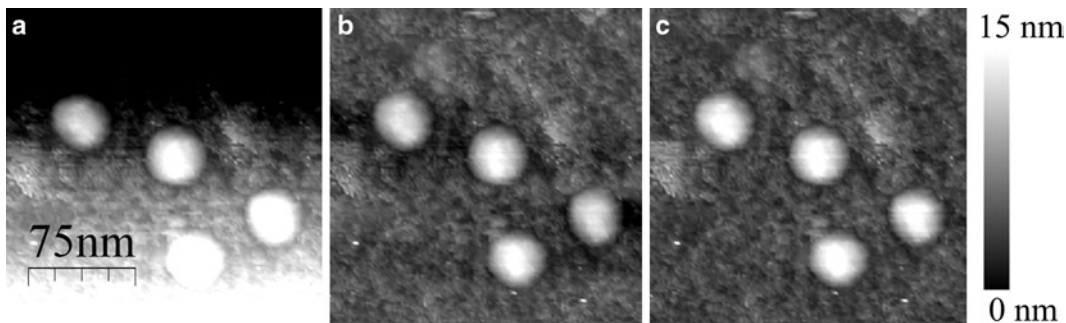


Fig. 7. Image flattening. **(a)** The unprocessed image shows a tilted background. **(b)** The line-fit-and-subtract filter is applied on the whole image. As a result, the background left and right to the ribosomal subunits is lowered and the particles appear to lie in a trough. **(c)** Now, the four particles are excluded from the line-fit-and-subtract routine. The background appears completely flat, and all particles have identical heights.

be significantly enhanced by performing a few image processing steps that will improve the representation of the data and help to bring up small topographical details.

1. Correct the tilt by flattening the image. Because the surface plane of the sample will hardly ever be perfectly perpendicular to the z-scan direction most images will appear tilted. Correct this by fitting a plane to the image and subtract this from the image, or by correcting the height and tilt of each scan line (see Note 24). Particular care has to be taken to exclude the sample molecules from the fitting procedure. Else, dark bands on the left and right sides of the object will be introduced, because the average height of each scan line will be set identical by the subtraction routine (Fig. 7).
2. To reduce the noise the trace and retrace images can be averaged. First, align the flattened images by calculating the lateral offset between both images via a cross-correlation function, and then, add up the pixel values and divide the sum value per pixel by 2 to maintain the correct height information (see Note 25).
3. To reveal fine structure in a sample, limit the range of the look up table (range of colors used to create the height image) to the object of interest; this will bring up the details but will result in an image that shows the rest of the sample as black or white (Fig. 8). Alternatively, to enhance the edges on an object, use a derivative filter, which calculates for each scan line its numerical derivative by replacing each pixel (n) value by the sum of its neighbors $(n+1)-(n-1)$. As a result, sharp transitions will give high values and flat areas will yield zero values. To maintain a realistic image, the original pixel value can be added: $(k \times n) + (n+1) - (n-1)$, where k gives the ratio between the original value and the derivative image (see Note 26).
4. To measure heights either (a) “draw” a topography line over the image, along which the height is measured. This method is

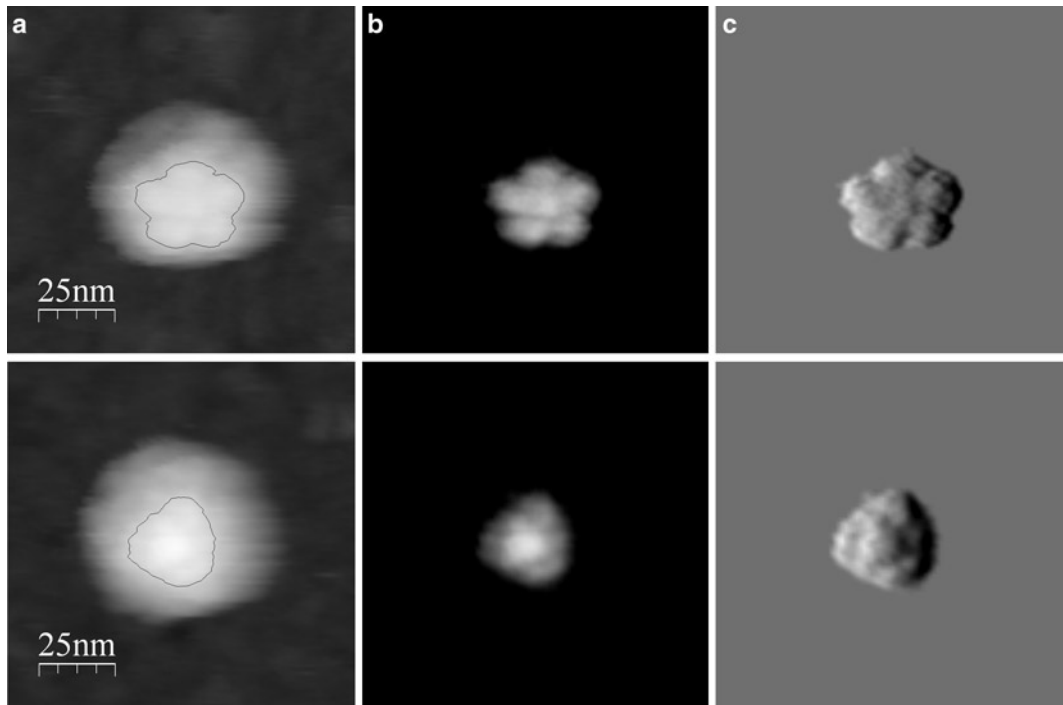


Fig. 8. Detail enhancement in AFM images. The scan shows a Parvovirus (MVM, scan kindly provided by C. Carrasco and P. J. de Pablo from the Universidad Autónoma, Madrid, Spain) (33). The first row shows MVM in the fivefold symmetry, and the second row shows the same in threefold symmetry. (a) The original image flattened as described in Fig. 7, the height of the virus is ≈ 22 nm, fine details cannot be recognized. (b) The same image with a reduced gray-scale range, to show only the highest 5 nm (this region is illustrated by a fine line in (a)). Now, details on top of the virus can be recognized. (c) The derivative filtered image shows more clearly the fine structure of both symmetries.

very sensitive to local contamination of the background, and when the topography profile is not along a single scan line, drift of the instrument and/or errors in the flattening procedure can strongly affect the results. To reduce the sensitivity to surface contamination and to increase the statistics, multiple topographical profiles should be aligned and averaged; or (b) Compose a histogram of the height of all the pixels of an image (that has been previously flattened following the procedure described before). If there are one or more objects their average height will show as a peak, the distance between this and background peak gives the average object height (see also Fig. 3c and Note 27).

5. Lateral distances may be affected by tip-sample dilation and drift. Because the dimensions of the scanning probe are large compared to the sample the scanned image will be formed by both the sample and the tip shape. Figure 9b shows the effects of dilation when a microtubule is scanned with a 20 nm radius parabolic tip. Dilation will affect the apparent width of an object but not its maximum height, nor the spacing between two features of identical height. In practice the radius of commercially

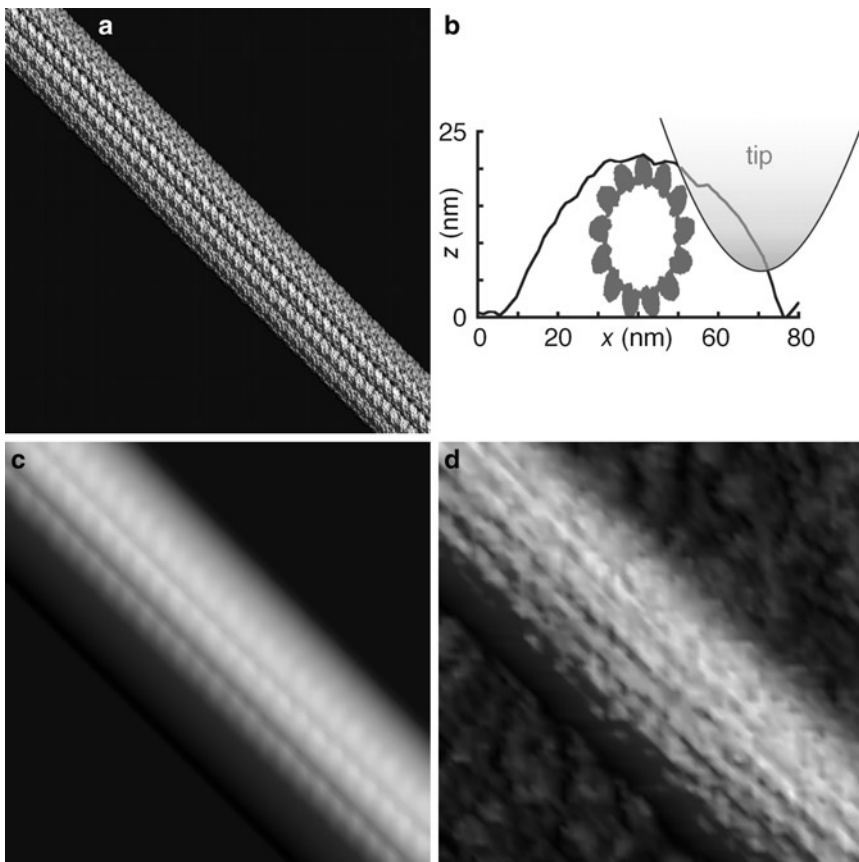


Fig. 9. Tip–sample dilation. (a) A top-view of a PDB reconstruction of a 200-nm long microtubule segment. The PDB file was kindly provided by Kenneth Downing (44). (b) Dilation effect of the tip. The graph shows the microtubule from image (a) and a parabolic tip. The z and x scales are different; therefore, the inserted microtubule cross-section appears deformed. Figure reprinted with kind permission from Springer Science + Business Media (43). (c) The PDB structure from image (a) diluted with a 10-nm parabolic tip, using the WSxM software. The width gets exaggerated due to the tip–sample dilation, but the protofilaments remain visible as lines parallel to the microtubule axis. (d) Real AFM scan of a 200-nm microtubule segment, showing a very similar dilation effect as predicted from (c). The protofilaments can still be recognized, but the tubulin monomers are masked by the noise.

available tips that are mounted on cantilevers that are suitable for low force imaging lies between 5 and 30 nm (see Note 28). In addition drift in x - y direction will cause a change in the apparent distance between two objects (see Note 29).

3.4. Comparing AFM Scans to PDB Structures

The structure of many proteins and protein assemblies has been determined with subnanometer resolution by X-ray crystallography or NMR, or has been estimated by fitting the X-ray/NMR structures into electron-density maps obtained by cryo-electron microscopy. Structural data is available at the protein data bank (<http://www.pdb.org>) which stores the atom coordinates of known structures in “PDB files” (40). These structures can be compared to AFM images to determine the orientation of particles and to

recognize substructures. To predict the effects of tip–sample dilation on a given structure, the basic operations are:

1. Read the PDB file.
2. Orientate this structure on a flat surface.
3. Resample the image with 256×256 pixels, where the height information is the maximum height of the PDB structure in each pixel. We performed these steps by a custom-written routine in LabVIEW.
4. Export the file in a format that can be read by the AFM software, in our case the WSxM software. The resulting AFM-like image is dilated by an imaginary parabolic tip with a typical radius ranging between 10 and 30 nm. Dilation simulations were performed with the WSxM software.
5. Figure 9 compares the dilated PDB structure of a microtubule with a real AFM scan. Protofilaments are visible in both the PDB-inferred image and real AFM scan.

3.5. Imaging of Sample Dynamics

To observe dynamics of samples, again the most important requirement is that the sample and its dynamics are not disturbed by the forces applied by the AFM tip. Next, the imaging parameters should be optimized such that the acquisition time is minimized but the relevant details of the sample remain visible.

1. Minimize the scan area to the object of interest, 150×150 nm or less.
2. Reduce the number of pixels and scan lines, 128×128 px, or even 64×64 px. A resolution of 1–3 nm/px is often sufficient for good image quality.
3. Increase the scan frequency and increase feedback parameters to maintain a constant image quality.
4. Once the limits are reached (see Note 22) a further increase in scan speed will lead to a clear loss in image quality as demonstrated in Fig. 10.

When the image acquisition rate is higher than the rate of the conformational changes of the sample, then the tens of pN applied by the AFM tip are likely to bias, or even prevent the conformational changes. However, if the conformational changes are fast compared to the image acquisition time, only the conformational states before and after the structural transitions will be observed, and the applied forces are less likely to affect sample dynamics. An example of the latter approach is the study of individual kinesin motor proteins over the microtubule lattice (19).

1. Dilute the microtubules to 10 mg/ml in 80 mM Pipes, pH 6.9, 1 mM EGTA, 1 mM MgCl₂, 10 μM taxol.

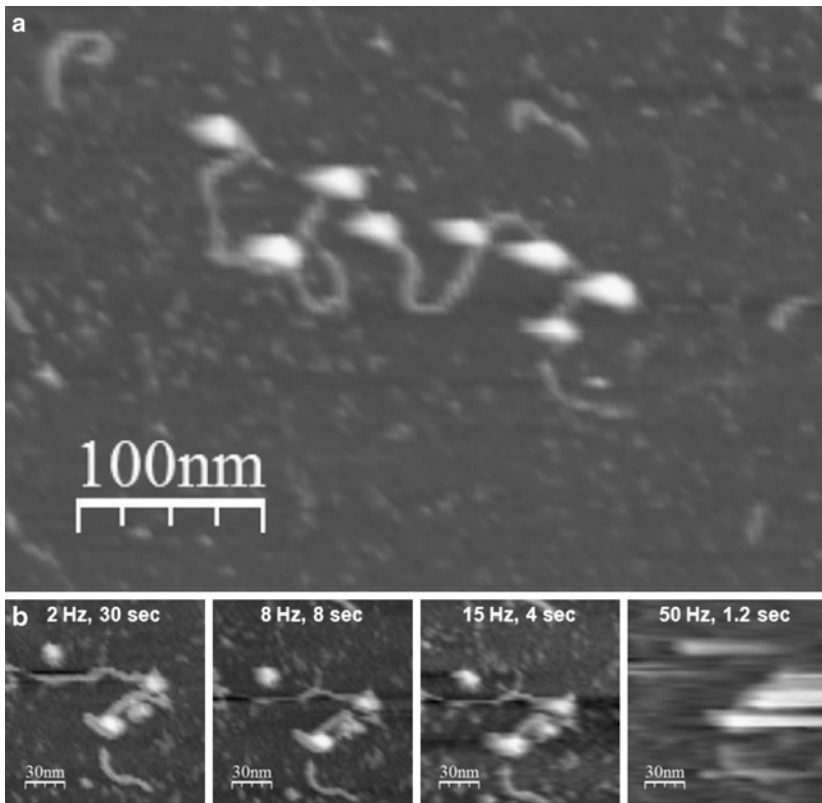


Fig. 10. Image quality depends on the scan speed. (a) A DNA partly compacted by eight nucleosomes bound (Imaging time: 250 s). (b) An image sequence showing repeated scans of a zoom of another piece of DNA with three nucleosomes bound and one unbound. The image was scanned with 64 × 64 pixels at different scan line frequencies. The imaging time varied from 30 s to 1.2 s, as indicated in the images. The image obtained in 4 s still shows an acceptable quality.

2. Pipette 40 μ l sample onto the silanized surface, and allow the microtubules to bind for 15 min.
3. Add dimeric kinesin motors in a equimolar ratio (kinesin:tubulin) to the sample.
4. Kinesin can be immobilized on the microtubule by using AMP-PNP, a nonhydrolyzable ATP analog. Figure 11a shows a microtubule that is partly decorated with kinesin (41).
5. To follow displacements of individual motors wash out the AMP-PNP by washing the sample with multiple volumes of buffer and add ATP in μ M concentrations. Figure 11b shows single moving kinesin motors (19).
6. In our experiments the maximum image acquisition rate of the instrument was about 10 s per image. This limit is set by the 1 kHz resonance frequency of the z-piezo scanner and the resonance frequency of the cantilever.

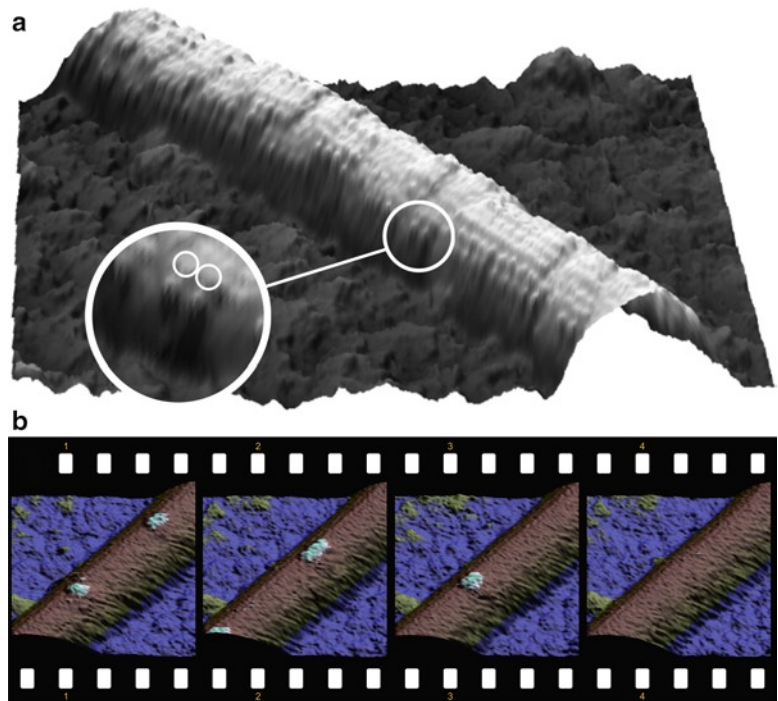


Fig. 11. Kinesin motor proteins on microtubules **(a)** A 450 nm long microtubule segment decorated with kinesin in presence of AMP-PNP shows a distinctive globular pattern. The inset shows an isolated motor of which both heads, spaced 8 nm apart, can be distinguished. **(b)** 4 sequential frames showing 2 single kinesin motors moving along a 200 nm long microtubule segment in presence of 0.5 μ M ATP. In the first frame two motors are visible, in the second frame both moved to the left lower corner of the image. In the third frame one motor moved out the imaged area, and in the last frame also the second motor disappeared. The acquisition time was 29 s per frame, the average motor velocity 3 nm/s.

4. Notes

1. Lateral forces can be measured by detecting the cantilever torsion, which can be done using a quadrant photodiode. Because the “torsional spring constant” of conventional cantilevers is much higher than their “bending spring constant,” this method is too insensitive to reduce the lateral forces to acceptable levels for bioimaging. For very stable samples such as 2D protein crystals with little variation in height, contact mode will give images with exceptional resolution (42).
2. If a sample needs to be mechanically tested by AFM indentation experiments, and there is the risk that tapping mode imaging damages the samples prior to force measurements: “Force mapping” allows performing low-resolution imaging and force measurements, simultaneously. Basically, force curves are performed in a raster of about 20×20 pixels. The height information can be reconstructed from the contact point of the FZ

curves on the object and at the surface. At the same time, the mechanics can be measured by evaluation of the FZ curves that were acquired on top of the object.

3. For fragile samples, the tip-sample contact time can be halved by lifting the tip during retrace for each scan line, potentially this also reduces the scan time. Care has to be taken that the height of tip retraction is superior to the expected height of the sample so that the tip does not touch the sample on the “way back.” This option is, however, not implemented on most AFMs.
4. To achieve high resolution, the instruments have to be isolated from vibrations. This can be achieved by active vibration-damping tables, or using a heavy stone slab suspended on the ceiling via four climbing ropes, each a few meters long. The sensitivity to vibrations varies from model to model: Often the larger, more complex AFM designs (especially combinations with inverted optical microscopes) are also the more sensitive ones. The same applies for acoustic noise: Some AFMs are rather insensitive to acoustic noise, whereas others need extensive isolation measures and quiet rooms.
5. Many AFM apparatuses are largely automated and it is often difficult for the experimentalist to understand how and when the software commands are translated to the hardware level, especially for the less experienced. In order to directly monitor the essential parameters, we use an oscilloscope to display the z-piezo signal versus the cantilever deflection in an *x-y*-plot. The required analog signals are available on most AFMs. The oscilloscope screen gives a direct visualization when the tip contacts the surface, if the tip remains in contact when the scan area is changed, if there is any adhesion between the tip and surface, when parameters are actually updated, if there is any additional noise, etc.
6. Most AFMs have a small clamp to hold the cantilever: Using such clamps can prove awkward (i.e., resulting in damaged chips); also, they may not be compatible with all types of cantilevers. For many of our experiments, we actually removed the standard clamp and use a very small amount of vacuum grease (Apiezon H) to stick the cantilever to the holder.
7. Excessive bending of the cantilever can occur when it gets immersed in liquid, which in some cases can lead to damage to the cantilever. To prevent this, pipette 10 µl of buffer onto the cantilever holder next to the cantilever so that the liquid wets the cantilevers from both sides. At any sample change the cantilever should remain immersed in liquid to prevent it to undergo further bending. In particular, when the cantilever is to be stored prior to a new series of experiments, it is best not to let it dry but to keep it immersed, mounted on the cantilever holder in a closed Petri dish with some soaked paper tissue to prevent evaporation.

8. In liquid, cantilever bending is very sensitive to temperature and flow. Once a cantilever is immersed, the “photodetector voltage” can drift considerably during the first few minutes but will decrease with the time spent by the cantilever in immersion.
9. Soft cantilevers used for bioimaging can be very sensitive to (nonwanted) adhesion of the tip to the surface. Putting the tip under a powerful UV lamp (254 nm, 5 W) for 15–30 min prior to use burns impurities stuck to the tip and, therefore, decreases the probability of adhesion at the start of the experiment.
10. When working with an open sample chamber the buffer will slowly evaporate during the experiment which will result in increased solute molarities. This change can be reduced by increasing the local humidity around the sample or by working with a closed sample chamber.
11. Centrifuge all buffers for 2 h at $200,000 \times g$, to spin down impurities, then aliquot the top half contents of the centrifuged tubes in 1 ml portions and store at -20°C . Use a fresh tube of buffer on each experimental day.
12. The cleaning procedures used depend on what is available in the lab. We achieved comparable results when cleaning the glass coverslips by “plasma cleaning” in a glow discharge apparatus.
13. Using the coverslip cleaning procedure for fluorescence microscopy showed us that the surfaces yield strong background fluorescence. To a large extent, this can be avoided by substituting ethanol with clean water.
14. For samples that bound only weakly to the silanized glass, we found out that fresh surfaces needed to be prepared on each experimental day; otherwise, the sample would not bind. For experiments with microtubules, best results were obtained with surfaces that were 5 days old at most.
15. To obtain clearly separated single molecule, one generally aims for a particle density of 10 molecules per μm^2 . Typically we pipette a drop of about 50 μl of the diluted sample onto the glass substrate. A 50 μl drop of buffer covers about $1 \times 10^8 \mu\text{m}^2$ (a 10 mm diameter circle). Assuming that all molecules bind to the surface, 1×10^9 molecules (i.e., 2×10^{-15} mole) are needed to reach the desired density, meaning that the sample concentration in a 50 μl drop has to be in the picomolar range. In practice, we find that this simple calculation predicts the surface coverage very well. When more than ten times the calculated concentration is required for a good surface coverage, it most likely indicates that the sample is poorly attached to the surface. It is important to make sure that the sample is bound to the surface at sufficient density to be easily detected in a micrometer-size scanning frame. Whereas the search for the sample may turn out to be cumbersome at too low surface

coverage, a too high sample concentration may pose problems with respect to the tip integrity.

16. Which cantilever for low force imaging? Thermal noise, which is in the order of 10 pN, defines the lower limit on the force that is exerted on the sample. The applied force is linked to the cantilever deflection via its spring constant: Thus the more accurately we can detect and correct the deflection the closer we can stay to this limit. It is mainly the accuracy of the z-piezo, its driving electronics and the feedback loop that determines how well the deflection can be controlled by adjusting the height of the cantilever with respect to the sample. The resulting accuracy during imaging (the error signal) is often worse than 1 nm. This error displacement translates into an error force by multiplying it with the cantilever spring constant. When one wants to control the forces with an accuracy of tens of pN, cantilevers with a spring constant of at most 0.1 N/m are required.
17. For the positioning of the laser spot onto the cantilever, mostly, a camera image is used that shows both the cantilever and the laser spot. After the photodiode has been centered, the signal can be further optimized by slightly adjusting the position of the laser spot until the sum signal of the photodiode is maximized. Recenter the photodiode afterward.
18. Depending on the exact positioning of the laser spot and the type of cantilever, the calibration will vary from experiment to experiment and should, therefore, be carried out systematically for each new experiment, or even several times during the experiment, especially when the cantilever is used to quantify the stiffness of the sample.
19. The collision of water molecules with the cantilever surface leads to small fluctuations in the bending of the cantilever, the thermal noise. The recording of this noise is best done with the tip at least 10 μm away from the surface. When the distance is less, the hydrodynamic damping of the surface will broaden the resonance peak (reduction of Q), which makes an accurate fitting more difficult.
20. For the cantilever spring constant calibration, use the proposed fitting method (Eq. 3) instead of using the integral as shown in Eq. 2: This will reduce the influence of other possible sources of (electronic or mechanical) noise that else would lead to an overestimation of the energy present in the thermal motion of the cantilever.
21. In liquid, the relative contribution of the pink and white noise will be very small. We always set A and B to zero prior to fitting thermal noise power spectra.
22. The operating frequency puts a limit on the maximum scan speed. For a good reading of the amplitude (i.e., to minimize the error signal), ≈ 10 oscillation cycles per pixel are required. For a

256×256 pixel image this corresponds to 6.5×10^5 cycles in total. Using a cantilever with a 10 kHz resonance frequency would, therefore, give a scan time of about a minute. (In practice it is often the resonance frequency of the z-piezo scanner and not that of the cantilever frequency that limits the scan speed).

23. To minimize the forces exerted on the sample, the amplitude of oscillation is preferentially kept as low as possible. However, at very low amplitude, the images will be more sensitive to noise and unwanted interaction between the tip and the sample, which can sometimes be remedied by choosing a slightly higher amplitude.
24. Often, a plane-fit-and-subtract correction is not sufficient, as drift in z-direction and low frequency noise (<10 Hz) cause a variation in height and tilt between the individual scan lines. Most software packages include a routine that performs a linear fit to each scan line and subtracts this fit from each scan line.
25. To further reduce the noise, one can average consecutive scans from the same sample, although this will be more sensitive to drift (because the time between the (to be) averaged scan lines is much larger): Often, it helps to scan successive images in the same y-direction (i.e., all images scanned from the top down).
26. The derivative processing modifies the height information in the images, so derivative images should obviously not be used for further height analysis of the structures.
27. During imaging, forces are applied to the sample; consequently, the measured height may be reduced depending on the softness of the sample (see also Table 1). Other sources of variations include the orientation of the particles on the surface (Fig. 8), the heterogeneity of particles, and the roughness of the background. In our hands, the minimal average roughness of a clean, flat glass surface is about 1 nm (Fig. 3d), but this can increase to several nanometers when the sample is added, depending on the purity of the buffer and the sample itself.
28. When the same tip has been used for a longer time (tens of minutes to hours), the probability of tip artifacts increases, which often shows as a double or shadow image in the scans and/or as an increased adhesion of the tip to the surface. Occasionally, the performance can be restored by bringing the z-piezo in oscillation for a few seconds (by increasing of the feedback parameters). Most often, however, only a change of cantilever will help recover good images and force curves with no adhesion components.
29. Drift in x - y - z does strongly depend on changes in temperature in the AFM instrument and in the lab. To minimize drift, one could leave the AFM machine switched on to leave it thermally equilibrated, and operate the instrument in a space that is temperature controlled (preferably within 1°C).

Acknowledgments

We thank Sebastian Hanke and Jan Knappe for performing the imaging of DNA and the thermal noise measurements, and Bodo Wilts, Christoph F. Schmidt, Pedro de Pablo, and Carolina Carrasco for useful discussions. F. Eghiaian and I.A.T Schaap are supported by the DFG Research Center for Molecular Physiology of the Brain (CMPB)/Excellence Cluster 171.

References

- Binnig, G., Quate, C. F., and Gerber, C. (1985) Atomic Force Microscope, *Phys. Rev. Lett.* **56**, 930–933.
- Martin, Y., Williams, C. C., and Wickramasinghe, H. K. (1987) Atomic force microscope–force mapping and profiling on a sub 100-Å scale, *J. Appl. Phys.* **61**, 4723.
- Hansma, P. K., Cleveland, J. P., Radmacher, M., Walters, D. A., Hillner, P. E., Bezanilla, M., Fritz, M., Vie, D., Hansma, H. G., Prater, C. B., Massie, J., Fukunaga, L., Gurley, J., and Elings, V. (1994) Tapping mode atomic force microscopy in liquids, *Appl. Phys. Lett.* **64**, 1738–1740.
- Xu, X., Carrasco, C., de Pablo, P. J., Gomez-Herrero, J., and Raman, A. (2008) Unmasking imaging forces on soft biological samples in liquids when using dynamic atomic force microscopy: a case study on viral capsids, *Biophys. J.* **95**, 2520–2528.
- Schaap, I. A. T., Carrasco, C., de Pablo, P. J., MacKintosh, F. C., and Schmidt, C. F. (2006) Elastic Response, Buckling, and Instability of Microtubules under Radial Indentation, *Biophys. J.* **91**, 1521–1531.
- Ivanovska, I. L., de Pablo, P. J., Ibarra, B., Sgalarik, G., MacKintosh, F. C., Carrascosa, J. L., Schmidt, C. F., and Witte, G. J. L. (2004) Bacteriophage capsids: tough nanoshells with complex elastic properties, *Proc. Natl. Acad. Sci. USA* **101**, 7600–7605.
- Goodman, R. P., Schaap, I. A. T., Tardin, C. F., Erben, C. M., Berry, R. M., Schmidt, C. F., and Turberfield, A. J. (2005) Rapid chiral assembly of rigid DNA building blocks for molecular nanofabrication, *Science* **310**, 1661–1665.
- (2007) Cell Mechanics, Volume 83 (Methods in Cell Biology). Academic Press.
- Rief, M., Gautel, M., Oesterhelt, F., Fernandez, J. M., and Gaub, H. E. (1997) Reversible unfolding of individual titin immunoglobulin domains by AFM, *Science* **276**, 1109–1112.
- Fernandez, J. M., and Li, H. (2004) Force-clamp spectroscopy monitors the folding trajectory of a single protein, *Science* **303**, 1674–1678.
- Florin, E. L., Moy, V. T., and Gaub, H. E. (1994) Adhesion forces between individual ligand-receptor pairs, *Science* **264**, 415–417.
- Hinterdorfer, P., and Dufrene, Y. F. (2006) Detection and localization of single molecular recognition events using atomic force microscopy, *Nat. Methods* **3**, 347–355.
- Puchner, E. M., Alexandrovich, A., Kho, A. L., Hensen, U., Schäfer, L. V., Brandmeier, B., Gräter, F., Grubmüller, H., Gaub, H. E., and Gautel, M. (2008) Mechanoenzymatics of titin kinase, *Proc. Natl. Acad. Sci. USA* **105**, 13385–13390.
- Morris, V. J., Kirby, A. R., and Gunning, A. P. Atomic Force Microscopy For Biologists. Imperial College Press.
- Fechner, P., Boudier, T., Mangenot, S., Jaroslawski, S., Sturgis, J. N., and Scheuring, S. (2009) Structural information, resolution, and noise in high-resolution atomic force microscopy topographs, *Biophys. J.* **96**, 3822–3831.
- Roy, R., Hohng, S., and Ha, T. (2008) A practical guide to single-molecule FRET, *Nat. Methods* **5**, 507–516.
- Müller, D. J., and Engel, A. (1999) Voltage and pH-induced channel closure of porin OmpF visualized by atomic force microscopy, *J. Mol. Biol.* **285**, 1347–1351.
- Moreno-Herrero, F., de Jager, M., Dekker, N. H., Kanaar, R., Wyman, C., and Dekker, C. (2005) Mesoscale conformational changes in the DNA-repair complex Rad50/Mre11/Nbs1 upon binding DNA, *Nature* **437**, 440–443.
- Schaap, I., Carrasco, C., de Pablo, P. J., and Schmidt, C. F. (2011) Kinesin walks the line: single motors observed by atomic force microscopy. *Biophys. J.* **100**, 2450–2456.

20. Ando, T., Kodera, N., Takai, E., Maruyama, D., Saito, K., and Toda, A. (2001) A high-speed atomic force microscope for studying biological macromolecules, *Proc. Natl. Acad. Sci. USA* **98**, 12468–12472.
21. van Noort, S. J., van Der Werf, K. O., de Groot, B. G., and Greve, J. (1999) High speed atomic force microscopy of biomolecules by image tracking, *Biophys. J.* **77**, 2295–2303.
22. Picco, L. M., Bozec, L., Ulcinas, A., Engledew, D., Antognozzi, M., Horton, M., and Miles, M. (2007) Breaking the speed limit with atomic force microscopy, *Nanotechnology* **18**.
23. Fantner, G. E., Schitter, G., Kindt, J. H., Ivanov, T., Ivanova, K., Patel, R., Holten-Andersen, N., Adams, J., Thurner, P. J., Rangelow, I. W., and Hansma, P. K. (2006) Components for high speed atomic force microscopy, *Ultramicroscopy* **106**, 881–887.
24. Kodera, N., Yamamoto, D., Ishikawa, R., and Ando, T. (2010) Video imaging of walking myosin V by high-speed atomic force microscopy. *Nature* **468**, 72–76.
25. Crampton, N., Yokokawa, M., Dryden, D. T. F., Edwardson, J. M., Rao, D. N., Takeyasu, K., Yoshimura, S. H., and Henderson, R. M. (2007) Fast-scan atomic force microscopy reveals that the type III restriction enzyme EcoP15I is capable of DNA translocation and looping, *Proc. Natl. Acad. Sci. USA* **104**, 12755–12760.
26. Yokokawa, M., Wada, C., Ando, T., Sakai, N., Yagi, A., Yoshimura, S. H., and Takeyasu, K. (2006) Fast-scanning atomic force microscopy reveals the ATP/ADP-dependent conformational changes of GroEL, *EMBO J.* **25**, 4567–4576.
27. Radmacher, M., Fritz, M., Hansma, H. G., and Hansma, P. K. (1994) Direct observation of enzyme activity with the atomic force microscope, *Science* **265**, 1577–1579.
28. Thomson, N. H., Fritz, M., Radmacher, M., Cleveland, J. P., Schmidt, C. F., and Hansma, P. K. (1996) Protein tracking and detection of protein motion using atomic force microscopy, *Biophys. J.* **70**, 2421–2431.
29. Viani, M. B., Pietrasanta, L. I., Thompson, J. B., Chand, A., Gebeshuber, I. C., Kindt, J. H., Richter, M., Hansma, H. G., and Hansma, P. K. (2000) Probing protein–protein interactions in real time, *Nat. Struct. Biol.* **7**, 644–647.
30. Kawaguchi, K., and Ishiwata, S. (2001) Nucleotide-dependent single- to double-headed binding of kinesin, *Science* **291**, 667–669.
31. Horcas, I., Fernández, R., Gómez-Rodríguez, J. M., Colchero, J., Gómez-Herrero, J., and Baro, A. M. (2007) WSXM: a software for scanning probe microscopy and a tool for nanotechnology, *Rev. Sci. Instrum.* **78**, 013705.
32. Williams, R. C., and Lee, J. C. (1982) Preparation of tubulin from brain, in *Structural and Contractile Proteins Part B: The Contractile Apparatus and the Cytoskeleton*, pp 376–385. Academic Press.
33. Carrasco, C., Carreira, A., Schaap, I. A. T., Serena, P. A., Gómez-Herrero, J., Mateu, M. G., and de Pablo, P. J. (2006) DNA-mediated anisotropic mechanical reinforcement of a virus, *Proc. Natl. Acad. Sci. USA* **103**, 13706–13711.
34. Gittes, F., and Schmidt, C. F. (1998) Signals and noise in micromechanical measurements, *Methods Cell Biol.* **55**, 129–156.
35. Viani, M. B., Schaffer, T. E., Paloczi, G. T., Pietrasanta, L. I., Smith, B. L., Thompson, J. B., Richter, M., Rief, M., Gaub, H. E., Plaxco, K. W., Cleland, A. N., Hansma, H. G., and Hansma, P. K. (1999) Fast imaging and fast force spectroscopy of single biopolymers with a new atomic force microscope designed for small cantilevers, *Rev. Sci. Instrum.* **70**, 4300–4303.
36. Hutter, J. L., and Bechhoefer, J. (1993) Calibration of atomic-force microscope tips, *Rev. Sci. Instrum.* **64**, 1868.
37. Proksch, R., Schaffer, T. E., Cleveland, J. P., Callahan, R. C., and Viani, M. B. (2004) Finite optical spot size and position corrections in thermal spring constant calibration, *Nanotechnology* **15**, 1344–1350.
38. Burnham, N., Chen, X., Hodges, C., Matei, G., Thoreson, E., Roberts, C., Davies, M., and Tendler, S. (2003) Comparison of calibration methods for atomic-force microscopy cantilevers, *Nanotechnology* **14**, 1–6.
39. Sader, J. E. (1998) Frequency response of cantilever beams immersed in viscous fluids with applications to the atomic force microscope, *J. Appl. Phys.* **84**, 64–76.
40. Berman, H. M., Westbrook, J., Feng, Z., Gilliland, G., Bhat, T. N., Weissig, H., Shindyalov, I. N., and Bourne, P. E. (2000) The Protein Data Bank, *Nucleic Acids Res.* **28**, 235–242.
41. Schaap, I. A. T., Hoffmann, B., Carrasco, C., Merkel, R., and Schmidt, C. F. (2007) Tau protein binding forms a 1 nm thick layer along protofilaments without affecting the radial elasticity of microtubules, *J. Struct. Biol.* **158**, 282–292.
42. Schabert, F. A., Henn, C., and Engel, A. (1995) Native *Escherichia coli* OmpF porin surfaces probed by atomic force microscopy, *Science* **268**, 92–94.
43. Schaap, I. A. T., de Pablo, P. J., and Schmidt, C. F. (2004) Resolving the molecular structure

- of microtubules under physiological conditions with scanning force microscopy, *Eur. Biophys. J.* 33, 462–467.
44. Snyder, J. P., Nettles, J. H., Cornett, B., Downing, K. H., and Nogales, E. (2001) The binding conformation of Taxol in beta-tubulin: a model based on electron crystallographic density, *Proc. Natl. Acad. Sci. USA* 98, 5312–5316.
45. Graveland-Bikker, J. F., Schaap, I. A. T., Schmidt, C. F., and de Kruijff, C. G. (2006) Structural and mechanical study of a self-assembling protein nanotube, *Nano Lett* 6, 616–621.
46. Wilts, B. D., Schaap, I. A., Young, M. J., Douglas, T., Knobler, C. M., and Schmidt, C. F. (2010) Swelling and Softening of the CCMV Plant Virus Capsid in Response to pH Shifts, *Biophys. J.* 98, 656a.
47. Li, S., Eghiaian, F., Sieben, C., Herrmann, A., and Schaap, I. A. T. (2011) Bending and puncturing the influenza lipid envelope. *Biophys. J.* 100, 637–645.

Chapter 7

Using Optical Tweezers to Study the Fine Details of Myosin ATPase Mechanochemical Cycle

Christopher Batters and Claudia Veigel

Abstract

Optical tweezers offer the capability to directly observe nanometre displacements and apply piconewton forces to single proteins. This method has been applied to the study of many different biological systems. Optical tweezers have proven to be particularly useful in studying the fine details of the mechanisms of molecular motor proteins, and how their movement is coordinated with ATPase activity. This includes actin, microtubule, and also DNA- and RNA-based motor systems. Here, we provide the information necessary to reproduce the “three-bead geometry” widely applied to the study of actomyosin interactions, the “paradigm system” for motors that only interact intermittently with their filament substrate, and discuss how single-molecule interactions can be detected, calibrated and analysed.

Key words: Myosin, Actin, Optical tweezers

1. Introduction

Optical tweezers rely on forces imparted to matter by light. As pioneered by Arthur Ashkin at Bell Laboratories, trapping of objects, from atoms to micron-sized beads, is based on transfer of momentum when light is scattered or refracted by the object (1–3). The light intensity gradient produced near the focus of a 1,064-nm laser beam creates a force sufficient to trap a micron-sized refractile object, such as a polystyrene or glass sphere, stably in three dimensions. The principle behind this technique is the one of conservation of momentum; a light beam carries a linear momentum, so the refraction of the light by a transparent object

results in a change in momentum. When the light vector changes direction, the sphere or bead – if its refraction index is higher than that of the surrounding medium – is drawn to the area of highest light intensity, creating a trap in the X - Y plane. Focusing the laser through an objective of high numerical aperture creates a three-dimensional light intensity profile, allowing the sphere to be drawn to the focus and to be trapped also in the Z -plane. The fundamental principles of optical tweezers are well established, and technical implementations and limitations to study motor proteins have been extensively reviewed (e.g. (4)).

Optical tweezers-based single-molecule experiments allow single-enzyme turnovers to be studied (4). The data generated from actomyosin interactions, if analysed correctly, contains a wealth of information including the following: the displacement produced by the force generating conformational change or “power stroke” in a single chemomechanical interaction cycle of the motor with its filament substrate, the number of interaction cycles before complete detachment from the filament (called processivity), and kinetic details. By aligning and averaging individual events of motor interaction with the filament, an ensemble analysis can resolve the specific features of the power stroke. Using this approach, it was revealed that the power stroke can occur in discrete mechanical sub-steps coupled to transitions in the ATPase cycle (5–7). Using low trap stiffness (0.02 pN/nm) one can observe actomyosin interactions under close to zero loads. However, it is also possible to use optical tweezers to apply forces. Using a feedback circuit while monitoring the bead position in real time, a force can be applied very rapidly to a myosin motor by moving the tweezers, following the detection of motor binding to the filament substrate (7–9).

In most studies, instead of manipulating biological material directly, it is usually attached to a polystyrene or glass microsphere. Proteins and DNA are too small to be stably trapped directly and would be damaged when exposed to very high light intensities near the focus of a laser beam. The reproducible size of microspheres also allows easy calibration of the system. In 1994, Finer et al. pioneered optical tweezers technology in “three-bead geometry” to study single muscle myosin motors and also applied a bright-field quadrant photodiode position sensor (4QD) (10–12). The “three-bead” method discussed in this chapter is essentially based on an optical tweezers apparatus described previously (13) and can be easily adapted to study many different proteins simply by altering the surface chemistry of the microspheres and by adjusting the bead geometries.

2. Materials

2.1. Polymerisation and Fluorescent Labelling of Actin

1. G-actin: Rabbit globular-actin ([14](#)).
2. Methanol.
3. RhPh: Tetramethylrhodamine-phalloidin.
4. AB⁻: 25 mM Imidazole-HCl, 25 mM KCl, 4 mM MgCl₂, 1 mM EGTA, 1 mM DTT, pH 7.4. Store -20°C.
5. AB⁺: AB⁻ + 2 mM ATP. Store -20°C.
6. 10× AB⁺: 250 mM Imidazole-HCl, 250 mM KCl, 40 mM MgCl₂, 10 mM EGTA, 10 mM DTT, 20 mM ATP, pH 7.4. Store -20°C.

2.2. Preparation of N-Ethylmaleimide Myosin Coated Beads for Trapping

1. Myosin in 50% glycerol at approximately 30 mg/ml.
2. 2× High salt: 1 M KCl, 40 mM Potassium buffer pH 6.5, 2 mM DTT, 4 mM MgCl₂.
3. 1× High salt: 0.5 M KCl, 20 mM Potassium buffer pH 6.5, 1 mM DTT, 2 mM MgCl₂.
4. NEM solution: 3 mg N-ethylmaleimide (NEM) in 235 µl H₂O + 5 µl 98% ethanol.
5. H₂O-DTT: 5 mM DTT in H₂O.
6. Trapping beads: 1.1-µm diameter polystyrene beads.
7. BSA-TRITC: Bovine Serum Albumin Tetramethyl-Rhodamine-Iso-Thiocyanate.

2.3. Preparation of Flow Cells

1. Microscope slides, 75 × 25 mm.
2. Coverslips: No. 1, 22 × 40 mm.
3. Coverslip spacers: No. 1, 3 × 40 mm.
4. Silica microspheres Ø2.1 µm.
5. UV curing adhesive.
6. Nitrocellulose 10% solution in amyl acetate (PLANO GmbH, Wetzlar, Germany).
7. Amyl acetate.
8. UV light box.

2.4. Calibration

1. Flow cells.
2. Ø1.1-µm diameter polystyrene beads.

2.5. Optical Trapping Procedure: Three-Bead Geometry

Make all solutions as a 10× stock and store -20°C in 1-ml aliquots

1. AB⁻CP: 25 mM Imidazole-HCl, 25 mM KCl, 4 mM MgCl₂, 1 mM EGTA, pH 7.4 supplemented with 2 mM creatine phosphate as ATP regeneration system ([15](#)), see Note 1.

2. AB⁻ scavenger: AB⁻ supplemented with 0.02 mg/ml catalase, 0.1 mg/ml glucose oxidase, 3 mg/ml glucose, 20 mM DTT; this is added as a 100× stock solution.
3. AB⁺ scavenger: AB⁻ scavenger supplemented with 2 mM ATP (16), see Note 2.
4. AB⁻ BSA: AB⁻ supplemented with 0.5 mg/ml BSA.
5. Creatine kinase, 0.1 mg/ml.

3. Methods

3.1. Polymerisation and Stabilisation of Actin Filaments

1. Polymerise actin by adding 10× AB⁺ to G-Actin at a ratio of 1:10 (v/v) and incubate for 2 h.
2. Actin is labelled with RhPh at a molar ratio of slightly over 1:1.
3. A RhPh-stock is made as a 6.6 μM solution in 100% methanol.
4. The RhPh-stock is divided into 2 μl aliquots (13.2 nM) and allowed to dry prior to storage at -20°C in the dark.
5. 10 nM of actin filaments are labelled by mixing with a single aliquot of RhPh. Leave this overnight to label completely.
6. Store at 4°C for several weeks.

3.2. Preparation of NEM Myosin Coated Beads

The polystyrene beads must be functionalised so that they strongly and irreversibly bind to actin filaments. This can be done in a variety of ways. Here, we describe a method that uses a chemically modified myosin that can no longer hydrolyses ATP.

1. Pipette 200 μl myosin (stored in 50% glycerol) into two 1.5-ml Eppendorf tubes (see Note 3).
2. Precipitate the myosin from solution by adding enough H₂O to fill the tubes, then centrifuge at 13,000×g for 6 min.
3. Remove supernatant, and solubilise the myosin by adding 150 μl of 2× High-Salt buffer to each of the pellets.
4. Combine solutions into one tube, take 250 μl and place in new 1.5 ml tube.
5. Add 5 μl of NEM solution to the myosin and vortex briefly.
6. Incubate the NEM-myosin solution at 23°C for 75 min (see Note 4).
7. The reaction is stopped by the addition of 1 ml H₂O-DTT solution to NEM-myosin.
8. Centrifuge NEM-myosin at 13,000×g for a further 6 min. If the resulting pellet is very small, re-suspend in water and spin again.

9. Remove the supernatant and add 2× High-Salt buffer (approximately 2× the volume of the pellet to ensure complete resuspension of myosin).
10. Centrifuge again for 6 min at 13,000× g to remove denatured myosin. Take 50 μl of the supernatant and add 450 μl of 1× High-Salt buffer to give a 1:10 diluted NEM-myosin solution.
11. Wash 1.1 μm polystyrene beads (in aqueous solution, 10% solid) twice in H_2O to remove surfactant present in the proprietary buffer and store at 2% (w/v) concentration in H_2O .
12. Mix 5 μl NEM-myosin (diluted 1:10 in 1× High-Salt buffer) with 30 μl of 1.1 μm polystyrene beads (see Note 5).
13. Add 2.5 μl of 0.1 mg/ml BSA-TRITC and make up to 100 μl using 1× High-Salt buffer. Incubate overnight at 4°C.
14. Pellet the beads at 8,000× g for 2 min using desktop centrifuge and re-suspend in 100 μl of AB⁻ buffer. Briefly sonicate. These beads can be stored at 4°C for 1 week.
15. Before using in the trapping experiments, add 1 ml of H_2O to the beads for 1 h.
16. Then, spin at 8,000× g for 2 min.
17. Re-suspend the pellet in 100 μl of AB⁻ BSA.
18. Spin for a second time at 8,000× g for 2 min and then re-suspend again in AB⁻ BSA.
19. The beads should be kept on ice and used the same day.

3.3. Preparation of Flow Cells

Flow cells are prepared in advance and stored for several weeks (17).

1. Glue two 3×40 mm coverslip spacers onto pre-cleaned microscope slide so they are the same width apart as the coverslips (22 mm).
2. Mix nitrocellulose and amyacetate at 1:10 ratio (v/v), make 1 ml solution (see Note 6).
3. Add silica microspheres to a concentration of 0.5% (e.g., 5 mg into 1 ml).
4. Spread 2.5 μl onto a coverslip and allow the solution to dry. The resulting surface density of beads is approximately one bead per 10 μm^2 (see Note 7).
5. Glue the pre-coated coverslip orthogonally to the microscope slide via the two strips of coverslips.
6. Leave the glue to flow overnight.
7. Place on UV box for 5 min to cure glue.
8. Store at room temperature in a sealed box.

3.4. Calibration

3.4.1. Calibrating the Four-Quadrant Detectors (see Fig. 1a)

It is critical before carrying out experiments with the optical tweezers to calibrate the instrument (18). One must determine both the sensitivity of the detectors and the power of the optical trap(s), and thus their stiffness. These calibrations must be carried out on the day that an experiment is performed. *Attention: laser emission can be very dangerous especially if it is invisible to human eye (e.g. 1,064 nm emission). Use appropriate precautions and protective gear when you work with optical trap set-up.*

The 4QD position sensor can be applied in bright-field mode using the microscope's halogen lamp or a laser diode for illumination. The calibrations described here assume that the AODs to steer the traps and the video camera have already been thoroughly calibrated.

1. Capture a Ø1.1-µm bead in one of the traps.
2. Get a good image by adjusting focus (see Note 8).
3. Change the focus to about 5 µm above the surface and then “centre” the bead over the 4QD. Use video image to do this.
4. Make sure that there are no 2.1-µm silica surface beads or any debris in the vicinity of the trapped bead on the video image.
5. Adjust the microscope to maximise the signal from the 4QD by maximising the illuminating light directed to the 4QD.
6. Apply a 100-nm square wave form to the x -position of the optical trap via the AODs.
7. Calibrate the bead movement measured from the 4QD against the movement of the trap.
8. Save a data trace of this calibration for reference later.
9. Repeat for the second detector.

3.4.2. Stiffness of the Optical Tweezers: Equipartition Principle (see Fig. 1b)

1. Record Brownian motion of a bead held in one of the optical traps. Stage and trap position are held fixed. Make sure that the trap is about 4–5 µm above the surface.
2. Turn the laser power down to experimental conditions and collect position data of the trapped bead at 1 kHz.
3. The variance of the signal $\langle x \rangle^2$ is inversely proportional to the stiffness of the system, κ_x , in the x -direction:

$$\langle x \rangle^2 = \frac{k_B T}{\kappa_x} \quad (1)$$

4. The trap stiffness can, therefore, be calculated from the mean squared displacement (variance) of Brownian motion of a single trapped bead.

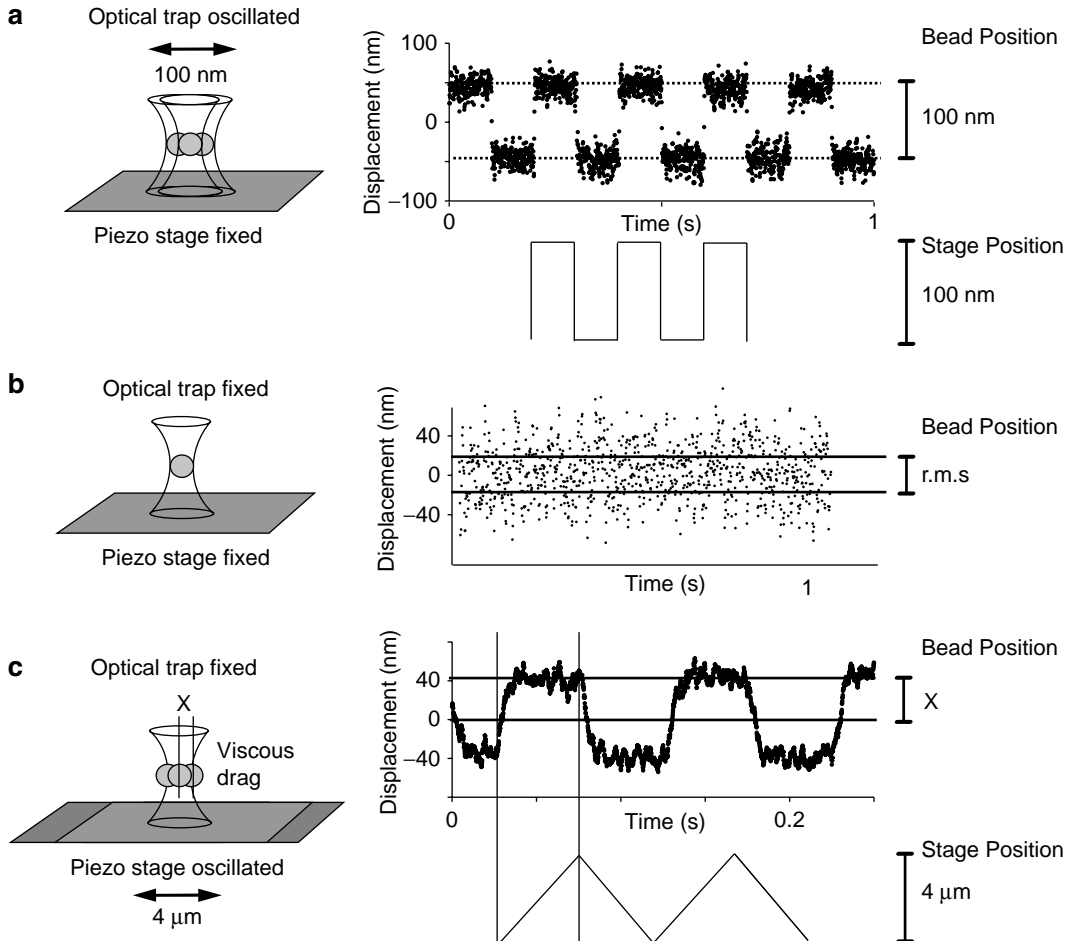


Fig. 1. Calibration of detector: (a) A 100-nm square wave is applied to a bead held in the optical tweezers. The displacement of this bead is measured and all data collected is corrected to this calibration factor. (b) Calibration of trap stiffness by thermal noise analysis: A single 1.1-μm bead is held in the optical tweezers and data is collected at 1 kHz. The graph shows the bead position vs. time – solid lines denote the ± 1 standard deviation of bead position. The trap stiffness can be determined from this information using the equipartition principle: $1/2\kappa_{\text{trap}} <x^2> = 1/2k_B T$. Where κ_{trap} =Trap stiffness, $<x^2>$ =variance, k_B =Boltzman constant, and T =Absolute temperature. In this example, the trap stiffness is $4.1/210 = 0.0195$ pN/nm. (c) Calibration of trap stiffness using Stoke's drag: A triangular wave is applied to the stage which holds the flow cell while a bead is held in the stationary optical tweezers. The movement of the stage creates a force, F , on the bead caused by the motion of the surrounding fluid. This causes the bead to be displaced a distance, x , from the trap centre; the greater the system stiffness the less the bead is displaced. F/X =Stiffness of the tweezers.

3.4.3. Stiffness of the Optical Tweezers: Stokes Calibration (see Fig. 1c)

1. Trap a bead and reduce the laser power to experimental conditions.
2. Apply a large amplitude triangular wave form to the piezo stage in x -direction (stage movement at a frequency of 20 Hz and a 4-μm peak-to-peak amplitude gives a force of about 0.75 pN on a 1 micron-sized bead in solution).

3. The displacement of the trapped bead should be described by a square wave as the acceleration on the stage displaces the bead from the centre of the trap (see Note 9).
4. The force applied divided by the displacement from the centre of the trap gives the stiffness of the trap.

**3.5. Optical
Trapping Procedure:
Three-Bead
Geometry**

NEM coated beads are captured in the optical traps and an actin filament is tethered between them. The microscope user must be dexterous, and we have found that successful optical trapping experiments are only possible once the user is very familiar with the equipment.

1. Dilute the myosin of interest to a concentration of 4 µg/ml in AB⁻ and allow binding to the coverslip surface for 5 min.
2. Block the surface with 100 µl AB⁻ BSA.
3. After blocking, replace the solution with AB⁻ scavenger supplemented with creatine kinase and ATP at 1–100 µM concentrations (see Note 10). This solution also contains RhPh-labelled actin filaments (6 ng/ml) and 2 µl NEM polystyrene trapping beads.
4. Using fluorescence microscopy (532 nm excitation) and 100× magnification capture an actin filament between two NEM-myosin coated polystyrene beads. Trapping is achieved by holding the traps in fixed positions while steering the stage using x and y manual mechanical controls to direct the beads towards the traps (see Note 11).
5. Approximately 2 pN of pretension is applied to the actin filament suspended between the two-trapped beads. This is achieved by moving one of the trapped beads in *x*-direction (i.e. parallel to the actin filament axis) away from the other bead, and observing the motion of the bead in the other, stationary trap (see Note 12).
6. Insert the 2.5× magnification lens (i.e., *Optovar*-lens on a Zeiss microscope) and, in bright field microscopy mode, position the bead-actin-bead “dumb-bell” in the vicinity of a silica surface bead (= “third” bead in the three-bead geometry, see Note 13).
7. Position the detectors so the beads cast an image onto the centre of the detectors.
8. Turn the light to full power and open all diaphragms. Reduce the power of the laser tweezers (see Note 14) and monitor interactions using the two 4QDs (as described previously (13, 19)).
9. To hunt for myosin interactions with actin, small movements of the surface beads are made using the computer controlled piezoelectric sub-stage (see Note 15).

3.6. Data Collection and Analysis

Optical tweezers measurements produce rich data allowing a variety of different parameters to be determined, some of which are discussed below. The raw data in the absence of binding events is dominated by Brownian noise. Interactions are easily identified from the background noise, as when myosin binds to actin, the bead–actin–bead dumb-bell is effectively grounded and an increase in the system stiffness occurs, resulting in a drop in Brownian noise (see Fig. 3a). The *on* (= myosin bound to actin) and *off* (= myosin not bound) time intervals allow the kinetics to be investigated and the displacements produced during binding allow the power-stroke size to be measured.

3.6.1. Determining the Size of the Power Stroke

Myosin attachment takes place with equal probability to the binding positions along the actin filament that become available to the immobilised myosin due to Brownian motion of the actin dumbbell that is trapped in the harmonic potential well of the optical tweezers ((13, 20, 21), see Fig. 2). The actin has a constrained amount of rotation (21); however, each actin monomer can be thought of as being equivalent, hence myosin cross-bridges can be created on any axial position of the actin filament (20, 21). The average size of the power stroke of a single myosin head is found by plotting a histogram of displacements from local mean position of all the binding events (20). The histogram plotted is fitted with a Gaussian function whose width is derived from the motion of the bead in the absence of attachments. The midpoint is shifted from zero by the average size of the power stroke, and the width is determined by the trap stiffness (20). It is important to note that to obtain an accurate measurement of the size of the power stroke using the method described above, the actin filament must have at least a small degree of freedom in rotational and translational position with respect to the immobilised myosin. This can be achieved in several ways; if the microscope has a small amount of inherent drift combined with the Brownian noise several actin monomers

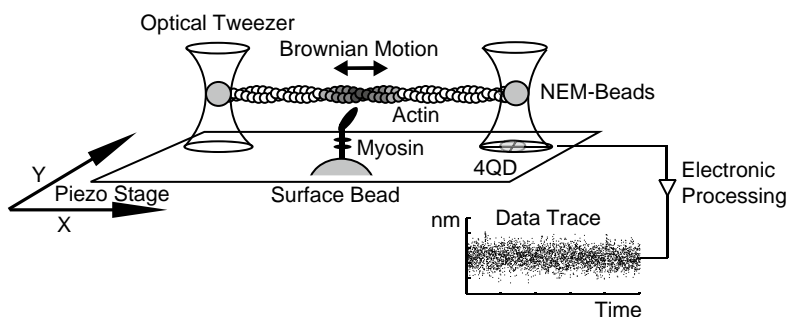


Fig. 2. Three-bead geometry. Two beads are held in the optical tweezers with an actin filament between them. A third bead acts as a pedestal with myosin bound to it. When binding events take place, they are recorded via a four quadrant photodiode. Binding events take place over a range of actin monomers due to Brownian motion. It is this movement that creates the Gaussian distribution of binding events seen in Fig. 3b.

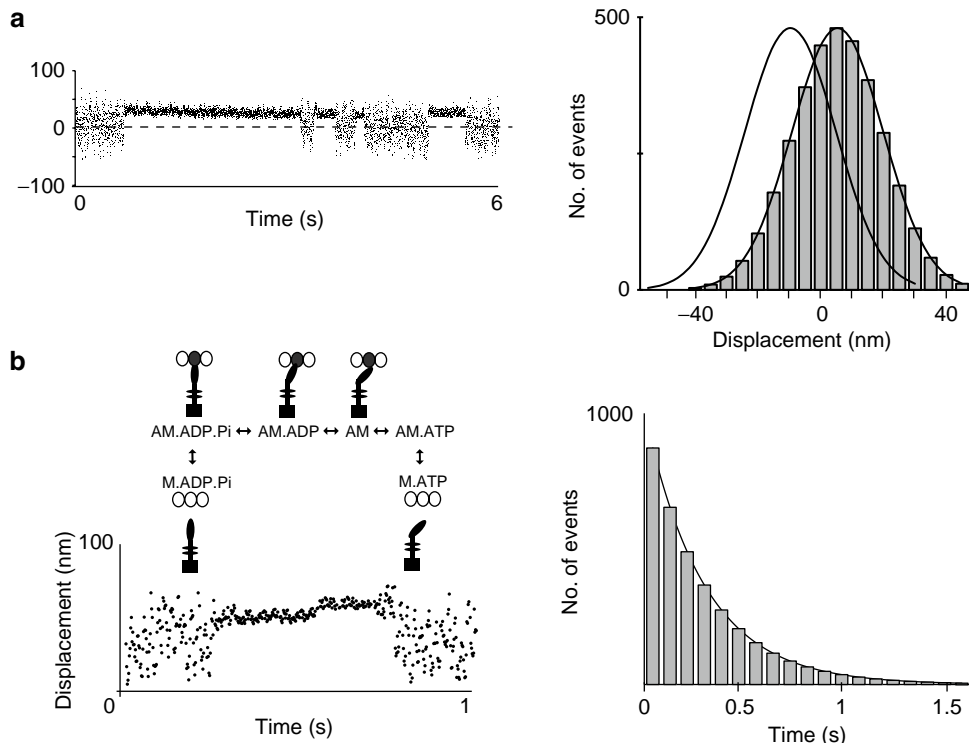


Fig. 3. (a) Raw data trace showing four actomyosin interactions. The distance from the centre position (black line) is determined for each event. Many hundreds of these displacements are measured and plotted in the histogram. (b) A single actomyosin event and the ATPase cycle are shown. The graph shows the distribution of actomyosin lifetimes demonstrating the stochastic nature of events and the single exponential fit to the data.

will be sampled. To make sure that several monomers are sampled the stage can be adjusted during an experiment or a small sinusoidal wave may be applied to the beads, thereby moving the actin filament back and forth, ensuring a range of monomers will be sampled. If the actin filament's movement is restricted, the distribution of measured displacements can be skewed.

If actin filaments used in the experiments are not polarity-labelled, their orientation in the trapped dumb-bell is unknown. However, the directionality of the power stroke of myosin is determined by the orientation of the actin filament. By collecting a statistically large enough data set from a single myosin head one can establish the orientation of the actin filament for that particular experiment. This way, data from different experiments can be pooled without mixing up data sets from actin filaments in different orientations. The accuracy of the measurement of the size of the power stroke is determined by the standard error of the mean $s.e.m. = \frac{\sigma}{\sqrt{N}}$. The standard deviation σ of the Gaussian distribu-

tion of displacement events is determined by the stiffness of the trap κ_{trap} (with $\sigma = \sqrt{\frac{k_B T}{\kappa_{\text{trap}}}}$, $k_B T$ thermal energy), and so it is constant; therefore, to reduce the error, the number of binding events N must be as large as possible. If experiments are carried out at a trap stiffness of 0.02 pN/nm for example, σ will be approximately 17 nm; hence, if $N=100$ the measured size of the power stroke has an error of $\pm(17/\sqrt{100})=1.7$ nm (see Note 16).

3.6.2. Lifetime Analysis

Myosin is an actin-activated ATPase. The lifetime of a single myosin binding event depends on the probability of an event ending; this probability is governed by the rate constants of the specific class of myosin and the concentration of ATP. Lifetimes of binding events are stochastic in nature, but the average lifetime obtained will be characteristic of a bulk measured rate constant. When plotted as a histogram a single exponential decay is produced (see Fig. 3b). The average lifetime in this example (Myosin-II, subfragment S1) derived from the gradient of the single exponential decay is approximately 347 ms. From the reciprocal of the average lifetime, the second-order rate constant k_{ATP} for ATP binding can be determined. With $k=\tau^{-1}=2.88$ s⁻¹ measured at 1.5 μM ATP, we determine a second-order rate constant for ATP binding $k_{\text{ATP}}=1.92$ μM⁻¹ s⁻¹ in these single-molecule experiments. This is in very good agreement with values determined for myosin II S1 in solution using stopped flow studies (22).

If one collects single-molecule data over a range of ATP concentrations, the Michaelis–Menten equation can be applied to determine the kinetic constants K_m and V_{max} of the myosin under investigation. It is possible to construct a saturation curve that can be fitted by a rectangular hyperbola. Using a Lineweaver–Burk plot allows graphical representation of the lifetime data.

4. Notes

1. Adjust the pH of the solution before adding creatine phosphate powder, as the latter breaks down rapidly at low pH.
2. The AB⁻ and AB⁺ solutions are degassed prior to use in order to reduce the concentration of dissolved oxygen. Following degassing, solutions are stored in 10-ml syringes to slow down the diffusion of oxygen. Smaller volumes (1 ml) of oxygen scavenger solutions are made using the degassed AB⁻ and AB⁺ stock solutions; these are also stored in syringes. All solutions are kept on ice.
3. Remove the ends of pipette tips to facilitate pipetting viscous solution containing glycerol.

4. For a detailed explanation of how NEM modifies motor proteins, see Wells and Yount (1982) (23).
5. Make a range of dilutions to test: 5 µl beads + 30 µl NEM-myosin, 5 µl beads + 40 µl NEM-myosin, 10 µl beads + 30 µl NEM-myosin, and 10 µl beads + 40 µl NEM-myosin.
6. Store nitrocellulose in a small glass tube, not in an Eppendorf, as the plastic of the tube slowly contaminates the solution.
7. Use a pipette tip as a wand to spread the nitrocellulose and mark the bottom left-hand corner for orientation.
8. At this point, sense where the coverslip is by focusing gently down. When the bead touches the coverslip, it will be pushed out of the trap and go white in the middle as it gets defocused.
9. This calibration must be done at least 5 µm from the coverslip surface.
10. Low ATP concentrations are used so binding events have a suitable duration. Creatine phosphate and creatine kinase are used to regenerate ATP and maintain the concentration.
11. Trapping requires the bead image to be defocused slightly just before trapping so that the bead lies in the plane between the objective and the trap; this causes the optical scattering forces to push the bead into a stable trapping position.
12. Do this by gently oscillating one of the traps left and right (in x -direction) gradually moving further out each time, monitor the position of the stationary bead until it is displaced approximately 100 nm from the trap centre.
13. Reduce the light intensity to allow the correct height to be established.
14. Interactions between the suspended actin filament and the surface-bound myosin molecules are measured at optical trap stiffnesses (k_{trap}) between 0.02 and 0.04 pN/nm at 22°C.
15. Routinely check the bead pair for drift so that it does not stick to the surface.
16. Series compliance: As well as correcting optical trapping data with the calibration factor, you must also correct the data for series compliance. This is due to the compliant connection between the NEM-coated beads and the actin filament (13).

References

1. Ashkin, A., Dziedzic, J. M., Bjorkholm, J. E., and Chu, S. (1986) Observation of a single-beam gradient force optical trap for dielectric particles. *Opt. Lett.* **11**, 288–290.
2. Ashkin, A. (1992) Forces of a single-beam gradient laser trap on a dielectric sphere in the ray optics regime. *Biophys. J.* **61**, 569–582.
3. Ashkin, A. (1997) Optical trapping and manipulation of neutral particles using lasers. *Proc. Natl. Acad. Sci. USA* **94**, 4853–4860.
4. Veigel, C., and Schmidt, C. F. (2011) Moving into the cell: Single molecule studies of molecular motors in complex environments. *Nature Review Mol. Cell Biol.* **12**(3), 163–176.

5. Veigel, C., Coluccio, L. M., Jontes, J. D., Sparrow, J. C., Milligan, R. A., and Molloy, J. E. (1999) The motor protein myosin-I produces its working stroke in two steps. *Nature* **398**, 530–533.
6. Veigel, C., Wang, F., Bartoo, M. L., Sellers, J. R., and Molloy, J. E. (2002) The gated gait of the processive molecular motor, myosin V. *Nat. Cell Biol.* **4**, 59–65.
7. Veigel, C., Molloy, J. E., Schmitz, S., and Kendrick-Jones, J. (2003) Load-dependent kinetics of force production by smooth muscle myosin measured with optical tweezers. *Nat. Cell Biol.* **5**, 980–986.
8. Veigel, C., Schmitz, S., Wang, F., and Sellers, J. R. (2005) Load-dependent kinetics of myosin-V can explain its high processivity. *Nat. Cell Biol.* **7**, 861–869.
9. Sellers, J. R., and Veigel, C. (2010) Direct observation of the myosin-Va power stroke and its reversal. *Nat. Struct. Mol. Biol.* **17**, 590–595.
10. Ghislain, L. P., and Webb, W. W. (1993) Scanning force microscope based on an optical trap. *Opt. Lett.* **18**, 1678–1680.
11. Finer, J. T., Simmons, R. M., and Spudich, J. A. (1994) Single myosin molecule mechanics—piconewton forces and nanometer steps. *Nature* **368**, 113–119.
12. Visscher, K., Gross, S. P., and Block, S. M. (1996) Construction of multiple-beam optical traps with nanometer-resolution position sensing. *IEEE J. Sel. Top. Quantum Electron.* **2**, 1066–1076.
13. Veigel, C., Bartoo, M. L., White, D. C. S., Sparrow, J. C., and Molloy, J. E. (1998) The stiffness of rabbit skeletal actomyosin cross-bridges determined with an optical tweezers transducer. *Biophys. J.* **75**, 1424–1438.
14. Pardee, J. D., and Spudich, J. A. (1982) Purification of muscle actin. *Methods Enzymol.* **85**, 164–181.
15. Kron, S. J., and Spudich, J. A. (1986) Fluorescent actin-filaments move on myosin fixed to a glass surface. *Proc. Natl. Acad. Sci. USA* **83**, 6272–6276.
16. Kishino, A., and Yanagida, T. (1988) Force measurements by micromanipulation of a single actin filament by glass needles. *Nature* **334**, 74–76.
17. Kron, S. J., Toyoshima, Y. Y., Uyeda, T. Q. P., and Spudich, J. A. (1991) Assays for actin sliding movement over myosin-coated surfaces. *Methods Enzymol.* **196**, 399–416.
18. Svoboda, K., and Block, S. M. (1994) Biological applications of optical forces. *Annu. Rev. Biophys. Biomol. Struct.* **23**, 247–285.
19. Molloy, J. E., and Padgett, M. J. (2002) Lights, action: optical tweezers. *Contemp. Phys.* **43**, 241–258.
20. Molloy, J. E., Burns, J. E., Kendrick-Jones, J., Tregear, R. T., and White, D. C. S. (1995) Movement and force produced by a single myosin head. *Nature* **378**, 209–212.
21. Steffen, W., Smith, D., Simmons, R., and Sleep, J. (2001) Mapping the actin filament with myosin. *Proc. Natl. Acad. Sci. USA* **98**, 14949–14954.
22. Cremo, C. R., and Geeves, M. A. (1998) Interaction of actin and ADP with the head domain of smooth muscle myosin: Implications for strain-dependent ADP release in smooth muscle. *Biochemistry* **37**, 1969–1978.
23. Wells, J. A., and Yount, R. G. (1982) Chemical modification of myosin by active-site trapping of metal-nucleotides with thiol crosslinking reagents. *Methods Enzymol.* **85**, 93–116.

Chapter 8

Quantum Dot Labeling Strategies to Characterize Single-Molecular Motors

Shane R. Nelson, M. Yusuf Ali, and David M. Warshaw

Abstract

Recent advances in single-molecule labeling and detection techniques allow high-resolution imaging of the motion of single molecules. Molecular motors are biological machines that convert chemical energy into mechanical work. Myosin Va (MyoVa) is a well-characterized processive molecular motor, essential for cargo transport in living organisms. Quantum dots (Qdots) are fluorescent semiconductor nanocrystals that are extremely useful for single-molecule studies in biological sciences. High-resolution video microscopy and single-particle tracking of a Qdot-labeled MyoVa motor molecule allow the detection of individual steps in vitro and in live cells.

Key words: Single molecule, Myosin, Actin, Total Internal Reflection Microscopy, Single-Particle Tracking, Steps

1. Introduction

Video microscopy and single-particle tracking of fluorescently labeled molecules allow detection of the motion and stepping dynamics of single molecules of motor proteins. Quantum dots (Qdots) offer a number of advantages over traditional fluorescent dyes. Although approximately the same size as a GFP molecule, they are more than 20 times as bright and are extremely photo-stable, which allows long-term observation. Qdots also demonstrate very narrow fluorescence emission spectra, but very broad excitation spectra. This allows easy multiplexing of experiments using a single-excitation wavelength, and even the possibility of simultaneous observation of multiple colors. This property also allows selection of excitation and emission wavelengths that are

very far apart (large Stokes shift), which reduces background autofluorescence in order to improve the signal-to-noise ratio. A large number of Qdot surface coatings are commercially available which allows for a variety of attachment strategies, both covalent and noncovalent.

Myosin Va (MyoVa) is an actin-based molecular motor that is involved in the short-range transport of a number of intracellular cargoes, including RNA, ER, melanocytes, and exocytic vesicles. A molecule of this motor comprises two heavy chains. Each heavy chain comprises an N-terminal motor domain that binds actin and hydrolyzes ATP, followed by a long neck domain consisting of 6IQ domains, where calmodulin light chains bind, while the C-terminal region forms the cargo-binding domain (CBD). In the absence of cargo, the C-terminal CBD interacts with the N-terminal motor domains to inhibit catalytic activity and motion (1). The motor moves along actin filaments in an alternating “hand-over-hand” mechanism, traveling 36 nm with each step. This distance matches the pseudo-repeat of the actin helix, allowing motion with minimal “spiraling” around the actin filament. The catalytic cycle of each motor domain is sensitive to both forward and backward strains, a feature known as “gating,” which ensures that the two heads remain catalytically out of phase with each other. This aspect allows the motor to take many successive steps in the same direction along the actin filament without detaching, the hallmark of processive movement.

The tight coupling between the mechanical and hydrolytic processes of the MyoVa motor molecule makes it an ideal system to explore enzymatic activity through observation of a physical process. It is even possible to observe the individual steps of a single motor molecule, where each step is a readout of a single catalytic cycle of a single enzyme molecule. *In vitro* approaches allow easy manipulation of the environment, such as temperature, ionic strength, and substrate availability. This approach can also be applied to analyze the activity of MyoVa in the context of a cellular environment, where complexities of the cytoskeleton and cytosol complicate even the simplest aspects of this motor’s activity.

2. Materials

The following stock reagents and buffers are common to all protocols presented in this chapter:

1. 1 M dithiothreitol (DTT) in dH₂O. Store in 0.5-mL aliquots at -20°C.
2. Bovine serum albumin (BSA): 10 mg/mL in dH₂O. Store in 100-μL aliquots at -20°C.

3. Actin buffer (AB) (10×): 250 mM imidazole, pH 7.4, 40 mM MgCl₂, 10 mM EGTA, 250 mM KCl. Store at 4°C.
4. Myosin buffer (10×): 250 mM imidazole, pH 7.4, 40 mM MgCl₂, 10 mM EGTA, 3 M KCl. Store at 4°C.
5. 0.1 M ATP disodium salt in dH₂O. Freeze in 100-μL aliquots at -20°C.

2.1. Protein: Quantum Dot Conjugation Strategies

2.1.1. MyoVa HMM to Streptavidin Qdot

1. Qdot 655 Streptavidin Conjugate (Invitrogen). Store at 4°C (see Note 1).
2. Biotinylated MyoVa heavy meromyosin (HMM): We use mouse MyoVa, truncated at amino acid 1098, which removes the C-terminal CBD and a part of coiled-coil rod domain to create an HMM construct. This construct is constitutively active in this assay. All constructs feature a C-terminal FLAG epitope for protein purification. For site-specific biotinylation, we use an 88 amino acid sequence segment from *E. coli* (2), which is biotinylated at a single lysine during expression in sf9 cells. Depending on the experiment, this sequence can be appended to the very N-terminus of the MyoVa sequence (termed N-bio) (3) or between the MyoVa and FLAG sequences (termed C-bio) (4).

2.1.2. Full-Length MyoVa to Carboxylated Qdot

1. Full-length MyoVa (FL-MyoVa) protein (5).
2. Qdot 655 ITK carboxyl quantum dots (Invitrogen).

2.1.3. MyoVa HMM-YFP (N-Bio) to Antibody-Conjugated Qdot

1. MyoVa HMM-yellow fluorescence protein (YFP) (N-Bio): Truncated at amino acid 1098 and includes an N-terminal biotin tag and C-terminal YFP sequence (6).
2. Anti-GFP antibody: (α -GFP, mAb 3E6, Invitrogen). Dissolve dry antibody in 1× actin buffer with 10 mM DTT to a final concentration of 0.5 mg/mL. Store in 10-μL aliquots at -20°C.
3. Qdot 655 goat F(ab')₂ anti-mouse IgG conjugate (H+L) (Invitrogen). Store at 4°C.

2.2. In Vitro Motility Assay

Many high-resolution imaging options are possible. We use Total Internal Reflection Fluorescence (TIRF) microscopy for its high signal-to-noise ratio. Our microscope configuration is as follows:

1. Nikon TE2000-U microscope equipped with a PlanApo (100×, 1.49 n.a.) objective lens configured for through-the-objective TIRF microscopy.
2. Excitation with argon laser (488-nm line).
3. Software-controlled emission filter wheel.
4. DVC-1412: GenIV intensified high-resolution 12-bit digital camera (DVC company, Austin, TX).

The following buffers and proteins can be prepared well in advance and will store well.

1. Creatine phosphate (CP, Sigma-Aldrich): 100 mM in dH₂O. Store in 100-μL aliquots at -20°C.
2. Creatine phosphokinase (CPK). Store at -20°C.
3. Oxygen scavengers: Combine 175 mg glucose, 1.35 mg catalase, and 2 mg glucose oxidase. We recommend preparing multiple aliquots according to the above recipe in individual 1.7-mL microcentrifuge tubes. These tubes should be stored dry at -20°C.
4. Fluorescently labeled actin: Filamentous actin (F-actin) is purified from chicken pectoralis as described by Pardee and Spudich (7). For fluorescent labeling, 1 μM F-actin is incubated overnight at 4°C in 1× actin buffer with 10 μM DTT and either 1 μM tetramethylrhodamine B isothiocyanate (TRITC) phalloidin or 1 μM Alexa 660 phalloidin.
5. N-ethylmaleimide (NEM) myosin: NEM-modified myosin prepared as described by Warshaw et al. (8).

The following solutions are made immediately prior to performing the experiment. Due to the presence of the oxygen scavenging system in almost all components, they remain usable for about 2 h. If longer experimentation times are required, we recommend preparing fresh buffers as necessary.

1. Prepare 1× myosin buffer: Combine 1 mL of 10× myosin buffer and 100 μL of 1 M DTT. Add enough dH₂O to make 10 mL.
2. Prepare oxygen scavengers: Dissolve one tube of oxygen scavengers with 600 μL dH₂O. Mix by gently pipetting up and down. Be careful not to form bubbles or aerate the solution. Mixture is rather viscous (see Note 2). Keep on ice.
3. Prepare 1× actin buffer: Combine 1 mL of 10× actin buffer, 100 μL 1 M DTT, 1 mg CPK, 100 μL 0.1 M creatine phosphate, and 200 μL oxygen scavengers (prepared fresh in item 2). Add enough water to make 10 mL. Keep on ice.
4. Prepare AB-BSA: Combine 50 μL 10 mg/mL BSA with 450 μL 1× actin buffer (from item 3). Keep on ice.
5. Prepare AB-BSA-ATP: Combine 50 μL BSA, 940 μL actin buffer, and 10 μL from 100 mM ATP stock. Keep on ice.
6. Prepare fluorescent actin: Dilute 10 μL TRITC phalloidin-labeled actin (1 μM) with 100 μL AB. Keep on ice (see Note 3).
7. Prepare NEM-myosin: Dilute NEM-myosin to 0.5 mg/mL in 1× myosin buffer. Keep on ice.
8. Prepare MyoVa:Qdot conjugate according to the protocol from Subheading 3.1.

2.3. In Vivo Motility Assay

1. Dulbecco's modified Eagle's medium (DMEM) supplemented with 10% fetal bovine serum (FBS).
2. Hypertonic loading buffer: DMEM, with 0.5 M sucrose, 10% w/v PEG 1000. Filter sterilize and store at 4°C.
3. Hypotonic lysis buffer: Combine 3 parts DMEM, 2 parts dH₂O. Filter sterilize and store at 4°C.
4. 35-mm glass bottom cell culture dish (MatTek, Ashland, MA).

3. Methods

3.1. Protein: Quantum Dot Conjugation

Qdots that are currently commercially available are all multivalent, meaning that they can bind multiple motor molecules. However, it is possible to conduct experiments on single molecules by carefully controlling the stoichiometry of mixing.

We have excellent results using Qdots and MyoVa in a 4 to 1 molar ratio. With these conditions, more than 77% of Qdots should have no motor bound, but remain silent in both the *in vivo* and *in vitro* conditions. Of Qdots that do have bound motor molecules (and are therefore observed in the assays), Qdots that have bound only a single motor molecule represent approximately 90% of the population, calculated using binomial equation (4).

There are a number of different strategies for conjugation of motor molecules to Qdots. The following are three different protocols that have proven successful with MyoVa.

3.1.1. MyoVa HMM to Streptavidin Qdot

The binding of streptavidin to biotin is among the strongest non-covalent interactions. Biotinylation of proteins can be done as a posttranslational modification in the host organism (1, 2), which allows for specific placement of the tag, or after protein purification in a more nonspecific manner (9).

This approach can be used to label either the N-terminal head (N-bio) or C-terminal tail domain (C-bio) of MyoVa HMM molecules. Using these conditions with the N-bio HMM construct, we observe 72-nm steps in the majority of trajectories (~97%). This indicates that most often, only one of two heads per molecule are bound by a Qdot. We rarely observe 36-nm steps (~3% of trajectories), which would be consistent with each head being bound with separate Qdots. If each head is bound with a different colored Qdot, it is possible to directly observe the hand-over-hand movement of MyoVa (3) (see Note 4). Qdots attached to the C-terminus of MyoVa show 36-nm steps, although the spatial resolution is reduced significantly, presumably due to the high flexibility in the coiled-coil tail domain.

1. Prepare 1× actin buffer: In a 15-mL conical tube, combine 1 mL of 10× actin buffer, 100 µL 1 M DTT, add dH₂O to bring the volume to 10 mL. Keep on ice.
2. Prepare AB-BSA: Add 450 µL 1× actin buffer to a 50 µL 10 mg/mL BSA aliquot. Final BSA concentration is 1.0 mg/mL. Keep on ice.
3. Dilute both MyoVa HMM-YFP and Qdot 655 Streptavidin Conjugates to 200 nM in AB-BSA.
4. Mix 4 µL of Qdots with 1 µL of MyoVa HMM-YFP (a 4:1 molar ratio) and incubate for 10 min at room temperature (see Note 5).

3.1.2. Full-Length MyoVa to Carboxylated Qdot

Full-length MyoVa is typically considered catalytically inactive, with the C-terminal CBD sterically blocking the catalytic cycle of the heads (1, 10, 11). However, nonspecific binding of this myosin's CBD to carboxylated Qdots does result in apparent motion presumably by disrupting the head-CBD interaction of the inhibited state.

1. Prepare 1× actin buffer: In a 15-mL conical tube, combine 1 mL of 10× actin buffer, 100 µL 1 M DTT, add dH₂O to bring the volume to 10 mL. Keep on ice.
2. Prepare AB-BSA (0.1 mg/mL BSA): Combine 990 µL 1× actin buffer with 10 µL 10 mg/mL BSA.
3. Dilute both full-length MyoVa and carboxy-Qdots to 200 nM in AB-BSA (0.1 mg/mL BSA).
4. Mix 4 µL Qdots with 1 µL FL-MyoVa and incubate for 10 min at room temperature.

3.1.3. MyoVa HMM-YFP to Antibody-Conjugated Qdot

Antibody-conjugated Qdots can be used to attach motor molecules in a specific manner, and are also suitable for single-molecule studies. It is important to use antibodies of high affinity (low K_d) for this application. This protocol describes conjugation of Qdot 655 antibodies to MyoVa molecules with a C-terminal YFP using an α-AFP monoclonal antibody.

1. Combine 2 µL goat α-mouse IgG-conjugated Qdot 655 (1 µM) with 2 µL 3E6 α-GFP mAb (3.3 µM).
2. Incubate for 60 min on ice.
3. During the above incubation, prepare 1× actin buffer: In a 15-mL conical tube, combine 1 mL of 10× actin buffer, 100 µL 1 M DTT, add dH₂O to bring the volume to 10 mL. Keep on ice.
4. Dilute MyoVa HMM-YFP protein to 500 nM in 1× actin buffer.
5. Mix 4 µL anti-GFP-coated Qdots (500 nM) with 1 µL MyoVa HMM-YFP (500 nM).
6. Incubate for 30 min on ice.

3.2. In Vitro Motility Assay

In vitro experiments allow easy and controlled manipulation of experimental conditions. Confinement of actin tracks to the two-dimensional cover glass surface provides idealized imaging conditions, which allows for acquisition of very high-resolution data. A 10- μ L flow cell chamber as described previously (8) was used and the following solutions are introduced into the flow cell (see Note 6).

1. Flow 20 μ L NEM-myosin into the flow cell and incubate for 2 min. The NEM-myosin binds to glass surface and serves to fix actin filaments to the glass surface. This attachment produces much better results than adhering actin directly to the glass.
2. Wash the flow cell with 6 volumes (120 μ L) 1 \times actin buffer to remove excess NEM-myosin.
3. Introduce 20 μ L AB-BSA into the flow cell and incubate at room temperature for 2 min. This is a “blocking” step to reduce nonspecific binding of motors or Qdots to the glass surface.
4. Wash the flow cell with 100 μ L of 1 \times actin buffer.
5. Introduce 20 μ L of fluorescent actin into flow cell and incubate at room temperature for 2 min.
6. Wash the flow cell with 100 μ L 1 \times actin buffer.
7. Dilute Qdot-labeled MyoVa to 0.2–1.0 nM in AB-BSA-ATP (see Note 7).
8. Flow 20 μ L into the flow cell and observe under microscope at $25 \pm 1^\circ\text{C}$. (See an example of the results possible using this approach as shown in Fig. 1).

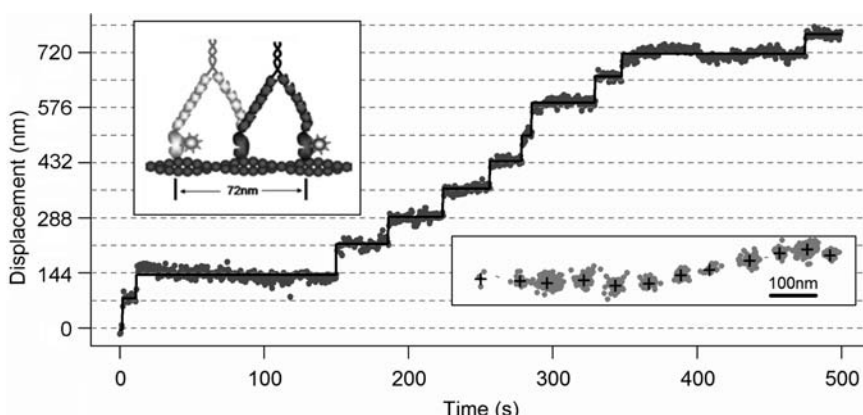


Fig. 1. In vitro stepping of N-bio myosin Va. 72-nm steps are apparent for a MyoVa HMM molecule labeled with a Qdot at the N-terminus of one head. As expected, the motion is linear and unidirectional (*lower right inset*). Although the entire molecule moves with 36-nm steps, the labeled head demonstrates a 72-nm displacement for each step (*upper left inset*).

To observe the Qdot-labeled motors and fluorescently labeled actin, we use a Nikon TE2000-U microscope equipped with a PlanApo (100 \times , 1.49 n.a.) objective lens for through-the-objective total internal reflection fluorescence (TIRF) microscopy (5, 6, 12). Fluors are excited with 488-nm argon laser line. A software-controlled filter wheel is used to switch between emission filters specific for Qdots or actin filaments (see Note 8 regarding correction between two imaging channels). Images are captured by using a DVC-1412:GenIV intensified high-resolution 12-bit digital camera (DVC company, Austin, TX) at 166-ms integration time. We normally record 300–800 frames at 2–5 frames/s.

For image analysis and high-resolution tracking, we utilize custom-written software that fits the position of Qdot-labeled MyoVa with a two-dimensional Gaussian, which approximates the Qdot point-spread function with 6-nm accuracy (3, 12, 13). We also have excellent results with the automatic particle-tracking plug-in Spot Tracker 2D (14) for Image J (version 1.34s) digital image processing software (National Institutes of Health, Bethesda) and the step-fitting algorithm developed by Kerssemakers et al. (15). To measure the run length and velocity, a manual particle-tracking plug-in MTrack J is often used. This program determines the centroid position based on the image intensity with 20 nm resolution. The velocity is determined as the mean of a Gaussian distribution while run length distributions are fitted with $p(x) = Ae^{-x/\lambda}$ to determine the characteristic run length λ , where $p(x)$ is the relative frequency of the motor traveling a distance x along a track and A is a constant.

Although the protocol presented here is for the characterization of a single motor molecule, increasing the MyoVa:Qdot mixing ratio results in the creation of small ensembles of motor molecules all bound to the same Qdot cargo. This approach can be extended further to study the interaction of combinations of heterologous motors, such as that reported by Ali et al. (5).

3.3. In Vivo Motility Assay

Qdot-labeled MyoVa molecules can also be delivered into the cytosol of cultured mammalian cells in order to study the activity of these motors in a physiological environment. Although several approaches are available for delivery of protein:Qdot conjugates into the cytosol, we had excellent results using an osmotic shock-based protocol described by Okada and Rechsteiner (16) (see Note 9).

1. Plate COS-7 cells into a 35-mm glass bottom dish at a low density ($\sim 10^5$ cells) in 1.5 mL DMEM with 10% FBS and grow under standard tissue culture conditions (37°C, 5% CO₂) overnight.
2. Prepare MyoVa:Qdot complexes using a high-affinity attachment (i.e., biotin:streptavidin) as described (Subheading 3.1.1).

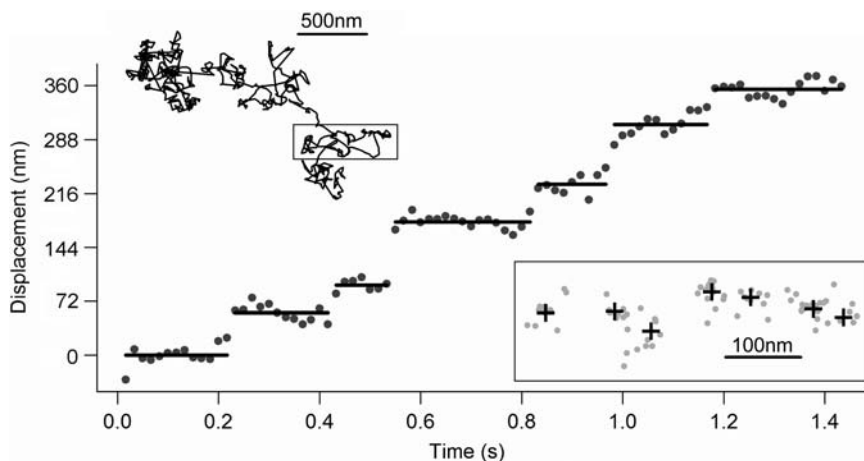


Fig. 2. *In vivo* stepping of N-bio myosin Va HMM. Qdot-labeled MyoVa HMM molecules delivered into cultured mammalian fibroblast cells (COS-7 cells) demonstrate random-looking trajectories (*upper left inset*). However, when imaged with high spatial (15 nm) and temporal (60 Hz) resolution, periods of linear movement can be detected (*boxed region in upper left inset, expanded in lower right inset*). When using a MyoVa construct that is labeled at its N-terminus, stepping behavior with the characteristic 72-nm step can be detected within these periods of linear movement.

3. Dilute MyoVa:Qdot conjugates into 1.5 mL hypertonic loading buffer for a final concentration of 30 pM Qdots.
4. Prewarm buffers and media to 37°C in a water bath.
5. Aspirate media from cells and replace with MyoVa:Qdot conjugates in loading buffer from step 3.
6. Incubate for 10 min at 37°C.
7. Aspirate loading buffer.
8. Add 4 mL of hypotonic lysis buffer.
9. Incubate for 2 min at room temperature.
10. Aspirate lysis buffer and add 1.5 mL DMEM.
11. Image immediately. An example of the MyoVa movements that can be detected with this approach is shown in Fig. 2.

4. Notes

1. In most of our experiments, we use Qdots which emit at 655 nm. But other Qdots, such as 565 nm, can be used and give similar results.
2. Oxygen scavengers reduce oxidative damage to proteins and photobleaching of organic fluors. This preparation retains function for about 2 h and cannot be refrozen or reused. In our experience, it is best to prepare fresh buffers if the experiment will run long instead of trying to “freshen up” the scavengers.

3. To maintain long actin filaments, we find it best to handle actin preparations carefully to avoid shearing. This includes transferring actin preparations using wide bore tips or slicing off the terminal ~1 cm from a standard pipette tip.
4. When labeling motor molecules where the motor domain is to be labeled, it is important to use limiting protein relative to the Qdots. If N-terminal domains of multiple motor molecules bind to the same Qdot, a situation analogous to a “three-legged race” ensues. However, when coupling motor molecules by their C-terminal or CBD, it is possible to use the Qdot as a cargo for transport by an ensemble of motor molecules. In this situation, it is possible to conjugate using a molar excess of myosin relative to the Qdots.
5. We occasionally flick the tube with a finger to ensure mixing for better attachment of motors to Qdot.
6. We find that the most effective way to introduce solutions into the flow cells is to devise a support such that the flow cell is held at about 20° to the horizontal. Place the pipette tip with the solution right at the lip on the upper edge of the flow cell and hold a Q-tip at the lower lip of the flow cell. Capillary action quickly draws in the first solution. Subsequent additions are drawn into the flow cell by wicking action of the Q-tip.
7. To measure the velocity and run length of MyoVa, we use saturating ATP (1–2 mM). To reduce the stepping rate to ~2 steps per second, we reduce the ATP concentration to 300 nM. As can be seen in Fig. 1, this allows better sampling and accuracy in order to observe the steps of the individual heads, also see ref. (3).
8. Chromatic aberrations can cause significant errors when trying to relate the positions of two different color Qdots. To compensate for this, we create a “color correction matrix” by simultaneously imaging both imaging channels during a raster scan of multicolor fluorescent beads (Ultra Rainbow Fluorescent Particles, Sphercotech, Libertyville, IL). The discrepancy between the apparent coordinates of individual beads between the two imaging channels at different locations within the field of view is then used to populate an “offset matrix,” which is interpolated to contain a correction value for every pixel in the field of view. Simply adding or subtracting the appropriate correction value allows the observed coordinates from one color image to be aligned with the corresponding coordinates in the other color image.
9. Internalization of Qdot-labeled MyoVa by this approach can be verified by labeling pinosomes by introducing 5 mg/mL FITC-Dextran 50k (Fluka) in the loading buffer and imaging prior to the hypotonic lysis step. Pinosomes appear as punctate

structures, some of which colocalize with Qdots. Subsequent osmotic shock lyses the pinosomes, resulting in a diffuse haze throughout the cell.

Acknowledgments

The authors thank Guy Kennedy for optomechanical support, Samantha Previs for technical expertise, and Kathleen Trybus for providing MyoVa protein. This work was supported by funds from the National Institutes of Health HL007944 (to S.R.N.) and HL059408, GM094229, and HL085489 (to D.M.W.).

References

1. Krementsov, D. N., Krementsova, E. B., and Trybus, K. M. (2004) Myosin V: regulation by calcium, calmodulin, and the tail domain. *J. Cell Biol.* **164**, 877–886.
2. Cronan, J. E., Jr. (1990) Biotinylation of proteins in vivo. A post-translational modification to label, purify, and study proteins. *J. Biol. Chem.* **265**, 10327–10333.
3. Warshaw, D. M., Kennedy, G. G., Work, S. S., Krementsova, E. B., Beck, S., and Trybus, K. M. (2005) Differential labeling of myosin V heads with quantum dots allows direct visualization of hand-over-hand processivity. *Biophys. J.* **88**, L30–32.
4. Hodges, A. R., Krementsova, E. B., and Trybus, K. M. (2007) Engineering the processive run length of Myosin V. *J. Biol. Chem.* **282**, 27192–27197.
5. Ali, M. Y., Lu, H., Bookwalter, C. S., Warshaw, D. M., and Trybus, K. M. (2008) Myosin V and Kinesin act as tethers to enhance each others' processivity. *Proc. Natl. Acad. Sci. USA* **105**, 4691–4696.
6. Baker, J. E., Krementsova, E. B., Kennedy, G. G., Armstrong, A., Trybus, K. M., and Warshaw, D. M. (2004) Myosin V processivity: multiple kinetic pathways for head-to-head coordination. *Proc. Natl. Acad. Sci. USA* **101**, 5542–5546.
7. Pardue, J. D., and Spudich, J. A. (1982) Purification of muscle actin. *Methods Cell Biol.* **24**, 271–289.
8. Warshaw, D. M., Desrosiers, J. M., Work, S. S., and Trybus, K. M. (1990) Smooth muscle myosin cross-bridge interactions modulate actin filament sliding velocity in vitro. *J. Cell Biol.* **111**, 453–463.
9. Hermanson, G. T. (2008) *Bioconjugate techniques*, 2nd ed., Elsevier Academic Press, Amsterdam; Boston.
10. Liu, J., Taylor, D. W., Krementsova, E. B., Trybus, K. M., and Taylor, K. A. (2006) Three-dimensional structure of the myosin V inhibited state by cryoelectron tomography. *Nature* **442**, 208–211.
11. Wang, F., Thirumurugan, K., Stafford, W. F., Hammer, J. A., 3rd, Knight, P. J., and Sellers, J. R. (2004) Regulated conformation of myosin V. *J. Biol. Chem.* **279**, 2333–2336.
12. Ali, M. Y., Krementsova, E. B., Kennedy, G. G., Mahaffy, R., Pollard, T. D., Trybus, K. M., and Warshaw, D. M. (2007) Myosin Va maneuvers through actin intersections and diffuses along microtubules. *Proc. Natl. Acad. Sci. USA* **104**, 4332–4336.
13. Yildiz, A., Forkey, J. N., McKinney, S. A., Ha, T., Goldman, Y. E., and Selvin, P. R. (2003) Myosin V walks hand-over-hand: single fluorophore imaging with 1.5-nm localization. *Science* **300**, 2061–2065.
14. Sage, D., Neumann, F. R., Hediger, F., Gasser, S. M., and Unser, M. (2005) Automatic tracking of individual fluorescence particles: application to the study of chromosome dynamic. *IEEE Trans. Image Process* **14**, 1372–1383.
15. Kerssemakers, J. W., Munteanu, E. L., Laan, L., Noetzel, T. L., Janson, M. E., and Dogterom, M. (2006) Assembly dynamics of microtubules at molecular resolution. *Nature* **442**, 709–712.
16. Okada, C. Y., and Rechsteiner, M. (1982) Introduction of macromolecules into cultured mammalian cells by osmotic lysis of pinocytic vesicles. *Cell* **29**, 33–41.

Chapter 9

Imaging Individual Myosin Molecules Within Living Cells

Tatiana A. Nenasheva, Gregory I. Mashanov,
Michelle Peckham, and Justin E. Molloy

Abstract

Myosins are mechano-enzymes that convert the chemical energy of ATP hydrolysis into mechanical work. They are involved in diverse biological functions including muscle contraction, cell migration, cell division, hearing, and vision. All myosins have an N-terminal globular domain, or “head” that binds actin, hydrolyses ATP, and produces force and movement. The C-terminal “tail” region is highly divergent amongst myosin types, and this part of the molecule is responsible for determining the cellular role of each myosin. Many myosins bind to cell membranes. Their membrane-binding domains vary, specifying which lipid each myosin binds to. To directly observe the movement and localisation of individual myosins within the living cell, we have developed methods to visualise single fluorescently labelled molecules, track them in space and time, and gather a sufficient number of individual observations so that we can draw statistically valid conclusions about their biochemical and biophysical behaviour. Specifically, we can use this approach to determine the affinity of the myosin for different binding partners, and the nature of the movements that the myosins undergo, whether they cluster into larger molecular complexes and so forth. Here, we describe methods to visualise individual myosins as they move around inside live mammalian cells, using myosin-10 and myosin-6 as examples for this type of approach.

Key words: Total Internal Reflection Fluorescence Microscopy, Single-molecule detection, Single-particle tracking, Myosin, Cell motility

1. Introduction

Many types of cell motility, including muscle contraction, are driven by the cyclical interaction of myosin with actin, coupled to the breakdown of ATP. Myosins belong to diverse superfamily of mechano-enzymes that share a conserved sequence that codes for the N-terminal, motor or “head” region, and have highly divergent, C-terminal, cargo-binding or “tail” regions that specify their cellular roles (1, 2). The well-studied myosin-2 from skeletal muscle was the first type of myosin to be discovered and is often termed

“conventional” myosin. The human genome has 13 genes for conventional myosin-2 isoforms and 26 genes encoding so-called unconventional myosins (3), which are classified into 11 further classes. The unconventional myosins play critical roles in human physiology, and mutations in many of these myosins have already been discovered to lead to diverse and severe pathologies.

Unconventional myosins are challenging to study because they are present at very low concentrations in the cell (4). However, some have been purified from tissue or expressed in vitro in sufficient quantity to allow the enzymology to be studied. A combination of biophysical approaches including X-ray crystallography, solution biochemical analysis, and single-molecule studies have greatly increased our basic understanding of the force generating mechanism. However, to gain a complete picture of how different myosins work, it is important to characterise their properties within the living cell where their native interacting partners (e.g., accessory proteins or cellular cargo) are also present. To this end, we have developed methods to visualise individual myosin molecules within live mammalian cells so that we can study their binding to membranes, cellular cargos, and the actin cytoskeleton. We can also measure their speed of movement and determine how different myosins are targeted to different regions of the cell.

Here, we describe methods to visualise eGFP-tagged myosins, which are transiently expressed within live mammalian cells at concentrations close to physiological levels. Because many of the myosins we study associate with the plasma membrane (2), Total Internal Reflection Fluorescence Microscopy (TIRFM) is ideal for observing individual molecules with high signal-to-background noise ratios (5). Unconventional myosins often associate with the plasma membrane (6, 7) or become immobilised on subcellular structures (including vesicles and the actin cytoskeleton). When this occurs, they have a low two-dimensional diffusion coefficient ($D_{\text{lat}} < 1 \mu\text{m}^2 \text{s}^{-1}$), which means that they diffuse sufficiently slowly within the plane of the evanescent field to be imaged using a video-rate (30–40 ms/frame) camera system. Image blurring due to the diffusive motion of membrane associated proteins is less than the diffraction limited spot size (as they move $<100 \text{ nm}$ in 40 ms). However, proteins that diffuse freely in the three-dimensional cytosolic space have a high diffusion coefficient ($D > 2 \mu\text{m}^2 \text{s}^{-1}$), and photons emitted by the fluorophore during a single video frame are blurred out over a large area due to diffusive motion, which means they can no longer be resolved as individual spots of light (8).

The evanescent field produced by total internal reflection of light at the interface between high and low refractive index media (e.g., glass and water) extends by a distance of about 100 nm (“1/e” penetration depth). Using laser excitation and sensitive video cameras, wide-field images of living cells grown on a glass coverslip can be obtained using TIRFM in which individual eGFP

fluorophores appear as separate spots of light. This approach means that the location of multiple individual myosin molecules can be extracted from each video picture, allowing their dynamic properties to be measured with 40 ms time resolution and 30 nm spatial resolution.

Although synthetic fluorophores (such as fluorescein, rhodamine, and cy-family dyes) have superior fluorescence properties compared to fluorescent protein tags (e.g., eGFP, YFP, RFP), it is much easier to express GFP-fusion proteins in a live cell rather than use microinjection or other methods to introduce synthetically labelled proteins. Furthermore, we know that recombinant fusion-proteins will have 100% of the fluorophore bound covalently to the protein of interest and the level of expression can be controlled using transient transfection methods. For this reason, we focus here on the use of fluorescent protein tags, which we find can be observed as individual spots of light that can be readily discriminated above background.

In this chapter, we describe the following: construction of the experimental chamber, practical design of the TIRF microscopy set-up, the choice of fluorescent marker and methods to collect and analyse large data sets (7). We also describe the use of two computer algorithms that enable automatic single-molecule (fluorophore) detection and tracking (9).

2. Materials

2.1. Flow-Cells and Imaging Chambers

1. Flow-cells are made from a microscope coverslip (No. 1) glued to a microscope slide using two, 3-mm wide, strips of coverslip as spacers to form a central channel with height of ~150 µm, length of 25 mm, width of 10 mm, volume of ~75 µl, and surface area of ~500 mm². Solutions are applied at one side of the channel and extracted from the other side using a piece of filter paper.
2. Proprietary, glass bottomed, cell culture dishes (MatTek, Ashland, MA) or multi-well glass bottomed chambers (LabTek, Thermo Fisher Scientific, UK) can be used for live-cell imaging. However, when high mechanical stability or solution exchange is required, custom-made, enclosed chambers are preferable (see Subheading 3 for details).

2.2. Solutions and Fluorescent Markers

1. Phosphate-buffered saline (PBS) solution, pH 7.4.
2. Foetal calf serum (*heat inactivated*) (Sigma-Aldrich, Poole Dorset, UK).
3. Hank's balanced salt solution containing 20 mM HEPES, pH 7.4.

4. Polyclonal anti-GFP antibodies, 5 µg/ml (33 nM) (Abcam, Cambridge, UK).
5. GFP solution (0.5–2 nM final concentration) (Clontech, Palo Alto, CA).
6. Cy3B (Amersham Pharmacia Biotech, UK).

2.3. Cell Culture and Transfection Procedures

1. Mammalian cells are cultured using standard procedures, and transferred onto glass coverslips and grown in the appropriate tissue culture medium 12–24 h prior to transfection.
2. Transfection reagent, e.g. Genejuice (Novagen, Merck Bioscience, Nottingham, UK) or Lipofectamine (Invitrogen, Paisley, UK).
3. Maxiprep DNA encoding myosin-6 or myosin-10 sequence fused in frame to eGFP.

2.4. Single-Molecule Microscopy and Analysis

1. Inverted microscope, Zeiss Aviovert-100TV (Ziess, UK).
2. Objective lens, Alpha-plan 100×, NA 1.45 (Ziess, UK).
3. Blue laser, 488 nm, 20 mW (Protera 488, Novalux, Sunnyvale, CA).
4. Green laser, 532 nm, 50 mW, (Suwtech 532-50, SP3-Plus Tunbridge Wells, UK).
5. Laser-grade beam expanders, lenses, and mirrors for TIRF illumination.
6. Microscope 37°C incubator (Solent Scientific, Segensworth, UK).
7. EMCCD camera, iXon-897BV (Andor, UK).
8. GMimPro image analysis software (<http://www.nimr.mrc.ac.uk/gmimpro/>).

3. Methods

3.1. Solution and Imaging Chamber

The cell culture medium, contains high concentrations of autofluorescent chemicals that cause significant background fluorescence under TIR illumination, even without the indicator phenol red. We found that the use of Hank's buffered salt solution reduced the level of background fluorescence (by about twofold). It has the additional advantage that it does not require CO₂ to regulate pH, and thus is well-suited for use with our sealed imaging chambers. To support the cells during long imaging intervals, we add 10% foetal calf serum (FCS). At this concentration, FCS does not increase the level of fluorescence background.

Although proprietary glass-bottomed imaging chambers can be used for live-cell imaging experiments, when extra mechanical stability, solution exchange or high resolution bright field imaging methods (such as DIC or phase contrast) are necessary, the fully

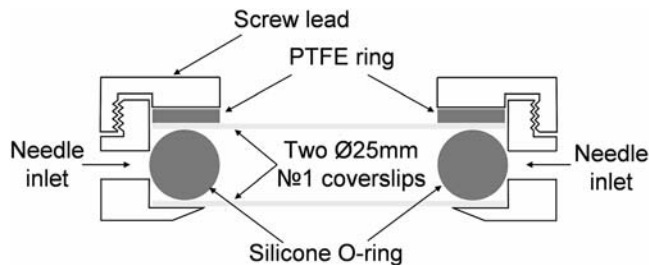


Fig. 1. Schematic view of imaging chamber used for single-molecule experiments with live cultured cells. A round coverslip with cultured cells is placed at the bottom of the chamber. A silicone O-ring, 2.5 mm thick, is used to separate the bottom from the top coverslip and create a sealed volume of about 0.8 ml. The solution in the chamber can be exchanged during imaging using two needles inserted through the silicone ring and connected to circulation.

enclosed, custom-built, imaging chamber (Fig. 1), in which cells are isolated from the room/incubator atmosphere, works best. Cells grown on a No. 1 round ($\varnothing 25$ mm) coverslip were placed into the chamber and covered by another coverslip separated by a silicone O-ring to create a sealed chamber.

The two ports, on opposite sides of the chamber, are used to insert hypodermic syringe needles connected to plastic tubing, which can be assembled into a gravitational or precision syringe-pump flow system (see Note 1). The sealed chamber, filled with Hank's solution, added serum and antibiotics can support live cells for a few days without serious deterioration of cell viability (estimated by cell adhesion to substrata and degree of cell migration). The top glass coverslip allows bright-field microscopy methods such as DIC to be used to image cells without polarisation distortions.

It is important to study living cells at physiological temperatures because many cell functions are strongly temperature dependent. There are two major methods of controlling temperature: (a) direct heating of the imaging chamber and the objective lens, using electrical heating elements embedded in the microscope stage and an objective lens jacket or (b) use of a microscope enclosure with circulating air. We use a perspex box (Solent Scientific, Segensworth, UK) and a custom-made air-flow heater system to control temperature around the entire TIRF microscope system. This method reduces temperature gradients around the imaging chamber and is suitable for solution exchange during the experiment (see Note 2).

3.2. Optical Set-Up

To achieve high signal-to-noise ratio images, we developed a “solid mirror” TIRFM design, described in detail previously (6). Briefly, two aluminium-coated mirrors ($\varnothing 3$ mm) (Comar Instruments, Cambridge, UK) are placed at the periphery of the objective lens back focal plane. One mirror directs the incoming laser beam towards the specimen, and the other couples the returning, totally internally reflected, laser beam out of the microscope imaging light

path. The angle of the returning beam depends upon the coverslip-to-objective lens distance. Thus, its angle of deflection can be used to automatically adjust the microscope focus by casting the beam onto a position sensitive photodiode. Because the aluminium-coated mirrors reflect light across the optical spectrum (with >95% efficiency), they can be used for multi-colour TIRF illumination (10, 11).

Spatial and temporal fluctuations in the excitation light can seriously affect the intensity of single-molecule fluorescence emission (see Note 2). Therefore, it is important to ensure that the illumination pattern is as uniform as possible across the field of view during the imaging period. Although monochromatic laser light sources are ideal for TIR illumination, their Gaussian intensity profile means that the illumination at the edge of the field of view is weaker than in the central region. To ameliorate this problem, the laser beam is expanded at a plane conjugate with the object plane, outside the microscope, and in addition, we use a field diaphragm in the same plane to create a relatively flat intensity profile. An alternative approach is to use a “flat top” optical component to reshape the laser beam profile (<http://www.newport.com/Refractive-Beam-Shapers/315393/1033/catalog.aspx>).

The critical angle for total internal reflection, θ_c , can be estimated to be $\sim 63^\circ$, from the following equation: $\theta_c = \arcsin(n_2/n_1)$, where n_2 and n_1 are the refractive indices for cell cytoplasm ($n_2 \sim 1.35$) and glass ($n_1 \sim 1.52$). However, because of diffraction effects, a laser beam is never perfectly collimated but always has some divergence ($\sim 1^\circ$). Therefore, the optimal angle of TIR illumination is usually set just above the theoretical, critical angle (5, 6) by about $1\text{--}2^\circ$. In practice, empirical adjustment of the incident angle is required to achieve the best signal-to-noise ratio (see Notes 3 and 4). The incident angle can be measured directly using a glass protractor (Comar Instruments, Cambridge, UK) and we find that $\sim 64^\circ$ is optimal for live-cell illumination.

The protractor that we use is made from flint glass, which has the same refractive index ($n=1.517$) as the coverslips and immersion oil used for experiments (see Note 5). It is placed on the microscope stage at the coverslip position (Fig. 2) and coupled to the objective lens (Alpha-plan, 100 \times , Zeiss, UK) by immersion oil ($n=1.518$, Immersol-518, Zeiss, UK). Blue light from a 488-nm laser is clearly visible inside the protractor (Fig. 2), so it is easy to collimate the laser beam and adjust its angle.

It is important to use high-grade, band-pass, emission filters for single and multi-colour imaging. They should have an optical density of at least 5 (i.e. attenuation to 0.001%) at the laser excitation wavelength(s) but with a transmission waveband that allows as much of the fluorescence emission to be collected as possible (i.e. transmission >90% at the emission wavelength) (see Notes 6 and 7).

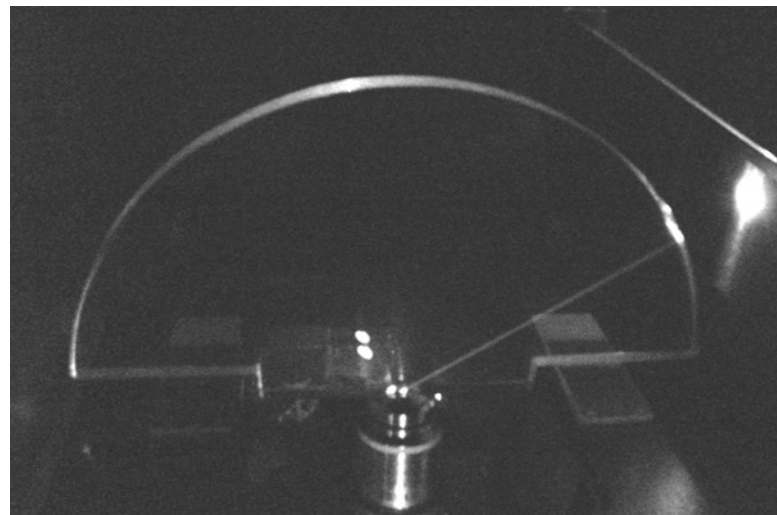


Fig. 2. A glass semi-cylindrical (“protractor”) placed on the microscope stage above the objective lens at the specimen plane can be used to measure and adjust the angle and divergence of the laser beam. The laser beam is seen as a bright line on the image, originating from the objective lens at an angle $\sim 64^\circ$ relative to vertical axis of objective lens. The protractor has a radius of 114.6 mm (2 mm per 1° at perimeter), which means that the beam divergence can be measured at the surface where the beam leaves the protractor (e.g. spot size of 4 mm will correspond to divergence of 2° , or 0.035 radian).

3.3. Camera

Single GFP can emit 10^5 to 10^6 photons (12) before photobleaching; therefore, the camera should be very sensitive and have low readout noise. The fast ($20\text{--}50\text{ frames s}^{-1}$) acquisition rate means that dark noise is less of a concern. Image-intensified, CCD cameras have sufficient sensitivity to image single fluorophores. However, the intensifier system creates temporal and spatial noise that degrades the image quality (13). Cooled, back-thinned, CCD cameras such as the Orca-ER (Hamamatsu Photonics, Japan) have excellent quantum efficiency, spatial resolution, and low dark noise and readout noise. However, the readout speed is slow (~ 2 Hz), which has the consequence that this type of camera is not well suited to imaging of rapidly diffusing molecules within live cells. Instead, such cameras are ideal for very weak fluorescence (or luminescence) signals that require longer exposure times (where low dark noise becomes a critical feature). Electron Multiplied CCD (EMCCD) cameras have increased sensitivity because the signal generated at every CCD element is multiplied before the readout process (see Note 8). Currently, such cameras are the best choice for high-speed single fluorophore imaging within live cells. In this chapter, we present results obtained using an iXon-897BV camera (Andor, Belfast, UK). Other manufacturers produce similar products and we expect that the technology will continue to advance rapidly.

3.4. The Choice of Fluorescent Marker

Fluorescent proteins, synthetic dyes, and Q-dots can be used for single-molecule visualisation but not all of them are suitable for tracking studies with high temporal and spatial resolution in live cells. It is important to choose the correct fluorescent tag for single-molecule imaging and tracking; otherwise, the quality of data may not be sufficient to make definitive conclusions because the duration of trajectories is too short or spatial resolution poor due to small number of photons detected per fluorophore per frame.

Fluorescent proteins are widely used for live-cell imaging. In most cases, it is straightforward to generate a DNA construct encoding the protein of interest fused, in frame, to eGFP (or variant). Standard transient transfection protocols for mammalian cell lines can then be optimised to generate a level of protein expression that enables single fluorophores to be identified. This requires systematic variation in transfection conditions (e.g. varying the amount of DNA and transfection reagent used). A major limitation of fluorescent protein usage is the limited photostability and, hence, the number of photons that fluorophore emits before the fluorophore is photobleached irreversibly. This becomes a serious problem when it is necessary to track fluorophores over a long period of time. Some synthetic dyes emit many more photons before photo-bleaching compared to fluorescent proteins (see below). But a major limitation when using synthetic fluorophores is the need to artificially label the protein of interest and deliver it to a live cell for imaging. One approach is to express the protein of interest fused to a short polypeptide tag and then add membrane permeable fluorescent dyes that will bind or react specifically with the tag. See following source for the review: http://www.neb.com/nebecomm/tech_reference/gene_expression_cellular_analysis/SNAP_tag_technologies.asp.

The labelling process is simplified if the protein of interest is embedded in the outer leaflet of the cell membrane, since it can then be labelled by external labelling. The example of labelling muscarinic receptors with a fluorescent ligand is discussed further here (10).

The photostability of different dyes can be compared by imaging these molecules attached to a coverslip under conditions similar to those used for the live cell (see Notes 9 and 10). For instance, GFP can be immobilised at a coverslip surface using an anti-GFP antibody. First, the glass surface is incubated for 5 min with the antibody-containing solution 5 µg/ml (33 nM), then it is washed with PBS, and replaced with a dilute solution of GFP, 0.2–20 ng/ml (i.e. up to 0.74 nM) for a further 5 min (9). The surface is then thoroughly washed with PBS to remove unbound molecules, before imaging the bound GFP molecules (Fig. 3a). Cy3B binds non-specifically to glass, but the viewing chamber (flow-cell) must be thoroughly washed to remove unbound dye (Fig. 3d). In these experiments, the photostability (P) is estimated by dividing the

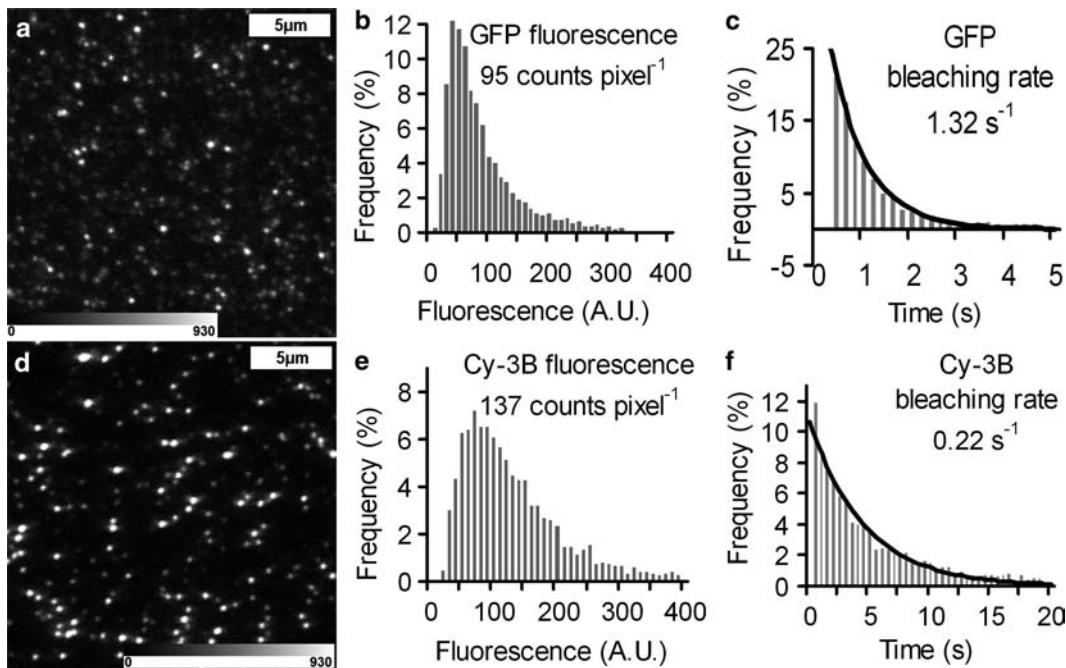


Fig. 3. GFP and Cy3B molecules imaged under TIRF illumination in vitro. Imaging rate 20 frames s^{-1} , intensity measured in $5 \times 5 \text{ pixel}^2$ area. (a) An image of GFP molecules bound to glass via antibodies. (b) Distribution of fluorescence intensities of single GFP molecules detected by SFDA (see text for details). (c) Distribution of photobleaching times of single GFP molecules. (Black line is a single exponential fit to this distribution). (d) An image of Cy3B molecules bound to glass imaged using TIRFM. (e) Distribution of fluorescence intensities of single Cy3B molecules detected by SFDA. (f) Distribution of photobleaching times of Cy3B molecules. (Black line is a single exponential fit to this distribution).

average level of fluorescence of the single molecules, I_{av} ($\text{counts } s^{-1}$), by the photobleaching rate, k_{bleach} (s^{-1}), ($P = I_{av}/k_{\text{bleach}}$). We have found that the photostability of Cy3B is 8.6 times higher compared to GFP (Note: both dyes were imaged in PBS solution without oxygen-scavenging system).

Another important issue is fluorophore “blinking” behaviour. This type of behaviour occurs when a molecule temporarily stops emitting photons (dark interval) and then subsequently resumes emission at the same rate as before (14). This can affect single-molecule tracking because the intensity and $X-Y$ position of the object is unknown during dark intervals, and this results in premature termination of tracking of the fluorophore trajectory in space and time. We compared the level of blinking of GFP and Cy3B molecules (blinking was defined as a drop of emission to zero level for at least one frame). About 20% of GFP molecules showed blinking behaviour (at least one period when the level of fluorescence temporally dropped to zero) compared to ~5% for Cy3B molecules.

3.5. Image Analysis

Because of the stochastic nature of single-molecule behaviour, a statistically meaningful number of individual molecules must be detected and their separate trajectories in space and time stored

and analysed. The methods of digital image processing that we have devised for automatic detection and tracking of hundreds of molecules, observed simultaneously, *in vitro* and within living cells has been described in detail previously (9). Single-molecule analysis software based on these algorithms is available free of charge for academic users (<http://www.nimr.mrc.ac.uk/gmimpro>). Here, we describe the principles of detection and tracking using two experimental examples: pleckstrin homology (PH) domains from myosin-10, which diffuse freely in the cytoplasm and bind to phosphoinositides at the plasma membrane (7) and myosin-6 molecules, which spend most of their time bound to the plasma membrane. The behaviour of myosin-6 molecules suggest that they can move randomly while bound to lipids in the membrane, but periodically bind to immobile structures.

3.5.1. Imaging Molecules that Bind to the Plasma Membrane

Single fluorescent molecules present in the cytoplasm move too fast to be detected at video-rate imaging (15) *and see above*, but when molecules bind to the plasma membrane they then move at the same speed as lipid diffusion. This is sufficiently slow that individual molecules can be visualised as isolated spots of light. The trajectories of the molecules can then be recorded and analysed at video rate (25–33 frames s⁻¹) (7, 15).

Here we describe the detection of eGFP labelled Pleckstrin Homology (PH) domains of myosin-10 (eGFP-PH123) that bind reversibly to phosphoinositol phospholipids (PIPs) at the plasma cell membrane (7). eGFP-PH123 was expressed in living cells at very low expression levels (<10 nM). We found that eGFP-PH123 domains bound tightly to plasma membrane in cultured mouse myoblasts and had very limited lateral mobility. Individual spots of light were observed that had the same properties as control specimens made using purified eGFP bound to a glass surface via antibody (Fig. 3a). We used our single fluorophore detection algorithm (SFDA) to identify individual fluorophores in a sequence of video images. Single fluorophores were identified on the basis of the so-called DISH criteria: the fluorescent spots of light had (1) Diffraction-limited size of fluorescent spot, (2) Intensity of emission is appropriate for a single fluorophore, (3) Single-step photo-bleaching of the fluorescent spot, and (4) Half-life of the fluorophore population before photobleaching occurred is directly proportional to laser excitation power.

Based on these criteria, we developed a three-pass computer algorithm (9), which performs spatial and temporal statistical tests on stored video sequences to identify individual fluorophores (see below). On the first pass, groups of pixels are analysed in time to test for the expected sudden change in intensity characteristic of rapid appearance and disappearance of single fluorophores (Fig. 1, and Eqs. 2 and 3 from (9)). Fluorescent spots that exhibit the correct amplitude and speed of intensity change and which also have the correct diffraction-limited size are then subjected to

a second round of analysis. The second pass performs a statistical analysis of the intensity levels before and after candidate changes in intensity are noted during the first pass (Eq. 6 from (9)). On the final pass of the algorithm, the trajectory in space and time for each candidate fluorophore is determined by tracking the centroid of each fluorescent spot. The computer program produces an output file that can be checked against the original raw data sets and which also contains all of the statistical information regarding the individual time trajectories for each fluorophore and the global statistics concerning average lifetimes.

Fluorescence images produced using TIRFM are typified by the fact that fluorophores diffuse very rapidly to and from the evanescent excitation region before and after binding at the plasma membrane (which is close to the coverslip interface). This means that spots of light appear rapidly and then persist at the membrane for several video frames until either they photobleach or the molecule detaches (Fig. 4a). In either case, the spot of light rapidly disappears. The time resolution of our system is insufficient to discriminate between unbinding followed by rapid diffusion out of the excitation field and instantaneous photobleaching. In fact, the average diffusion time for a small protein in cytoplasm (e.g. diffusion coefficient, $D \approx 1 \times 10^{-11} \text{ m}^2 \text{s}^{-1}$) from an evanescent field of depth, $x = 100 \text{ nm}$, is given by $x^2/2D \approx 0.5 \text{ ms}$. Because photobleaching is directly proportional to laser power, whereas unbinding is independent of illumination power, photobleaching can be factored out from unbinding by systematically changing the average laser power.

To accomplish this, time-lapse illumination was employed. In every 5-s interval, the laser was switched on for 0.33, 0.55, 1.05, or 1.55 s or left on continuously for the full 5 s. The illumination “duty cycle ratio” was varied over the range from ~7 to 100%. This approach offers the advantage that signal-to-noise ratio of the camera system and the TIR angle during the period of illumination remains constant. Figure 4b shows a few example trajectories (intensity measured in the same area of 5×5 pixels) of eGFP-PH123 molecules arriving at the plasma membrane during time-lapse illumination (7% average laser power).

When the cells were continuously illuminated at high laser power, the average fluorescence of the whole cell decreased. The exponential time course of bulk photobleaching was similar to the average lifetime of the individual fluorescent spots ($\tau \approx 2.5 \text{ s}$ in Fig. 4c). The conclusion from this finding is that most of the observed fluorophores are probably being photobleached during the observation period. When time-lapse illumination was used (duty ratio of 0.07), fluorescent spots arrived and remained at the membrane for many seconds (Fig. 4b), the average lifetime of the spots increased to 14 s (Fig. 4d), and some lasted as long as hundreds of seconds. eGFP-PH123 that detached from the membrane before photobleaching diffused from the excitation field so rapidly

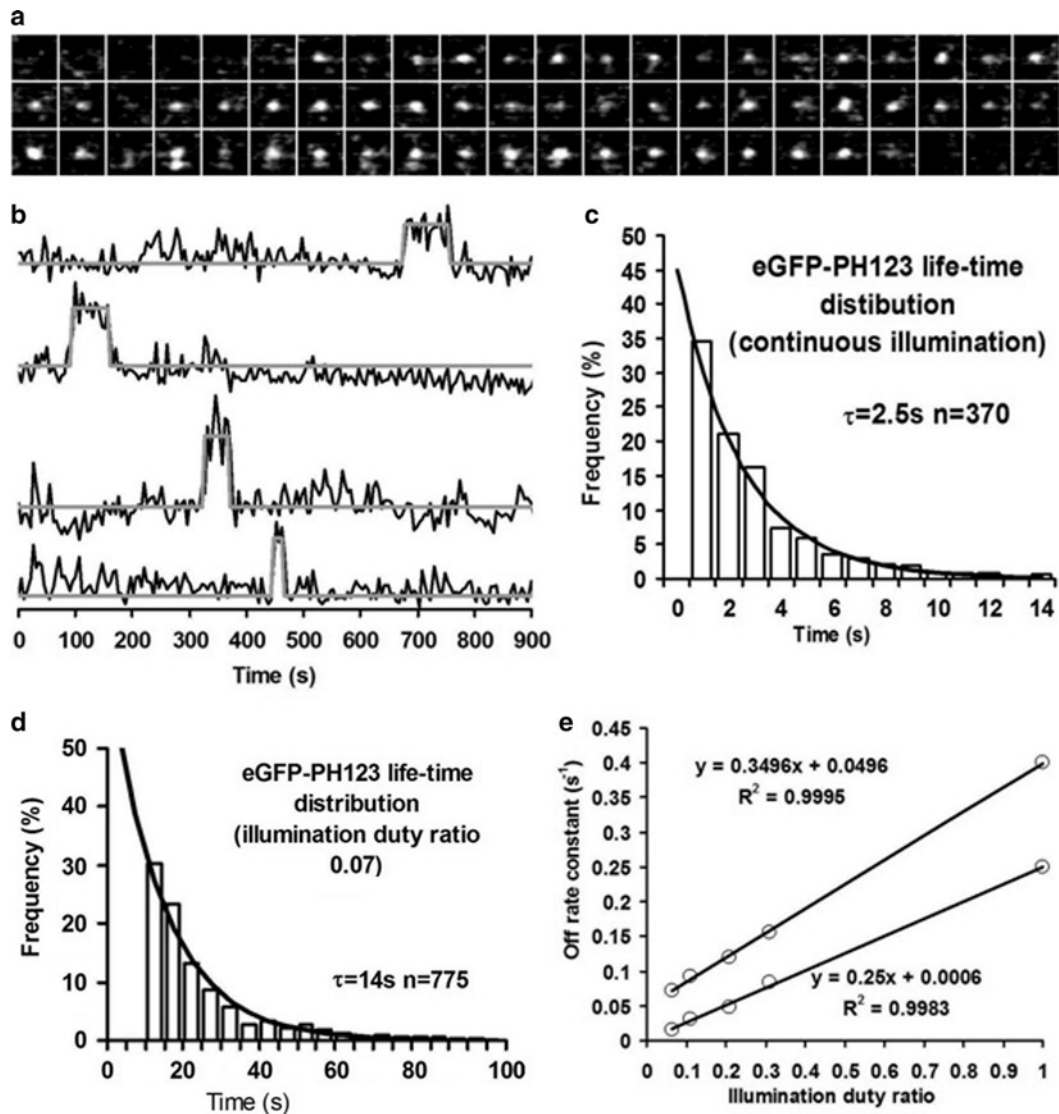


Fig. 4. eGFP-PH123 dynamics at plasma membrane of cultured mouse myoblasts. (a) Image sequence of single PH123 molecule “landing” at the plasma membrane and dissociating from it. Image size is $1.7 \times 1.7 \mu\text{m}^2$, time interval 100 ms. (b) Time lapse imaging of PH123 molecules “landing” at the plasma membrane. Fluorescence intensity trajectories show a stepwise increase when molecule appears in the image and a stepwise drop when fluorophore disappears due to dissociation or photobleaching. (c) Distribution of the time before photobleaching occurred as measured for bound PH123 molecules under continuous illumination (black line – exponential fit to this distribution). (d) Distribution of the time before photobleaching occurred as measured for bound PH123 molecules under time-lapse illumination (black line – exponential fit to this distribution). (e) Calculation of eGFP-PH123 dissociation rate (see text for details). This figure was adopted from ref. 7.

(0.5 ms) that our camera system could not directly distinguish this from instantaneous photobleaching.

Illumination power was varied systematically as before (using purified eGFP bound to an antibody-coated coverslip), and the average lifetime of the fluorophores before photobleaching was

found to depend linearly upon illumination power. However, a plot of the rate constant derived for the disappearance of the spots (k'_{off} =inverse of the half-life) versus average laser power (Fig. 4e) now showed a non-zero intercept. k'_{off} should be the sum of two rate processes, photobleaching and detachment (k_{pb} and k_d , respectively). Photobleaching rate, k_{pb} , will be proportional to illumination power, ξ , and assuming that these processes are irreversible, $k'_{\text{off}} = \xi \times k_{\text{pb}} + k_d$. Thus, at high average laser power, the dominant process will be $\xi \times k_{\text{pb}}$, whereas at low power ($\xi \approx 0$), it will be k_d . This analysis for eGFP-PH123 in living cells showed that at zero illumination, $k'_{\text{off}} = k_d = 0.05 \text{ s}^{-1}$. By contrast, eGFP molecules attached via antibodies to glass had an extremely slow detachment rate, k_d and, therefore, k'_{off} extrapolated to near zero at zero laser power (Fig. 4e).

The apparent binding rate of eGFP-PH123 at the plasma membrane was estimated by analysing the “landing rate” (i.e., the distribution of dark intervals before a fluorescent spot appeared within a given area of membrane or sample quadrat). Landing rate depended in a linear way upon the observation window bin size (i.e. area of the sample quadrat). Best estimates of landing rate were obtained using a $5 \times 5 \text{-}\mu\text{m}^2$ area. We found that the apparent binding rate, k'_{on} , of eGFP-PH123 at the plasma membrane was $0.28 \times 10^{-3} \text{ }\mu\text{m}^{-2} \text{ s}^{-1}$ (see Fig. 5 from (6) for details). The apparent binding rate, k'_{on} , depends upon the concentration of free eGFP-PH123 in the cell, the density of binding sites (with the correct phosphoinositol moiety), and the concentration of any competing PH domains. The expression level of eGFP-PH123 was found to be $\sim 10 \text{ nM}$ by comparing the fluorescence signal measured in the

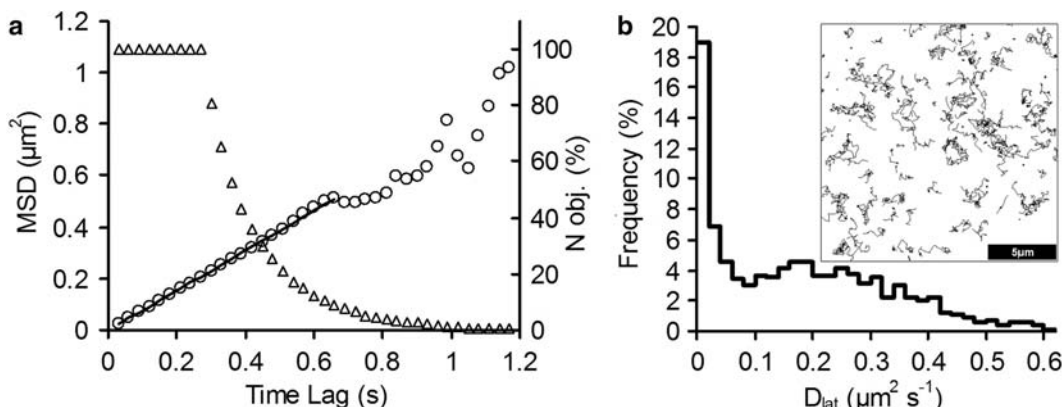


Fig. 5. eGFP-PH12 mobility at plasma membrane of cultured endothelial cells at 23°C. (a) 3165 single-molecule trajectories from eight cells were used to build the MSD-dT plot shown (circles). Linear fit (black line) gives $D_{\text{lat}} = 0.193 \text{ }\mu\text{m}^2 \text{ s}^{-1}$. Triangles show number of trajectories (right Y axis) that contribute to MSD calculations at given time lag. (b) Distribution of mobility of individual eGFP-PH12 molecules. Averaged $D_{\text{lat}} = 0.191 \text{ }\mu\text{m}^2 \text{ s}^{-1}$. Inset – Trajectories of individual eGFP-PH12 molecules on the HUVEC membrane. Some immobile objects (dot like trajectories) give rise to immobile fraction, normally not present in Gamma distribution characteristic for freely diffusing objects.

cytosol of cells to that of free eGFP in solution by confocal microscopy. Using this estimate of the concentration of free eGFP-PH123, the apparent second-order rate constant for binding, k_b , is calculated as $0.028 \mu\text{M}^{-1} \mu\text{m}^{-2} \text{s}^{-1}$.

3.5.2. Detecting Molecules Diffusing at Plasma Membrane of Living Cells

The computer algorithm described above (SFDA) is not suitable for single-molecule detection and tracking when molecules move rapidly. The filtering and statistical tests need to be modified to allow intensities to be tracked in space and time. To track individual fluorophores moving at the plasma membrane of living cells, video data must be acquired at high speed. This is because the lateral diffusion coefficient (D_{lat}) of a protein in membrane is large compared to the Point Spread Function (PSF) of the fluorophore, and its image is, therefore, smeared out (or blurred) by its diffusive motions. For instance, if $D_{\text{lat}} \approx 0.5 \mu\text{m}^2 \text{s}^{-1}$ then the spot will move by about $\sim 1.4 \mu\text{m}$ within 1 s. Here, we assume that raw data are collected at sufficient speed that fluorophore movement during individual video frames is small compared to the idealised PSF measured in control, fixed samples (fluorophores attached to glass surface).

We developed a different detection algorithm (automatic single-particle tracking or ASPT) to identify the locations of single fluorophores within each video frame and then track their positions between consecutive video frames. The first phase works by pattern-matching regions of the image to the known PSF of a single fluorophore (Fig. 2 and Eq. 8 from (9)). Idealised fluorophore centroids are then stored as an array of x, y, t locations. The second phase of the ASPT routine links object coordinates between adjacent video frames using a nearest-neighbour algorithm. If the tracked objects move close to each other ($\sim \text{FWHM}$) and their images coalesce, then if the resulting image deviates significantly from the idealised single fluorophore PSF, both tracks will be terminated. However, if the resulting image approximates that of a single fluorophore, then only one track is terminated. Once the object tracks have been identified, the original intensity data are used to refine our estimate of the fluorophore centroids with sub-pixel resolution (as for SFDA above). Finally, to discriminate single fluorophores from multi-fluorophore clusters the original intensity data can be inspected to ensure that each object exhibits single-step appearance and disappearance (photobleaching) and has an average intensity similar to that of known single fluorophores measured in our *in vitro* control specimens.

We used the ASPT algorithm to track two different constructs, eGFP-PH12 and eGFP-PH123, within human umbilical vein endothelial cells (HUVECs) at 23°C . The mobility of both constructs was much higher than eGFP-PH123 mobility measured in mouse myoblasts under the same conditions (16). By tracking the movement of many hundreds of individual eGFP-PH12 molecules,

we obtained an estimate of the diffusion coefficient from a plot of MSD (mean squared displacement) against time lag between measurements (Δt) [where $D_{\text{lat}} = \text{MSD}/(4\Delta t)$] (Fig. 5a). Furthermore, by studying the movement of individual fluorophores, we can test if the behaviour of the population is homogeneous. We expect the distribution of estimated individual diffusion coefficients to be similar to a Maxwell–Boltzmann (or Gamma) distribution (16, 17) (see Fig. 5b). In the data set presented here, we find that the diffusive behaviour does not deviate greatly from this simple homogeneous diffusive model. However, one should note that the raw data sets contain individual molecules that appear stationary during the observation period, while others show very rapid motion (see Fig. 5b inset). This apparent variation in mobility is explained by the statistics of thermal motion and demonstrates the importance of collecting large data sets and not focusing attention on what appear to be “interesting” rare events at either extremes of the distribution.

The second type of information that can be obtained from analysis of diffusional paths is whether individual molecules diffuse in a homogeneous fashion over all time scales. The issue here is not whether there is variability between molecules but whether individual molecules behave in a non-ideal manner (e.g., MSD is no longer directly proportional to time). Anomalous diffusion can be caused by spatial heterogeneities such as cytoskeletal networks, lipid rafts, or protein crowding. By calculating the MSD over all possible pairs of positions (separated by all possible time lags) (see Fig. 5a for details), one can test if the gradient (hence diffusion coefficient) is constant or if it “bends over” or shows inflexions at longer sample times. In the experiment presented here, we find that the gradient of the MSD versus dT plot is well fitted by a straight line, so diffusive motion is adequately described by a simple random walk over the maximum measured time and length scales (see Note 11).

The average mobility of individual eGFP-PH12 molecules was $0.191 \mu\text{m}^2/\text{s}$, $N_{\text{obj}}=3,165$ (Fig. 5b) which was very close to the estimate obtained from the gradient of the MSD versus dT graph ($0.193 \mu\text{m}^2/\text{s}$) (straight line on Fig. 5a). There is also a significant fraction (19%) of immobile objects (objects with $D_{\text{lat}} < 0.02 \mu\text{m}^2/\text{s}$) (see Note 12) shown on Fig. 5b, and some dot-like trajectories can be seen on Fig. 5b inset. It is difficult to judge the mechanism of immobilization of some molecules but other researchers also report the presence of unexpectedly large numbers of immobile objects (18) within the population of freely diffusing molecules. This fraction can be easily partitioned from the main population because of significant differences in their mobility (Fig. 5b).

Finally, we studied a full-length myosin-6-eGFP construct (19) expressed in mouse 3T3 fibroblasts and human endothelial cells (HUVECs) (Fig. 6a, b). We found that its mobility differs from

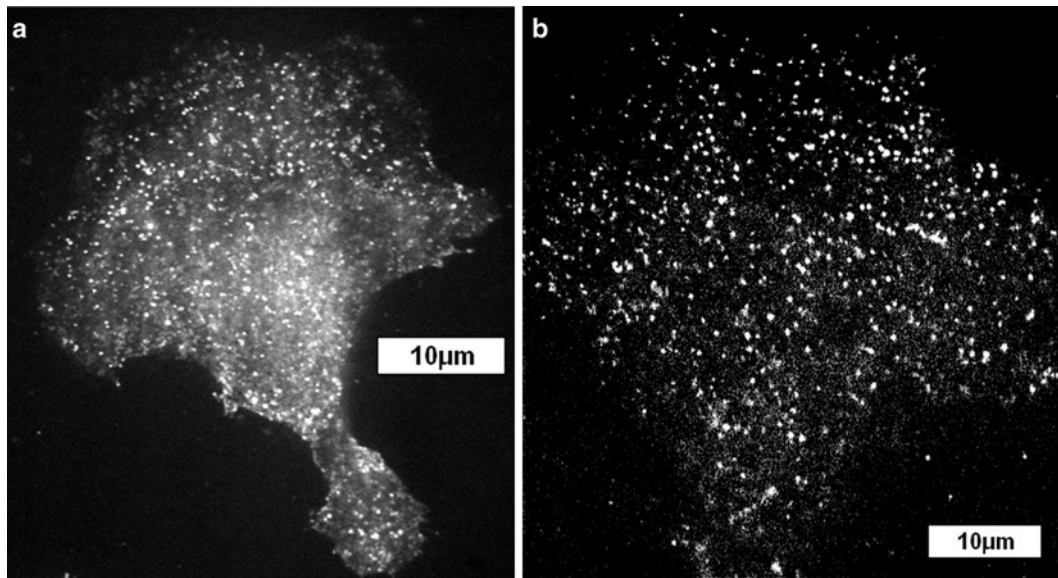


Fig. 6. Images of myosin-6 molecules (eGFP chimera) bound to plasma membrane of live eukaryotic cells (TIRFM imaging). (a) Mouse (3T3) fibroblast. (b) Endothelial cell (HUVEC).

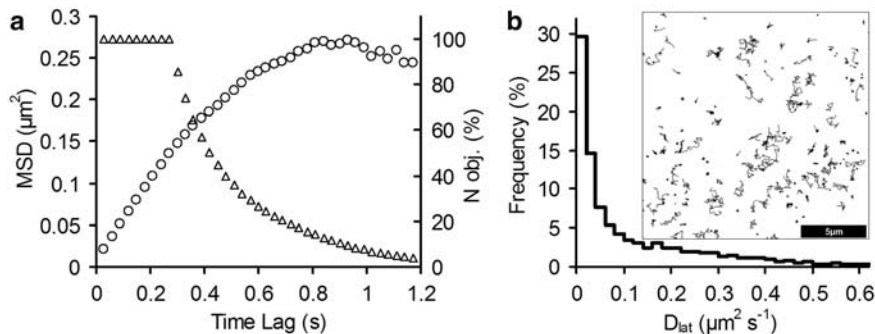


Fig. 7. Myosin-6 mobility in endothelial cells. (a) 8498 single-molecule trajectories from five cells were used to build the MSD-dT plot (circles). The triangles show the number of trajectories (right Y axis) that contribute to MSD calculations at a given time lag. (b) Distribution of mobility of individual eGFP-Myosin-6 molecules. Averaged $D_{\text{lat}} = 0.124 \mu\text{m}^2 \text{s}^{-1}$. Inset – Trajectories of eGFP-Myosin-6 molecules on the plasma membrane of a HUVEC. A number of objects have very limited mobility (dot-like trajectories) and the shape of their distribution is quite different from the Gamma distribution characteristic of freely moving molecules.

the simple random walk found above using eGFP-tagged PH domains.

The mobility of myosin-6 is less (average $D_{\text{lat}} = 0.129 \mu\text{m}^2 \text{s}^{-1}$, $N_{\text{obj}} = 8,498$) than the eGFP-tagged PH domains. Furthermore, the distribution of D_{lat} values measured for many individual molecules was very different from the Gamma distribution (Fig. 7b) that is characteristic of freely diffusing objects (Fig. 5b). Instead, the distribution was better approximated by a single exponential function with significant fraction of molecules (~30%) having $D_{\text{lat}} < 0.02 \mu\text{m}^2 \text{s}^{-1}$. The slope of MSD-dT plot (Fig. 7a) was

reduced at longer time intervals also suggesting some abnormalities in movement pattern.

When we investigated individual trajectories of eGFP-myosin-6 molecules, we noticed that besides immobile and mobile molecules, some mobile molecules stopped moving for a short period of time and then resumed moving again (Fig. 8a–e). Transient binding to an immobile element of the cell probably causes this type of movement, which we term transient confinement (or stalling) (see Note 13) (20). Trajectories that exhibit stalling behaviour can be detected by analysing the immediate velocity of tracked objects (dotted line on Fig. 8a–e). When a molecule binds to an anchor (e.g. actin filaments or transmembrane anchoring proteins), its X and Y coordinates do not change with time, and its velocity (first derivative of distance) drops close to zero (see Note 14). This simple criterion can be used to identify stalled periods during a

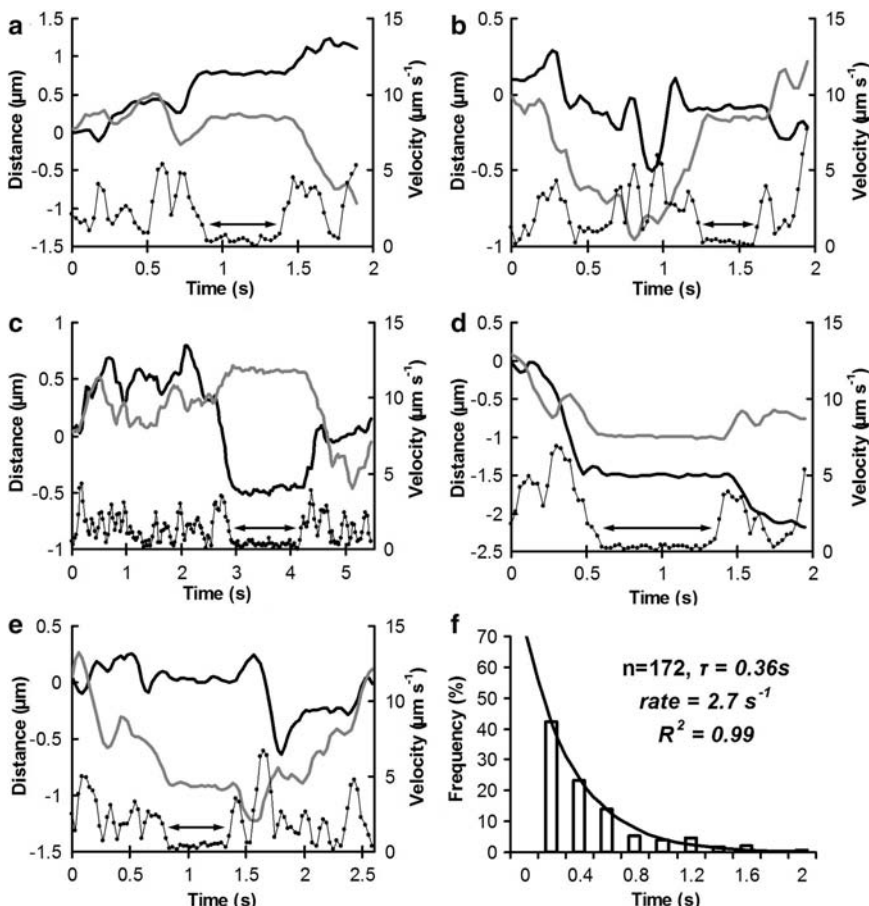


Fig. 8. Trajectories of individual myosin-6 molecules moving at plasma membrane of cultured endothelial cells used to study myosin-6 dissociation from substrata. (a–e) Individual trajectories black line – X , grey line – Y coordinates, black dotted line object's velocity (right Y axis) (Periods of immobilisation marked by arrows). (f) Distribution of “stop” times for myosin-6. Exponential function fit (black line) gives “off” rate $\approx 2.7 \text{ s}^{-1}$.

trajectory (20). This allows the immobile lifetime to be measured and hence the dissociation rate from the anchoring structure. We found that the periods of immobility for myosin-6 molecules have an exponential distribution (Fig. 8f). An exponential fit to this data gave a dissociation rate of 2.7 s^{-1} .

4. Notes

1. Peristaltic pumps should not be used for direct infusion into the imaging chamber because pressure oscillations will affect coverslip Z position and lead to focus oscillations and drift.
2. Single-molecule measurements, especially XY position measurements with nanometer accuracy, are severely affected by mechanical vibration; therefore, air fans and other similar equipment should be tested for its affect on XY measurements. It is also practical to enclose laser paths to isolate it from airflow fluctuations which could increase illumination fluctuations.
3. The beam divergence will increase if the beam angle is increased.
4. It is better to use “laser-grade” lenses in the illumination path to keep beam shape and divergence close to its theoretical limit.
5. If the refractive index for the protractor is not the same as for coverslip used for imaging, then Snell’s law should be used to correct the angle measured by protractor: $\sin(i)/\sin(r) = n_2/n_1$ (where i is incident angle, r is refracted angle, and n_1 and n_2 are refractive indices).
6. If a multi-wavelength gas laser is used for illumination, then a narrow band-pass excitation filter should be used to block residual emission of other wavelengths that may seriously affect imaging if these wavelengths are close to those of the emission spectra.
7. Detailed histograms of filter optical densities can be obtained from the web sites of leading filters/mirrors manufacturers: <http://www.omegafilters.com>, <http://www.chroma.com>, <http://www.semrock.com>.
8. Intensified and EMCCD cameras amplify the signal so that one detected photon generates many electrons (counts) registered by camera (depending on camera gain). Therefore, the actual number of detected photons per molecule per frame is much smaller than the number of counts per molecule per frame reported by the camera. This is important to note because the precision of tracking depends on square root of the number of detected photons (not counts).
9. The same camera should be used for all measurements and the level of illumination should not be saturating.

10. It is good practice to compare single-molecule live-cell imaging data with imaging “in vitro” using the same fluorophore because it provides information about the fluorescence intensity of single fluorophores and their photobleaching rate in the same imaging conditions.
11. The number of short trajectories is always high compare to long ones (Fig. 5a, triangles) because it is difficult to track the same object in crowded conditions, and because single fluorophores often bleach during the imaging interval. Therefore, there is always a higher amount of data for short time intervals (short trajectories), and the plot of MSD (mean square deviation) versus time (T) is noisier for longer intervals (Fig. 5a) due to lack of data.
12. Live cells have a high level of background fluorescence, which affects tracking results; thus, even immobile objects will show some residual level of mobility as a result of noise.
13. Some molecules remain bound to “anchors” during the whole period of tracking, which is limited by GFP bleaching. These “immobile” molecules give rise to the immobile fraction in the distribution (Fig. 7b).
14. There is some probability that freely diffusing molecules slow down (“stop”) for short periods of time (1–2 imaging intervals in our conditions). This can arise from the stochastic nature of single-molecule movements (random walk). But the probability of long periods of immobility is very low. Therefore, if we select objects that show long “stops” (>5–7 frames in our conditions), we can exclude accidental “stopping” events from the analysis.

Acknowledgments

The authors would like to thank Dr. Tom Cater and Laura Knipe (National Institute for Medical Research, London, UK) for cell culture support. T.A. Nenasheva was supported by Physiological Society (London) junior fellowship.

References

1. Sellers, J. R. (2000) Myosins: a diverse superfamily. *Biochim. Biophys. Acta* **17**, 3–22.
2. Oliver, T. S., Berg, J. S., and Cheney, R. E. (1999) Tails of unconventional myosins. *Cellular and Molecular Life Sciences* **56**, 243–257.
3. Peckham, M and Knight, P.J. (2009) When a predicted coiled coil is really a single alpha helix, in myosins and other proteins. *Soft Matter* **5**, 2493–2503.
4. Berg, J. S., and Cheney, R. E. (2002) Myosin-X is an unconventional myosin that undergoes intrafilopodial motility. *Nat. Cell Biol.* **4**, 246–250.
5. Axelrod, D. (1992) Total Internal Reflection Fluorescence. *Plenum Press, New York*.

6. Mashanov, G. I., Tacon, D., Knight, A. E., Peckham, M., and Molloy, J. E. (2003) Visualizing single molecules inside living cells using total internal reflection fluorescence microscopy. *Methods* **29**, 142–152.
7. Mashanov, G. I., Tacon, D., Peckham, M., and Molloy, J. E. (2004) The spatial and temporal dynamics of pleckstrin homology domain binding at the plasma membrane measured by imaging single molecules in live mouse myoblasts. *J. Biol. Chem.* **279**, 15274–15280.
8. Yanagida, T., Ishii, Y. (2003) Stochastic processes in nano-biomachines revealed by single molecule detection *BioSystems* **71**, 233–244
9. Mashanov, G. I., and Molloy, J. E. (2007) Automatic detection of single fluorophores in live cells. *Biophys. J.* **92**, 2199–2211.
10. Hern, J. A., Baig, A. H., Mashanov, G. I., Birdsall, B., Corrie, J. E. T., et al. (2010) Formation and dissociation of M₁ muscarinic receptor dimers seen by total internal reflection fluorescence imaging of single molecules. *PNAS* **107**, 2693–2698.
11. Friedman, L.J., Chung J., and Gelles, J. (2006) Viewing dynamic assembly of molecular complexes by multi-wavelength single-molecule fluorescence. *Biophys. J.* **91**, 1023–1031.
12. Kubitscheck, U., Kuckmann, O., Kues, T., and Peters, R. (2000) Imaging and tracking of single GFP molecules in solution. *Biophys. J.* **78**, 2170–2179.
13. Thompson, R.E., Larson, D.R., and Webb, W. W. (2002) Precise nanometer localization analysis for individual fluorescent probes. *Biophys. J.* **82**, 2775–2783.
14. Pierce, D. W., Hom-Booher N., Vale R. D. (1997) Imaging individual green fluorescent proteins. *Nature* **388**, 338.
15. Sako, Y., Minoghchi, S., and Yanagida, T. (2000) Single-molecule imaging of EGFR signalling on the surface of living cells. *Nat. Cell Biol.* **2**, 168–172.
16. Mashanov, G. I., Nenasheva, T. A., and Molloy, J. E. (2006) Cell biochemistry studied by single-molecule imaging. *Biochem. Soc. Trans.* **34**, 983–988.
17. Saxton, M. J. (1997) Single-Particle Tracking: The Distribution of Diffusion Coefficients. *Biophys. J.* **72**, 1744–1753.
18. Douglass, A. D., and Vale, R. D. (2005) Single-molecule microscopy reveals plasma membrane microdomains created by protein-protein networks that exclude or trap signalling molecules in T-cells. *Cell* **121**, 937–950.
19. Belyantseva, I. A., Boger, E.T., Naz, S., Frolenkov, G. I., Sellers, J, R, Ahmed, Z,M, et al. (2005) Myosin-XVa is required for tip localization of whirlin and differential elongation of hair-cell stereocilia. *Nat. Cell Biol.* **7**, 148–157.
20. Mashanov, G. I., Nobles, M., Harmer, S. C., Molloy, J. E., and Tinker, A. (2010) Direct observation of individual KCNQ1 potassium channels reveals their distinctive diffusive behavior. *J. Biol. Chem.* **285**, 3664–3675.

Chapter 10

Single-Molecule Measurements Using Microneedles

Toshio Yanagida, Yoshiharu Ishii, and Akihiko Ishijima

Abstract

Myosin is both an enzyme and a molecular motor that hydrolyzes ATP and interacts with actin filaments for force generation. Manipulation techniques with microneedles and laser traps have recently been developed to capture and manipulate the actomyosin interaction for the purpose of revealing the mechanics of this system. Combined with single-molecule imaging techniques, the coupling between chemical processes (ATP hydrolysis) and mechanical processes (myosin force generation) has been directly determined. In this chapter, we describe these two manipulation techniques, especially microneedle method, in detail.

Key words: Microneedle, Single-molecule manipulation, Laser trap, Myosin, Mechanochemical coupling, Single-molecule imaging

1. Introduction

Molecular motors such as myosins or kinesins convert the chemical energy released from ATP hydrolysis into mechanical work to perform their function, which include muscle contraction, cellular motility, and intracellular transport (1). The recent development of single-molecule detection techniques including single-molecule manipulation and imaging techniques has allowed elementary molecular motor mechanical processes to be monitored at unprecedented spatial resolutions (2).

Manipulation techniques have been developed to capture and manipulate very fragile biomolecules of nanometer size in aqueous solution without damaging them. These techniques have been used for allowing biomolecules to interact in specific arrangement for observation and measuring forces exerted on biomolecules. Regarding actomyosin, single actin filaments have been manipulated using glass microneedle or laser trap methods to allow for myosin step movement and force generation to be measured at the

single-molecule level (3–5). Single myosin molecules have also been captured by a cantilever attached to the tip of a microneedle for manipulation, which has enabled the details of the step movement during ATP hydrolysis to be observed (6, 7). By combining with the visualization of ATP turnover, which was allowed by single-molecule fluorescence imaging (8, 9), the timing of the chemical input and mechanical output of myosin has been directly compared at the single-molecule level (10). Below, we describe two manipulation methods used for these observations.

1.1. Manipulation Techniques

The microneedle technique involves attaching it to a biomolecule (11). First, very thin glass needles are made by pulling heated glass rods. The obtained microneedles are used to attach biomolecules at their tip. Once attached, the biomolecules can be manipulated without compromising their structure or function.

The microneedle is flexible such that it deflects when an external force is applied through the attached biomolecule (Fig. 1).

A restoring force pulls the microneedle back to its original position. The deflection of the microneedle ceases when the restoring force balances the externally applied force. Thus, the attached biomolecules behave as they attach to a spring. Therefore, the force applied to the biomolecule can be measured from the displacement of the microneedle tip if the spring constant of the microneedle is known.

The laser trap is another popular method that manipulates biomolecules by using the force generated from a laser beam (12). This technique takes advantage of the fact that small dielectric beads can be trapped at the focal point of a focused laser (Fig. 2). When focused laser light passes the beads, the light is diffracted at the beads' surface to change the momentum of the laser's photon.

The force caused by the momentum change pulls the beads toward the focal point. The handler can adjust the focal point by manipulating the laser, which in turn moves the trapped beads. Because biomolecules themselves are too small to be trapped directly, they are bound to the trapped beads. When the trapped beads are pulled by an external force, the trap force pulls the beads back to the original focal point, creating an effect analogous to the microneedle. Thus, the laser trap too can be used for force measurements (13, 14).

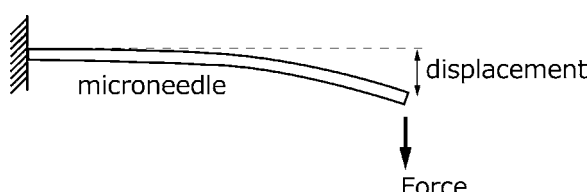


Fig. 1. Microneedle and bending motion. Glass microneedles attached to biomolecules bends when an external force is applied, which is used for force measurements.

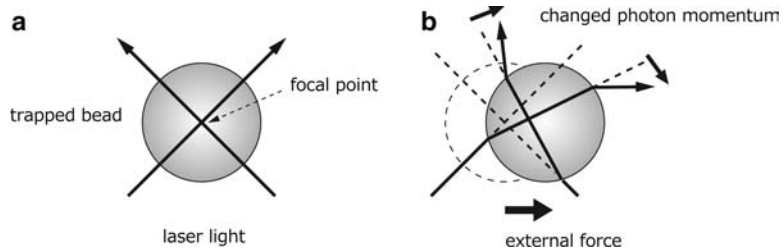


Fig. 2. Laser trapping. **(a)** Dielectric particle such as a bead is trapped to a focal point of a focused laser. **(b)** When a bead is displaced from the focal point, trapping force toward the focal point, which is created by change in photon momentum of laser beams, is exerted on the bead pulling back to the focal position.

Table 1
Comparison of microneedle and laser trap methods

	Microneedle	Laser trap
User-friendliness	Needs to handle one needle at a time Needles are fragile and difficult to handle	Easy to prepare bead solution
Time resolution	Short stiff needles needed for better time resolution. Fast events may be observed by slowing reaction frequency	Laser trap time resolution is generally better than for microneedle method
Optics	No special optics required	Powerful IR laser is required Possible interference with other optical systems on the microscope
Stiffness	Depends on thickness of a microneedle	Depends on laser intensity
Target rotation	No rotational freedom of an object attached to a microneedle	Hard to control rotation of a bead in a trap

Advantages and disadvantages of the two methods are compared in Table 1.

2. Materials

2.1. Custom-Made Materials

1. Thin glass needle, ~0.3 µm in diameter (see Note 1).
2. Scanning probe: A ZnO whisker crystal is attached to the tip of the thin glass microneedle to capture single myosin molecules (6, 7) (see Note 2).
3. Fluorescently labeled ATP (15, 16) (see Note 3).
4. One-headed myosin–myosin rod cofilaments (17) (see Note 4).

2.2. Chemicals and Solutions

1. Tetramethylrhodamine-labeled phalloidin (Molecular Probes).
2. Assay Buffer: 25 mM KCl, 5 mM MgCl₂, 20 mM HEPES-KOH, pH 7.6.
3. Low-salt buffer: 1 mM CaCl₂, 1 mM ATP, 2 mM HEPES buffer, pH 7.4.
4. An oxygen scavenging system: 4.5 mg/ml Glucose, 36 µg/ml Catalase, 216 µg/ml glucose oxidase, 0.1% v/v β-mercaptoethanol.

2.3. Instruments

1. A glass electrode puller (Narishige, PD-5) for microneedles preparation. Use binocular microscope (e.g., Olympus SZH-10) to control the process.
2. An inverted fluorescence microscope (TE2000, Nikon) on a vibration-free table (TDI-189LA, HELTZ). The stage is manipulated by a three-axis manipulator (MP-285, SUTTER INSTRUMENT).
3. Micromanipulator (Narishige WR88) and piezo-acutuator (Micro-kinetics Corp.. CTC-6094-5) used to manipulate a microneedle.
4. Tips of microneedles and microbeads are illuminated with infrared light originated from a halogen lamp (Philips, model 13512, 12 V, 50 W).
5. A He-Ne laser (05-LHP-925, MELLES GRIOT; $\lambda = 632.8$ nm) used to excite Cy5 dyes and a frequency-doubled Nd:YAG laser (COMPASS 315 M-100, COHERENT; $\lambda = 532$ nm) used to excite Cy3 dyes.
6. CCD camera (CCD1, MC681SPD-R0B0, Texas Instruments), coupled to an image intensifier (I.I.) (II, C8600, Hamamatsu Photonics) used to capture fluorescent images of myosin and actin filaments ($\lambda_{em} = 670$ nm).
7. An avalanche photodiode (APD, SPCM-AQR-16, Perkin Elmer optoelectronics) is used for a higher sampling rate and for quantitative analysis of the fluorescence intensity.
8. Two optical traps are generated by an infrared YAG laser (T10-8S, Spectraphysics, CA; $\lambda = 1,064$ nm).
9. A quadrant photodiode detector (QPD, S994-13, Hamamatsu Photonics).

3. Methods

3.1. Stiffness of Glass Microneedles

The stiffness of a glass microneedle can be calibrated by measuring the deflection caused when a steel wire with known weight is placed on it. We use very thin steel wire with a density of 3.8 mg/m.

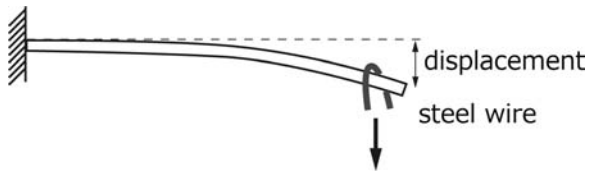


Fig. 3. Stiffness determination for standard microneedles. Stiffness is calibrated for standard microneedle using U-shaped steel wire of known weight.

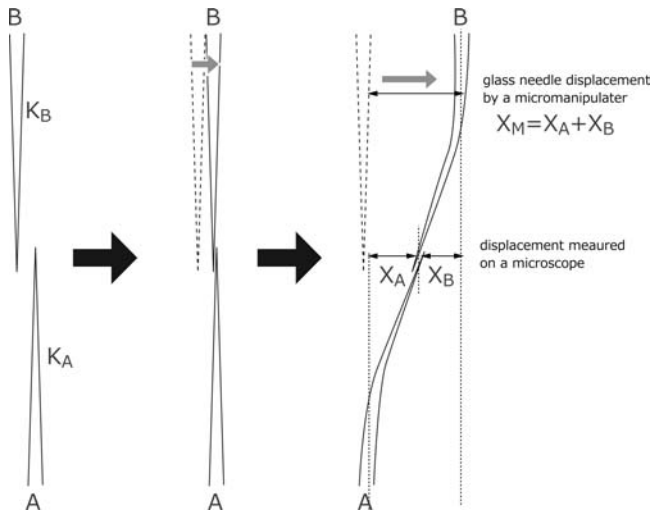


Fig. 4. Cross-calibration for microneedles. Stiffness of microneedle is calibrated using a standard microneedle. Ratio of displacement is determined by the ratio of two microneedle stiffness.

1. Cut a steel wire to less than 1 mm in length and measure its length precisely using a microscope. Calculate its weight using density formula.
2. Bend the short steel wire into a U shape using tweezers.
3. The microneedle of interest attached to micromanipulator is placed horizontally under a microscope. A second stiff glass microneedle is placed at an angle to the first microneedle.
4. Using the stiff microneedle, the U-shaped steel wire is hung onto the first microneedle (Fig. 3).
The displacement of the tip of the microneedle is used to determine the stiffness.
5. This procedure is repeated several times with different steel wires. The average is defined as the stiffness.
This microneedle is considered the standard and is used to determine the stiffness of subsequent microneedles.
6. For this, the subsequent microneedle and standard microneedle are attached to micromanipulators on opposite ends of a horizontal plane under a microscope and brought together until the two tips contact (Fig. 4).

7. At this point, the microneedles are further pushed together causing one to bend. The displacement of the two needles depends on their ratio stiffness.

$$K_A / K_B = (X_M - X_A) / X_A$$

where K_A and K_B are stiffness of the fixed needle, A, and moving needle, B, respectively. X_M and X_A are the displacements of the manipulator and the tip of needle A, respectively. Since the stiffness of one of the microneedles is known, we can estimate the stiffness of the other microneedle.

To accurately determine the stiffness, we require $K_A/K_B < 3$. To prepare microneedles of various stiffnesses, one needs various standard microneedles of various stiffnesses. We have several “parent” standard needles and about ten “child” standard needles. “Grandchild” needles are used for our experiments.

3.2. Stiffness Determination from Thermal Variation

The position of a microneedle varies thermally with time due to random collisions with surrounding water molecules (Fig. 5).

The position varies around an equilibrium point, the distribution of which is represented by a Gauss distribution. Because the magnitude of the variation is related to the stiffness of the micro-needle, it can be used to determine the stiffness.

1. Record the position of the tip of microneedle with time. Or take the displacement vs. time data before or after the force measurements.
2. According to the equipartition law, the magnitude of the thermal variation is related to the stiffness,

$$K \langle x^2 \rangle / 2 = k_B T / 2$$

where x is the displacement from the equilibrium point, k_B is Boltzmann coefficient, and T is absolute temperature, and $\langle \rangle$

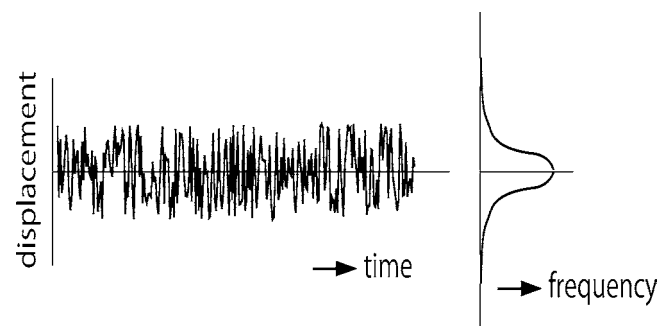


Fig. 5. Thermal variation of displacement with time. The displacement varies with time due to thermal variation. Shown at right is a distribution of displacement obtained from the time record.

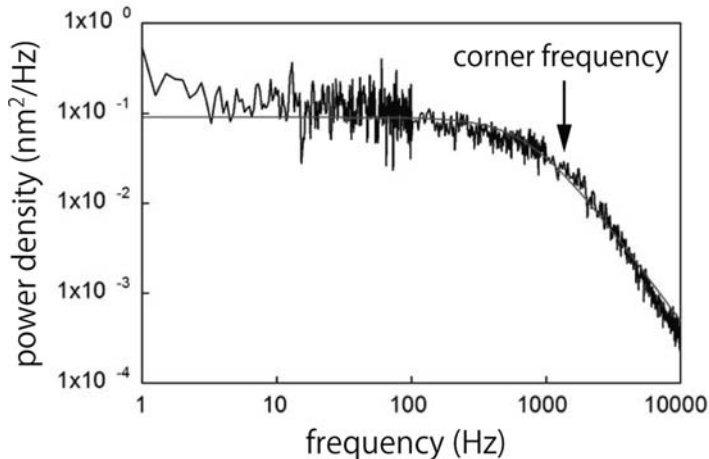


Fig. 6. Power spectrum of thermally varied displacement. Power spectrum is calculated from thermally varied displacement record. Corner frequency is estimated to calculate stiffness of microneedles or beads.

represents an average over time. The thermal variation increases inversely with the microneedle flexibility.

- Estimate $\langle x^2 \rangle$ from the data. At room temperature, $k_B T$ is 4.14 pN nm. For example, the stiffness is ~1 pN/nm when the mean square distance is 2 nm, 0.1 pN/nm when the mean square distance is 6.4 nm, and 0.01 pN/nm when the mean square distance is 20 nm.

This also applies to laser trap measurements. The position of a laser-trapped bead thermally varies with time depending on the stiffness of the trap. Therefore, the stiffness of the trap can be determined from the thermal variation of the beads.

Thermal variation includes various modes of frequency. The power spectrum for thermal variation of microneedles or laser-trapped beads has also been used to determine stiffness (Fig. 6).

The corner frequency, f_C , is the frequency at which the power density is half that at 0 Hz and can be described as a function of stiffness and the friction coefficient ζ ,

$$f_C = K / (2\pi\zeta)$$

3.3. Nanometry

The displacement of a myosin step is of nanometer order. The resolution of an optical microscope is limited by the diffraction limit of light, which is about a half wavelength, or a few hundred nanometers. However, this limitation is on separation of two points under a microscope and less of a concern when observing position changes, which should be measurable to an accuracy of less than

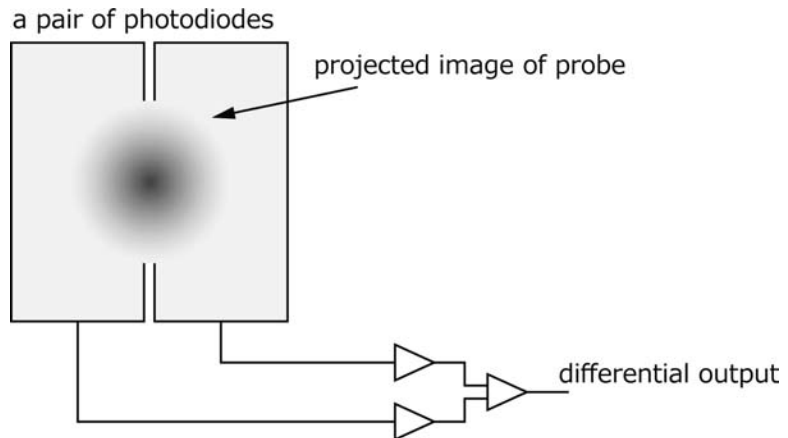


Fig. 7. Nanometry measurements. Signals from a tip of microneedle or a bead (*circle*) is projected onto a pair of photodiode. Differential output depends on displacement.

the diffraction limit. Therefore, in theory, the displacement of the tip of a microneedle or of a bead in a laser trap can be determined with nanometer accuracy. Experimentally, nanometer accuracy has been accomplished by using a set of photodiodes. Imaging a microneedle or beads is accomplished by projecting signals from the microneedles or beads onto a set of two or four photodiodes in which differential output is recorded (Fig. 7).

In the case of two photodiodes, the differential output is recorded as the probe displacement changes in one dimension.

1. To increase contrast, attach a nickel particle of 1–2 μm in diameter to the tip of needle with epoxy resin.
2. Adjust the position of the signals from a microneedle or beads on the center of the two photodiodes. When the signals are on the center, the current from the two photodiodes are equal.
3. The displacement of the microneedle in the nanometer range is calibrated. Measure the differential output signals when the photodiode pair is moved from 0.025 to 15 μm with the needle fixed. The photodiode pair is moved by a piezo actuator in the range of <1 μm and by a micromanipulator in the range of >1 μm .
4. Measure the displacement by reading the differential output signals.

Two-dimension displacements can be measured similarly by using a set of four photodiodes.

Figure 8 shows a theoretical simulation for the output versus displacement.

The output increases linearly with displacement while the displacement is less than half the radius of the image, but deviates from linearity when the image displaces beyond this limit.

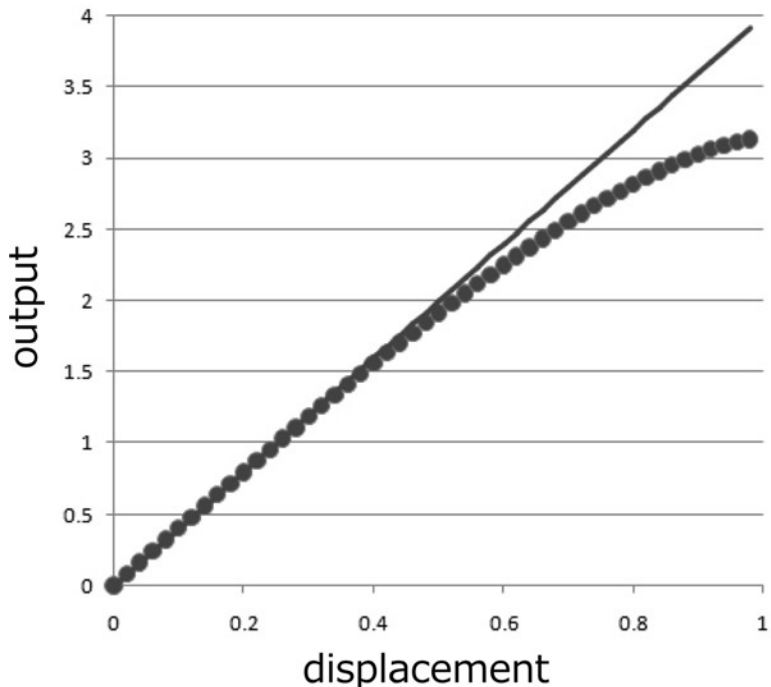


Fig. 8. Simulation for output of a photodiode detector versus displacement. Output signals of a pair of two photodiodes are simulated as a function of displacement. The output signals increase linearly and deviate from linearity as displacement increases.

3.4. Manipulation of Actin Filaments

Actin filaments are fluorescently labeled by attaching tetramethylrhodamine labeled-phalloidin, which keeps the filamentous form stable for observation (18, 19).

1. Actin in low-salt buffer is mixed with tetramethylrhodamine-labeled phalloidin at the molar ratio of 1:1. Actin is polymerized to F-actin by adding 0.1 M KCl and 2 mM MgCl₂.
2. To manipulate the filaments, a microneedle mounted onto a micromanipulator is treated with silicon and coated with monomeric myosin or NEM-treated myosin. It is also possible to attach an actin filament via streptavidin–biotin system.
3. Actin filaments are then attached to the microneedles by monitoring fluorescent actin filaments under a microscope.

3.5. Physical Properties of Actin Filaments

Using actin filaments captured by a microneedle, mechanical properties of actin filaments can be measured. For example, we can measure tensile force of actin filaments.

1. Fluorescently labeled actin filaments disperse in solution. Each end is captured to a myosin-coated microneedle (3). The two microneedles are mounted on oppositely placed micromanipulators under a fluorescence microscope. One microneedle is

very flexible and used to measure force, while the other is stiff and used to pull the filament.

2. Pull the stiff microneedle away from the flexible microneedle, while the flexible microneedle is fixed. The flexible micro-needle bends when the actin filament is pulled (Fig. 9). The flexible microneedle bends more as the stiff microneedle is pulled more.
3. Finally, the actin filament breaks. The force immediately before this moment is recorded as the tensile strength of the filament. Knowing the stiffness of the flexible microneedle and the displacement of the bend enables one to estimate the force applied.

3.6. Force Generated by Interacting with Myosin

Next, measure the force exerted on actin filaments caused by interaction with myosin molecules. It has been demonstrated that fluorescently labeled actin filaments move along myosin molecules on a coverslip in the presence of ATP. To visualize this motion, one can coat the surface of a coverslip with myosin and then inject a solution containing fluorescent actin filaments and ATP (20, 21). The force caused by this interaction can be measured by attaching a glass microneedle to an actin filament using described above in vitro motility assay.

1. Cover the chemical etched glass in SIGMACOTE®. Allow the treated glass to air-dry in a fume hood. Rinse the glass surface with MilliQ water.
2. Flow BSA solution (10 mg/ml in AB) into the chamber, incubate for 2 min in a moist box, and wash using 100 µl assay buffer.
3. Flow myosin in assay buffer into the chamber, incubate for 5 min, and wash using 1 ml of assay buffer.
4. Flow assay buffer containing an oxygen scavenging system to reduce photobleaching.
5. One end of the actin filament is attached to the flexible microneedle while the other is attached to the myosin-coated coverslip.
6. In the presence of ATP, the actin filament moves as a result of interacting with myosin, bending the microneedle. Thus, the displacement of the tip of the microneedle monitors the displacement of the actin filament.

In the in vitro motility assay, many myosin molecules are simultaneously involved in displacing a single actin filament. Instead of coating a coverslip with myosin molecules coated at random orientation, myosin molecules in the filament are used.

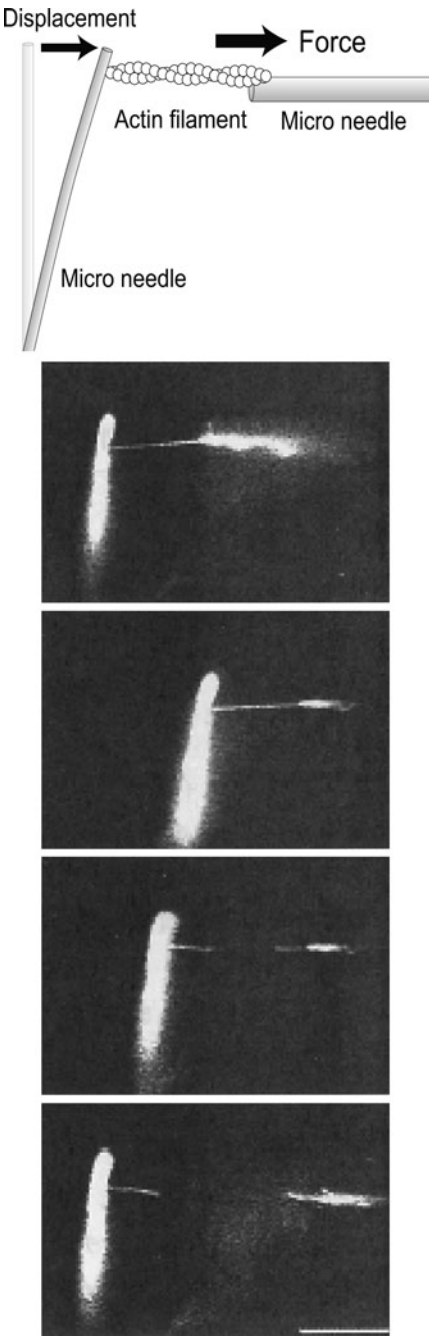


Fig. 9. Manipulation of an actin filament and measurement of its tensile force. An actin filament fluorescently labeled is manipulated by flexible and stiff microneedle (left and right needles, respectively) at both ends and pulled by the stiff needle until actin filament is broken. The force that breaks the bond between actin monomers in the filament is estimated.

1. One-headed myosin–myosin rod cofilament is coated onto a coverslip. To visualize cofilament, fluorescently labeled myosin rods are included.
2. Fluorescence actin filament is attached to a flexible microneedle and a coverslip.
3. Let the actin filament to interact with one-headed myosin–myosin rod cofilament in the presence of ATP.

In these circumstances, myosin molecules are organized in one direction along the filament. We can control the orientation between myosin and actin filament. Another advantage of this system is that it is possible to reduce the number of myosin heads on the filament, even to a single myosin head if a one-headed myosin–myosin rod cofilament is used. Thus, we can measure the interaction of an actin filament with a single myosin molecule using a cofilament of one-headed-myosin with myosin rods.

3.7. Manipulation of Single Myosin Molecules

A scanning probe consisting of a streptavidin-coated, biotinylated ZnO whisker crystal at the tip of a glass microneedle is used to manipulate single myosin molecules (see Note 5).

1. Myosin S1 (which constitutes the myosin head or motor domain) is fluorescently labeled with Cy3 to allow us to confirm single-molecule attachment to the scanning probe.
2. Myosin S1 is first attached to fluorescent actin bundles in the absence of ATP.
3. The scanning probe is then brought to the fluorescent actin bundles to enable contact with a myosin S1 molecule. The bundles are placed perpendicular to the probe to ensure that the myosin heads interact with actin filaments at right angles.
4. In order to count the number of the myosin S1 molecules captured by the probe, the Cy3 fluorescence intensity and its photobleaching is observed under illumination at 532 nm. It is important to know how many myosin molecules are captured at the tip of the scanning probe to interpret the results. The fluorescence intensity can be compared to that from single Cy3-labeled myosin S1 attached to a glass surface. The fluorescence from a single molecule drops to the baseline in a single stepwise manner after being illuminated for a certain time, a phenomenon known as photobleaching. Therefore, it is possible to count the number of S1 molecules attached to the scanning probe by counting the number of steps in the photo-bleaching process.
5. Move the stage and see whether the fluorescent spot moves with the stage or not. This is to check whether the observed fluorescence spots are from myosin bound to the probe or the stage. Unlike fluorescence spots from molecules bound to

stage, those bound to the probe do not move when the stage moves.

6. The displacement of the tip of the scanning probe is recorded in the presence of ATP.

3.8. Laser Trapping

An actin filament is captured by applying two laser traps, one at each end where a bead is attached via a biotin–streptavidin system.

1. The two laser traps are generated by dividing a laser beam of an infrared YAG laser ($\lambda = 1,064$ nm) into two beams. The position of one beam is fixed. The position of the other is adjusted by two orthogonal Galvano scanners controlled by a computer.
2. The force caused by a myosin head interacting with the filament is determined by measuring the displacement of the second bead from the trap center. The beads are illuminated with infrared light from a halogen lamp and a band path filter.

3.9. Coupling Between ATP Hydrolysis and Myosin Mechanical Events

3.9.1. Force Measurement

Cy5-dye-labeled single actin filaments and one-headed myosin–myosin rod cofilaments, which consist of a one-headed myosin and myosin rod, can be observed under epifluorescence optics equipped with a He–Ne laser and an image intensifier coupled CCD camera (see Notes 6 and 7).

1. A single actin filament is captured and suspended in solution with dual optical traps by using a YAG laser.
2. The actin filament is suspended taut and brought into contact with a single one-headed myosin molecule from a myosin–myosin rod cofilament bound to the surface of a rectangular pedestal (~7 μm wide and ~1 μm high) on a glass slide. The force and displacement caused by the single myosin head are determined by measuring the displacement of the bead, which can reach nanometric accuracy.

3.9.2. Measurement of ATP Turnovers

Individual ATP hydrolysis cycles by single one-headed myosin molecules can be measured by directly observing the association–dissociation events of the fluorescent analog 2'-O-, 3'-O-Cy3-EDA-ATP (Cy3-ATP) (9). Cy3-ATP is excited by the evanescent field generated by prism-type total internal reflection fluorescence microscopy (TIRFM).

1. The laser beam is incident on the interface between a fused silica coverslip (high reflective index) and the aqueous solution (low reflective index) at an angle greater than the critical angle for total internal reflection.
2. This produces an evanescent field into the solution from the surface of the slide glass with a 1/e penetration depth of approximately 150 nm. To measure the ATP association and

dissociation events, 10–25 nM Cy3-ATP is applied to the solution. At this concentration range, the background fluorescence originated from free Cy3-ATP in solution is sufficiently low to observe Cy3-ATP and Cy3-ADP fluorescent spots bound to the myosin head.

3. Because the affinity of myosin for ATP ($\sim 10^{-11}$ M $^{-1}$) is much greater than that of ADP ($\sim 10^{-6}$ M $^{-1}$), the Cy3-nucleotide association–dissociation events should correspond to individual ATP turnover events (see Notes 8 and 9).

4. Notes

1. A thin glass needle, ~ 0.3 μm in diameter, is made from a thick glass rod, ~ 1 mm in diameter. A glass pipette puller is used to heat the middle of the glass rod and to pull the ends of the rod to separate them at the middle. The glass microneedle can then be used for manipulation if it is sufficiently stiff or for mechanical measurements if it is sufficiently flexible. Accounting for the fact that the needle is a cylinder, the stiffness of the microneedle is determined by its thickness and length:

$$K = 3E\pi r^4 / 4L^3$$

where K is stiffness, L is the length of the cylinder, and r is the radius of the crosssection. E is Young's modulus, 7.1×10^{10} Nm 2 for glass. It should be noted that the stiffness varies with the fourth power of the radius and inversely with the third power of the length. For example, a glass microneedle of 1 mm in length with a radius of 0.5 μm has a stiffness of 0.167 pN/nm, which can be used for both manipulation and mechanical measurements. The stiffness of microneedles can be measured experimentally (see Subheading 3.1).

2. The ZnO whisker crystal has a tetrapod-like structure with legs typically 5–10 μm in length and ~ 15 nm in tip radius, and the curvature radius of the crystal is small enough to contact a single myosin molecule. To attach myosin, the ZnO whisker crystal is first amino-silanized and then biotinylated. The biotinylated ZnO whisker crystal is attached to the tip of the thin glass microneedle with epoxy resin such that one of the legs points downward (use a micromanipulator and a binocular microscope).
3. Synthesis of fluorescently labeled ATP: EDA-ATP (2'-O-, 3'-O-[*N*-[2-aminoethyl]carbamoyl]-ATP), the precursor of Cy3-ATP (2'-O-, 3'-O-Cy3-EDA-ATP), is synthesized and purified according to the methods of Jameson and Eccleston (15).

Cy3-ATP is synthesized from EDA-ATP and Cy3-NHS-ester (GE Healthcare Life Sciences). Following the purification using an FPLC anion exchange chromatography on DEAE cellulose column (DE52, Whatman), the isomers of Cy3-ATP (2'-O- and 3'-O-Cy3-EDA-ATP) are then separated by a following HPLC reverse phase chromatography on Novapack C18 (16). The purity should be greater than 99%, determined by HPLC reverse phase chromatography based on Oiwa's method.

4. One-headed myosin–myosin rod cofilaments have been used as a tool to attach single myosin molecules in known orientations onto a glass surface without damaging the myosin, as would be the case if it was directly attached (17). To form copolymerized filaments, the salt concentration of the solution containing a mixture of one-headed myosin and myosin rods is decreased from 0.6 M to 0.15 M by dialysis. To visualize the cofilament, 1% of the rod population is Cy5-labeled. A low ratio of one-headed myosin to myosin rod (1:1,000) ensures that only one or two myosin heads on average is present in one cofilament of 5–8 μm in length. The number of one-headed myosin molecules in the cofilament can be counted by observing the fluorescence of the Cy3-ATP molecules bound to the heads of the cofilament.
5. Manipulation by microneedles. The microneedle method has been used to manipulate and measure the force generated by an actin filament. Generally speaking, this method is less popular than the laser trap method, mainly because more handling skill is required. Although both techniques can be used for the same experiments, only the microneedle technique has revealed the substeps taken by a single motor molecule such as myosin (22–24). This may be because the reaction process is significantly slowed in the microneedle method. When observing the movement of a myosin head, one must consider how the arrangement between the protein and the scanning probe and the degrees of freedom of motion affect the results. In the microneedle system, the motion of the myosin heads is restricted to mimic their behavior in muscle (7). Therefore, these results are more likely to represent how a single myosin head operates in muscle.
6. Direct determination of coupling between enzyme input and output signals. Myosin is an enzyme as well as a molecular motor. The energy released from ATP hydrolysis is used for force generation. Therefore, it is important to know the coupling between ATP hydrolysis and mechanical events of myosin. However, it is difficult to determine the coupling and timing between two events experimentally. In the case of substeps of myosin, it has been tested if the interval between the steps depends on ATP concentration. The substeps caused by Brownian movement are defined as steps of which interval

is independent of ATP concentration, while the steps coupled with ATP hydrolysis is dependent on ATP concentration. Simultaneous measurements of chemical and mechanical events at the single-molecule level have directly determined the coupling. Single-molecule measurements have provided the opportunity to measure and compare these two parameters simultaneously from the same molecule.

7. From biochemical and physiological myosin studies, it has been suggested that force generation is associated with the release of phosphate in which the interaction between myosin and actin changes from a weak binding state to a strong binding state during the ATP hydrolysis cycle (25). However, no direct experimental evidence has yet been obtained. In our previous paper, it has been reported that the dissociation of myosin from actin filaments occurs at the same time as the binding of ATP to myosin, but that the timing of the force generation varies after the dissociation of ADP (10). In relation to the biochemical data, more measurements are needed to interpret these results, meaning further improvement of the microneedle technique is required.
8. Photobleaching. Because both the fluorescence signals for Cy3 photobleaching and dissociation from a nucleotide declines suddenly, it is difficult to distinguish the two. It is important to know photobleaching rate in the measurement system. Photobleaching rate must be slow enough to observe the dissociation event at the laser power sufficient to observe single fluorophores.
9. Fluorescence background. When the concentration of Cy3-ATP increases to more than 100 nM, the fluorescent spots become obscured because of the increased background fluorescence due to free Cy3-ATP molecules in solution. However, this concentration range is not physiological and is less than the K_m values for almost all myosin types and many other enzymes. In some cases, Cy3 conjugation reduces the affinity of ATP for myosin. To measure ATP turnover under the physiological conditions, unmodified ATP is added in addition to Cy3-ATP. It is possible to monitor the timing of the reactions when observing the timing of mechanical events.

References

1. Schliwa, M. (ed) (2002) Molecular motors. *Wiley-vch, Germany*.
2. Yanagida, T., Ishii Y., (ed) (2007) Single molecule dynamics in life science. *Wiley-vch, Germany*.
3. Kishino, A., Yanagida, T. (1988) Force measurements by micromanipulation of a single actin filament by glass needles. *Nature* **334**, 74–76.
4. Ishijima, A., Doi, T., Sakurada, K., et al. (1991) Sub-picowatt force fluctuations of actomyosin in vitro. *Nature* **352**, 301–306.
5. Ishijima, A., Harada, Y., Kojima, H., et al. (1994) Single-Molecule Analysis of the Actomyosin Motor Using Nano-Manipulation. *Biochem. Biophys. Res. Commun.* **199**, 1057–1063.

6. Kitamura, K., Tokunaga, M., Iwane, A.H., et al. (1999) A single myosin head moves along an actin filament with regular steps of 5.3 nanometres. *Nature* **39**, 129–134.
7. Kitamura, K., Tokunaga, M., Esaki, S., et al. (2005) Mechanism of muscle contraction based on stochastic properties of single actomyosin motors observed in vitro. *Biophysics* **1**, 1–19.
8. Funatsu, T., Harada, Y., Tokunaga, M., et al. (1995) Imaging of single fluorescent molecules and individual ATP turnovers by single myosin molecules in aqueous solution. *Nature* **374**, 555–559.
9. Tokunaga, M., Kitamura, K., Saito, K., et al. (1997) Single molecule imaging of fluorophores and enzymatic reactions achieved by objective type total internal reflection fluorescence microscopy. *Biochem. Biophys. Res. Commun.* **235**, 47–53.
10. Ishijima, A., Kojima, H., Funatsu, T., et al. (1998) Simultaneous Observation of Individual ATPase and Mechanical Events by a Single Myosin Molecule during Interaction with Actin. *Cell* **92**, 161–171.
11. Kamimura, S., Takahashi, K. (1981) Direct measurement of the force of microtubule sliding in flagella. *Nature* **293**, 566–568.
12. Ashkin, A., Dziedzic, J.M. (1985) Observation of radiation-pressure trapping of particles by alternating light beams. *Phys. Rev. Lett.* **54**, 1245–1248.
13. Finer, J.T., Simmons, R.M., Spudich, J.A. (1994) Single myosin mechanics: piconewton forces and nanometre steps. *Nature* **368**, 113–119.
14. Molloy, J.E., Burns, J.E., Kendrick-Jones, J., et al. (1995) Movement and force produced by a single myosin head. *Nature* **378**, 209–212.
15. Jameson, D.M., Eccleston, J.F., (1997) Fluorescent nucleotide analogs: synthesis and applications. *Methods Enzymol.* **278**, 363–390.
16. Oiwa, K., Eccleston, J.F., Anson, M., et al. (2000) Comparative single-molecule and ensemble myosin enzymology: Sulfoindocyanine ATP and ADP derivatives. *Biophys. J.* **78**, 3048–71.
17. Tanaka, H., Ishijima, A., Honda, M., et al. (1998) Orientation dependence of displacements by a single one-headed myosin relative to the actin filament. *Biophys. J.* **75**, 1886–1894.
18. Wulf, E., Deboben, A., Bautz, F.A., et al. (1979) Fluorescent phallotoxin, a tool for the visualization of cellular actin. *Proc. Natl. Acad. Sci. USA* **76**, 4498–4502.
19. Yanagida, T., Nakase, M., Nishiyama, K., et al. (1984) Direct observation of motion of single F-actin filaments in the presence of myosin. *Nature* **307**, 58–60.
20. Kron, S.J., Spudich, J.A. (1986) Fluorescent actin filaments move on myosin fixed to a glass surface. *Proc. Natl. Acad. Sci. USA* **83**, 6272–6276.
21. Harada, Y., Noguchi, A., Kishino, A., et al. (1987) Sliding movement of single actin filaments on one-headed myosin filaments. *Nature* **326**, 805–808.
22. Steffen, W., Smith, D., Simmons, R., et al. (2001) Mapping the actin filament with myosin. *Proc. Natl. Acad. Sci. USA* **98**, 4949–54.
23. Ruff, C., Furch, M., Brenner, B., et al. (2001) Single-molecule tracking of myosins with genetically engineered amplifier domains. *Nature Struct. Biol.* **8**, 226–229.
24. Capitanio, M., Canepari, M., Cacciafesta, P., et al. (2006) Two independent mechanical events in the interaction cycle of skeletal muscle myosin with actin. *Proc. Natl. Acad. Sci.* **103**, 87–92.
25. Lynm, R.W., Taylor, E.W. (1971) Mechanism of adenosine triphosphate hydrolysis by actomyosin. *Biochemistry* **10**, 4617–4624.

Chapter 11

Fluorescent Nucleoside Triphosphates for Single-Molecule Enzymology

Christopher P. Toseland and Martin R. Webb

Abstract

The interconversion of nucleoside triphosphate (NTP) and diphosphate occurs in some of the most important cellular reactions. It is catalyzed by diverse classes of enzymes, such as nucleoside triphosphatases, kinases, and ATP synthases. Triphosphatases include helicases, myosins, and G-proteins, as well as many other energy-transducing enzymes. The transfer of phosphate by kinases is involved in many metabolic pathways and in control of enzyme activity through protein phosphorylation. To understand the processes catalyzed by these enzymes, it is important to measure the kinetics of individual elementary steps and conformation changes. Fluorescent nucleotides can directly report on the binding and release steps, and conformational changes associated with these processes. In single-molecule studies, fluorescent nucleotides can allow their role to be explored by following precisely the temporal and spatial changes in the bound nucleotide. Here, the selection of fluorophores and nucleotide modifications are discussed and methods are described to prepare ATP analogs with examples of two alternate fluorophores, diethylaminocoumarin and Cy3.

Key words: Fluorescent nucleotides, ATP, GTP, Motor proteins, TIRF microscopy

1. Introduction

The conversions of ATP to ADP and GTP to GDP are mediated by a wide range of enzymes. These include motor proteins such as myosins, helicases, and kinesins, along with proteins from signaling pathways, such as kinases and G-proteins. With respect to many motor proteins, the energy from the ATP hydrolysis is coupled to changes in protein conformation, and/or protein–track interactions, enabling functions such as muscle contraction, DNA unwinding, and modulation of protein–protein interactions.

Fluorescence nucleotides are widely applied to investigate solution kinetics of such triphosphatases and kinases. For example, they are used to measure the kinetics of individual steps in the enzymic

reaction (binding, hydrolysis, product release, and associated structural changes) and to understand fully how such activities are coupled to the protein function. In such measurements, a change in the fluorescence properties is required to give a signal associated with the process of interest. Most often, this change is in intensity, but other properties such as anisotropy are also used. Importantly, significant fluorescence changes are more important in this type of use than overall fluorophore brightness. In addition, fluorophore photobleaching is usually not a major problem, as light sources can be of lower intensity than those for single-molecule visualization, described below.

The use of fluorescent nucleotides in single-molecule assays has increased over the past 15 years, and this has been especially driven by the study of motor proteins, in which there is a precise relationship between movement and nucleotide hydrolysis. Total internal reflection fluorescence microscopy (TIRFM) is readily used to visualize individual fluorescent ATP and ADP molecules allowing the measurements of ATP turnovers by single myosin molecules (1–4). For such measurements, a bright, photostable, fluorophore is a major factor: the light sources must be intense to get sufficient photons emitted from single complexes. More recently, single-molecule fluorescence measurements have been combined with translocation measurements to show the coupling between ATPase activity and translocation along actin (4). TIRFM selectively excites molecules within 100–200 nm of the surface, dramatically reducing the background fluorescence from unbound fluorophores in the bulk solution. This improvement in the signal-to-noise ratio allows detection of individual fluorescent ATP molecules, when bound to surface-attached proteins. However, the possibility of further improvement in the signal-to-noise ratio, through a fluorescence intensity increase on protein binding, could improve either the spatial or temporal, resolution of measurements. This chapter considers only the use of fluorescence intensity measurements of a single fluorophore on the nucleotide. However, developments such as spFRET (single-particle Förster Resonance Energy Transfer) (5) has clear potential to extend the applications of fluorescent nucleotides.

In this chapter, the selection of the fluorophores and types of nucleotide modifications are discussed. Two example syntheses, purifications, and characterizations are described that result in fluorescent adducts, differing both in the type of fluorophore and in the linkage between the fluorophore and nucleotide. The structures of the two adducts are shown in Fig. 1.

1.1. Selection of the Labeling Position

Fluorescent adenine and guanine nucleotides have been widely used to report upon binding, protein release and structural changes (6–11). Fluorophores are sensitive probes, easily used at submicro-molar concentrations, and can have properties that report rapidly, even on small perturbations in the region of the fluorophore. Thus, ATP and analogs have been modified with fluorophores at several

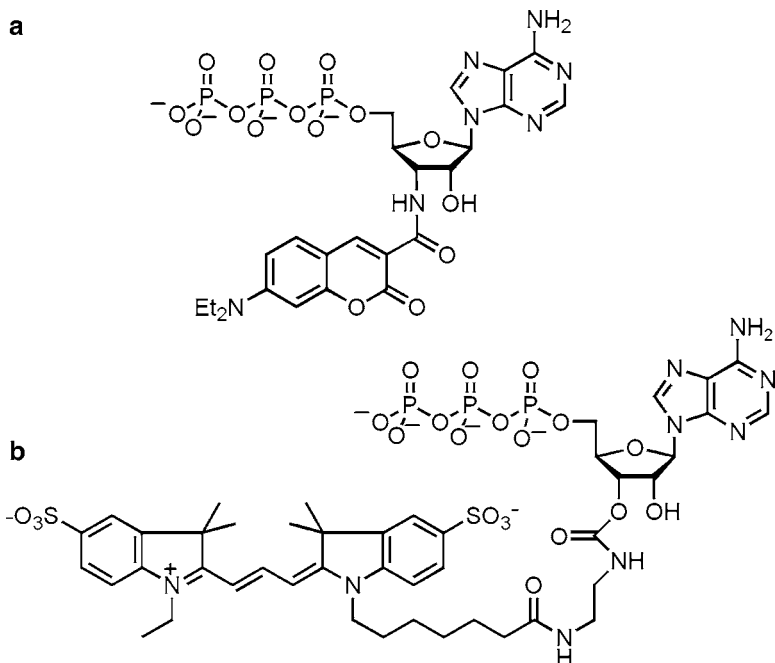


Fig. 1. Fluorescent nucleotide analogs. (a) Deac-aminoATP and (b) Cy3-edaATP.

locations in the molecular structure and the range of modifications has been reviewed (12, 13). The choice of attachment site is important, both to get a fluorophore in a position to report but also to modify the parent nucleotide without significant perturbation of the biochemical properties. First, the purine base can be made fluorescent either by modification or by using a fluorescent analog of the natural base, as in the case of formycin triphosphate (FTP) (8). However, such modifications may disrupt the protein–nucleotide interactions, as there is often high selectivity in the base binding site of proteins (13). The phosphate chain can also be modified, as with γ -AMNS-ATP for investigations of *Escherichia coli* RNA polymerase (14), but these modifications frequently disrupt the cleavage step by preventing correct binding of the phosphates or by blocking access to the γ -phosphate. Ribose modifications are often the most successful, whereby the analog closely mimics the activity of ATP. In many enzymes that bind GTP or ATP, the 2'- and/or 3'-hydroxyl groups of the ribose are partly exposed to the protein surface, while the base and phosphates are well buried. This allows a ribose label to sit at the entrance to the binding site and potentially report on changes in that region, with only a small effect on the binding and catalytic properties.

1.2. Selection of Fluorophore

When fluorescent analogs are to be used for microscopy, the main criteria for choices of fluorophore are high fluorescence intensity (high extinction coefficient and fluorescence quantum yield), excitation and emission maxima best suited to the excitation source,

without interference from other components in the system, and stability against photobleaching. With some fluorophores, the extinction coefficient and particularly the quantum yield can change significantly with the chemical environment of the fluorophore. Such changes can be problematic in choosing a suitable fluorophore, but if the intensity changes are monitored, then changes in intensity can be harnessed, as described below for a diethylaminocoumarin. Long-wavelength fluorophores, such as the cyanine dyes (e.g., Cy3), have good properties for fluorescence microscopy and have been used for detecting fluorescence from single molecules. Typically, fluorophores that excite at longer wavelengths are relatively large moieties with multiring structures and may have significantly hydrophobic regions. This may lead to nonspecific binding to proteins and surfaces. There are now many commercially available fluorophore-labeling reagents that give variations on quantum yield, photostability, and wavelengths. A discussion of this variety is outside the scope of this chapter. For additional information and for commercial sources of such labels as well as ATP analogs see: <http://www.invitrogen.com>, <http://www.sigmal-drich.com>, <http://www.roche-applied-science.com> and <http://www.jenabioscience.com>. Quantum dots have significant potential for future use, but their large size relative to nucleoside triphosphates is likely to make them difficult to apply generally here.

1.3. Selection of the Linker Between Nucleotide and Fluorophore

As described above, labeling at the ribose hydroxyl groups has been useful because this modification may not lead to large perturbations of the biochemical properties. However, such labeling of the hydroxyl groups leads to the formation of a mixture of 2'- and 3'-isomers, whose biochemical and fluorescent properties may differ when bound (13). This problem can be circumvented by using a parent nucleotide, in which only one hydroxyl is available for modification, for example the commercially available 2'-deoxyATP, or the synthetic 3'-amino-3'-deoxyATP (15). Alternatively, the isomers of some labeled nucleotides interconvert only very slowly and can be successfully separated by chromatography and stored as single isomers (3, 16).

As mentioned in the above section, fluorophores for fluorescence microscopy are relatively large and so may disrupt the biochemical cycle. To ameliorate this problem, several linkers are available to space the fluorophores further away from the catalytic site. Essentially, a zero-length linker is achieved by direct labeling of the amine group on the ribose ring of 3'-amino-3'-deoxyATP. Longer chemical linkers can use different lengths of diamino-n-alkanes, such as 2'(3')-O-[N-(2-aminoethyl)-carbamoyl]ATP (edaATP (17)) and 2'(3')-O-[N-(3-aminopropyl)carbamoyl]ATP (pdaATP (15)). In some cases, including Cy3, the commercially available labels include a spacer chain between the fluorophore and the reactive group used for attachment. In these cases, the

fluorophore will be positioned further away from the protein and, therefore, should not interfere significantly with the nucleotide association and catalysis. However, moving the fluorophore further away from the protein may reduce any changes to fluorescent properties on binding. All modifications may be deleterious to the enzymic activity, and therefore, it is important to assess the impact of these changes. Methods to assess these effects are described later.

1.4. Other Considerations

The requirements for the synthesis of ATP analogs vary widely. Those described here are relatively simple labeling reactions, performed under aqueous conditions, so potentially high yields can be obtained using conditions and equipment available in most laboratories. The success of the labeling depends both on the chemical reactions per se and on the properties of the fluorophore. For example, very hydrophobic groups may impair the success of a reaction that occurs perfectly well with simpler labels. The purification of the product also may depend on the physical properties of the fluorescent label. Two specific examples are described for the labeling nucleotides at the ribose ring with Cy3 and diethylaminocoumarin (Fig. 1).

The visualization of the binding of fluorescent nucleotides to proteins by light microscope has been limited by technical problems such as the nonspecific binding of the fluorescent nucleotide to the coverslip. This has limited the maximum nucleotide concentration that could be used with analogs such as 2'(3')-(Cy3-O-[*N*-(2-aminoethyl)carbamoyl])ATP (Cy3-edaATP, Fig. 1b (3)) to <100 nM. Fluorescent groups may also bind to macromolecules such as proteins, independently of the nucleotide and its binding site, and particularly if used at high concentration. A control, such as displacing the labeled with unlabeled nucleotide, will test if such nonspecific binding occurs.

The fluorescent ATP analog, (3'-(7-diethylaminocoumarin-3-carbonylamino)-3'-deoxyadenosine-5'-triphosphate (deac-amino-ATP)) (Fig. 1a) has a low quantum yield when in solution, but this increases dramatically when bound to some proteins. This generates large fluorescence changes, such as the 20-fold increase when bound to myosin Va (18). This enables a distinction between coverslip bound “background” molecules and those bound by proteins (4), which may compensate for the relatively low optimal excitation wavelength and photostability.

2. Materials

2.1. Labeling

1. 2',3'-O-(2-Aminoethyl-carbamoyl)-adenosine-5'-triphosphate (edaATP) (Jena Biosciences) (see Note 1).
2. 3'-Amino-3'-deoxyATP triethylammonium salt (aminoATP) (15).

3. Cy3 N-hydroxysuccinimide ester (NHS-ester) (GE Healthcare).
4. 7-Diethylaminocoumarin-3-carboxylic acid (Invitrogen).
5. 20 mM Sodium bicarbonate, pH 8.4.
6. Dimethylformamide (DMF).
7. Tributylamine.
8. Isobutyl chloroformate.
9. HPLC system, preferably with both absorbance and fluorescence detectors.
10. Strong anion exchange (SAX) Partisphere column (0.4×10 cm) (Whatman).
11. 0.4 M $(\text{NH}_4)_2\text{HPO}_4$ adjusted to pH 4.0 with concentrated HCl.
12. HPLC-grade Methanol.
13. HPLC-grade Acetonitrile.

2.2. Purification

1. DEAE cellulose column (2×30 cm).
2. Triethylamine (technical grade).
3. Glass distillation apparatus suitable for up to 500 ml and having ground glass joint.
4. Boiling chips.
5. Dry ice.
6. 2-L Buchner flask, with bung and plastic tubing on the side arm, connected to a glass-sinter gas bubbler.
7. Chromatography system (fraction collector, gradient maker, pump, etc.) at 4°C with absorbance and fluorescence detector, if possible.

2.3. Concentration

1. Rotary evaporator, equipped with a cold finger condenser and high-vacuum oil pump.
2. Methanol (highest grade available).
3. Isopropanol (technical grade).
4. Dry ice.

2.4. Characterization

1. Spectrophotometer.
2. HPLC system, preferably with both absorbance and fluorescence detectors.
3. Strong anion exchange (SAX) Partisphere column (0.4×10 cm) (Whatman).
4. 0.4 M $(\text{NH}_4)_2\text{HPO}_4$, pH 4 with concentrated HCl.
5. HPLC-grade methanol.
6. HPLC-grade acetonitrile.
7. Fluorescence spectrophotometer.

2.5. ATPase Assay

1. MDCC-PBP (**19**). Phosphate binding protein (A197C) from *E. coli*, labeled with (*N*-[2-(1-maleimidyl)ethyl]-7-diethylamino coumarin-3-carboxamide) (Invitrogen) (see Note 2).
2. Rhodamine-PBP (**20**). Phosphate binding protein (A17C, A197C) from *E. coli*, labeled with 6-iodoacetamidotetramethylrhodamine (see Note 2).
3. Fluorescence spectrophotometer.
4. Inorganic phosphate standard solution.

3. Methods**3.1. Synthesis of Cy3-edaATP**

This method is based on that described by Oiwa et al. (**3**) and gives mixed (2',3') isomers (Fig. **1b**).

3.1.1. Labeling

1. Mix 4 µmol Cy3 NHS-ester with 20 µmol edaATP in 20 mM sodium bicarbonate, pH 8.4, for 1 h at room temperature (see Note 3).
2. Analyze the reaction mixture using HPLC to confirm the formation of Cy3-edaATP. Equilibrate a Partisphere SAX column with 0.4 M $(\text{NH}_4)_2\text{HPO}_4$ with 20% (v/v) methanol: flow rate of 1 ml/min at room temperature (see Notes 4 and 5).
3. Add an aliquot of the reaction mixture (1–10 nmol) to 100 µL of the running buffer.
4. Inject the solution onto the column.
5. Follow the absorbance at 254 nm and fluorescence with excitation of 550 nm and emission of 570 nm. The chromatogram will show the elution of Cy3 NHS-ester, edaATP, and Cy3-edaATP, respectively (see Note 6).
6. Inject known standards of Cy3 NHS-ester and edaATP at the same concentration as the reaction mixture to identify peaks.

3.1.2. Preparation of Triethylammonium Bicarbonate Solution

1. Distil triethylamine (500 ml), discarding the first and last 10% of the distillate. Use the middle 80% of the distillate (see Note 7).
2. Add cold (4°C), distilled, deionized water to 139.4 ml distilled triethylamine to give 1 L of a 1 M solution (see Note 8).
3. In a fume hood, put dry ice in the Buchner flask, and with the solution in ice, bubble CO₂ through the solution until the pH is 7.5–7.6 (approximately 2 h) using the scintered glass bubbler. Keep the Buchner flask, containing the dry ice, raised above the solution to reduce the risk of sucking back.
4. Store triethylammonium bicarbonate (TEAB) at 4°C in a well-stoppered container. It lasts approximately 1–2 months, but the pH gradually rises with time. In this case, rebubble CO₂ through it.

3.1.3. Purification of Nucleotide

- Preequilibrate the DEAE-cellulose column with 10 mM TEAB, pH 7.6 at 1 ml/min at 4°C.
- Alter the pH of the reaction mixture to 7.6 using acid or base, reduce the conductivity by dilution in water so it is close to that of 10 mM TEAB and load onto the column.
- Wash the column with 10 mM TEAB, pH 7.6 at a flow rate of 1 ml/min until no more pink material is eluted.
- Elute the nucleotide with a linear gradient of 10–800 mM TEAB (total volume 600 ml). Follow the absorbance at 254 nm. Unreacted edaATP is eluted first followed by Cy3-edoATP (see Note 9).
- Identify the fractions containing Cy3-edoATP by measuring the absorbance at 550 nm and 260 nm.

3.1.4. Concentration

- Pool fractions containing Cy3-edoATP and remove TEAB by rotary evaporation. Use a flask with a capacity at least four times the volume of the solution.
- Fill the condenser with dry ice-isopropanol.
- Add the pooled fractions to the flask, rotate, and slowly apply the vacuum to begin evaporation. Warm the flask in a water bath at 30°C. Reduce the volume to ~5 ml. When the solution volume is reduced to 10–20%, frothing may begin (see Note 10).
- Add methanol (~10% of initial solution volume) and repeat the evaporation.
- Repeat methanol additions and evaporation three times: during this it should be possible to remove essentially all the solvent before adding more methanol. At the final stage, evaporate all of the methanol. The Cy3-edoATP will remain as a gum.
- Dissolve in <3 ml methanol and transfer to a pear flask (10 ml) and reconcentrate, with very careful application of the vacuum to avoid frothing. Finally, dissolve in water or buffer and adjust to pH ~6–7 before storing at –80°C (see Note 11).

3.1.5. Characterization

- Measure the absorbance spectra of Cy3-edoATP in 50 mM Tris-HCl, pH 7.5 between 220 and 700 nm. Taking the extinction coefficient for the Cy3 to be 150,000 M⁻¹ cm⁻¹ at 552 nm (21) and the extinction coefficient for adenosine to be 15,200 M⁻¹ cm⁻¹ at 260 nm, calculate the concentration of the nucleotide (see Note 12).
- Characterize Cy3-edoATP by HPLC using the same method as above. The major peak should be Cy3-edoATP. Check for the presence of Cy3-edoADP, edoATP, and edoADP. Determine the purity by integrating the Cy3-edoATP peak with any other peaks (see Note 13).

3. Measure the fluorescence excitation and emission spectrum of Cy3-edaATP in 50 mM Tris–HCl (pH 7.5). Typically, 1 μ M in a solution of 60 μ l will be used. Use the peak wavelength from the absorbance measurement as the excitation wavelength to measure the emission. Then, use the peak in the emission spectrum for the excitation spectrum. Add an excess of the protein of interest to the sample (e.g., 10-fold) and repeat the measurement (see Notes 14 and 15). Compare the two spectra to determine the change in fluorescence when bound to protein.

3.1.6. Generating Cy3-edaADP

1. Cy3-edaADP can be obtained by hydrolysis of Cy3-edaATP. Add the desired concentration of Cy3-edaATP (e.g., 100 μ M) to rabbit skeletal muscle myosin (1 mg/ml) in 1 mM MgCl₂, 0.2 mM dithiothreitol (DTT), and 10 mM Tris–HCl, pH 7.0. 4°C for 2 h (see Note 16).
2. Centrifuge the sample at 235,000 $\times g$ at 4°C to remove the myosin.
3. Analyze the product using HPLC, as described above.
4. Store the supernatant at –80°C.

3.2. Synthesis of Deac-aminoATP

This method is based on that described by Webb et al. (15) and gives a single product as reaction occurs only at the 3'-amine (Fig. 1a).

3.2.1. Labeling

This method requires the starting material 3'-amino-3'-deoxyATP (15).

1. Activate 7-diethylaminocoumarin-3-carboxylic acid (16.4 mg, 62.8 μ mol) by dissolving in dry DMF (1 ml), cooling it on ice, and adding tributylamine (25 μ l, 103 μ mol) and isobutyl chloroformate (10 μ l, 77 μ mol).
2. Leave the reaction mixture on ice for 50 min.
3. Add 3'-amino-3'-deoxyATP (40 μ mol, triethylammonium salt) in water (300 μ l) to the activated coumarin and stir at room temperature for 2 h.
4. Analyze the reaction mixture using HPLC to confirm the formation of deac-aminoATP. Equilibrate a Partisphere SAX column with 0.4 M (NH₄)₂HPO₄ with 5% (v/v) acetonitrile at a flow rate of 1.5 ml/min at room temperature.
5. Add an aliquot of the reaction mixture (1–10 nmol) to 100 μ l of the running buffer.
6. Inject the solution onto the column.
7. Follow the absorbance at 254 nm and fluorescence with excitation 435 nm and emission 465 nm. Elution times are approximately 1.6 min for 7-diethylaminocoumarin-3-carboxylic acid, 3.5 min for 3'-amino-3'-deoxyATP, and 13 min for deac-aminoATP (see Note 6).

3.2.2. Purification

1. The reaction mixture was purified on a DEAE-cellulose column. Equilibrate the column with 10 mM TEAB, pH 7.6 at 1 ml/min at 4°C.
2. Alter the pH of the reaction mixture to 7.6 using acid or base, reduce the conductivity by dilution in water so it is close to that of 10 mM TEAB and load on to the column.
3. Wash the column with 10 mM TEAB, pH 7.6 at a flow rate of 1 ml/min for two column volumes.
4. Elute the nucleotide with a linear gradient of 10–600 mM TEAB (total volume 1 L). Follow the absorbance at 254 nm (see Note 17). Unreacted aminoATP is eluted first followed by deac-aminoATP.

3.2.3. Concentration

The product deac-aminoATP is concentrated as described for Cy3-edaATP and stored at –80°C.

3.2.4. Characterization

1. Measure the absorbance spectra of deac-aminoATP in 50 mM Tris–HCl, pH 7.5 between 220 and 700 nm. Taking the extinction coefficient for the coumarin to be 46,800 M⁻¹ cm⁻¹ at 429 nm and for adenosine to be 15,200 M⁻¹ cm⁻¹ at 260 nm, calculate the concentrations of the nucleotide (see Note 12).
2. Characterize deac-aminoATP by HPLC using the same method as above. The major peak should be deac-aminoATP. Determine the purity by integrating the deac-aminoATP peak with any other peaks.
3. Measure the fluorescence spectra as described for Cy3-edaATP, but using the corresponding excitation and emission peaks for the coumarin (Fig. 2).
4. Follow the same procedure described for the Cy3-edaATP to generate the diphosphate.

3.3. Assess the Effects of Modifications

The method described here is for an ATPase or GTPase. This specific example uses a DNA helicase *Bacillus stearothermophilus* PcrA. The easiest method to provide an overall assessment of the effect of an ATP modification is to measure a steady-state ATPase assay. Should there be a change in the steady-state parameters (greater than 20%), then the individual steps of the ATP cycle could be investigated. It is common for the diphosphate affinity to increase with modifications to the ribose ring (9, 18, 22, 23).

It is also highly recommended that a functional activity assay is performed, such as measuring DNA unwinding by a DNA helicase or an in vitro motility assay with myosin. This is an alternate assessment of the modification effect: the label may interfere with one criterion which may not be noticeable in the other.

1. Prepare a mixture (60 µl) of 2 nM PcrA helicase, 500 nM dT₂₀ oligonucleotide and 10 µM MDCC-PBP (or 6IATR-PBP) in a

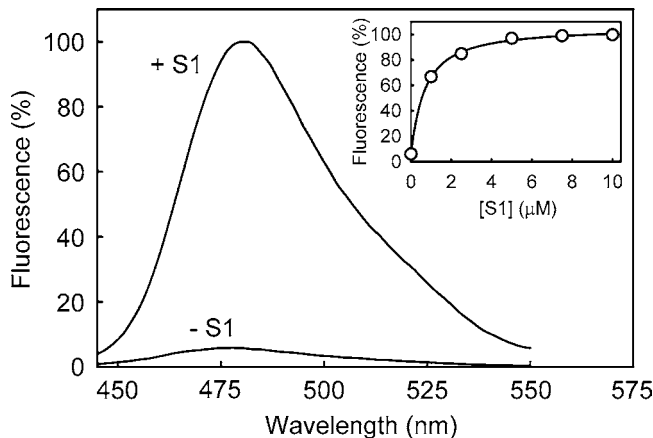


Fig. 2. Fluorescence change upon binding of deac-aminoADP to myosin S1. Excess myosin S1 was added to bind all nucleotides. Deac-aminoADP (0.3 μM) was excited at 435 nm and 10 μM S1 was added. *Inset* shows the titration of myosin S1 into a solution of deac-aminoADP. This highlights the need to saturate the nucleotide to determine the maximum fluorescence change. Myosin S1 was added to a solution of 0.1 μM nucleotide, and the fluorescence was monitored at 480 nm, with excitation at 435 nm.

buffer containing 50 mM Tris–HCl, pH 7.5, 3 mM MgCl₂ and 150 mM NaCl.

2. Record the fluorescence by exciting at 436 nm and emission at 465 nm for MDCC-PBP, or excitation 555 nm and emission 575 nm for 6IATR-PBP.
3. Add ATP at various concentrations (1 mM to 0.5 μM) (see Note 18).
4. Repeat the measurements at the same concentrations of deac-aminoATP or Cy3-edaATP (see Note 18).
5. Perform a calibration of the fluorescence signal using known concentrations of inorganic phosphate.
6. Compare the V_{\max} and K_m values for the native and modified nucleotides.

4. Notes

1. It is also possible to synthesize edaATP (3, 15, 17).
2. MDCC-PBP is available commercially from Invitrogen, but cannot be used with diethylaminocoumarin-labeled nucleotides because the fluorophores are the same. Similarly, 6IATR-PBP cannot be used if a fluorophore with similar wavelengths is present, such as Cy3 or other rhodamine.
3. Use an excess of nucleotide over Cy3 NHS-ester due to the expense of the fluorophore.

4. Filter and degas the $(\text{NH}_4)_2\text{HPO}_4$ and then add the HPLC grade methanol.
5. Alternatively, the reaction can be followed by thin-layer chromatography on silica plates (13).
6. Using the fluorescence detection is approximately 100-fold more sensitive than absorbance. If necessary, absorbance peaks can be collected, their fluorescence measured in a fluorimeter, and their full absorbance spectrum measured in a spectrometer.
7. Do not store distilled triethylamine for later use without redistillation: it decomposes on storage. It may be possible to use high-purity triethylamine without distillation, but triethylamine does form impurities on storage. The distillation ensures that only volatile components end up in the TEAB solution.
8. Triethylamine itself is only partially miscible with water: there will be two layers initially, which becomes a single solution after some CO_2 has been absorbed.
9. Alternatively, follow the fluorescence of Cy3 using an excitation of 550 nm and emission of 570 nm.
10. Apply and remove the vacuum slowly to prevent the solution splashing and frothing, and so passing into the condenser.
11. Aliquot the ATP into small amounts before freezing to avoid freeze-thaw cycles. It is advisable to check the purity of the nucleotide by HPLC periodically during long-term storage.
12. The ratio between the molar amount of the fluorophore and adenosine should be ~1. If not, there is likely to be contaminating fluorophore in the preparation.
13. Determine the limit of sensitivity for the instrument by injecting known amounts. Typically, 1% contamination should be detected; for example, if 10 nmol is injected, it should be possible to detect 0.1 nmol. It is possible that a greater amount of nucleotide will have to be injected.
14. Ideally, the addition of excess protein to the nucleotide sample would lead to the maximum potential signal change. However, this is dependent on the affinity between nucleotide and protein.
15. Unless the protein has a low hydrolysis rate constant, or the protein requires an activator, it is likely that any fluorescence change occurs due to the formation of diphosphate. The diphosphate fluorescence change should be measured independently.
16. It is also possible to begin the labeling with edaADP and repeat the same protocol as described above to produce the fluorescent diphosphate. In addition, it is possible to use other ATPases or commercially available glycerol kinase with d-glyceraldehyde (albeit that ribose-modified nucleotides are poor substrates for

this kinase) to achieve the hydrolysis of the triphosphate (24). The resulting ADP analog is purified by a desalting column (PD10) or repeating the ion-exchange chromatography.

17. Alternatively, follow the fluorescence of the diethylaminocoumarin using an excitation of 430 nm and emission of 465 nm.
18. Avoid diluting the ATP samples to low concentrations. Use 60× concentrated stocks. By adding 1 μ l of the ATP to the 60 μ l reaction mixture, the correct ATP concentration is achieved.

Acknowledgments

We would like to thank the various coworkers, who have been involved in synthesis and use of fluorescent nucleotides and are coauthors of publications cited here. We thank the Medical Research Council, UK (C.P.T. and M.R.W.) and European Molecular Biology Organization (C.P.T) for financial support.

References

1. Funatsu, T., Harada, Y., Tokunaga, M., Saito, K., and Yanagida, T. (1995) Imaging of single fluorescent molecules and individual ATP turnovers by single myosin molecules in aqueous solution. *Nature* **374**, 555–559.
2. Ishijima, A., Kojima, H., Funatsu, T., Tokunaga, M., Higuchi, H., Tanaka, H., and Yanagida, T. (1998) Simultaneous observation of individual ATPase and mechanical events by a single myosin molecule during interaction with actin. *Cell* **92**, 161–171.
3. Oiwa, K., Eccleston, J. F., Anson, M., Kikumoto, M., Davis, C. T., Reid, G. P., Ferenczi, M. A., Corrie, J. E., Yamada, A., Nakayama, H., and Trentham, D. R. (2000) Comparative single-molecule and ensemble myosin enzymology: sulfoindocyanine ATP and ADP derivatives. *Bioophys. J.* **78**, 3048–3071.
4. Sakamoto, T., Webb, M. R., Forgacs, E., White, H. D., and Sellers, J. R. (2008) Direct observation of the mechanochemical coupling in myosin Va during processive movement. *Nature* **455**, 128–132.
5. Ha, T. (2001) Single-molecule fluorescence resonance energy transfer. *Methods* **25**, 78–86.
6. Henn, A., Cao, W., Hackney, D. D., and De La Cruz, E. M. (2008) The ATPase cycle mechanism of the DEAD-box rRNA helicase, DbpA. *J. Mol. Biol.* **377**, 193–205.
7. Moore, K. J., and Lohman, T. M. (1994) Kinetic mechanism of adenine nucleotide binding to and hydrolysis by the *Escherichia coli* Rep monomer. 2. Application of a kinetic competition approach. *Biochemistry* **33**, 14565–14578.
8. Rossomando, E. F., Jahngen, J. H., and Eccleston, J. F. (1981) Formycin 5'-triphosphate, a fluorescent analog of ATP, as a substrate for adenylylate cyclase. *Proc. Natl. Acad. Sci. USA* **78**, 2278–2282.
9. Toseland, C. P., Martinez-Senac, M. M., Slatter, A. F., and Webb, M. R. (2009) The ATPase Cycle of PcrA Helicase and Its Coupling to Translocation on DNA. *J. Mol. Biol.* **392**, 1020–1032.
10. Woodward, S. K., Eccleston, J. F., and Geeves, M. A. (1991) Kinetics of the interaction of 2'(3')-O-(N-methylanthraniloyl)-ATP with myosin subfragment 1 and actomyosin subfragment 1: characterization of two acto-S1-ADP complexes. *Biochemistry* **30**, 422–430.
11. Phillips, R. A., Hunter, J. L., Eccleston, J. F., and Webb, M. R. (2003) The mechanism of Ras GTPase activation by neurofibromin. *Biochemistry* **42**, 3956–3965.
12. Cremo, C. R. (2003) Fluorescent nucleotides: synthesis and characterization. *Methods Enzymol.* **360**, 128–177.
13. Jameson, D. M., and Eccleston, J. F. (1997) Fluorescent nucleotide analogs: synthesis and applications. *Methods Enzymol.* **278**, 363–390.
14. Yarbrough, L. R., Schlageck, J. G., and Baughman, M. (1979) Synthesis and properties

- of fluorescent nucleotide substrates for DNA-dependent RNA polymerases. *J. Biol. Chem.* **254**, 12069–12073.
15. Webb, M. R., Reid, G. P., Munasinghe, V. R., and Corrie, J. E. (2004) A series of related nucleotide analogues that aids optimization of fluorescence signals in probing the mechanism of P-loop ATPases, such as actomyosin. *Biochemistry* **43**, 14463–14471.
16. Webb, M. R., and Corrie, J. E. (2001) Fluorescent coumarin-labeled nucleotides to measure ADP release from actomyosin. *Biophys. J.* **81**, 1562–1569.
17. Cremo, C. R., Neuron, J. M., and Yount, R. G. (1990) Interaction of myosin subfragment 1 with fluorescent ribose-modified nucleotides. A comparison of vanadate trapping and SH1-SH2 cross-linking. *Biochemistry* **29**, 3309–3319.
18. Forgacs, E., Cartwright, S., Kovacs, M., Sakamoto, T., Sellers, J. R., Corrie, J. E., Webb, M. R., and White, H. D. (2006) Kinetic mechanism of myosinV-S1 using a new fluorescent ATP analogue. *Biochemistry* **45**, 13035–13045.
19. Brune, M., Hunter, J. L., Howell, S. A., Martin, S. R., Hazlett, T. L., Corrie, J. E., and Webb, M. R. (1998) Mechanism of inorganic phosphate interaction with phosphate binding protein from *Escherichia coli*. *Biochemistry* **37**, 10370–10380.
20. Okoh, M. P., Hunter, J. L., Corrie, J. E., and Webb, M. R. (2006) A biosensor for inorganic phosphate using a rhodamine-labeled phosphate binding protein. *Biochemistry* **45**, 14764–14771.
21. Mujumdar, R. B., Ernst, L. A., Mujumdar, S. R., Lewis, C. J., and Waggoner, A. S. (1993) Cyanine dye labeling reagents: sulfoindocyanine succinimidyl esters. *Bioconjug. Chem.* **4**, 105–111.
22. Kurzawa-Goertz, S. E., Perreault-Micale, C. L., Trybus, K. M., Szent-Gyorgyi, A. G., and Geeves, M. A. (1998) Loop I can modulate ADP affinity, ATPase activity, and motility of different scallop myosins. Transient kinetic analysis of S1 isoforms. *Biochemistry* **37**, 7517–7525.
23. Talavera, M. A., and De La Cruz, E. M. (2005) Equilibrium and kinetic analysis of nucleotide binding to the DEAD-box RNA helicase DbpA. *Biochemistry* **44**, 959–970.
24. Webb, M. R. (1980) A method for determining the positional isotope exchange in a nucleoside triphosphate: cyclization of nucleoside triphosphate by dicyclohexylcarbodiimide. *Biochemistry* **19**, 4744–4748.

Chapter 12

Probing the Mechanics of the Complete DNA Transcription Cycle in Real-Time Using Optical Tweezers

Christoph G. Baumann and Stephen J. Cross

Abstract

RNA polymerase (RNAP) is a DNA-dependent motor protein that links ribonucleotide polymerization to force generation and DNA translocation through its active site, i.e., mechanical work. Single-molecule studies using optical tweezers have allowed researchers to probe the load-dependent ribonucleotide incorporation rate and processivity of both single-subunit viral and multisubunit prokaryotic and eukaryotic RNAPs engaged in transcription elongation. A single-molecule method is described here, which allows the complete transcription cycle (i.e., promoter binding, initiation, elongation and termination) to be followed in real-time using dual-trap optical tweezers and a unique “three-bead” geometry. This single-molecule transcription assay can be used to probe the mechanics of both stationary and moving RNAP–DNA complexes engaged in different stages of transcription.

Key words: Single molecule, Optical trapping, T7 RNA polymerase, Transcriptional initiation, Molecular motor

1. Introduction

The ability to probe the mechanics of a biomolecular motor at the single-molecule level allows the energetics, load-dependent kinetics, and processivity of individual biochemical steps to be elucidated. RNA polymerase (RNAP) is a familiar biomolecular motor, for which single-molecule studies of both single- and multisubunit species have demonstrated an ability to generate a mechanical force during ribonucleotide polymerization (1). Typically, single-molecule mechanical studies of the transcription cycle involve probing the individual stages, e.g., promoter binding, initiation, and elongation, in isolation. For example, previous single-molecule mechanical studies of *Escherichia coli* RNAP have only allowed initiation (2)

and elongation (artificially halted by ribonucleotide starvation) (3–7) to be observed in isolation from the other transcriptional stages. More recently, single-molecule studies of transcription elongation by RNAP II from *Saccharomyces cerevisiae* have been completed (8). In this chapter, a single-molecule transcription assay (SMTA) is described that allows, for the first time, direct observation of promoter binding, initiation, and processive elongation by a single RNAP molecule in real-time (9). The single-subunit RNAP from bacteriophage T7 (T7 RNAP) is used as a model system; however, this SMTA could be used for the study of a surface-immobilized multisubunit RNAP after the necessary modifications to the DNA sequence of the template.

To promote DNA binding and transcription initiation in the SMTA, a DNA molecule tethered between two optically trapped microspheres is held near a third microsphere sparsely coated with RNAP and immobilized on a coverslip surface (Fig. 1a). By driving the optical trap holding the upstream microsphere with a triangular waveform, while monitoring the bright-field image of the downstream microsphere with a four-quadrant photodiode detector (4QD), it is possible to observe the onset of promoter binding, promoter escape (productive initiation), and processive elongation by a single RNAP. When the DNA molecule is free of the surface, the oscillatory motion of the upstream optically trapped microsphere is transmitted to the downstream microsphere via DNA-mediated mechanical coupling (Fig. 1b, large amplitude regions). Interaction events (Fig. 1c, arrows) are detected as a “decoupling” of the motion of the “passive” downstream microsphere from the “driven” upstream microsphere. A histogram of the downstream microsphere positions for a typical DNA tether during the binding events shows the interactions occur within a preferred region of the DNA (± 20 nm) close to the known promoter site. A histogram of the lifetimes for the observed events is fit by a single exponential, with a decay constant of 2.9 ± 0.05 s⁻¹, corresponding to the rate constant for dissociation of the T7 RNAP–promoter DNA binary complex (k_{off}). This is in close agreement with previous bulk measurements of k_{off} (3.4–4.0 s⁻¹) for this class of T7 promoter under similar conditions (10). This implies that the observed interactions are specific and report formation of T7 RNAP- ϕ 13 promoter DNA binary complexes.

Following promoter escape, transcription elongation is observed as a movement of the downstream microsphere away from the optical trap center toward the surface-bound microsphere (Fig. 1c). The trace in Fig. 1c shows that multiple transcription events (labeled events 1 and 2) are observed with a single DNA tether. Every T7 RNAP-coated surface-bound microsphere tested has a characteristic downstream microsphere position at the beginning of each DNA interaction; thus, it is assumed that a unique single T7 RNAP molecule was probed repeatedly during each experiment. The ability to

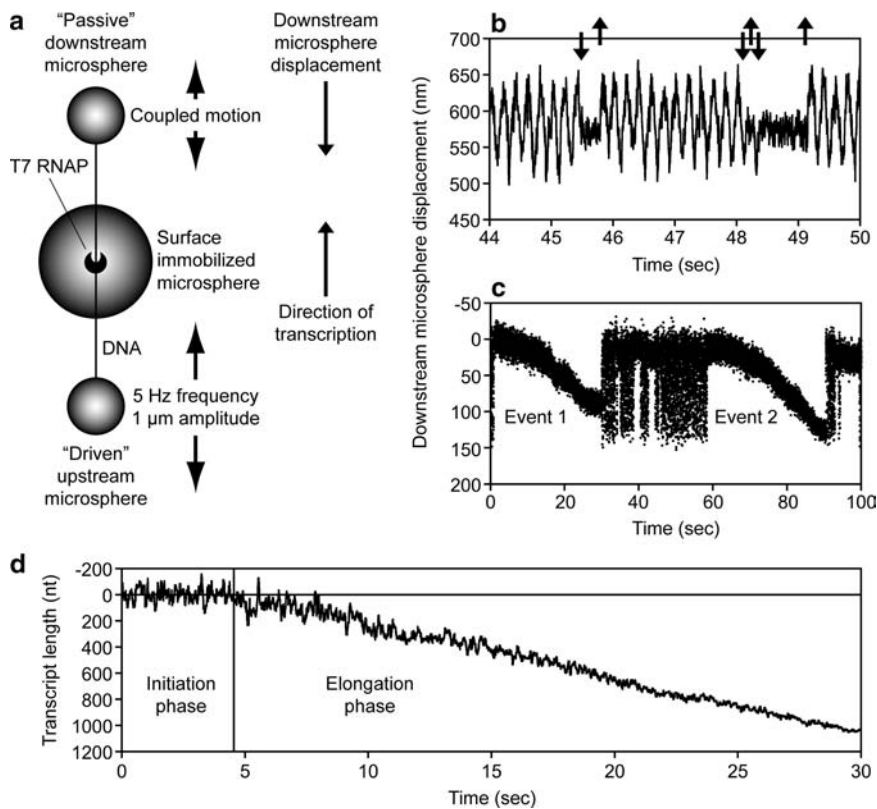


Fig. 1. Representative displacement versus time data acquired with the single-molecule transcription assay (SMTA). **(a)** A top-down, scale view of the “three-bead” geometry used for the SMTA. A DNA molecule tethered between two optically trapped microspheres is held near a third coverslip-bound microsphere sparsely coated with T7 RNAP. The optical trap holding the upstream microsphere is “driven” with a 5 Hz/1 μ m triangular waveform while monitoring the position of the “passive” downstream microsphere. **(b)** When the DNA molecule is free of the surface, the oscillatory motion of the upstream optically trapped microsphere is transmitted to the downstream microsphere via the DNA tether (large amplitude regions). DNA interactions (arrows) are observed as a “decoupling” of the motion of the passive downstream microsphere. **(c)** Transcription causes the downstream microsphere to move toward the central coverslip-bound microsphere after DNA binding. Multiple transcription events by the same T7 RNAP (see events 1 and 2) are often observed on a single DNA tether. **(d)** The displacement of the downstream microsphere observed during transcription was corrected for DNA elasticity, converted to RNA transcript length in nucleotides (nt) and median filtered (12.5 Hz). During transcription, the downstream microsphere was pulled away from the trap center leading to an increase in the force that the RNAP worked against. This is observed as a drop in positional “noise” as transcript length increases, i.e., the compliance of the DNA tether is inversely proportional to the applied force. A transcription event usually begins with a stationary initiation phase and is followed by a processive elongation phase characterized by a constant transcriptional velocity of 40–50 nt/s.

observe multiple enzymatic runs in this SMTA allows statistical analysis to be carried out on the results obtained with an individual enzyme, something that hitherto has not been possible with other SMTA. During elongation, continuous movement of the downstream microsphere was observed until either (1) the RNAP released the DNA tether in a sequence-independent manner or (2) the downstream microsphere reached the limit of the useable range of

the trap (located ~400 nm from the trap centre), thus pulling the microsphere from the trap. The velocity of processive transcription elongation was evaluated from a linear regression of the data after correction for the nonlinear elasticity of the DNA molecule (Fig. 1d). A mean transcriptional velocity of 43 ± 3.2 nucleotides/s was obtained at 22°C, which is consistent with in vitro rates of ribonucleotide incorporation (11).

After promoter binding and before processive elongation, a lag phase was observed in which the RNAP is stationary (Fig. 1d). The lifetime of this stationary complex was determined from the lag time, beginning with the DNA binding event and ending at the intersection of the fitted straight line corresponding to the elongation phase. The lag times, ranging from 1.3 to 4.6 s in the events observed, are significantly longer than the average lifetimes of the T7 RNAP–promoter DNA binary complexes ($1/k_{\text{off}} = 0.34$ s) and the short lifetime (~0.01 s) of the open complex in the presence of initiating ribonucleotides (12). It is concluded that they represent the rate-limiting transition on the pathway to the elongation complex.

2. Materials

2.1. Buffers and Special Reagents

1. 25 mM MES buffer: Dissolve 1.22 g anhydrous 2-[*N*-morpholino]ethanesulfonic acid (MES, Sigma) in water (heating to 50°C will aid dissolution) and add 31 ml of 0.1 M NaOH. Allow solution to cool and then increase the volume to 250 ml with water and check pH = 6.
2. Phosphate-buffered saline (PBS): Dissolve 8 g NaCl, 0.2 g KCl, 1.44 g Na₂HPO₄, and 0.24 g KH₂PO₄ in 800 ml of water. Adjust pH to 7.4 and increase volume to 1 L, then sterilize by autoclaving or filtering.
3. Surface-blocking buffer (SBB): 40 mM Tris–HCl, pH 8, 50 mM NaCl, 6 mM MgCl₂, 1 mg/ml acetylated-BSA and 1 mM dithiothreitol.
4. Transcription buffer (TB): 40 mM Tris–HCl, pH 8, 50 mM NaCl, 6 mM MgCl₂, and 1 mM dithiothreitol.
5. Tris–EDTA (TE) buffer: 10 mM Tris–HCl, pH 8 and 1 mM Na₂EDTA.
6. 10× TE buffer: 100 mM Tris–HCl, pH 8 and 10 mM Na₂EDTA.
7. 1 M glycine: Dissolved in PBS, pH 7.4.
8. 2% (w/v) sodium azide: Dissolved in filtered water. Handle stock solution with caution, as azide is very toxic.
9. 20 mg/ml acetylated-BSA (Sigma).

10. 1 mg/ml antidigoxigenin F_{ab} fragment (anti-DIG, Roche): Prepared in PBS, pH 7.4.
11. 1 mg/ml TRITC-BSA (tetramethylrhodamine B isothiocyanate bovine serum albumin, Sigma): Prepared in PBS, pH 7.4.
12. 1% nitrocellulose: Diluted to 0.1% (v/v) with isoamyl alcohol or acetone.

2.2. Preparation of Labeled Microspheres

1. 4% (w/v) white aldehyde-sulfate polystyrene-latex microspheres (diameters = 1.1 and 2 μm, Interfacial Dynamics Corporation).
2. 1% (w/v) streptavidin-coated polystyrene-latex microspheres (SA-MS, diameter = 1 μm, Interfacial Dynamics Corporation).
3. Mouse monoclonal anti-His₆ IgG_{2a} (antibody concentration = 1.4–2.8 μg/μl, GE Healthcare): Supplied in clarified mouse ascites fluid with 0.1% sodium azide added.
4. 1 mg/ml protein A (Sigma, from *Staphylococcus aureus*): Prepared in 25 mM MES buffer, pH 6.

2.3. Preparation of DNA Templates

1. *Bcl*I restriction endonuclease (15 U/μl, New England Biolabs, NEB).
2. *Sfi*I restriction endonuclease (20 U/μl, NEB).
3. *Stu*I restriction endonuclease (20 U/μl, NEB).
4. Terminal transferase (TdT, 20 U/μl, NEB).
5. 10 mM biotin-11-2'-deoxyuridine-5'-triphosphate (biotin-dUTP, Yorkshire Bioscience Ltd.).
6. 100 mM digoxigenin-11-2'-deoxyuridine-5'-triphosphate (DIG-dUTP, GE Healthcare).
7. 10 mM 1',2'-dideoxythymidine-5'-triphosphate (ddTTP, Roche Applied Science).
8. Bacteriophage T7 DNA (T7 DNA, Yorkshire Bioscience Ltd.): Purchased as a 500 μg/ml stock.
9. NucAway™ spin columns (Ambion).

2.4. Dual-Trap Optical Tweezers

1. These studies require an optical tweezers setup capable of generating two independent and steerable traps (13). The “three-bead” geometry allows a DNA molecule, tethered between two optically trapped microspheres, to be held in the vicinity of a RNAP immobilized on a third coverslip-bound microsphere (Fig. 2). Epifluorescence ($\lambda_{\text{ex}} = 540$ nm for TRITC) and bright-field illumination are used for imaging the microspheres with an intensified CCD and standard CCD, respectively. The bright-field image is split, enabling the image of each microsphere to be focused on a separate 4QD for high-speed position measurements. The *x* and *y* position of the microscope stage is controlled using piezo actuators (Physik Instrumente).

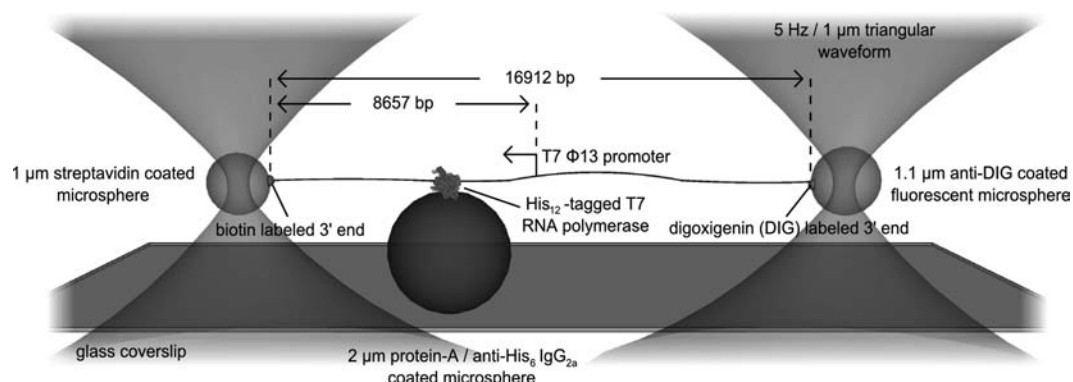


Fig. 2. "Three-bead" optical tweezers geometry used in single-molecule transcription assay (not to scale). A 16,912-bp DNA fragment containing the T7 ϕ 13 promoter near the center is tethered between optically trapped anti-digoxigenin (anti-DIG) and streptavidin (SA) coated microspheres (diameters = 1.1 and 1 μ m, respectively) and held at a relative extension of 0.7. The relative extension of the DNA tether must be maintained at this value for productive initiation by T7 RNAP to occur. The anti-DIG-coated microsphere is also labeled with fluorescent rhodamine B, thus it can be differentiated from the nonfluorescent SA-coated microsphere. This allows the upstream end of the tether to be identified using epifluorescence microscopy prior to transcription initiation. His₁₂-tagged T7 RNAP is attached via anti-His₆ IgG_{2a} to a coverslip-immobilized microsphere (diameter = 2 μ m). The anti-DIG- and SA-coated microspheres are manipulated with steerable optical traps to bring the ϕ 13 promoter and T7 RNAP into close proximity, thus permitting transcription initiation. The force exerted by the immobilized RNAP on the DNA tether during transcription is observed as movement of the downstream, nonfluorescent SA-coated microsphere.

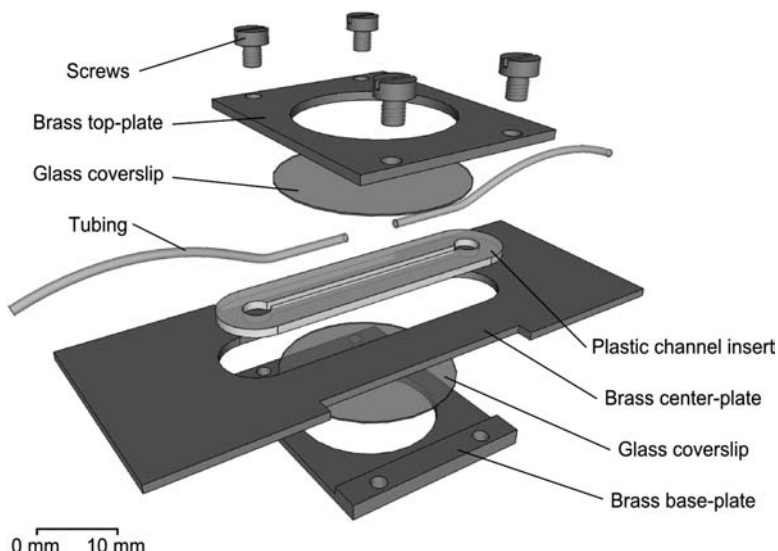


Fig. 3. Exploded diagram (approximately to scale) of the custom-built flow cell used for buffer exchange in the single-molecule transcription assay. The brass center-plate has the same dimensions as a microscope slide (26 mm \times 68 mm \times 1 mm). The plastic tubing (outside diameter = 1 mm) fits tightly into a recess in the plastic channel insert and is affixed in place with epoxy. High vacuum grease (Dow Corning) is used to provide a seal between the glass coverslips (no. 1.5, diameter = 22 mm) and the plastic channel insert. The device is secured by screws, which are tapped into the brass base-plate. The large round windows (diameter = 18 mm) in the brass top- and bottom-plates (29 mm \times 24 mm) enable the use of a bright-field condenser (*top*) and an oil-immersion 100 \times (NA 1.3) objective (*bottom*). Optical tweezers manipulation is performed in the central region between the plastic tubes.

2. Buffer exchange is done using a custom-built flow cell (Fig. 3) and a syringe pump to deliver liquids with a slow constant flow rate. A plastic syringe with a 25-gauge needle attached is connected to the inlet tubing.
3. No. 1.5 borosilicate glass coverslips (diameter = 22 mm).

3. Methods

3.1. Preparation of Microspheres Labeled with Anti-DIG and TRITC-BSA

1. The aldehyde-sulfate microspheres (diameter = 1.1 μm) are washed in the following manner: 0.6 ml 4% (w/v) aldehyde-sulfate microsphere suspension is added to 0.6 ml PBS in a BSA-coated tube (see Note 1). The microspheres are mixed by vortexing and then sonicated for 10 s to dissociate aggregated microspheres (see Note 2). The suspension is centrifuged (see Note 3) at $1,500 \times g$ for 1 min to pellet the microspheres. The supernatant is immediately removed with a micropipette and the aldehyde-sulfate microsphere pellet is resuspended in 1.2 ml PBS by vortexing (not sonication). The aldehyde-sulfate microspheres are washed two more times in this manner.
2. After the final wash, the pellet is resuspended in 935 μl PBS by vortexing. In subdued light (TRITC is a light-sensitive fluorophore), add 225 μl 1 mg/ml anti-DIG, followed by 40 μl 1 mg/ml TRITC-BSA. The solution is vortexed after adding each protein-containing solution and then incubated for 5 h at room temperature ($\sim 20^\circ\text{C}$) in a foil-wrapped tube with constant gentle mixing – a slow rotary turntable set at an angle ($= 45^\circ$ to 90°) works well.
3. After the incubation period, the solution is centrifuged at $1,500 \times g$ for 1 min to pellet the microspheres. The supernatant is immediately removed with a micropipette, and the magenta-colored microsphere pellet is resuspended in 1.2 ml 1 M glycine. At this stage, mild vortexing is used to resuspend pellet, as vigorous vortexing may shear protein off the microspheres. The suspension is incubated for 40 min at room temperature ($\sim 20^\circ\text{C}$) in a foil-wrapped tube with constant gentle mixing as above.
4. After the incubation period, the solution is centrifuged and the supernatant removed as above. The magenta-colored microsphere pellet is resuspended in 900 μl PBS (add first) and 100 μl 20 mg/ml acetylated-BSA. The solution is vortexed after adding each solution. The suspension is centrifuged and the supernatant removed as above. The TRITC-BSA/anti-DIG labeled microspheres (AD-MS) are washed twice in this manner.

5. After the final wash, the supernatant is discarded and the AD-MS pellet is resuspended in 895 μ l PBS, 100 μ l 20 mg/ml acetylated-BSA and 5 μ l 2% sodium azide (to prevent microbial growth). The ~2% (w/v) AD-MS suspension is transferred to a BSA-coated tube (see Note 1). The AD-MS are stored at 4°C in a foil-wrapped tube until needed.

3.2. Preparation of End-Labeled DNA for Single-Molecule Manipulation

DNA templates for the single-molecule experiments are prepared by digesting T7 DNA with combinations of restriction endonucleases (Fig. 4a). This yields a DNA fragment with the T7 RNAP specific ϕ 13 promoter sequence located at a variety of positions along the template (see Note 4, Fig. 4b). The following is the protocol for digesting and labeling T7 DNA to prepare a template with the ϕ 13 promoter located at a central position within a 16,912 bp fragment (contour length (L_o)=5.72 μ m):

1. The 3'-ends of T7 DNA are first blocked with ddTTP using TdT. The tailing reaction is prepared as follows: 45 μ l 500 μ g/ml T7 DNA, 6 μ l 10x restriction endonuclease buffer (NEB Buffer 4 for TdT), 6 μ l 2.5 mM CoCl₂, 2 μ l 10 mM ddTTP, and 1 μ l TdT (20 units). The reaction is mixed (see Note 5) and incubated for 2.5 h at 37°C (see Note 6). Post reaction, TdT is heat-inactivated by incubating for 20 min at 75°C.
2. The following are added to the above tailing reaction for the restriction digestion with *Sfi*I: 0.5 μ l 10 mg/ml acetylated-BSA (see Note 7) and 1 μ l *Sfi*I stock (20 units). The reaction is mixed and incubated for 12–18 h at 50°C. Post reaction, the digestion is quenched by adding 2 μ l 0.5 M EDTA. A 1- μ l aliquot is removed from the reaction for analysis by 1% agarose gel electrophoresis to check for complete DNA digestion.
3. The quenched reaction is loaded on to a NucAway™ spin column hydrated with restriction endonuclease buffer (NEB Buffer 4 with 250 μ M CoCl₂) according to the manufacturer's instructions. The column is centrifuged at 750 $\times g$ for 2 min and the eluant (~50 μ l) is transferred from the spin column to a fresh microcentrifuge tube.
4. The following are added to the above eluant for 3'-end labeling with biotin-dUTP: 10 μ l 250 μ M biotin-dUTP and 1 μ l TdT (20 units). The reaction is mixed and incubated for 1 h at 37°C. After 1 h, 2 μ l 10 mM ddTTP is added and the incubation is continued for a further 2 h to block the 3'-ends. Post reaction, TdT is heat-inactivated by incubating for 20 min at 75°C.
5. The following is added to the above tailing reaction for the restriction digestion with *Stu*I: 2 μ l *Stu*I stock (20 units). The reaction is mixed and incubated for 12–18 h at 37°C. Post reaction, the digestion is quenched by adding 2 μ l 0.5 M

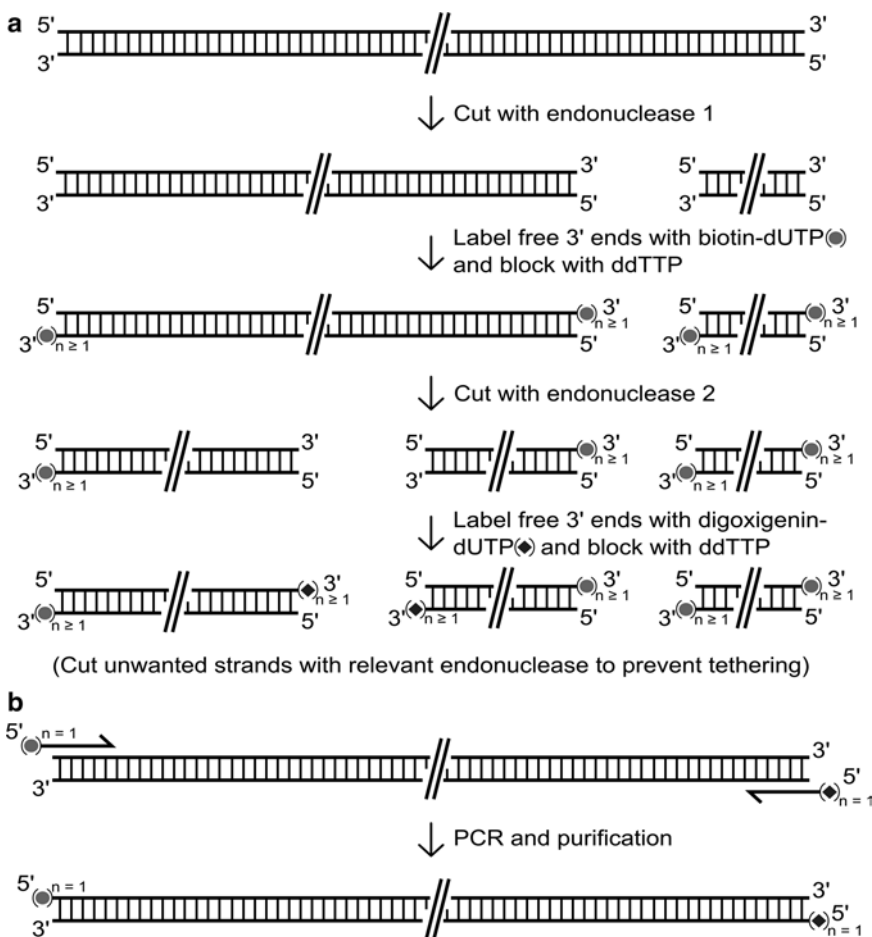


Fig. 4. Two methods for preparing the end-labeled DNA template. (a) DNA template is excised from bacteriophage T7 DNA using restriction endonucleases. Each end of the DNA template is labeled with digoxigenin- or biotin-dUTP using terminal transferase. Free 3'-ends are generated between the tailing reactions using unique restriction endonucleases. Following each tailing reaction, the 3'-ends are blocked with ddTTP to prevent double end-labeling. (b) DNA is amplified via PCR using forward and reverse primers labeled at the 5'-ends with biotin and digoxigenin, respectively (see ref. 19 for details).

EDTA. A 1- μ l aliquot is removed from the reaction for analysis by 1% agarose gel electrophoresis to check for complete DNA digestion.

6. The quenched reaction is loaded on to a NucAway™ spin column hydrated with restriction endonuclease buffer (NEB Buffer 4 with 250 μ M CoCl₂) according to the manufacturer's instructions. The column is centrifuged at 750 $\times g$ for 2 min and the eluant (~50 μ l) is transferred from the spin column to a fresh microcentrifuge tube.
7. The following are added to the above eluant for 3'-end labeling with DIG-dUTP: 10 μ l 250 μ M DIG-dUTP and 1 μ l TdT

(20 units). The reaction is mixed and incubated for 1 h at 37°C. After 1 h, 2 µl of 10 mM ddTTP is added and the incubation is continued for a further 2 h to block the 3'-ends. Post reaction, TdT is heat-inactivated by incubating for 20 min at 75°C.

8. The following is added to the above reaction for the restriction digestion with *BcI*I (see Note 8): 1.3 µl *BcI*I stock (20 units). The reaction is mixed and incubated for 24 h at 50°C. Post reaction, the digestion is quenched by adding 2 µl 0.5 M EDTA. A 1-µl aliquot is removed from the reaction for analysis by 1% agarose gel electrophoresis to check for complete DNA digestion.
9. The quenched reaction is loaded on to a NucAway™ spin column hydrated with TE according to the manufacturer's instructions. The column is centrifuged at 750×*g* for 2 min and the eluant (~50 µl) is transferred from the spin column to a fresh microcentrifuge tube. If required immediately, the labeled DNA is stored at 4°C. Long-term storage is done at -20°C.

3.3. Preparation of Microspheres Labeled with Protein A

1. The aldehyde-sulfate microspheres (diameter=2 µm) are washed in the following manner: 0.6 ml 4% (w/v) aldehyde-sulfate microsphere suspension is added to 0.6 ml 25 mM MES in a BSA-coated tube. The microspheres are mixed by vortexing for 30 s. The suspension is centrifuged at 1,500×*g* for 2 min at room temperature (~20°C) to pellet the microspheres. The supernatant is immediately removed with a micropipette and the microsphere pellet is resuspended in 1.2 ml 25 mM MES by vortexing. The microspheres are washed two more times in this manner.
2. After the final wash, the microspheres are resuspended in 700 µl 25 mM MES and mixed by vortexing for 30 s. The labeling reaction is started by adding 500 µl 1 mg/ml protein A. The suspension is mixed by gently pipetting the solution up and down with a 1 ml micropipette. The tube is incubated overnight at room temperature (~20°C) with constant gentle mixing – a slow rotary turntable set at an angle works well.
3. After the incubation period, the solution is centrifuged as above to pellet the microspheres. The supernatant is immediately removed with a micropipette and the microsphere pellet is resuspended in 1.2 ml 1 M glycine. At this stage, mild vortexing is used to resuspend the pellet, as vigorous vortexing may shear protein off the microspheres. The suspension is incubated for 40 min at room temperature (~20°C) with constant gentle mixing as above.
4. After the incubation period, the solution is centrifuged and the supernatant removed as above. The microsphere pellet is

resuspended in 900 µl PBS (add first) and 100 µl of 20 mg/ml acetylated-BSA. The solution is gently vortexed after adding each solution. The suspension is centrifuged and the supernatant removed as above. The protein A labeled microspheres (PA-MS) are washed three more times in this manner.

- After the final wash, the supernatant is discarded and the pellet is resuspended in 895 µl PBS, 100 µl 20 mg/ml acetylated-BSA, and 5 µl 2% (w/v) sodium azide (to prevent microbial growth). The ~2% (w/v) PA-MS suspension is transferred to a BSA-coated tube and stored at 4°C until needed.

3.4. Preparation of Microsphere-Immobilized T7 RNAP for the Single-Molecule Transcription Assay

T7 RNAP (with N-terminal His₁₂-tag (14)) and its site-directed mutants are purified by metal-affinity chromatography (see Note 9). The immobilization of T7 RNAP on PA-MS is done in small batches using mouse anti-His₆ IgG_{2a} (see Note 10). These batches are stored at 4°C for weeks at a time. Immobilization efficiency is quantified by analyzing aliquots of T7 RNAP-labeled PA-MS by SDS-PAGE and comparing to standards of known RNAP concentration. The activity of surface-immobilized T7 RNAP is confirmed by adding aliquots of microspheres to an in vitro transcription assay (15) – samples containing microspheres require constant gentle mixing during the assay.

- The PA-MS are washed in the following manner: 50 µl ~2% (w/v) PA-MS is added to 100 µl TB. The microspheres are mixed by gently vortexing for 30 s. The suspension is centrifuged at 1,500×g for 2 min to pellet the microspheres. The supernatant is immediately removed with a micropipette and the PA-MS pellet is resuspended in 100 µl TB by gentle vortexing. The microspheres are centrifuged and washed two more times in this manner.
- After the last wash, the PA-MS are resuspended in 50 µl TB (add first) and 4 µl mouse anti-His₆ IgG_{2a}. The solution is gently vortexed after adding each solution. The suspension is incubated for 1 h at 4°C with constant vortexing.
- After the incubation period, the supernatant is removed and the microspheres are washed three times with 100 µl TB as above.
- After the final wash, the antibody-coated PA-MS are resuspended in 200 µl TB containing 0.5 µM T7 RNAP (see Note 11) and transferred to a fresh tube. The suspension is incubated for 1 h at 4°C with constant vortexing.
- After the incubation period, the supernatant is removed and the microspheres are washed three times with 100 µl TB as above. After the final wash, the T7 RNAP-coated PA-MS (RNAP-MS, ~0.1% (w/v)) are resuspended in 1 ml TB and used in the single-molecule transcription assay or stored at 4°C until needed.

3.5. Preparation of DNA Tethered to Microspheres for Single-Molecule Experiments

1. Stock solutions of thoroughly washed microspheres are prepared fresh each day.
2. A stock solution of thoroughly washed SA-MS is prepared by adding 8 μ l 1% (w/v) SA-MS to 100 μ l TE in a microcentrifuge tube. The microsphere suspension is centrifuged at 1,000 $\times g$ for 1 min. The supernatant is immediately removed with a micropipette and the SA-MS pellet is resuspended in 100 μ l TE. The SA-MS are washed two more times in this manner.
3. After the final wash, the SA-MS pellet is resuspended in 50 μ l TE yielding a ~0.1% (w/v) microsphere suspension.
4. A mixture of end-labeled DNA and SA-MS is prepared by combining the following: 831 μ l water (see Note 12), 100 μ l 10 \times TE, 40 μ l 5 M NaCl, 25 μ l ~0.1% (w/v) SA-MS, and 4 μ l end-labeled DNA (~4.2 nM DNA chain concentration).
5. The SA-MS–DNA solution is gently mixed and incubated for at least 1 h on ice prior to use. The solution is mixed occasionally to prevent sedimentation of the microsphere suspension. Alternatively, the tube is placed at 4°C on a turntable mixer set at an angle to keep the microspheres in suspension.
6. A stock solution of thoroughly washed AD-MS is prepared by adding 10 μ l ~2% (w/v) AD-MS to 100 μ l TE in a microcentrifuge tube. The microsphere suspension is centrifuged at 1,000 $\times g$ for 1 min. The supernatant is immediately removed with a micropipette and the AD-MS pellet is resuspended in 50 μ l TE to yield a ~0.4% (w/v) solution. The AD-MS stock is stored on ice in a foil-wrapped tube (TRITC is a light-sensitive fluorophore) until needed.
7. A DNA tethering solution containing both microsphere types and the end-labeled DNA is prepared by combining the following reagents: 825 μ l water, 100 μ l 10 \times TE, 26 μ l 5 M NaCl, 50 μ l SA-MS–DNA solution (from step 5 above), and 1 μ l ~0.4% (w/v) AD-MS (from step 6 above). It is important that the NaCl concentration is maintained near 100–200 mM in the DNA tethering solution as this prevents unwanted nonspecific interactions between SA-MS and DNA. The concentration of DNA chains and microspheres is ~0.84 pM and 1–4 $\times 10^{-4}$ (w/v), respectively. This MS–DNA solution is stored on ice in a foil-wrapped tube and used immediately to form single DNA tethers. This MS–DNA tethering mixture is prepared fresh daily.

3.6. Manipulation of a Single DNA Tether Using Optical Tweezers

1. To capture a single DNA molecule between two microspheres, a custom-built flow cell is assembled (Fig. 3). The objective-side coverslip (no. 1.5) is coated with 0.1% nitrocellulose to aid immobilization of protein-coated microspheres on this surface.

2. The coverslip surface is sparsely coated with PA-MS by injecting 200 μl 4% PA-MS into the flow cell with a plastic syringe and allowing to stand for 5 min at room temperature ($\sim 20^\circ\text{C}$). A fresh syringe filled with 1 mg/ml acetylated-BSA is attached to the inlet tubing and the PA-MS solution is flushed from the flow cell with 200 μl of this solution. The acetylated-BSA solution is allowed to stand for 5 min at room temperature before the flow cell is flushed with 200 μl MS-DNA solution (from Subheading 3.5) by attaching a fresh syringe filled with this solution. Afterward, the inlet and outlet tubes are sealed with blocked 25-gauge needles to prevent evaporation.
3. The flow-cell is then fitted to the microscope upon which the optical tweezers are constructed. The nitrocellulose-coated surface is brought into focus, aided by the presence of surface-bound PA-MS. The optical trapping laser is turned on and, while viewing under epi-fluorescence illumination ($\lambda_{\text{ex}} = 540 \text{ nm}$), an AD-MS is located and captured in one of the laser traps. The microscope is then switched to bright-field illumination and another microsphere is captured. The microscope is switched back to epifluorescence illumination to check that the second microsphere is a nonfluorescent SA-MS. After capturing a pair of differentially labeled microspheres, they are moved until the images of the two microspheres just overlap. A 5 Hz/8 μm amplitude triangular waveform is then applied to the x -axis of the piezo-driven microscope stage for ~ 30 s to generate a “virtual” flow past the microspheres. Afterward, the two microspheres are slowly moved apart to check for the presence of a DNA tether.
4. The elastic properties of the DNA tether are characterized by obtaining force (F) versus extension (x) data. From this data, it is possible to determine L_o and confirm whether a single or multiple DNA molecules are forming the tether. In order to obtain the F versus x data, the distance between the microspheres is increased incrementally using an automated DNA stretch-relax cycle. The microsphere-to-microsphere distance is determined for each video frame image and used to obtain x (or end-to-end distance) of the DNA molecule after subtracting the microsphere radii. The displacement of the microsphere from the trap center (defined as the microsphere position before starting the DNA stretch-relax cycle, i.e., relative extension = $x/L_o < 0.3$ and net $F=0$) is converted to F by calibrating the optical trap stiffness (see Note 13). The inextensible worm-like chain model of DNA elasticity (16) is then used to relate F , x , L_o , persistence length (L_p), and thermal energy (kT) at a given temperature (T).

3.7. Probing the DNA Transcription Cycle in Real-Time Using Optical Tweezers

1. In preparation for the single-molecule transcription assay, the custom-built flow cell is assembled (Fig. 3). The objective-side coverslip (no. 1.5) is coated with 0.1% nitrocellulose to aid immobilization of RNAP-MS (from Subheading 3.4) on this surface.
2. The coverslip surface is sparsely coated with RNAP-MS by injecting 200 μ l ~0.1% (w/v) RNAP-MS (from Subheading 3.4) into the flow cell with a plastic syringe and allowing to stand for 5 min at room temperature (~20°C). The flow cell outlet tubing must be placed in a beaker of water to prevent the formation of a hanging drop on the outlet tubing as it disrupts liquid in the flow cell upon detachment. A fresh syringe filled with SBB is attached to the inlet tubing and unbound RNAP-MS are flushed from the flow cell with 500 μ l SBB. The SBB solution is allowed to stand for 5 min to block the remaining sites on nitrocellulose with BSA before the flow cell is flushed with 200 μ l MS-DNA solution (from Subheading 3.5) using a fresh syringe.
3. A fresh syringe (see Note 14) containing TB plus 250 μ M each of CTP, GTP, ATP and UTP is connected to the inlet tubing before attempting to form a DNA tether. The vibrations caused when connecting a new syringe can dislodge microspheres from the optical traps.
4. The protocol in Subheading 3.6 is used to capture two differentially labeled microspheres in the optical traps and tether a single DNA molecule between the microspheres. The optical traps are positioned with the SA-MS on the left, i.e., transcription by T7 RNAP causes the downstream SA-MS to move from left to right (Fig. 2). Several F versus x curves are recorded, and L_o and L_p are calculated to ensure that the tether is a single DNA molecule. The expected L_o value for the DNA template prepared in Subheading 3.2 is 5.72 μ m, while L_p is ~50 nm in the buffer ($[NaCl] \approx 130$ mM) used for DNA tethering (17).
5. Once a suitable DNA molecule is obtained, the power of the optical trapping laser is increased to ensure that the microspheres are not lost during buffer exchange. The flow cell contents are exchanged by washing with 300 μ l TB plus 250 μ M of each ribonucleotide triphosphate. The ribonucleotide triphosphate concentration is kept low to slow down the rate of transcription initiation (K_m for the initiating nucleotide GTP is 600 μ M (18)). Following successful buffer exchange, the laser power is returned to its original level and a surface-bound RNAP-MS is located.
6. The center of the left optical trap holding the downstream SA-MS is determined by relaxing the DNA molecule to $x/L_o < 0.3$ (net $F=0$) and recording the position of the

microsphere image on the 4QD. To initiate RNAP–DNA interactions, the DNA molecule is held at $x/L_o \approx 0.7$ and its center (site of the ϕ 13 promoter) is brought into light contact with a surface-immobilized RNAP-MS by adjusting the optical focus. It is important to prevent the optically trapped microspheres from making contact with the coverslip surface. A 5 Hz/1.0 μm amplitude triangular waveform is applied to the laser trap holding the upstream AD-MS, while the position of the downstream SA-MS is monitored using the 4QD or a CCD camera.

7. RNAP–DNA interactions are detected as a decoupling of the passive downstream microsphere's motion from the driven upstream microsphere. For transcription elongation events, the displacement of the downstream microsphere along the x -axis is corrected for DNA elasticity using the aforementioned worm-like chain model (with $L_p = 50 \text{ nm}$) and converted to a distance in nucleotides using a B -helix rise of 0.338 nm/base pair. Typical analyses done on the acquired displacement versus time data are described in Fig. 1.

4. Notes

1. Passive adsorption of acetylated-BSA to the microcentrifuge tube walls is done to prevent unwanted binding of anti-DIG and protein A. Tubes are coated with acetylated-BSA as follows: 0.5 ml 2 mg/ml acetylated-BSA in PBS is added to each microcentrifuge tube. The sealed tubes are incubated for 2 h at room temperature ($\sim 20^\circ\text{C}$) with gentle mixing. After 2 h, the BSA solution is discarded. The tube is washed twice with water and drained well before use.
2. A sonicating water bath (Ultrawave Ltd.) is used for this step.
3. A bench-top microcentrifuge can be used for this centrifugation step.
4. It is also possible to prepare the end-labeled DNA template directly from bacteriophage T7 DNA by PCR (Fig. 4b) using forward and reverse primers labeled at the 5'-ends with biotin and digoxigenin, respectively (19).
5. It is important that all samples containing long linear DNA fragments are gently mixed to avoid shearing of the DNA.
6. A thermocycler (Px2, Thermo Electron Corp.) with a heated lid is used for the isothermal incubation of enzymatic reactions.
7. It is imperative that acetylated-BSA is used for all molecular biology work, as acetylation inactivates any contaminating DNases.

8. Digestion with *BcI*I is done to prevent the unwanted tethering of the other shorter DNA fragment during the optical tweezers experiments.
9. *Escherichia coli* BL21 (DE3) transformed with the pDL21 plasmid is used to express recombinant His₁₂-tagged T7 RNAP. A 10 ml volume of Luria–Bertani (LB) broth with 200 µg/ml ampicillin is inoculated with this strain and incubated overnight at 37°C with shaking (~200 rpm). The overnight culture is used to inoculate 500 ml LB broth, which is grown as above to an OD₆₀₀ of ~0.7 before adding isopropyl β-D-1-thiogalactopyranoside (IPTG) to 1 mM. After an additional 3 h of growth, the cells are pelleted by centrifuging at 6,000 × g for 15 min at 4°C. The cell pellet is resuspended in lysis buffer (20 mM sodium phosphate, pH 7.7, 300 mM NaCl, 10 mM imidazole, 10 µg/ml bacitracin, 0.1 mM benzamidine, and 1 mM phenylmethylsulphonyl fluoride). The cells are lysed by sonicating (Misonix Sonicator 3000, Cole-Parmer) on ice using six 15 s bursts with 30 s pauses between bursts. After sonication, DNase I (Sigma) is added to 5 µg/ml and the lysate is incubated for 20 min on ice. The cell lysate is clarified by centrifuging at 48,000 × g for 30 min at 4°C prior to purification by metal-affinity chromatography using a 1 ml HiTrap Ni²⁺-chelating column (GE Healthcare). A linear gradient of imidazole (10–500 mM) in the chromatography buffer (20 mM sodium phosphate, pH 7.7, 300 mM NaCl and 5 mM β-mercaptoethanol) is used to elute T7 RNAP from the column. Column fractions containing T7 RNAP are identified by SDS-PAGE analysis, combined, dialyzed for 24 h at 4°C against storage buffer (20 mM sodium phosphate, pH 7.7, 300 mM NaCl, 0.1 mM EDTA, 1 mM dithiothreitol, and 50% (v/v) glycerol) and stored at -20°C.
10. Mouse monoclonal anti-T7 RNAP IgG₁ can also be used to surface-immobilize this enzyme in an active form; however, this requires the coupling of protein G to the aldehyde-sulfate polystyrene-latex microspheres.
11. The solution concentration of T7 RNAP is determined empirically and adjusted so that one of 5–10 RNAP-coated microspheres yields a specific DNA interaction in the SMTA.
12. All buffers and reagents are prepared using water with a resistivity of 18.3 MΩ cm.
13. The optical traps are calibrated using two methods: the viscous drag *F* on a trapped microsphere in laminar flow (Stokes' law) and the variance in the position (>2 kHz sampling rate) of a trapped microsphere (equipartition theorem). The trap stiffness is typically in the range of 0.01–0.02 pN/nm.
14. A syringe pump and 0.5-ml glass syringe (Hamilton) are used here to inject this volume into the flow cell.

Acknowledgments

The authors would like to thank M.L. Bartoo, J.G. Hoggett, J.E. Molloy, A.J. Noël, U. Seger, G.M. Skinner, R. Thieleczek, and C. Veigel for assistance with development of the single-molecule transcription assay, instrument modifications, or data analysis. This work was supported by the BBSRC.

References

- Herbert, K. M., Greenleaf, W. J., and Block, S. M. (2008) Single-molecule studies of RNA polymerase: motoring along. *Annu. Rev. Biochem.* **77**, 149–176.
- Revyakin, A., Ebright, R. H., and Strick, T. R. (2004) Promoter unwinding and promoter clearance by RNA polymerase: Detection by single-molecule DNA nanomanipulation. *Proc. Natl. Acad. Sci. USA* **101**, 4776–4780.
- Yin, H., Wang, M. D., Svoboda, K., Landick, R., Block, S. M., and Gelles, J. (1995) Transcription against an applied force. *Science* **270**, 1653–1657.
- Wang, M. D., Schnitzer, M. J., Yin, H., Landick, R., Gelles, J., and Block, S. M. (1998) Force and velocity measured for single molecules of RNA polymerase. *Science* **282**, 902–907.
- Davenport, R. J., Wuite, G. J. L., Landick, R., and Bustamante, C. (2000) Single-molecule study of transcriptional pausing and arrest by *E. coli* RNA polymerase. *Science* **287**, 2497–2500.
- Neuman, K. C., Abbondanzieri, E. A., Landick, R., Gelles, J., and Block, S. M. (2003) Ubiquitous transcriptional pausing is independent of RNA polymerase backtracking. *Cell* **115**, 437–447.
- Shaevitz, J. W., Abbondanzieri, E. A., Landick, R., and Block, S. M. (2003) Backtracking by single RNA polymerase molecules observed at near-base-pair resolution. *Nature* **426**, 684–687.
- Galburt, E. A., Grill, S. W., and Bustamante, C. (2009) Single molecule transcription elongation. *Methods* **48**, 323–332.
- Skinner, G. M., Baumann, C. G., Quinn, D. M., Molloy, J. E., and Hoggett, J. G. (2004) Promoter binding, initiation and elongation by bacteriophage T7 RNA polymerase. A single-molecule view of the transcription cycle. *J. Biol. Chem.* **279**, 3239–3244.
- Jia, Y. P., Kumar, A., and Patel, S. S. (1996) Equilibrium and stopped-flow kinetic studies of interaction between T7 RNA polymerase and its promoters measured by protein and 2-aminopurine fluorescence changes. *J. Biol. Chem.* **271**, 30451–30458.
- Chamberlin, M., and Ring, J. (1973) Characterization of T7-specific ribonucleic acid polymerase. I. General properties of the enzymatic reaction and the template specificity of the enzyme. *J. Biol. Chem.* **248**, 2235–2244.
- Stano, N. M., Levin, M. K., and Patel, S. S. (2002) The +2 NTP binding drives open complex formation in T7 RNA polymerase. *J. Biol. Chem.* **277**, 37292–37300.
- Veigel, C., Bartoo, M. L., White, D. C. S., Sparrow, J. C., and Molloy, J. E. (1998) The stiffness of rabbit skeletal actomyosin cross-bridges determined with an optical tweezers transducer. *Biophys. J.* **75**, 1424–1438.
- He, B., Rong, M., Lyakhov, D., Gartenstein, H., Diaz, G., Castagna, R., et al. (1997) Rapid mutagenesis and purification of phage RNA polymerases. *Protein Expr. Purif.* **9**, 142–151.
- Chamberlin, M. J., Nierman, W. C., Wiggs, J., and Neff, N. (1979) A quantitative assay for bacterial RNA polymerases. *J. Biol. Chem.* **254**, 10061–10069.
- Bustamante, C., Marko, J. F., Siggia, E. D., and Smith, S. B. (1994) Entropic elasticity of lambda-phage DNA. *Science* **265**, 1599–1600.
- Baumann, C. G., Smith, S. B., Bloomfield, V. A., and Bustamante, C. (1997) Ionic effects on the elasticity of single DNA molecules. *Proc. Natl. Acad. Sci. USA* **94**, 6185–6190.
- Martin, C. T., and Coleman, J. E. (1989) T7 RNA polymerase does not interact with the 5'-phosphate of the initiating nucleotide. *Biochemistry* **28**, 2760–2762.
- Fuller, D. N., Gemmen, G. J., Rickgauer, J. P., Dupont, A., Millin, R., Recouvreux, P., et al. (2006) A general method for manipulating DNA sequences from any organism with optical tweezers. *Nucleic Acids Res.* **34**, e15.

Chapter 13

A Single-Molecule Approach to Visualize the Unwinding Activity of DNA Helicases

Natalia Fili, Christopher P. Toseland, Mark S. Dillingham,
Martin R. Webb, and Justin E. Molloy

Abstract

Almost all aspects of DNA metabolism involve separation of double-stranded DNA catalyzed by helicases. Observation and measurement of the dynamics of these events at the single-molecule level provide important mechanistic details of helicase activity and give the opportunity to probe aspects that are not revealed in bulk solution measurements. The assay, presented here, provides information about helicase unwinding rates and processivity. Visualization is achieved by using a fluorescent single-stranded DNA-binding protein (SSB), which allows the time course of individual DNA unwinding events to be observed using total internal reflection fluorescence microscopy. Observation of a prototypical helicase, *Bacillus subtilis* AddAB, shows that the unwinding process consists of bursts of unwinding activity, interspersed with periods of pausing.

Key words: DNA unwinding, Helicase, SSB, Single molecule, TIRF microscopy

1. Introduction

Double-stranded DNA (dsDNA) is the most stable form of DNA, but it must be unwound transiently to form the single-stranded DNA (ssDNA) intermediates required for processes such as DNA replication, repair, and recombination. In each of these processes, duplex unwinding is catalyzed by a class of ubiquitous motor proteins, the DNA helicases. These reactions occur typically in the range 10–1,000 bp/s depending on the specific helicase, and generally the translocation is driven by ATP hydrolysis (1).

Both mechanically and optically based single-molecule methods have been used to determine translocation and unwinding rates, along with force production (2–7). These methods have determined key aspects of helicase mechanisms.

This chapter describes a method that we developed recently (8) to visualize, in real time, the unwinding of individual double-stranded DNA (dsDNA) molecules by DNA helicases. Single-stranded DNA-binding protein (SSB) is a homotetrameric protein involved in various aspects of DNA metabolism, and we have exploited its high specificity and its rapid and tight binding to ssDNA (9, 10) for use as a probe to detect ssDNA produced by helicase activity. We use fluorescently labeled SSB to give an optical readout of helicase activity, and total internal reflection fluorescence microscopy (TIRFM) combined with a sensitive CCD camera to observe simultaneously many individual DNA unwinding events.

This assay is based on measuring the product formation and so has some advantages over other assays used for measuring dsDNA separation, namely, dye displacement assays. Binding the dye to dsDNA may cause inhibition of the helicase translocation and/or DNA cleavage (11, 12).

Two experimental approaches are described whereby either biotinylated dsDNA or biotinylated helicase is immobilized on an inert surface (Fig. 1) at a low surface density. As the helicase unwinds the DNA substrate, fluorescently labeled SSB molecules accumulate on the growing ssDNA products, which results in localized spots of gradually increasing fluorescence intensity. The fluorescence increase reports the amount of ssDNA product produced by unwinding of individual dsDNA molecules and,

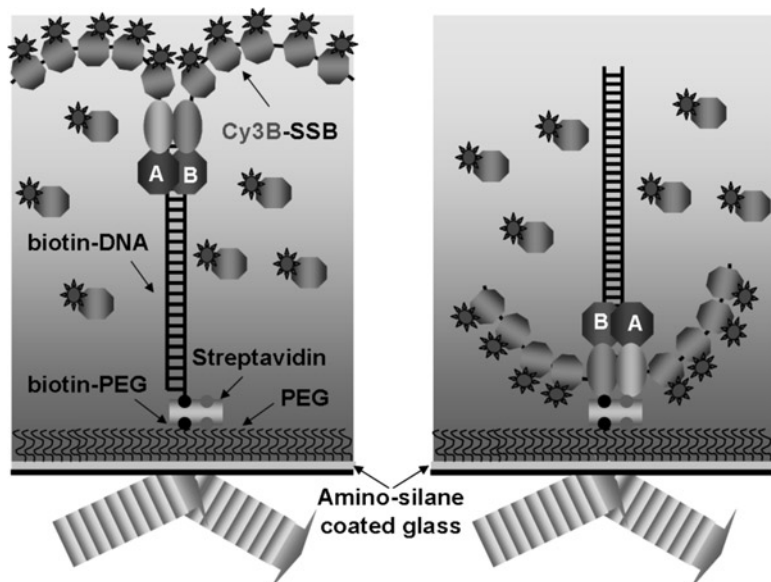


Fig. 1. Experimental scheme of the helicase assay. Biotinylated dsDNA or biotinylated helicase is immobilized on a PEGylated surface coated with streptavidin. DNA unwinding is initiated by addition of ATP in the presence of Cy3B-SSB. As the helicase unwinds its substrate, Cy3B-SSB accumulates on the growing ssDNA products. This results in a localized increase in fluorescence, which is visualized by TIRFM.

hence, provides information on the processivity and unwinding rate of the helicase. The method is compatible with an established bulk solution assay (13), which also utilizes a fluorescent version of SSB to report helicase activity. This is advantageous because the two approaches are complementary. The bulk measurements are quick to perform and can be applied to numerous DNA substrates (linear fragments, forked or gap junctions, partial duplexes, and plasmids of any length). By contrast, the single-molecule assay is best suited to linear DNA fragments, the length of which is limited by the penetration depth of TIRF evanescent wave (~100 nm) to ~2 kb. Because of signal averaging, the bulk methods give very reliable estimates of unwinding rate. However, the single-molecule experiments can reveal new mechanistic details about individual unwinding events that are masked in the bulk measurements.

In this chapter, we present how this method is applied, exemplified by the helicase-nuclease AddAB from *Bacillus subtilis*. AddAB has a role in DNA recombination. It contains a single helicase motor domain in the A subunit and a nuclease domain in each of the A and B subunits. AddAB binds with high affinity to dsDNA blunt ends, unwinds the duplex, and simultaneously degrades the ssDNA product. AddAB is a processive helicase regulated by the specific pentameric sequence 5'-AGCGG-3' termed Chi_{Bs} (14). In order to avoid the effect of Chi_{Bs} and of DNA degradation, the measurements are done with a nuclease-deficient mutant AddA^{NB^N} on DNA substrates devoid of Chi_{Bs} (Chi₀). Observation of the helicase activity of AddA^{NB^N} with single-molecule resolution reveals bursts of unwinding activity punctuated by prolonged pauses. These details are obscured in conventional bulk phase measurements.

2. Materials

2.1. Surface Chemistry

1. Vectabond (Vector Laboratories, Peterborough, UK).
2. Meo-PEG-COO-Su, MW 5,000 (Iris Biotech GmbH, Marktredwitz, Germany) (see Note 1).
3. Biotin-PEG-COO-Su, MW 5,000 (Iris Biotech GmbH, Marktredwitz, Germany) (see Note 1).
4. Glass coverslips (22 mm × 50 mm, No. 1).
5. Microscope Slides (25 × 75 × 1 mm).
6. Glass spacers (3 mm × 40 mm, No. 1).
7. Stainless-steel Coverslip Staining Rack (Raymond A Lamb Ltd., East Sussex, UK).
8. Glass Trough with Glass Lid, (Raymond A Lamb Ltd., East Sussex, UK).
9. UV-curing, Loctite 350 Adhesive, (RS Components, UK).

10. Streptavidin is dissolved at 1 mg/ml in TB buffer (see Subheading 2.4), aliquoted and stored at -20°C.
11. Cy3-Streptavidin, stored as 1 mg/ml solution at 4°C.
12. Biotin, 200 µg/ml solution in distilled H₂O stored in aliquots at -20°C.

2.2. PCR

1. Template: a suitable DNA sequence that could be used as substrate for the helicase under study. The DNA fragment should contain sequences required for the loading of the helicase or the complex containing the helicase, such as the *oriD* sequence in the case of PcrA-RepD (15). Also, the template could contain regulatory sequences, such as Chi sequences in the case of AddAB (14) and RecBCD (16). In this assay, the template used for AddA^NB^N was the pSP73-JY0 plasmid, which contains a 5.27-kb region of the *Escherichia coli* K12W311 genome devoid of Chi_{BS} sequences (8).
2. Primers: suitably designed depending on the PCR template. To generate biotinylated DNA fragments of various lengths, a single 5'-Biotin-TEG (see Note 2) forward primer is used in combination with a number of nonbiotinylated reverse primers which are designed to anneal at different sites along the DNA template. The same primer pairs, but without the biotin-TEG tag, could be used to generate nonbiotinylated fragments, which could be used for negative control experiments and for studying the activity of immobilized helicase.
3. Phusion® Hot Start High-Fidelity DNA Polymerase (New England BioLabs, Herts, UK) (see Note 3).
4. Agarose, for analysis of PCR products by electrophoresis.
5. 50× Tris-acetate-EDTA (TAE) stock. 1× TAE is used for preparation of agarose gels and as a running buffer during electrophoresis.
6. Ethidium bromide, 10 mg/ml of Ethidium bromide solution.
7. 6× Blue/Orange Loading Dye.
8. 1 kb Plus DNA Ladder (Invitrogen, UK).
9. Mini-Sub cell GT electrophoresis system and a PowerPac Basic power supply (Bio-Rad, Hertfordshire, UK).
10. UV transilluminator.
11. QIAquick Gel Extraction Kit (Qiagen, West Sussex, UK).
12. Ethanol precipitation reagents: Ethanol, 3 M CH₃COONa, pH 5.2, Ethanol (70% v/v).
13. UV spectrophotometer.
14. DCC-SSB (see Subheading 3.5) for assessing the presence of ssDNA contaminants into the PCR preparation.
15. Fluorescence Spectrophotometer.

2.3. ssDNA Probe

Cy3B-labeled, W88C mutant of the single-stranded DNA-binding protein (SSB) from *E. coli*, termed Cy3B-SSB (8) (see Notes 4 and 5).

2.4. Helicase Assay

1. 100 mM ATP solution in 25 mM Tris-HCl, pH 7 (see Note 6).
2. TB Buffer: 25 mM Tris-HCl, pH 7.5, 10 mM NaCl.
3. H Buffer: 25 mM Tris-HCl, pH 7.5, 200 mM NaCl, 2 mM MgCl₂.
4. Cy3B-SSB: 1.25 μM Cy3B-SSB in H buffer containing 5 μM Bovine Serum Albumin (BSA) to prevent SSB from sticking to surfaces.
5. Oxygen scavenger system: consisting of 10 mg/ml glucose, 50 μg/ml glucose oxidase, 400 μg/ml catalase, 500 μg/ml BSA, 1 mM DTT, 1 mM ascorbic acid, and 1 mM methyl viologen (see Note 7).
6. ATP regeneration system, consisting of 100 μg/ml creatine phosphokinase and 500 μg/ml creatine phosphate. These components are added to the reaction buffer when low ATP concentrations are used.

2.5. TIRF Microscopy

This assay was performed using a custom-made, objective-type TIRFM (8).

1. 532 nm, 50 mW, solid-state laser (Suwtech 532-50 with 1500 LDC controller, SP3-Plus) was used for excitation.
2. An electron-multiplying charge-coupled device (EMCCD) camera with high quantum efficiency, dynamic range, and signal-to-noise ratio (e.g., iXon897 BV, Andor) was used for imaging.

3. Methods

This assay is potentially applicable for the study of many different DNA helicases. In most cases, no modification of the helicase is required. However, several features of the helicase should be taken into consideration:

1. DNA Substrate. In order to be immobilized on the surface, the DNA substrates need to be end-modified with biotin. This can be achieved by PCR or a ligase reaction (see Subheading 3.5) or possibly by other methods such as annealing to a biotinylated oligonucleotide. Some helicases, however, use specific DNA substrates (whole plasmids, forked or Gap junctions, partial duplexes etc), the generation or immobilization of which could not always be feasible or straightforward.
2. Processivity. At high salt concentration, the assay has a theoretical resolution of 65 bases (65-base binding mode, see

Subheading 3.1). Therefore, to monitor an unwinding time course, the helicase should have a processivity of at least few hundred base pairs.

3. Unwinding Rate. A relatively slow helicase (unwinding rate of a few bases per second) would require long imaging times, during which the observed time-course could be limited by photobleaching. On the contrary, in the case of a rapid helicase (unwinding rate of hundreds of base pairs per second), the observed unwinding rate could be limited by SSB binding. All of these characteristics can be assessed using solution studies (17–19).
4. Additional Functions. Besides catalyzing unwinding, many DNA helicases have additional functions, such as nuclease activity. In this chapter, the assay is exemplified using the activity of the nuclease-inactive mutant AddA^{D1172A}B^{D961A} (AddA^NB^N).

3.1. Selection of the ssDNA Biosensor Experimental Conditions

The helicase assay monitors DNA unwinding by measuring the SSB binding on the growing ssDNA; therefore, the selection of the SSB concentration and the buffer conditions are critical. These will determine the maximum theoretical observed rate (limited by the first-order SSB binding rate to the ssDNA) that can be measured by the assay and, therefore, its suitability to study specific helicases. The binding stoichiometry of SSB to ssDNA greatly depends on salt concentration and protein-to-DNA ratio: at high salt conditions and low protein-to-DNA ratio binding predominantly occurs with a stoichiometry of ~65 bases per SSB tetramer, whereas low salt concentrations and high protein-to-DNA ratio favors binding with a stoichiometry of ~35 bases per tetramer (9). Given the nature of this assay, the binding stoichiometry and kinetics of SSB on ssDNA determine the limitations of the assay and, therefore, should be carefully taken into account. In addition, the effect of SSB on helicase activity (see Note 8) could also affect the interpretation of the data.

1. Select buffer conditions to ensure a single SSB binding mode. The buffer conditions contribute to the binding mode of SSB to ssDNA. Therefore, it is important to select conditions that ensure one predominant mode (20). Buffer conditions should also be compatible with the helicase activity, since salt concentration could have big effect on the processivity of the helicase (13). Selecting the optimum buffer conditions for the helicase is advisable. If a different buffer has to be used, then the helicase should be characterized under these conditions (13).
2. Determine the affinity and confirm the binding mode of Cy3B-SSB in the helicase assay buffer. This is achieved by performing a titration of ssDNA to the Cy3B-SSB. This methodology is outside the scope of this review, but this is described by Kunzelmann et al. (20).

3. Select SSB concentration to ensure rapid, high-affinity binding.

It is advisable to use at least tenfold higher concentration than the K_d measured under similar conditions. Additionally, SSB binding should occur faster than the unwinding rate of the helicase (r_{helicase}). At given buffer conditions and SSB concentration ([SSB]), the binding rate (k_{binding}) of SSB to ssDNA should be: $k_{\text{binding}} \text{ (SSB/s)} = k_{\text{on}} \times [\text{SSB}]$. For a given binding mode at these conditions (y bases/SSB, $y=65$ or 35 bases), the maximum rate (r_{max}) that can be observed is calculated from: $r_{\text{max}} \text{ (bp/s)} = k_{\text{on}} \times [\text{SSB}] \times y$. The r_{max} should be significantly greater than r_{helicase} .

For example, the assay performed at high ionic strength and at 25 nM SSB-Cy3B results in the following (8). The 65 -base binding should predominate (20), and the observable maximum unwinding rate was calculated to be ~ 600 bp/s ($= 36 \times 10^7 \text{ M}^{-1} \text{ s}^{-1} \times 25 \text{ nM} \times 65 \text{ bp}$).

3.2. Selection of the Optimum Surface Chemistry

The single-molecule analysis of DNA helicases *in vitro* requires the surface immobilization of either the helicase or its DNA substrate. The immobilization strategy should ensure the specific tethering of the helicase or the DNA on the surface, preserve the functionality of the immobilized molecule, and prevent the nonspecific absorption of other components of the assay. To this end, several different approaches have been described (21, 22). The specific tethering of the molecule of interest is usually achieved via the high-affinity interaction of streptavidin with biotin functionalized glass surfaces. Passivation of the surface by coating with nonspecific blocking proteins (such as BSA or casein), the linear or star-shaped polymer polyethylene glycol (PEG), or lipid bilayers ensures that helicase activity is maintained and that there is minimum background fluorescence caused by the nonspecific binding of the SSB probe. The selection of the immobilization strategy greatly depends on the components of the assay and has to be optimized for a specific application. The optimum surface chemistry for this helicase assay is based on the use of aminosilane coated surfaces coupled to aminoreactive linear PEG (succinimidyl ester PEG), a fraction of which is end-modified with biotin. This surface allows the specific immobilization of DNA and helicase molecules and abolishes the nonspecific absorption of both DNA and Cy3B-SSB to the underlying surface (Fig. 2).

3.2.1. Plasma Cleaning

Commercially available coverslips, although usually precleaned, are covered with organic contaminants, which could interfere with the immobilization process and could introduce fluorescent background, which reduces data quality. Such contaminants can be removed through treatment with harsh solvents (chemical etching). These include concentrated KOH or HCl in water or ethanol, or a

Cy3B-SSB

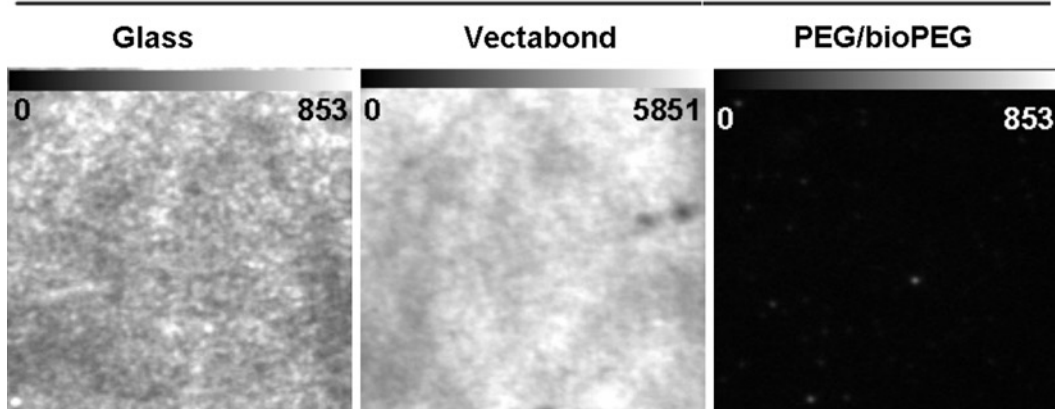


Fig. 2. PEGylation prevents the nonspecific absorption of Cy3B-SSB on the underlying surface. Glass coverslips following plasma cleaning, Vectabond treatment, and PEGylation were incubated with 25 nM Cy3B-SSB. Surface fluorescence was observed using TIRFM.

mixture of sulfuric acid and hydrogen peroxide in water (23). Contaminants can also be removed by exposing the coverslips to gas plasma discharge. There is no need to use specific gas such as argon. Air plasma is sufficient for this application. If a commercial plasma cleaner is available, plasma cleaning is recommended because it is simpler and less time-consuming.

1. Place coverslips into the stainless-steel rack.
2. Place the rack at the center of plasma cleaner chamber, close the chamber, and start the vacuum pump.
3. Wait until the vacuum gage indicates that the pressure of the chamber has reached approximately 2 Torr.
4. Turn the power on and set the level to high until you observe a purplish glow.
5. Expose the coverslips to the plasma discharge for 5 min.
6. Turn power off, open the valve to let air in, and remove the coverslips.
7. Store coverslips in a closed container at room temperature.

3.2.2. Surface Functionalization

The plasma-cleaned surfaces are functionalized with the amino-silane reagent Vectabond, which yields a dense coating of primary amines, which can react with the succinimidyl ester PEG. Surface coating is performed as recommended by the manufacturer.

1. Immerse one rack of plasma-cleaned coverslips, laid down, in the first glass trough containing 200 ml of acetone and incubate for 5 min. Coverslips tend to stick to each other. Therefore, using forceps, separate coverslips so that their whole surface is exposed to the acetone.

2. Using forceps, transfer the rack into the second trough containing 1/50 dilution of Vectabond in acetone (200 ml final volume) and incubate for 5 min. Coverslips tend to stick to each other. Using forceps, separate them so their whole surface is treated with the Vectabond.
3. Transfer the rack on a tissue paper so that the excess of Vectabond is removed and immediately immerse into the third trough containing distilled water. Using forceps, move the rack in/out of the water ~10 times, replace the water, and wash for ~10 times again.
4. Lay the rack down on a tissue to remove the excess water, separate the coverslips, and store the rack upright in a tip-box on the bench. To accelerate the drying process, store the racks under vacuum in the desiccator. Once the coverslips have dried, proceed to the PEGylation. Otherwise, the Vectabond-coated coverslips can be stored at room temperature for up to 3 months.

3.2.3. Surface PEGylation

PEGylation refers to the covalent attachment of succinimidyl PEG to the exposed amines of the Vectabond-treated coverslips. The conjugated polymer forms a dense brush which blocks the nonspecific absorption of components to the highly adhesive Vectabond-coated surface.

1. Prepare 500 ml of 100 mM NaHCO₃, pH 8.3. No pH adjustment is usually required. It is recommended to prepare the buffer just before use because its pH tends to change over time.
2. Dissolve 1 g aliquot of Meo-PEG-NHS (25 % w/w) and 60 mg of Biotin-PEG-COO-Su (1.5 % w/w) in 4 ml of 100 mM NaHCO₃. Mix well until the solution is clear. The 4 ml PEG/Biotin-PEG solution is sufficient for coating 26 coverslips.
3. Coat a large rectangular container (e.g., 500 cm² cell culture dish) with parafilm. Cover all four sides of the dish with wet tissues, to create a humid environment and prevent the coverslips from drying.
4. Place 13 Vectabond-treated coverslips on the parafilm, apply 300 µl of PEG/Biotin-PEG solution and place a second coverslip on top. The second coverslip is placed slowly so that the solution is evenly spread without formation of bubbles.
5. Close the lid and incubate the coverslip sandwiches for 3 h at room temperature, in the dark (see Note 9).
6. Fill three small beakers with 100 mM NaHCO₃ and three with distilled water (dH₂O) and place them in a row.
7. Using forceps, disassemble the sandwiches one by one (so that coverslips do not dry) and remove excess PEG solution on each coverslip by resting its edge on a tissue. Wash the coverslip

by immersing it ~10 times first into each of the NaHCO₃ and then the dH₂O beakers. Replace NaHCO₃ solution and dH₂O after washing six coverslips (see Note 10).

8. Place the washed coverslips on a rack. *Be careful! The coverslips are coated only on one side.* Therefore, it is crucial to always place them facing the same side of the rack. It could be helpful to put a mark on the rack indicating the coated side.
9. Store the coverslips in a desiccator under vacuum, in the dark, for maximum 3 weeks. Storage in the cold could prolong their life span (see Note 11).

3.3. Flow-Cell Construction

The PEGylated coverslips are used to construct two-channel cruciform flow-cells. This maximizes the use of the expensive PEGylation reagents and allows direct side-by-side comparison between two experimental conditions, avoiding the complication of surface variability.

1. Channel preparation (this step can be done while the coverslips are being coated with the PEG). Using UV glue, glue three coverglass spacers (No. 1 coverslip cut to 3 mm×40 mm), spaced by ~5 mm, with the long axis orthogonal to the axis of the microscope slide, to form two parallel channels. Use the right amount of glue so that the area underneath the spacer is covered without the glue overflowing. With the forceps press on the spacers so that the glue forms a uniform layer between the spacer and the slide and eliminate air bubbles. Allow the UV-glue to set by incubating the slides in a UV light box for 10 min.
2. Flow-cell assembly: Glue a PEGylated coverslip, with the coated side facing inward, onto the three spacers to generate two parallel channels that run across the width of the microscope slide. Again, it is critical to use the right amount of glue, which is sufficient to create a uniform layer without overflowing and sealing the channels. With the forceps, lightly press on the coverslip, to ensure that it is completely horizontal and eliminate any air bubbles. Allow the UV-glue to set by incubating the slides in a UV light box for 10 min. The PEGylated coverslip should protrude by about 12 mm on either side of the slide. These protrusions facilitate the addition of experimental solutions to the channel: during sample preparation, the slide is tilted slightly and new solution is added to the upper side of the channel, whereas old solution is removed from the lower side of the channel, using the capillary action of a tissue paper. The volume required to fill in one channel is 20–30 µl.
3. Storage: Lay the PEGylated flow-cells flat on plastic containers (e.g., tissue culture dishes) and store them at room temperature in the dark, desiccated under vacuum, for maximum 3 weeks. Storage at 4°C or even –20°C could prolong their life span (see Note 11).

3.4. Assessing the Functionality of PEGylated Flow-Cells

It is important to assess the efficiency and uniformity of PEGylation as well as the functionality of each batch of PEGylated surfaces. A simple and easy way is to incubate the PEGylated surfaces with Cy3-Streptavidin in the absence and presence of biotin. The two-channel flow-cells allow comparison of the two conditions on a single surface.

1. Dilute 1/50 the 1 mg/ml Cy3-Streptavidin stock in TB buffer to obtain 50 μ l of 20 μ g/ml (= 0.33 μ M) solution.
2. Repeat the same dilution of Cy3-Streptavidin in the presence of 2 μ l of 200 μ g/ml free biotin (= 33 μ M, final concentration). This 100-fold excess of free biotin ensures saturation of the streptavidin binding sites.
3. Incubate for 15 min at room temperature.
4. Apply one solution on each channel of the PEGylated flow-cell.
5. Incubate for 15 min at room temperature.
6. Wash each channel six times using 50 μ l TB buffer.
7. Visualize fluorescence using TIRF. When comparing signal intensities, use the same setting of Look-Up-Table (LUT). An example of successful PEGylation is shown in Fig. 3 (see Note 12).

Alternatively, the efficiency of PEGylation can be assessed by the addition of any fluorescently labeled component of the assay (e.g., Cy3B-SSB). Apply 25 nM Cy3B-SSB (the working concentration for the assay) on the PEGylated surface and observe the background fluorescence (Fig. 4). This gives information about the blocking capacity of the surface, but not about its functionality, i.e. the presence of biotin on the surface. Unsuccessful or partial PEGylation results in patchy fluorescence background.

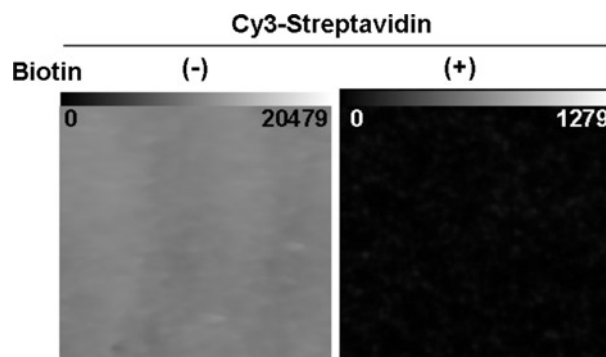


Fig. 3. Example of functional PEGylated surfaces. Freshly made PEGylated surfaces were incubated with 20 μ g/ml Cy3-Streptavidin in the presence and absence of 100-fold excess of free biotin. Saturation of the binding sites of Cy3-Streptavidin with biotin abolishes coating of the PEG/Biotin-PEG surface with Streptavidin, which confirms the presence of Biotin on the surface. Also, the uniformity of the coating indicates complete coverage of the surface with PEG.

PEGylated Surface

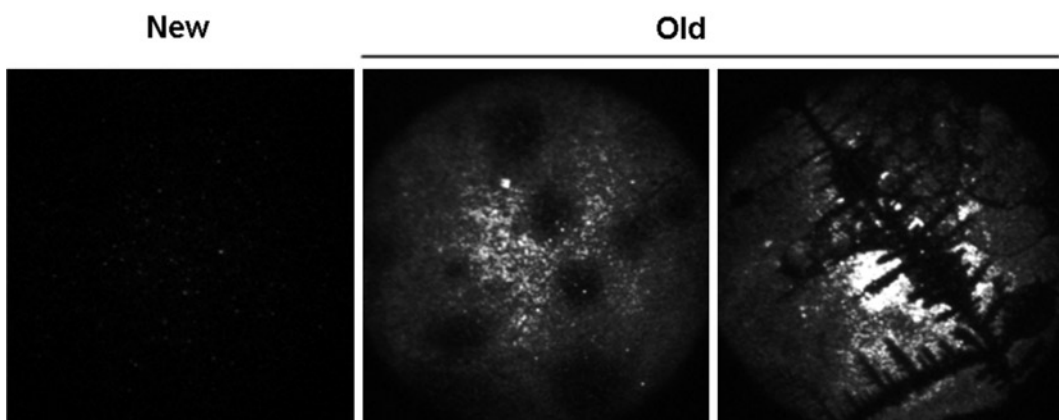


Fig. 4. Examples of degradation of the PEG coating. Freshly made PEGylated coverslips were incubated with 25 nM Cy3B-SSB and surface fluorescence was observed using TIRFM. Prolonged storage of the coated surfaces results in degradation of the coating, leading to patchy fluorescence background. Old surfaces are also characterized by extensive crystals.

3.5. Preparation of DNA Substrates

PCR is a simple and quick way to generate biotinylated and nonbiotinylated dsDNA fragments of various lengths. It can be applied on any sequence and requires only selection of various primer pairs that are suitably spaced on the DNA template (see Subheading 2.2). Although very versatile, PCR could present some disadvantages (see Note 13). Alternatively, DNA substrates can be generated by restriction enzyme digestion (see Note 14).

3.5.1. PCR Reaction and DNA Purification

The protocol below is suitable for the generation of DNA fragments up to 3 kb (see Note 15) and assumes the use of Phusion Hot Start polymerase and the Bio-Rad's Mini-Sub cell GT electrophoresis system. The high purity and the length homogeneity of the DNA fragments are critical for obtaining high-quality data. It is, therefore, highly recommended to purify the PCR products by agarose gel extraction. This allows the detection of PCR side-products and their separation from the main product. Subsequent ethanol precipitation ensures further improvement of DNA purity.

1. Following the instructions of the manufacturer, prepare $6 \times 50 \mu\text{l}$ PCR reaction mix (final volume of $300 \mu\text{l}$) and aliquot it into six PCR tubes.
2. Select the cycling conditions, as recommended by the manufacturer, and perform the reaction.
3. Spin down the reactions and pull them together in one tube.
4. Mix the $300 \mu\text{l}$ PCR reactions with $60 \mu\text{l}$ of $6\times$ Orange/blue loading dye.
5. Prepare one 1 % (w/v) agarose gel in $1\times$ TAE containing $1 \mu\text{g}/\text{ml}$ ethidium bromide. $100 \mu\text{l}$ agarose solution is sufficient for a

- single gel (see Note 15). Before casting the gel, unify all but one the wells of a 1.5-mm comb into a single long well using tape.
6. Load the DNA ladder and the PCR reaction mix and run the gel in 1× TAE at 100 V for approximately 1–2 h, until a good separation of the ladder is achieved (see Note 15).
 7. Expose the gel to UV light and, using a scalpel, extract the band that has migrated at the correct size. A successful PCR should result in a single band (see Note 16). Minimize the exposure of the DNA to the UV. Prolonged exposure will damage the DNA and may affect the activity of the helicase.
 8. Extract the DNA from the gel using the QIAquick Gel Extraction Kit, as recommended by the manufacturer.
 9. Mix the eluted DNA with two volumes of ethanol and the required volume of 3 M CH₃COONa to achieve a final concentration of 0.3 M CH₃COONa. Mix well.
 10. Store the mixture for at least 1 h at -20°C (the mixture could also be stored at -20°C overnight).
 11. Centrifuge for 15 min at 14,000×*g* and 4°C and discard the supernatant.
 12. Wash with 70 % (v/v) ethanol and centrifuge for 5 min at 14,000×*g* and 4°C.
 13. Discard supernatant and air-dry at room temperature.
 14. Resuspend in 150–200 µl 10 mM Tris-HCl, pH 8.5.
 15. Measure the concentration of the DNA using a UV spectrophotometer. The above procedure should result in a concentration of approximately 50 ng/µl.

3.5.2. Assessing the Level of ssDNA Contamination

This measurement will require the use of a fluorescence spectrophotometer and a different fluorescent SSB, DCC-SSB (13). DCC-SSB exhibits a sixfold increase in fluorescence when bound to DNA; therefore, it is a sensitive detector of ssDNA contamination.

1. Prepare a 25 nM DCC-SSB solution in the helicase buffer. Presence of 5 µM BSA will prevent DDC-SSB from sticking to the sides of the tube or cuvette. Calibrate the signal from DCC-SSB with a standard ssDNA solution of known concentrations of ssDNA binding sites (for more details see ref. 13, 20).
2. Add an excess of the DNA fragment (in terms of binding sites) to a fresh DCC-SSB solution. Measure the fluorescence change. Use the calibration to determine the amount of ssDNA contamination (see Note 17).

3.6. Intensity Calibration

The TIRFM approach used here involves excitation of the surface-immobilized specimen by an exponentially decaying evanescent field. Quantitation requires that the relationship between the

optical signal intensity and the amount of ssDNA·Cy3B-SSB is established. It is important to define the maximum DNA length below which fluorescence intensity has a linear dependence on DNA length. This sets an upper limit in the length of DNA substrates that can be used with this assay and, therefore, the processivity that can be measured. The relationship between intensity and DNA length can be used as an empirical calibration to quantify the amount of SSB bound and, therefore, the length of ssDNA product as well as to correlate changes in the unwinding rate with sequence repeats along the DNA substrate.

3.6.1. Generation of Biotinylated Cy3B-SSB·ssDNA Complexes

This can be achieved either using helicase activity (see Note 18) or by heat denaturation (see Note 19) of biotinylated dsDNA of various lengths in the presence of excess Cy3B-SSB (see Note 20).

1. Helicase activity: Mix 70 pM of biotinylated dsDNA of various lengths with 10 nM AddA^NB^N and 1 mM ATP in H Buffer. Incubate each sample for 5 min at room temperature (see Note 21).
2. Heat denaturation: In a PCR tube prepare 10 µl of 700 pM dsDNA of various lengths in denaturation buffer (50 mM Tris–HCl pH 7.5, 10 % (w/v) sucrose, 2 mM (CH₃COO)₂Mg, and 2 mM DTT). Using a thermocycler, heat-denature the dsDNA fragments at 95°C for 10 min. Place the different samples immediately on ice to avoid reannealing of the duplex and mix with 90 µl of ice-cold Cy3B-SSB in H buffer to achieve a final concentration of 25 nM Cy3B-SSB. Keep on ice for 30 min (see Note 21).
1. Apply 30 µl of 20 µg/ml streptavidin in TB buffer on each channel of the PEGylated flow-cell and incubate for 15 min at room temperature.
2. Wash six times using 50 µl of TB buffer to remove excess protein.
3. Immobilize the products of helicase activity or heat denaturation and incubate for 15 min at room temperature.
4. Wash with 50 µl of H Buffer containing 25 nM Cy3B-SSB and supplemented with the Oxygen Scavenger system.
5. Visualize the immobilized complexes by TIRFM. Using the same acquisition parameters (laser power and camera exposure time) as for the helicase assay, record the intensity of immobilized Cy3B-SSB·DNA complexes.

3.6.3. Fluorescence Intensity as a Function of DNA Length

Using an image processing software (such as the custom-written software freely available at <http://www.nimr.mrc.ac.uk/gnimpro>, ImageJ, or other) obtain the intensity distribution of the immobilized complexes. Then, plot the average or Gaussian mean of the

intensity distribution against the DNA length. When developing this assay, the calibration curve revealed that the dependency of the mean intensity on the DNA length was linear for substrates up to 2 kb.

3.7. Helicase Assay

3.7.1. AddA^NB^N Activity on Immobilized dsDNA

1. Apply 30 μ l of 20 μ g/ml streptavidin in TB buffer on each channel of the PEGylated flow-cell and incubate for 15 min at room temperature.
2. Using the capillary action of a tissue paper placed at the bottom of the channel, wash six times using 50 μ l of TB buffer to remove excess protein.
3. Flow in 50 μ l of 200–500 pM of biotinylated dsDNA in TB buffer and incubate for 15 min at room temperature (see Note 22).
4. Wash six times using 50 μ l of TB buffer to remove unbound dsDNA.
5. Flow in 50 μ l of 10 nM AddA^NB^N in H buffer containing 25 nM Cy3B-SSB, the oxygen scavenger system and the ATP regeneration system, if required. Incubate for 5 min at room temperature, to allow the helicase to bind its substrate (see Note 23). Alternatively, flow in 1 mM ATP in the above buffer (see Note 24).
6. Place the flow-cell on the microscope and record the background fluorescence of the surface (see Note 25).
7. Initiate dsDNA unwinding by flowing in 50 μ l of 1 mM ATP in the same buffer as in step 5 (see Note 26). Alternatively, initiate unwinding by 10 nM AddA^NB^N.
8. Record dsDNA unwinding using the optimum acquisition rate (frames per second) so that the events are completed within the duration of the record with maximum temporal resolution.

3.7.2. Activity of Surface-Immobilized AddA^NB^N

1. Coat the PEGylated flow-cell with streptavidin as described above.
2. Flow in 50 μ l of 2.5 nM biotag-AddA^NB^N in TB buffer and incubate for 15 min at room temperature.
3. Wash six times using 50 μ l of TB buffer to remove unbound helicase.
4. Flow in 50 μ l of 1 nM nonbiotinylated dsDNA in H buffer containing 25 nM Cy3B-SSB, the oxygen scavenger system and the ATP regeneration system, if required. Incubate for 5 min at room temperature, to allow the helicase to bind its substrate.
5. Initiate unwinding by flowing in 50 μ l of 1 mM ATP in the same buffer as in the previous step.

An example of the above experiments is summarized in Fig. 5. The assay should be repeated with different DNA lengths and a variety

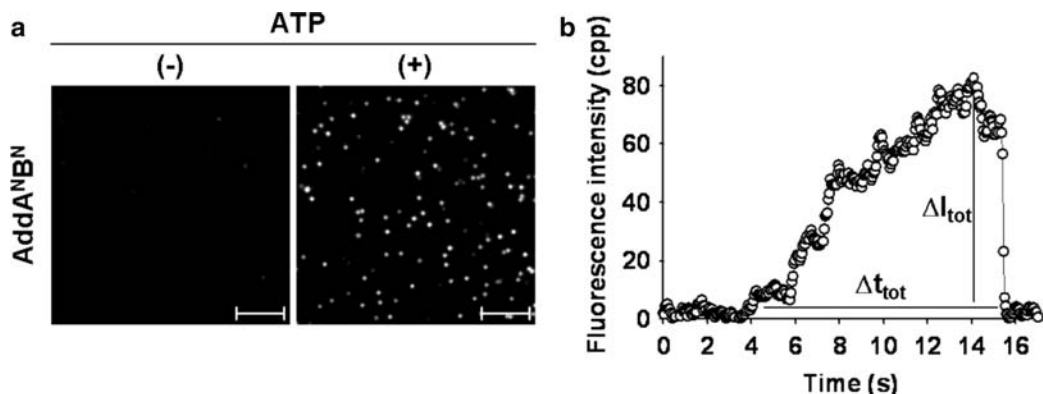


Fig. 5. Monitoring the unwinding of multiple dsDNA molecules by AddA^{NB}^N in real time. Biotinylated 1.5-kb Chi₀ dsDNA fragments were immobilized on the PEGylated surface through biotin–streptavidin interaction and incubated with the nuclease inactive mutant AddA^{NB}^N. **(a)** Addition of 1 mM ATP resulted in the appearance of multiple fluorescence spots of increasing intensity, each corresponding to the unwinding of a single dsDNA molecule. Scale bar, 5 μ m. **(b)** Representative example of an intensity time-course that reflects the helicase activity of AddA^{NB}^N is shown here. The single-step decrease in intensity at the end of the time-course represents the simultaneous release of the two ssDNA products due to the disruption of the biotin–streptavidin interaction by AddA^{NB}^N.

of helicase and ATP concentrations (see Note 27). It is also important to perform the assay with double the Cy3B-SSB concentration to test that the observed rate is not limited by SSB binding (see Note 28).

3.8. Data Analysis

In this assay, the data have the form of time-courses of increasing intensity, which can be obtained by image processing of the video recordings. Analysis of the image sequence can be achieved with any computer software capable of the following:

1. Identifying all the fluorescent spots of increasing intensity present.
2. Discarding spots of constant or instantaneously increasing intensity (see Note 29).
3. Determining the intensity as a function of time.

Such custom-written software is freely available at <http://www.nimr.mrc.ac.uk/gmipro/>

Each time-course is characterized by two parameters, the total increase in intensity (ΔI_{tot}) and total duration of unwinding (Δt_{tot}). Therefore, the next step in the analysis is to plot the distribution of these two parameters at different experimental conditions. These distributions will provide information about features of the helicase such as processivity, unwinding rate, and heterogeneity in the population. They will also provide validation of the experiments and allow comparison with bulk measurements.

Finally, the intensity time-courses should be analyzed for the presence of unwinding intermediates, such as pausing and bursts of

activity. This can be achieved using custom-written software that can do the following:

1. Smooth the intensity data by running average or median filter using the appropriate window size to remove noise (see Note 30).
2. Calculate the first derivative as a function of time.
3. Use a threshold to separate pause phases from unwinding phases (see Note 31).

4. Notes

1. These PEG derivatives are sensitive to humidity, so extensive handling in air could degrade them. It is recommended to purchase PEG in single-use aliquots.
2. 5'-Biotin primers (labeled with Biotin Phosphoramidite) could also be used. However, the labeling with Biotin-TEG (BiotinTEG Phosphoramidite) provides an additional linker of ten atoms between the biotin and the DNA. The long linker ensures that the biotin is freely available to bind to the streptavidin-coated surface.
3. The choice of the polymerase is crucial for obtaining high-quality data. Some polymerases tend to dissociate during amplification, generating dsDNA products containing ssDNA overhangs. Such overhangs would bind SSB and, therefore, result in background fluorescence, even in the absence of helicase. The performance of the polymerase can vary between PCR reactions. All such prematurely terminated side-products cannot be separated by agarose gel electrophoresis. Among the polymerases tested, the Phusion Hot Start gave the minimum, if any, detectable ssDNA contamination. The purity of the PCR products can be assessed as described in Subheading 3.5.
4. Cy3B-SSB was purified and labeled as previously described (13) so that each SSB subunit contains one Cy3B. Cy3B-SSB should be stored at micromolar to millimolar concentrations at -80°C. It is recommended to avoid freeze-thaw cycles. Cy3B-SSB binds ssDNA tightly and rapidly.
5. Among several fluorescently labeled SSB mutants, Cy3B-SSB was selected as the best because it combined the fast association kinetics and high affinity for ssDNA with good optical properties, such as high quantum yield, high photostability, and long excitation and emission wavelengths.
6. It is recommended to adjust the pH of the ATP solution at pH 7, which ensures higher stability. Measure the exact concentration

of ATP in solution by measuring the absorbance at 254 nm using a UV spectrometer (extinction coefficient at 254 nm = $15.4 \text{ cm}^{-1} \text{ mM}^{-1}$). Store at -20°C and avoid multiple freeze–thaw cycles.

7. A fluorescence-based assay requires conditions that ensure photostability of the fluorescent label and minimum photobleaching. This is usually achieved by a combination of oxygen removal and quenching of the triplet state by means of reducing agents (24). The oxygen scavenger system should be optimized for the specific fluorophore used. For this assay, minimum photobleaching was achieved with the glucose oxidase–catalase oxygen scavenger supplemented with mixture of reducing (ascorbic acid) and oxidizing (methyl viologen) agents (25). With a laser power of 0.5 mW, the photobleaching rate was $\sim 0.009 \text{ s}^{-1}$.
8. The fact that SSB is a natural component of DNA metabolism is an advantage of this assay, as it allows simulation of the native conditions of DNA unwinding. However, there are several examples of SSB interacting with, and regulating the activity of various DNA helicases (26–28). It is, therefore, important to assess and be aware of the effect of SSB on the helicase under investigation, especially when SSB has not previously been used in the characterization of the helicase. This can be easily achieved by bulk measurements of the helicase activity in the presence and absence of SSB (29).
9. The reaction results in the gradual formation of small air bubbles. This can be used as an indicator to the fact that the reaction is occurring.
10. Do not wash or scrub the coverslip surface excessively, since the coating is not very stable and could wash away.
11. If the surfaces are stored for more than 3 weeks, their functionality should be tested before use (see Subheading 3.4). Old surfaces tend to lose the PEG coating exposing the underlying Vectabond layer. This results in high fluorescent background when fluorescent molecules are applied on the surface. Also, extensive crystals can be observed (Fig. 4).
12. This experiment tests the presence of free biotins on the surface and also can reveal an unsuccessful or partial PEGylation. If the coating has failed, high fluorescent background will be observed in both channels. This background corresponds to the nonspecific absorption of Cy3-Streptavidin to the underlying surface. In the case of partial or inefficient coating, patches of high fluorescence against a dark background will be observed on the (+) biotin channel.
13. PCR can generate various side-products, such as fragments of different sizes as well as incomplete products containing ssDNA overhangs (see Subheading 2.2). The selection of the polymerase

and optimization of the PCR conditions are critical to minimize the presence such contaminants. In addition, extensive purification and assessment of the quality of the product is essential to obtain a high-quality DNA substrate.

14. Restriction enzyme digestion can overcome some of the limitations of PCR. In that case, the digested fragments can be labeled with biotin using terminal transferase (30).
15. PCR can be used for the generation of very long fragments up to 48 kb. Phusion Hot Start polymerase is suitable for amplification up to 20 kb, whereas for longer fragments a special polymerase, such as the EXL DNA polymerase (Stratagene), should be used. In addition, the percentage of agarose, the voltage, and the duration of the electrophoresis have to be optimized. For instance, PCR products above 10 kb should be separated in a 0.4% agarose gel and electrophoresis should be performed for 18 h at 25 V.
16. If PCR side products are present, modify the conditions of the PCR. Usually, more stringent conditions (higher annealing temperature, shorter denaturation etc) could eliminate the side products. However, if this cannot be avoided, run the gel for longer time to achieve good separation of the main product from the additional bands.
17. It is important to use at least a tenfold excess of SSB binding sites over DCC-SSB. This excess will give the greatest sensitivity because background fluorescence from unbound DCC-SSB will be minimal. The greater sensitivity allows for a greater accuracy when determining the ssDNA contamination. The formula to calculate the concentration of binding sites is as follows: $[dsDNA \text{ molar concentration}] \times [dsDNA \text{ length in nucleotides per strand}] \times [2 \text{ strands}] / [65 \text{ nucleotides per SSB}]$.
18. When helicase activity is used to generate the ssDNA-Cy3B-SSB complexes, it is important to know whether unwinding occurs from both ends of the substrate. In this case, the two unwound single strands can be held together by the opposite moving helicases, and therefore, the intensity of the immobilized complex will be double of the one expected for a single strand. Unidirectional unwinding is preferable and could be achieved either by using a helicase which requires a specific sequence to be loaded on the DNA or by preincubating the dsDNA with streptavidin. The latter option, however, can be applied to helicases that do not disrupt the biotin-streptavidin interaction (8).
19. Heat denaturation, when successful, generates single strands labeled with Cy3B-SSB. These complexes should have half the intensity of the final products of the helicase assay. However, depending on the sequence, denaturation is not always complete and should be optimized.

20. Excess of Cy3B-SSB tetramers is crucial to achieve saturation of the ssDNA products with SSB and prevent reannealing. As a rule of thumb, the concentration of SSB and dsDNA should ensure a ratio of 1 SSB per 20 bases of ssDNA. The assay is performed at 25 nM Cy3B-SSB. Therefore, the required molar concentration of dsDNA is calculated on the basis of the longer dsDNA fragment as follows: [dsDNA length] × [2 strands]/[20 bases per SSB].
21. Both reactions generate 140 pM Cy3B-SSB·ssDNA products which, when immobilized, should provide the optimum surface density of fluorescent spots. If reactions are performed with higher dsDNA concentrations, serial dilution should be performed so that the immobilized products appear as discrete fluorescent spots.
22. Serial dilutions should be performed to achieve the optimum immobilization density so that the unwinding events appear as discrete fluorescent spots. The optimum dsDNA concentration could be defined by labeling the immobilized dsDNA with a dimeric cyanine dsDNA specific dye (Invitrogen), such as YoYo-1, PoPo-1, etc.
23. Depending on the helicase, it may be advantageous to incubate the coverslips at a specific temperature and/or to use a microscope enclosed in an incubator. This can improve the efficiency of helicase loading and activity.
24. This option is recommended in the case of helicases whose affinity for DNA is enhanced by ATP. Also, it is advisable when low ATP concentrations are used, because it allows the ATP concentration to be equilibrated before initiation of the reaction.
25. Until the helicase reaction is initiated, only a few, if any, fluorescent spots of constant intensity should be observed. These would correspond to ssDNA contaminants or Cy3B-SSB aggregates nonspecifically absorbed on the surface.
26. AddA^NB^N is added to this solution to ensure that the helicase is not washed out when ATP is added. This may not be necessary, if the helicase has high affinity for the dsDNA.
27. These measurements allow characterization of the helicase and also serve as controls for the assay. The total increase in intensity and duration of unwinding should increase with the DNA length. Moreover, the duration of unwinding will increase with decreasing ATP concentration, whereas the total increase in intensity should be ATP independent. Furthermore, change in helicase concentration could result in a change in the number of observed events. Changes in unwinding rate may be observed if the helicase forms oligomers or the helicase has a low processivity. If these points are not observed in the assay, then it is likely there is a problem in the conditions.

28. This control will confirm that unwinding is not limited by the rate of SSB binding. If the observed rate of unwinding and the maximum increase in intensity both increase with SSB concentration, then this would indicate that SSB binding is rate limiting. However, it should be noted that, depending on the range of SSB concentration used, change in the maximum increase in intensity could also be attributed to the appearance of a 35-base binding.
29. Spots of constant intensity correspond to background spots such as Cy3B-SSB aggregates or immobilized incomplete PCR products containing single-stranded sections (see Subheading 3.5). The spots of instantaneous intensity increase are the result of free Cy3B-SSB-ssDNA complexes colliding with the surface. These can be caused, for example, by the release of ssDNA from the surface by helicases that disrupt the biotin-streptavidin interaction.
30. The window size will have to be optimized depending on the amount of noise in the data. It is important not to remove features from the unwinding trace.
31. The threshold will have to be optimized. It is important to apply one set of conditions to the whole dataset. Owing to noise and fluctuations in the signal, it may not be possible to have ideal conditions for every trace.

References

1. Singleton, M. R., Dillingham, M. S., and Wigley, D. B. (2007) Structure and mechanism of helicases and nucleic acid translocases. *Annu. Rev. Biochem.* **76**, 23–50.
2. Bianco, P. R., and Kowalczykowski, S. C. (1997) The recombination hotspot Chi is recognized by the translocating RecBCD enzyme as the single strand of DNA containing the sequence 5'-GCTGGTGG-3'. *Proc. Natl. Acad. Sci. USA* **94**, 6706–6711.
3. Dohoney, K. M., and Gelles, J. (2001) Chi-sequence recognition and DNA translocation by single RecBCD helicase/nuclease molecules. *Nature* **409**, 370–374.
4. Dumont, S., Cheng, W., Serebrov, V., Beran, R. K., Tinoco, I., Jr., Pyle, A. M., and Bustamante, C. (2006) RNA translocation and unwinding mechanism of HCV NS3 helicase and its coordination by ATP. *Nature* **439**, 105–108.
5. Myong, S., Bruno, M. M., Pyle, A. M., and Ha, T. (2007) Spring-loaded mechanism of DNA unwinding by hepatitis C virus NS3 helicase. *Science* **317**, 513–516.
6. Perkins, T. T., Li, H. W., Dalal, R. V., Gelles, J., and Block, S. M. (2004) Forward and reverse motion of single RecBCD molecules on DNA. *Biophys. J.* **86**, 1640–1648.
7. Spies, M., Dillingham, M. S., and Kowalczykowski, S. C. (2005) Translocation by the RecB motor is an absolute requirement for {chi}-recognition and RecA protein loading by RecBCD enzyme. *J. Biol. Chem.* **280**, 37078–37087.
8. Fili, N., Mashanov, G. I., Toseland, C. P., Batters, C., Wallace, M. I., Yeeles, J. T., Dillingham, M. S., Webb, M. R., and Molloy, J. E. (2010) Visualizing helicases unwinding DNA at the single molecule level. *Nucleic Acids Res.* **38**, 4448–4457.
9. Lohman, T. M., and Ferrari, M. E. (1994) *Escherichia coli* single-stranded DNA-binding protein: multiple DNA-binding modes and cooperativities. *Annu. Rev. Biochem.* **63**, 527–570.
10. Raghunathan, S., Kozlov, A. G., Lohman, T. M., and Waksman, G. (2000) Structure of the DNA binding domain of *E. coli* SSB bound to ssDNA. *Nat. Struct. Biol.* **7**, 648–652.
11. Akerman, B., and Tuite, E. (1996) Single- and double-strand photocleavage of DNA by YO,

- YOYO and TOTO. *Nucleic Acids Res.* **24**, 1080–1090.
12. Eggleston, A. K., Rahim, N. A., and Kowalczykowski, S. C. (1996) A helicase assay based on the displacement of fluorescent, nucleic acid-binding ligands. *Nucleic Acids Res.* **24**, 1179–1186.
 13. Dillingham, M. S., Tibbles, K. L., Hunter, J. L., Bell, J. C., Kowalczykowski, S. C., and Webb, M. R. (2008) Fluorescent single-stranded DNA binding protein as a probe for sensitive, real-time assays of helicase activity. *Biophys. J.* **95**, 3330–3339.
 14. Chedin, F., Seitz, E. M., and Kowalczykowski, S. C. (1998) Novel homologs of replication protein A in archaea: implications for the evolution of ssDNA-binding proteins. *Trends Biochem. Sci.* **23**, 273–277.
 15. Soultanas, P., Dillingham, M. S., Papadopoulos, F., Phillips, S. E., Thomas, C. D., and Wigley, D. B. (1999) Plasmid replication initiator protein RepD increases the processivity of PcrA DNA helicase. *Nucleic Acids Res.* **27**, 1421–1428.
 16. Spies, M., Bianco, P. R., Dillingham, M. S., Handa, N., Baskin, R. J., and Kowalczykowski, S. C. (2003) A molecular throttle: the recombination hotspot chi controls DNA translocation by the RecBCD helicase. *Cell* **114**, 647–654.
 17. Dillingham, M. S., Wigley, D. B., and Webb, M. R. (2000) Demonstration of unidirectional single-stranded DNA translocation by PcrA helicase: measurement of step size and translocation speed. *Biochemistry* **39**, 205–212.
 18. Dillingham, M. S., Wigley, D. B., and Webb, M. R. (2002) Direct measurement of single-stranded DNA translocation by PcrA helicase using the fluorescent base analogue 2-aminopurine. *Biochemistry* **41**, 643–651.
 19. Slatter, A. F., Thomas, C. D., and Webb, M. R. (2009) PcrA helicase tightly couples ATP hydrolysis to unwinding double-stranded DNA, modulated by the initiator protein for plasmid replication, RepD. *Biochemistry* **48**, 6326–6334.
 20. Kunzelmann, S., Morris, C., Chavda, A. P., Eccleston, J. F., and Webb, M. R. Mechanism of interaction between single-stranded DNA binding protein and DNA. *Biochemistry* **49**, 843–852.
 21. Rasnik, I., McKinney, S. A., and Ha, T. (2005) Surfaces and orientations: much to FRET about? *Acc. Chem. Res.* **38**, 542–548.
 22. Visnapuu, M. L., Duzdevich, D., and Greene, E. C. (2008) The importance of surfaces in single-molecule bioscience. *Mol. Biosyst.* **4**, 394–403.
 23. Paul R. Selvin, T. H. (2008) *Single-molecule techniques: a laboratory manual*
 24. Rasnik, I., McKinney, S. A., and Ha, T. (2006) Nonblinking and long-lasting single-molecule fluorescence imaging. *Nat. Methods* **3**, 891–893.
 25. Vogelsang, J., Kasper, R., Steinhauer, C., Person, B., Heilemann, M., Sauer, M., and Tinnefeld, P. (2008) A reducing and oxidizing system minimizes photobleaching and blinking of fluorescent dyes. *Angew. Chem. Int. Ed. Engl.* **47**, 5465–5469.
 26. Atkinson, J., Guy, C. P., Cadman, C. J., Moolenaar, G. F., Goosen, N., and McGlynn, P. (2009) Stimulation of UvrD helicase by UvrAB. *J. Biol. Chem.* **284**, 9612–9623.
 27. Cadman, C. J., and McGlynn, P. (2004) PriA helicase and SSB interact physically and functionally. *Nucleic Acids Res.* **32**, 6378–6387.
 28. Shereda, R. D., Bernstein, D. A., and Keck, J. L. (2007) A central role for SSB in *Escherichia coli* RecQ DNA helicase function. *J. Biol. Chem.* **282**, 19247–19258.
 29. Webb, M. R. (2010) Fluorescent biosensors to investigate helicase activity. *Methods Mol. Biol.* **587**, 13–27.
 30. Skinner, G. M., Baumann, C. G., Quinn, D. M., Molloy, J. E., and Hoggett, J. G. (2004) Promoter binding, initiation, and elongation by bacteriophage T7 RNA polymerase. A single-molecule view of the transcription cycle. *J. Biol. Chem.* **279**, 3239–3244.

Chapter 14

Real-Time Single-Molecule Observation of Green Fluorescent Protein Synthesis by Immobilized Ribosomes

Ryo Iizuka, Takashi Funatsu, and Sotaro Uemura

Abstract

The dynamics of full protein synthesis and the co-translational folding processes are not fully understood. We have developed a novel method, using a combination of ribosome display and single-molecule techniques, for monitoring the synthesis, co-translational folding, and maturation of a complete polypeptide chain at the single-molecule level. This method enabled us to observe the appearance of green fluorescent protein fluorescence after de novo synthesis of the complete protein. Here, we provide the information necessary to reproduce this method, which will be valuable in revealing the dynamics of the co-translational folding and maturation of nascent polypeptides.

Key words: Ribosome display, Translation, Protein folding, Green fluorescent protein, SecM, Translation arrest, Single-molecule fluorescence imaging, Total internal reflection fluorescence microscopy

1. Introduction

Protein folding is one of the most basic and challenging research areas in biology. Most of our understanding in this area comes from studies investigating the refolding of denatured proteins. However, as many studies point out, the folding and maturation of newly synthesized proteins and proteins refolded *in vitro* differ substantially. It has been shown that protein folding occurs co-translationally in both eukaryotes and prokaryotes (1). There appear to be significant differences in folding rates between co-translational folding and the refolding of the full-length polypeptide, and also in the folding pathways involved and the yields obtained (1). Therefore, one major goal is to understand how the nascent chains fold. In particular, single-molecule studies can provide valuable information about these heterogeneous processes that comprise multiple pathways and asynchronous events.

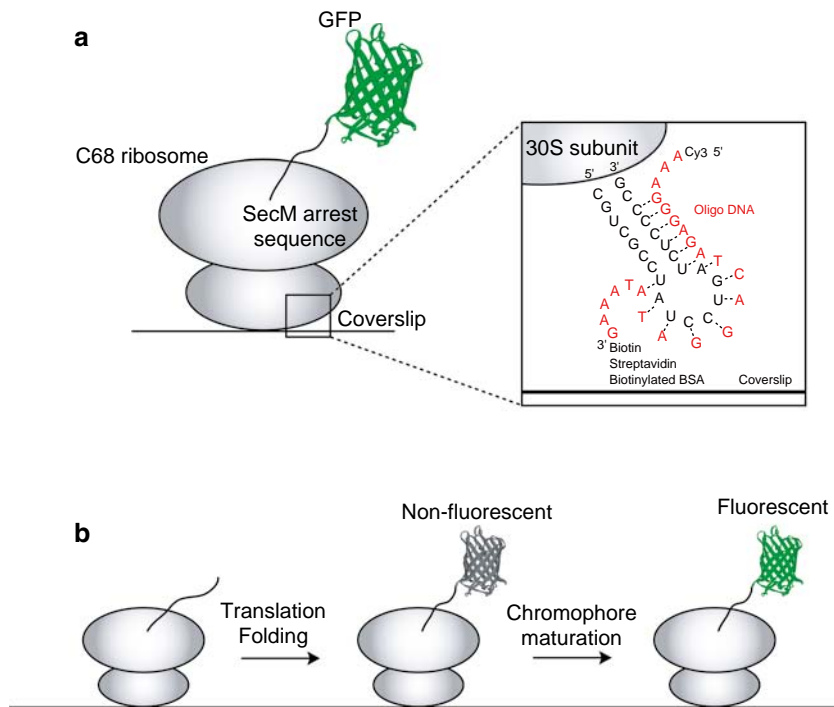


Fig. 1. (a) Experimental design. C68 ribosomes are specifically immobilized on a glass surface in the presence of an in vitro transcription/translation system and template DNA. Nascent chains are stalled on immobilized ribosomes using the SecM arrest sequence, which interacts with the ribosomal exit tunnel, thereby interfering with translation elongation. Inset: C68 ribosome has a 23-nucleotide extension in the surface-accessible loop of 16S rRNA on the 30S ribosomal subunit, and can be labeled with Cy3 and biotin via hybridization of the DNA oligonucleotide with the extension. Ribosomes prehybridized with the oligonucleotide are immobilized on the glass surface via biotinylated-BSA and streptavidin. (b) Schematic representation of the observation of GFP fluorescence after de novo synthesis. After the beginning of protein synthesis, co-translational folding of nascent chain occurs. When the protein is fully folded, an autocatalytic maturation leads to the chromophore formation of GFP, thus turning the protein fluorescent.

We have developed a single-molecule method to monitor the translation and folding of proteins in real time (Fig. 1) (2). The method involves a combination of ribosome display and single-molecule techniques. Ribosomes are specifically immobilized on a glass surface via a biotin–streptavidin linkage to allow monitoring of protein synthesis and folding (Fig. 1a). Additionally, the nascent polypeptide chains are stalled on the immobilized ribosomes using the Secretion Monitor (SecM) arrest sequence (3). The SecM peptide interacts with the peptide exit tunnel inside the 50S subunit, thereby interfering with translation elongation (4–6).

Here, we describe a method for studying the folding and maturation of green fluorescent protein (GFP) immediately after de novo synthesis (Fig. 1b).

1.1. Ribosomes for Single-Molecule Imaging

We employed a C68 mutant ribosome genetically inserted into a 23-nucleotide extension in the surface-accessible loop (Helix 44) of the 16S rRNA on the 30S ribosomal subunit to achieve surface

immobilization (7) (Fig. 1a, *inset*). The C68 ribosome can be labeled and immobilized on a glass surface by hybridization with an oligonucleotide containing a fluorophore at the 5' end and biotin at the 3' end to the extension loop (2, 7) (Fig. 1a, *inset*). The labeling method has high specificity, efficiency and stability, and does not interfere with the normal function of the ribosomes (2, 7).

1.2. In Vitro Transcription/Translation System for Ribosome Display

Ribosome-associated nascent chains are synthesized using the PURE (Protein synthesis Using Recombinant Elements) system. The PURE system is a coupled, cell-free transcription/translation system reconstituted from the purified components necessary for translation in *E. coli* (8, 9). The advantage of this system is that its composition can be easily modified according to the purpose of experiment. The systems are commercially available from Wako Pure Chemical Industries, Ltd. (Japan) as “PURESYSTEM” kits. We used the PURESYSTEM Δ1 Ribosome kit. The kit contains all the components required for transcription and translation, except for the ribosomes. Thus, we are able to use purified C68 mutant ribosomes in our experiments. The absence of nucleases and proteases is also essential for ribosome display. Also, the PURE system is more suitable for single-molecule imaging than the S30 cell extract system due to the lower levels of autofluorescence produced (10, 11).

1.3. DNA Template for Ribosome Display

Figure 2 shows a schematic drawing of the DNA construct used to display GFP on the ribosome. The gene encoding GFP is introduced downstream of the T7 promoter and the ribosome binding site (RBS) (the Shine-Dalgarno sequence) (Fig. 2a). GFP requires slow post-translational modification of the folded protein to become fluorescent. To improve the proper folding and chromophore formation of GFP, we designed a construct incorporating GFP_{UV3} (also referred to as folding reporter GFP or GFP_{sol}) (12), which contains the “enhanced GFP” mutations (F64L/S65T) (13) and the “cycle 3” mutations (F99S/M153T/V163A) (14) (see Note 1).

The spacer sequence, composed of a Gly-Ser linker, protein D (residues 21–110), and a second Gly-Ser linker, is included downstream of the GFP gene to provide sufficient distance between the displayed GFP and the ribosome. This allows the GFP to fold into its correct conformation (Fig. 2a, b) (see Note 2) (15, 16). In addition, the SecM arrest motif (150-FXXXXWIXXXXGIRAGP-166) is positioned downstream of this spacer sequence to stabilize the ribosome-nascent chain complex (3, 16, 17) (Fig. 2a, b). The SecM arrest motif is known to bind tightly to the ribosomal exit tunnel, and to arrest ribosome elongation efficiently in this PURE system (16, 18, 19). We introduced both a codon for proline and a termination codon downstream of the SecM arrest motif (Fig. 2b) to reinforce ribosome stalling (20, 21).

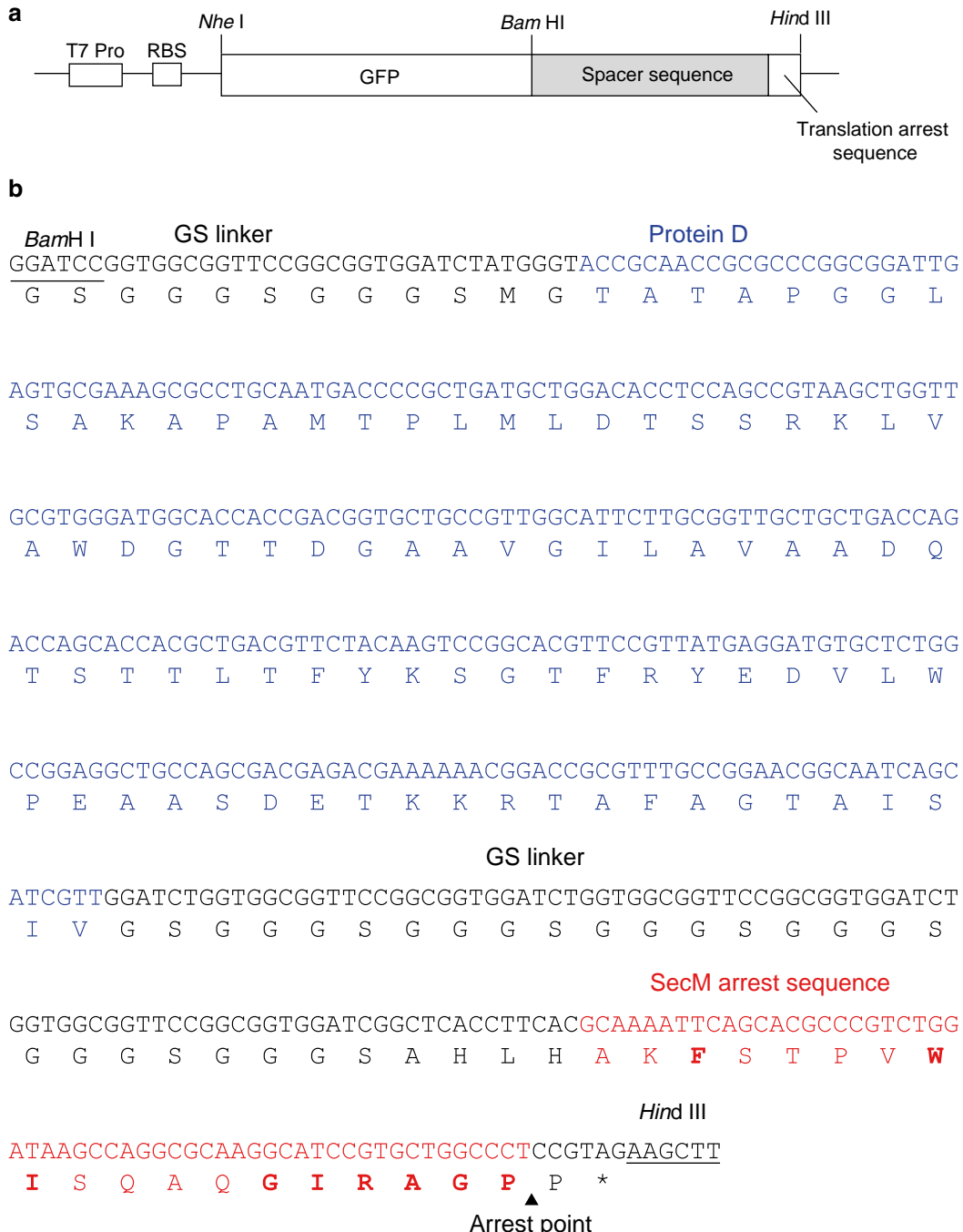


Fig. 2. (a) Schematic drawing of the DNA construct used in the GFP display system. The T7 promoter (T7 Pro) is followed by a RBS and the GFP_{UV3} gene, which is cloned into the *Nhe* I/*Bam* H I restriction sites. The GFP_{UV3} gene is followed by the spacer sequence and the translation arrest sequence, which are cloned into the *Bam* H I/*Hind* III restriction sites. (b) DNA and deduced amino acid sequence of the spacer sequence and arrest sequence. The spacer sequence consists of a Gly-Ser linker (GS; 10 amino acids), protein D from λ phage (T21-V110; 90 amino acids), and a second Gly-Ser linker (26 amino acids) (see Note 2). The spacer sequence provides sufficient distance between the displayed protein and the ribosome to allow the protein to fold into its correct conformation (15, 16). The translation arrest sequence is composed of the arrest sequence of SecM from *E. coli* (A148-P166; 19 amino acids) plus a Pro residue. Amino acids shown to be essential for translation arrest are shown in bold.

2. Materials

2.1. Preparation of Template DNA for Ribosome Display

1. Gene for GFP_{UV3} mutant (F64L/S65T/F99S/M153T/V163A; see Note 1): Use as a PCR template.
2. Plasmid pD-SecM-pURE1: A gift from Dr. Yoshihiro Shimizu and Prof. Takuya Ueda (The University of Tokyo). The plasmid contains the spacer sequence and SecM arrest sequence (Fig. 2b). Use as a PCR template.
3. PCR primers: Forward primer for GFP_{UV3} gene: 5'-CTAGCTAGC AAAGGAGAAGAACTCTTCACTG-3'. This primer includes a *Nhe* I site (underlined) and the N-terminal sequence of GFP_{UV3}; Reverse primer for the GFP_{UV3} gene: 5'-CGGGATCC TTTGTATAGTTCATCCATG-3'. The primer includes a *Bam*H I site (underlined) and the sequence for the C terminus of GFP_{UV3} without a stop codon; Forward primer for the sequence encoding the spacer and the translation arrest motif: 5'-CGGGATCCGGTGGCGGTTC-3'. The primer includes a *Bam*H I site (underlined) and the N-terminal sequence of the spacer; reverse primer for the sequence encoding the spacer and the translation arrest motif: 5'-**CCCAAGCTT**CTA CGGAGGGCCAGCACGGATG-3'. The primer includes a *Hind* III site (underlined), a stop codon (bold), a codon for proline (italic), and the arrest sequence for the C terminus of SecM.
4. DNA polymerase.
5. Restriction enzymes (*Nhe* I, *Bam*H I, and *Hind* III).
6. DNA ligase.
7. Expression vector: The vector must contain a T7 promoter and a RBS with the appropriate spacing upstream of a start codon. We recommend pET21a-c or pET23a-c (Novagen; see Note 3).

2.2. Ribosome Purification

1. Glycerol stock of *E. coli* expressing ribosome with an extension in helix 44 (C68 ribosome) (7): A gift from Prof. Joseph D. Puglisi (Stanford University).
2. LB medium (2 L).
3. 100 mg/mL carbenicillin: Sterilize by filtering through a 0.2-μm pore size filter and store at -20°C.
4. 20% (w/v) glucose: Sterilize by filtering through a 0.2-μm pore size filter and store at 4°C.
5. RNase inhibitor (e.g., SUPERase In; Applied Biosystems; AM2696).
6. Protease inhibitor (e.g., Protease Inhibitor Cocktail for use with bacterial cell extracts; Sigma-Aldrich; P8465).
7. Ultracentrifuge.

8. Buffer A (150 mL): 20 mM Tris-HCl, pH 7.5, 100 mM NH₄Cl, 10 mM MgCl₂, 0.5 mM EDTA, and 6 mM β-mercaptoethanol. Prepare fresh. Store at 4°C.
9. Buffer B (50 mL): 20 mM Tris-HCl, pH 7.5, 500 mM NH₄Cl, 10 mM MgCl₂, 0.5 mM EDTA, 6 mM β-mercaptoethanol, and 37% (w/v) sucrose. Prepare fresh. Store at 4°C.
10. Buffer C (50 mL): 20 mM Tris-HCl, pH 7.5, 60 mM NH₄Cl, 5 mM MgCl₂, 0.5 mM EDTA, and 6 mM β-mercaptoethanol. Prepare fresh. Store at 4°C.
11. Buffer D (50 mL): 20 mM Tris-HCl, pH 7.5, 60 mM NH₄Cl, 5 mM MgCl₂, 0.5 mM EDTA, 6 mM β-mercaptoethanol, and 10% (w/v) sucrose. Prepare fresh. Store at 4°C.
12. Buffer E (50 mL): 20 mM Tris-HCl, pH 7.5, 60 mM NH₄Cl, 5 mM MgCl₂, 0.5 mM EDTA, 6 mM β-mercaptoethanol, and 40% (w/v) sucrose. Prepare fresh. Store at 4°C.
13. Gradient maker and fractionator (e.g., Gradient Station; BioComp Instruments, Inc.; #153).
14. Fraction collector.

2.3. GFP Synthesis Monitoring in Bulk

1. PURESYSTEM classic II mini (Wako Pure Chemical Industries, Ltd.; 635-15701). Store all components at -80°C and avoid multiple freeze-thaw cycles. PURESYSTEM Δ1 Ribosome (Wako Pure Chemical Industries, Ltd.; 631-15661) is also available to check the synthesis activity of the purified C68 ribosomes.
2. Nuclease-free water.
3. Fluorometer with a Peltier temperature controller.
4. Microcuvette (3 × 3 × 37 mm; Jasco).

2.4. Sample Preparation for Microscope Experiments

1. DNA oligonucleotide (Synthetic; e.g., IDT): 5'-Cy3-AAAGGGAGATCAGGATATAAAG-biotin-3'. The oligonucleotide is labeled with Cy3 at the 5' end and biotin at the 3' end. The underlined sequence is complementary to a 23-nucleotide extension in helix 44 of the 16S rRNA (Fig. 1a, *inset*). The synthesized oligonucleotide should be HPLC-purified. Dissolve the oligonucleotide in nuclease-free water to a concentration of 100 μM and store at -20°C.
2. Micro-ultracentrifuge.
3. PURESYSTEM Δ1 Ribosome.
4. Coverslips (18 × 18 mm, 0.12–0.17 mm thick; Matsunami).
5. Glass slides (76 × 26 mm, 0.8–1.0 mm thick; Matsunami).
6. O₂ plasma cleaner. We routinely use the FEMTO plasma system (Diener electronic GmbH) to get rid of the fluorescence impurities on the surface of cover slips.

7. Polyester film (~50 μm thickness, e.g., Lumirror #50-S10, Toray Industries Inc.).
8. Paper clips.
9. Nail polish.
10. 3.0 mg/mL biotinylated BSA (see Note 4): Store in aliquot at -20°C. Thawed aliquot is kept at 4°C.
11. 0.33 mg/mL streptavidin (Invitrogen; S-888): Store in aliquot at -20°C. Thawed aliquots are kept at 4°C.
12. Imaging buffer: 50 mM Tris-acetate, pH 7.5, 5 mM ammonium acetate, 0.5 mM calcium acetate, 5 mM magnesium acetate, 0.5 mM EDTA, 100 mM KCl, and 5 mM β -mercaptoethanol. Filter it through a 0.2- μm sterile filter.

2.5. Microscope Experiment and Data Analysis

1. Fluorescent microspheres (e.g., TetraSpeck microspheres, 0.1 μm , fluorescent blue/green/orange/dark red; Invitrogen; T7279).
2. Electron multiplying charge-coupled device (EM-CCD) camera (e.g., C9100-13; Hamamatsu Photonics).
3. 488 nm laser for GFP excitation (e.g., Sapphire 488-200 CDRH; Coherent).
4. 532 nm laser for Cy3 excitation (e.g., COMPASS 315M-100; Coherent).
5. Inverted microscope (e.g., IX-71; Olympus).
6. Objective lens (e.g., ApoN 60xOTIRFM, NA 1.49; Olympus).
7. Dichroic mirror for GFP detection (e.g., 505DRLP; Omega Optical).
8. Dichroic mirror for Cy3 detection (e.g., Q565LP; Chroma Technology).
9. Emission filter for GFP detection (e.g., FF01-520/35-25; Semrock).
10. Emission filter for Cy3 detection (e.g., FF01-593/40-25; Semrock).

3. Methods

3.1. Preparation of Template DNA for Ribosome Display

1. Amplify the genes encoding the GFP_{UV3}, spacer and translation arrest motif by two separate polymerase chain reactions using the primer sets as described in Subheading 2.1.
2. Digest the PCR products with the appropriate restriction enzymes (fragment encoding GFP_{UV3}, *Nhe* I/*Bam*H I; fragment encoding spacer and translation arrest motif, *Bam*H I/*Hind* III), and co-ligate them into the *Nhe* I and *Hind* III restriction sites in the pET21 vector.

3.2. Ribosome Purification

Ribosomes from *E. coli* can be purified following the published protocol with slight modification (22). To avoid nuclease contamination, wear gloves during purification, and use nuclease-free tips and tubes.

1. Inoculate a few microliters from a glycerol stock of *E. coli* expressing C68 ribosomes into 5 mL of LB medium containing 100 µg/mL carbenicillin and 5% (w/v) glucose. Incubate with shaking at 37°C overnight.
2. Inoculate 2.5 mL of overnight culture into 1 L of LB medium containing 100 µg/mL carbenicillin and 1% (w/v) glucose. Incubate with shaking at 37°C until OD₆₀₀ reaches 0.5.
3. Place the flask on ice for approximately 30 min, and then harvest the cells by centrifugation at 5,000 ×*g* for 10 min at 4°C.
4. Resuspend the cells in 100 mL of Buffer A, and centrifuge as above. Remove the supernatant and store the cells as a frozen pellet at -80°C, or continue with purification.
5. Resuspend the harvested cells in 20 mL of Buffer A containing RNase inhibitor and protease inhibitor, and disrupt them using a French Press or sonicator.
6. Pellet the cell debris by centrifuging at 20,000 ×*g* for 15 min at 4°C.
7. Layer 10 mL of the clarified supernatant onto Buffer B (15 mL) in centrifuge tubes, and pellet the ribosomes by ultracentrifugation at 100,000 ×*g* for 22 h at 4°C.
8. Resuspend the ribosome pellets in 3 mL of ice-cold Buffer C. Resuspension is slow and requires constant, gentle agitation.
9. Prepare linear 10–40% sucrose gradients in ultracentrifuge tubes using Buffer D and E, and load ~1.5 mL of sample onto the gradients.
10. Centrifuge at 80,000 ×*g* for 20 h at 4°C using a swing rotor.
11. Fractionate the gradients (~0.5 mL per fraction). Dilute each fraction 100-fold with Buffer D and measure the absorbance at 260 nm. Pool the fractions containing the 70S ribosomes and determine the concentration of ribosomes using the molar extinction coefficient ($5 \times 10^7 \text{ M}^{-1} \text{ cm}^{-1}$) at 260 nm. Freeze the ribosomes in liquid nitrogen and store at -80°C until use.

3.3. GFP Synthesis Monitoring in Bulk

An example of the result is shown in Fig. 3. To verify protein synthesis, it is useful to use a plasmid containing a T7 promoter, a RBS before the ATG start codon, and the gene for GFP_{UV3}, as a control template. It is noted that the PURE system is very sensitive to nuclease contamination, so we recommend wearing gloves and the use of nuclease-free tips.

1. Thaw Sol. A and Sol. B supplied in the protein synthesis kit on ice (see Note 5).

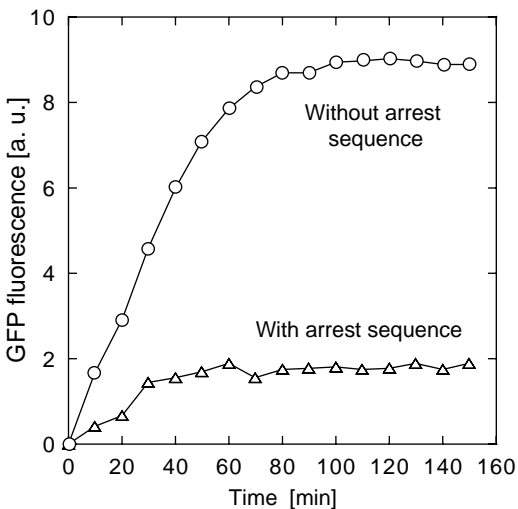


Fig. 3. Time course of GFP fluorescence in the PURE system. GFP with or without the arrest sequence was synthesized using the PURESYSTEM, and the appearance of GFP fluorescence was continuously monitored at the indicated time points. The reactions were initiated by the addition of plasmid DNA to the reaction mixtures (Time 0). Circles, GFP without arrest sequence; triangles, GFP with arrest sequence.

2. Assemble the components in a tube, on ice, in the following order:

Nuclease-free wa ter	to 100 μ L
Sol. A	25 μ L
Sol. B	10 μ L
Ribosome (final 300 nM)	$\times \mu$ L (optional, use only in $\Delta 1$ Ribosome)
Template DNA (0.5 μ g)	$\times \mu$ L (see Note 6)

3. Mix gently, centrifuge briefly, and transfer to a microcuvette.
4. Monitor GFP fluorescence at 510 nm by exciting at 488 nm, while incubating at 37°C.

3.4. Sample Preparation for Microscope Experiments

1. Clean the coverslips using a plasma cleaner for 15 min under oxygen plasma (see Note 7). Keep them in the plastic case for 5–7 days prior to the experiments (see Note 8).
2. Incubate 0.5 μ M of the C68 ribosomes with 10 μ M of the Cy3-/biotin-modified DNA oligonucleotide in a total volume of 20 μ L for 30 min at 30°C. To remove unbound oligonucleotide, layer the above mixture onto imaging buffer containing 10% (w/v) sucrose in a centrifuge tube and pellet the ribosomes by ultracentrifugation at 180,000 $\times g$ for 1 h at 4°C. Remove as much supernatant as possible and resuspend the ribosomes in the residual supernatant (see Note 9). Aliquot the ribosomes, freeze in liquid nitrogen, and store at –80°C until use.

3. Make a flow chamber with a volume of 15 μL by placing a coverslip onto a glass slide using two polyester spacers and fastening them with paper clips (see Note 10).
4. Flow 15 μL of 3.0 mg/mL biotinylated BSA into the chamber and incubate for 2 min. Wash the chamber with 30 μL of imaging buffer.
5. Introduce 15 μL of 0.33 mg/mL streptavidin into the chamber. Incubate for 2 min and then wash the chamber with 30 μL of imaging buffer.
6. Immobilize ~20 pM C68 ribosomes modified with biotin-DNA to the surface. Incubate for 2 min and wash the chamber with 30 μL of imaging buffer.
7. Thaw Sol. A and Sol. B contained in the protein synthesis kit on ice, and assemble the following components in a tube in the order listed below:

Nuclease-free water	to 20 μL
Sol. A	5 μL
Sol. B	1 μL
Template DNA (0.5 μg)	$\times \mu\text{L}$ (see Note 6)

8. Flow 20 μL of the mixed solution into the chamber (see Note 11).
9. Remove the paper clips, polyester spacers, and the excess buffer, and seal the chamber using nail polish to prevent the final solution from evaporating during observation.

3.5. Microscope Experiments and Data Analysis

Fluorescence images are taken using a time exposure of 200 ms. Immediately afterward, the stage is moved quickly to avoid photo-bleaching of molecules due to the absence of oxygen-scavenging enzymes. GFP and Cy3 fluorescence is detected using total internal reflection (TIR) excitation with 488 and 532 nm lasers.

1. The co-localization position for both GFP and Cy3 images is calibrated by nonspecifically immobilized fluorescent microspheres.
2. Mount the flow chamber on the stage. After the GFP images are recorded using a time exposure of 200 ms for 20 s, Cy3 images are detected at the same image position by changing the dichroic filter and laser source quickly for image co-localization.
3. At the indicated time points, repeat steps 2–3.
4. Nearly 170 \times 170 pixels were picked up from the center of a 512 \times 512 pixel whole image area. Using Adobe Photoshop, the subtracted images were filtered by Gaussian blurring with a five-pixel radius to obtain a high signal-to-noise ratio (Fig. 4).

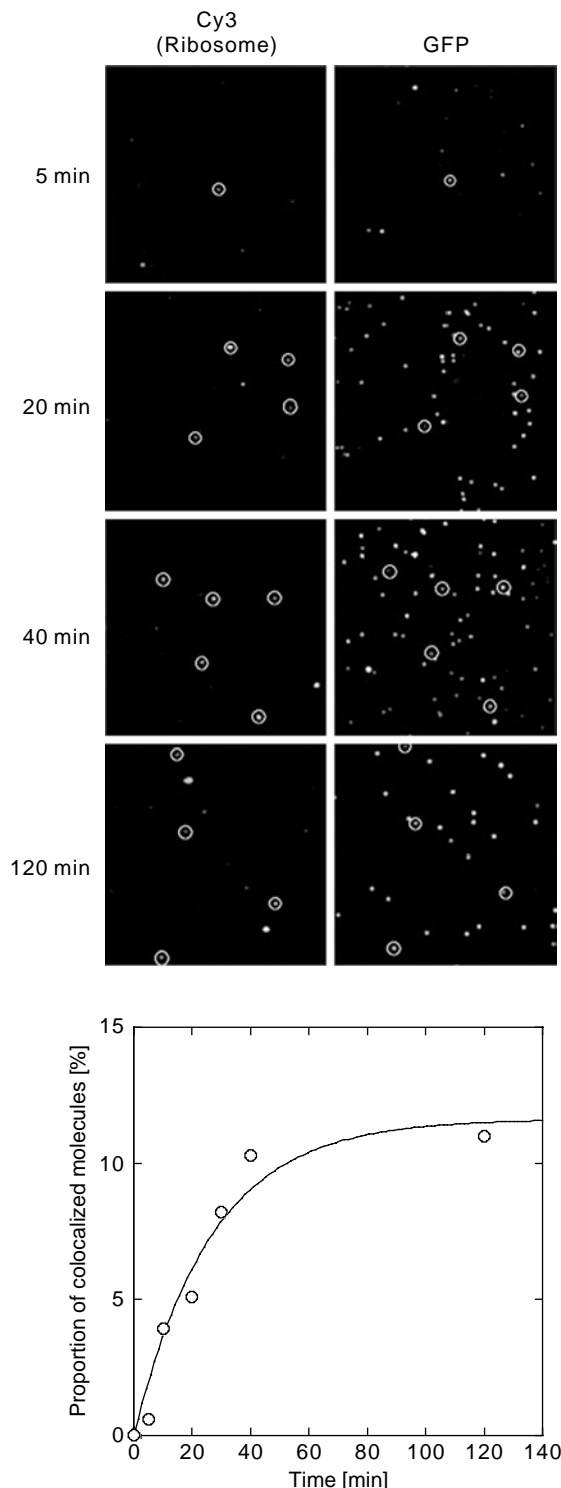


Fig. 4. (a) Fluorescence images of Cy3-labeled ribosomes (left panel) and GFP molecules (right panel). GFP was synthesized and displayed on the surface-immobilized ribosomes. The white circles highlight co-localized spots of GFP and Cy3. (b) Time course of the population of co-localized fluorescence molecules.

4. Notes

1. The variant used in our previous study (2) contains the original Q80R mutation from PCR cloning (23). Q80R is known to be a neutral mutation.
2. Protein D is a small major capsid protein (110 amino acids) from λ phage and is essential for stable head morphogenesis. The protein has been shown to be a monomeric protein with efficient expression properties when expressed in *E. coli* (24). T21-V110 of protein D, lacking the unstructured N-terminal tail, has also been shown to retain the biophysical properties of the full-length protein (15, 25).
3. pET vectors contain the highly efficient RBS (AAGGAGG) with the appropriate spacing upstream of a start codon. They also contain a translation enhancer (the epsilon sequence) upstream of the RBS, which has been shown to improve protein synthesis (26). Especially useful is the *Nhe* I site immediately following the start codon in the pET21a-c and pET23a-c vectors, as it is readily amenable to vector construction. We used a pET21c vector (2).
4. We usually use acetylated BSA from Sigma-Aldrich (B-2518) modified with EZ-Link Maleimide-PEG₂-Biotin from Thermo SCIENTIFIC (21901) because of the low fluorescence impurities present in both reagents.
5. Template DNA for protein synthesis should be nuclease-free. It is noted that plasmid DNA prepared from many commercial kits often contains RNase A. PCR products can be also used as the template DNA for the protein synthesis reaction in the PURE system. Follow the recommendations and guidelines in manufacturer's manual to prepare the template DNA.
6. Sol. A (containing salts, tRNAs, and other agents) and Sol. B (containing enzymes and ribosomes) must be thawed on ice just before use and multiple freeze-thaw cycles avoided because some enzymes present in these reagents may be inactivated.
7. A plasma cleaner is a more rapid and effective method of cleaning cover slips than chemical washing (27).
8. Ribosomes have a tendency to adsorb nonspecifically onto the coverslips just after cleaning with the plasma cleaner. The coverslips need to be stored for 5–7 days after cleaning to avoid the adsorption.
9. The hybridization of C68 ribosomes and the Cy3-/biotin-modified DNA oligonucleotide can be confirmed by agarose gel electrophoresis followed by fluorescence detection using a fluorescence scanner (7).

10. Double-sided sticky tape can be used instead of polyester film.
11. Since molecular oxygen is required for chromophore formation of GFP, the final solution does not contain the enzymatic oxygen-scavenging system. We have previously shown that the oxygen-scavenging system prevents chromophore formation of GFP (2).

Acknowledgments

The authors thank Prof. Takuya Ueda and Dr. Yoshihiro Shimizu (The University of Tokyo) for the gift of plasmid pD-SecM-pURE1 and for helpful discussion, and Prof. Joseph D. Puglisi (Stanford University) for the gift of *E. coli* expressing C68 ribosomes.

References

1. Fedorov, A. N., and Baldwin, T. O. (1997) Cotranslational protein folding. *J. Biol. Chem.* **272**, 32715–32718.
2. Uemura, S., Iizuka, R., Ueno, T., Shimizu, Y., Taguchi, H., Ueda, T., Puglisi, J. D., and Funatsu, T. (2008) Single molecule imaging of full protein synthesis by immobilized ribosomes. *Nucleic Acids Res.* **36**, e70.
3. Nakatogawa, H., and Ito, K. (2002) The ribosomal exit tunnel functions as a discriminating gate. *Cell* **108**, 629–636.
4. Ban, N., Nissen, P., Hansen, J., Moore, P. B., and Steitz, T. A. (2000) The complete atomic structure of the large ribosomal subunit at 2.4 Å resolution. *Science* **289**, 905–920.
5. Nissen, P., Hansen, J., Ban, N., Moore, P. B., and Steitz, T. A. (2000) The structural basis of ribosome activity in peptide bond synthesis. *Science* **289**, 920–930.
6. Yusupov, M. M., Yusupova, G. Z., Baucom, A., Lieberman, K., Earnest, T. N., Cate, J. H., and Noller, H. F. (2001) Crystal structure of the ribosome at 5.5 Å resolution. *Science* **292**, 883–896.
7. Dorywalska, M., Blanchard, S. C., Gonzalez, R. L., Kim, H. D., Chu, S., and Puglisi, J. D. (2005) Site-specific labeling of the ribosome for single-molecule spectroscopy. *Nucleic Acids Res.* **33**, 182–189.
8. Shimizu, Y., Inoue, A., Tomari, Y., Suzuki, T., Yokogawa, T., Nishikawa, K., and Ueda, T. (2001) Cell-free translation reconstituted with purified components. *Nat. Biotechnol.* **19**, 751–755.
9. Shimizu, Y., Kanamori, T., and Ueda, T. (2005) Protein synthesis by pure translation systems. *Methods* **36**, 299–304.
10. Kolb, V. A., Makeyev, E. V., Ward, W. W., and Spirin, A. S. (1996) Synthesis and maturation of green fluorescent protein in a cell-free translation. *Biotechnol. Lett.* **18**, 1447–1452.
11. Jermutus, L., Kolly, R., Földes-Papp, Z., Hanes, J., Rigler, R., and Plückthun, A. (2002) Ligand binding of a ribosome-displayed protein detected in solution at the single molecule level by fluorescence correlation spectroscopy. *Eur. Biophys. J.* **31**, 179–184.
12. Ito, Y., Suzuki, M., and Husimi, Y. (1999) A novel mutant of green fluorescent protein with enhanced sensitivity for microanalysis at 488 nm excitation. *Biochem. Biophys. Res. Commun.* **264**, 556–560.
13. Patterson, G. H., Knobel, S. M., Sharif, W. D., Kain, S. R., and Piston, D. W. (1997) Use of the green fluorescent protein and its mutants in quantitative fluorescence microscopy. *Biophys. J.* **73**, 2782–2790.
14. Crameri, A., Whitehorn, E. A., Tate, E., and Stemmer, W. P. (1996) Improved green fluorescent protein by molecular evolution using DNA shuffling. *Nat. Biotechnol.* **14**, 315–319.
15. Matsuura, T., and Plückthun, A. (2003) Selection based on the folding properties of proteins with ribosome display. *FEBS Lett.* **539**, 24–28.
16. Matsuura, T., Yanagida, H., Ushioda, J., Urabe, I., and Yomo, T. (2007) Nascent chain,

- mRNA, and ribosome complexes generated by a pure translation system. *Biochem. Biophys. Res. Commun.* **352**, 372–377.
- 17. Evans, M. S., Ugrinov, K. G., Frese, M. A., and Clark, P. L. (2005) Homogeneous stalled ribosome nascent chain complexes produced *in vivo* or *in vitro*. *Nat. Methods* **2**, 757–762.
 - 18. Muto, H., Nakatogawa, H., and Ito, K. (2006) Genetically encoded but nonpolypeptide prolyl-tRNA functions in the A site for SecM-mediated ribosomal stall. *Mol. Cell* **22**, 545–552.
 - 19. Ohashi, H., Shimizu, Y., Ying, B. W., and Ueda, T. (2007) Efficient protein selection based on ribosome display system with purified components. *Biochem. Biophys. Res. Commun.* **352**, 270–276.
 - 20. Hayes, C. S., Bose, B., and Sauer, R. T. (2002) Proline residues at the C-terminus of nascent chains induce SsrA-tagging during translation termination. *J. Biol. Chem.* **277**, 33825–33832.
 - 21. Hayes, C. S., and Sauer, R. T. (2003) Cleavage of the A site mRNA codon during ribosome pausing provides a mechanism for translational quality control. *Mol. Cell* **12**, 903–911.
 - 22. Powers, T., and Noller, H. F. (1991) A functional pseudoknot in 16S ribosomal RNA. *EMBO J.* **10**, 2203–2214.
 - 23. Chalfie, M., Tu, Y., Euskirchen, G., Ward, W. W., and Prasher, D. C. (1994) Green fluorescent protein as a marker for gene expression. *Science* **263**, 802–805.
 - 24. Forrer, P., and Jaussi, R. (1998) High-level expression of soluble heterologous proteins in the cytoplasm of *Escherichia coli* by fusion to the bacteriophage lambda head protein D. *Gene* **224**, 45–52.
 - 25. Yang, F., Forrer, P., Dauter, Z., Conway, J. F., Cheng, N., Cerritelli, M. E., Steven, A. C., Plückthun, A., and Wlodawer, A. (2000) Novel fold and capsid-binding properties of the λ -phage display platform protein gpD. *Nat. Struct. Biol.* **7**, 230–237.
 - 26. Ollins, P. O., and Rangwala, S. H. (1989) A novel sequence element derived from bacteriophage T7 mRNA acts as an enhancer of translation of the *lacZ* gene in *Escherichia coli*. *J. Biol. Chem.* **264**, 16973–16976.
 - 27. Selvin, P. R., and Ha, T. (2007) Single-Molecule Techniques. Cold Spring Harbor Laboratory Press, NY.

Chapter 15

Single-Molecule Measurements of Topoisomerase Activity with Magnetic Tweezers

Yeonee Seol and Keir C. Neuman

Abstract

Magnetic tweezers provide a versatile tool enabling the precise application of force and torque on individual biomolecules. These properties make magnetic tweezers uniquely suited for the study of DNA topology and topoisomerases at the single-molecule level. Single-molecule approaches, which are complementary to ensemble biochemical and structural approaches, have provided remarkable insights into the mechanisms of topoisomerase activity and interactions with DNA. Here, we describe how to make single-molecule measurements of topoisomerase activity with a magnetic tweezers instrument. We provide detailed instructions for preparing and characterizing DNA substrates, flow cells, and supercoilable DNA tethers. We then describe magnetic tweezers measurements of supercoil relaxation by single topoisomerases.

Key words: Magnetic tweezers, Single molecule, DNA topology, DNA topoisomerase

1. Introduction

Cellular DNA encompasses a variety of topological states: over- and under-winding of the double helix (positive and negative supercoils), interlinking between two DNA molecules (catenation), and intramolecular linking of DNA (knotting) (1). Such variation in DNA topology is a pervasive factor influencing a multitude of cellular activities including gene expression, DNA packaging and condensation, and chromosome segregation (2–4). Eukaryotic and prokaryotic genomes are maintained in defined topological states. In vivo, DNA topology is dictated by an interplay between the physical binding and wrapping of DNA by structural proteins and the activity of topoisomerases that transiently introduce single- or double-stranded breaks in the DNA (2).

Extensive biochemical and structural studies have provided a framework to understand how topoisomerases alter DNA topology (5–7). Over the past 15 years, single-molecule techniques have increasingly been used to elucidate the detailed mechanisms of topoisomerases (8, 9). Magnetic tweezers, in particular, are well suited to study topoisomerases as they are uniquely capable of controlling and measuring the topology of individual DNA molecules (10–14).

Magnetic tweezers typically consist of a pair of small permanent magnets arranged with their opposite poles separated by a small gap (~1 mm) placed above a flow-cell on an inverted microscope. The magnets impose an upward force on the magnetic bead in the range of 0.1–100 pN (10^{-12} N), which can be controlled by changing the vertical position of the magnets. The DNA molecule tethering the magnetic bead can be stretched and twisted by adjusting the position and rotation of the magnets. A microscope objective images the bead onto a CCD camera, and the three-dimensional position of the bead is obtained with 2–5 nm accuracy in real time (30–200 frames per second) by image processing (13, 15). With this relatively simple set-up, the topology of individual DNA molecules, subjected to well-controlled pulling forces, can be precisely controlled, and the corresponding changes in DNA extension can be measured with high accuracy. Several excellent reviews and guides for designing and building magnetic tweezers are available (10, 12, 13, 16). Here, we focus on single-molecule topoisomerase assays rather than the details of the magnetic tweezers instrumentation.

Single-molecule topoisomerase assays using magnetic tweezers complement ensemble biochemical assays in several important aspects (8, 9). First, enzymatic rates measured in single-molecule assays are not affected by the presence of a subpopulation of inactive enzyme, which can artificially lower the average rate measured in an ensemble assay. In some instances, average supercoil relaxation rates significantly underestimated the single-enzyme rate (4). Furthermore, the processivity, i.e., the number of catalytic cycles per binding event, can be directly measured from single-molecule records. This is facilitated by the high degree of positive and negative supercoiling achievable with a magnetic tweezers, and by the fact that changes of a single linking number are observable. Finally, tension in the DNA can dramatically affect enzymatic rates, or indeed the catalytic pathway (17). Analysis of these effects can provide molecular level details of the physical mechanisms of topoisomerase activity (8).

Here, we present detailed procedures to measure the activity of human topoisomerase II α supercoil relaxation. These protocols can be readily adapted to measure the activity of other type I and type II topoisomerases.

2. Materials

2.1. Coilable DNA Substrate Preparation

2.1.1. PCR Reaction

1. Two PCR templates: pET28a plasmid (EMD4 Biosciences) for the 5 kb DNA center fragment and pBluescript II KS + plasmid (Stratagene) for the handles.
2. Two sets of PCR primers to generate a 5 kb DNA and a 500 bp DNA handle fragment.
 pET28a forward: 5'-GGACCTGCTTCCAACGCCATAT
 TCAACGGAAACG-3'
 pET28a reverse: 5'-GGGTCTCGACCAAACAGCTGATTG
 CCCTTCAC-3'
 pBluescript II KS forward: 5'-GGACCTGCTTCGTTGTGG
 CGTAATCATGGTCATAG-3'
 pBluescript II KS reverse: 5'-GGGTCTCGTGGTTATAGTCC
 TGTCGGGTTTC-3'
3. PCR reaction mixture for 5 kb DNA: 1 U of Phusion DNA polymerase (F-530S, Finnzymes), 0.2 mM dNTPs, 1 ng of pET28a, 0.5 μ M each of pET28a forward and reverse primers in 50 μ l 1 \times PCR reaction buffer.
4. PCR reaction mixture for 500 bp DNA handles: 1 U of Phusion DNA polymerase, 10 mM each of dATP, dCTP, and dGTP, 0.12 mM dTTP, 0.08 mM biotin-16-dUTP for Handle 1 or 0.08 mM digoxigenin-11-dUTP for Handle 2, 1 ng of pBluescript KS + II, 0.5 μ M each of pBluescript II forward and reverse primers in 50 μ l 1 \times PCR reaction buffer.
5. Thermocycler for PCR reaction and PCR cleanup kit for purification of PCR products.

2.1.2. Restriction Enzyme Digestion and T4 DNA Ligase Reaction

1. Restriction enzyme reaction mixture for 5 kb DNA fragment: 30 U of BsaI, 20 U of BfuAI, ~1.2 μ g of pET28 PCR product in 50 μ l 1 \times RE buffer.
2. Restriction enzyme reaction mixture for 500 bp DNA fragment: 30 U of BsaI or 20 U of BfuAI, ~2 μ g of digoxigenin or biotin labeled 500 bp handle in 50 μ l 1 \times RE buffer.
3. T4 DNA ligase reaction mixture: 2 μ l of T4 DNA ligase, 10 nM of digested 5 kb DNA fragment, 20 nM of digested biotin labeled 500 bp DNA (Handle 1), 20 nM of digested digoxigenin labeled 500 bp DNA (Handle 2) in 50 μ l 1 \times ligase buffer.

2.2. Flow-Cell and Stuck-Bead Preparation

1. Flow-cell assembly: #1½ cover glass (24 mm \times 60 mm), #1 cover glass (22 mm \times 40 mm), 5 mm \times 45 mm strips of 80 μ m thick adhesive transfer tape (8153 LE, 3M), silicone vacuum grease (Beckman) and 5 min epoxy (Devcon), flow-cell adaptor

(custom-made, eMachine Shop), PrecisionGlide needle, 18 G1, and Tygon tubing (I.D. 0.04 in., O.D. 0.085 in.).

2. Cover-slip cleaning: KOH pellets (ACS grade), 95% ethanol (ACS grade), 1 l glass beaker, cover glass holder (see Note 4), and sonicator (2510, Branson).
3. Stuck bead preparation: 1 μ l of 4% (w/v) polystyrene beads (1 μ m; A37294, Invitrogen), stuck bead buffer (SB) (13 mg/ml NaHCO₃ in water), and stuck bead wash buffer (SBW): 10 mM Tris-HCl (pH 7.5), and 100 mM MgCl₂.
4. Flow-cell wash buffer (WB): 1× PBS, 1% w/v BSA, and 0.04% Tween-20.

2.3. DNA Tethering

1. DNA incubation mixture: 6 μ l of 200 μ g/ml anti-digoxigenin, 0.32 nM DNA ligation product in 50 μ l 1× PBS.
2. Magnetic bead wash buffer 1 (BWB): 10 mM Tris-HCl, pH 7.5, 1 M NaCl, 1% w/v magnetic beads (Dynabeads MyOne Streptavidin T1; 35601, Invitrogen).

2.4. Topoisomerase II α Assay

1. Topoisomerase II α dilution buffer: 10 mM Tris-HCl, pH 7.7, 0.5 mM dithiothreitol, 0.1 mM EDTA, 40% glycerol, 750 mM KCl, and 1 mM phenylmethanesulfonyl fluoride (PMSF). Aliquot into 100 μ l volumes and store at -20°C.
2. 5× Topoisomerase II α reaction buffer: 50 mM Tris-HCl, pH 8.0, 0.5 mM EDTA, and 500 mM KCl.
3. 1× Topoisomerase II α reaction buffer: 8 ml of 5× Topoisomerase II α reaction buffer, 1.6 ml of 10% w/v BSA, 0.8 ml of 2% v/v Tween-20, 400 μ l of 100 mM PMSF, and water up to 40 ml. Filter the buffer, aliquot into 5 ml volumes, and store at -20°C.
4. Make 100 mM ATP in water and quickly adjust to pH 7 with NaOH in order to prevent autohydrolysis of ATP. Aliquot into 50 μ l volumes and store at -20°C.

3. Methods

To measure the supercoil relaxation activity of topoisomerases, it is critical to make rotationally constrained, i.e., supercoilable or “coilable,” DNA tethers. Non-nicked DNA is rotationally constrained through multiple attachments to the bead at one end and to the surface at the other. The most commonly used linkers are biotin-streptavidin and digoxigenin-anti-digoxigenin. To construct DNA with multiple biotin moieties on one extremity and multiple digoxigenin moieties on the other, we produce three PCR products that we cut and ligate together (18). Standard PCR is used to make the

Coilable DNA substrate assembly

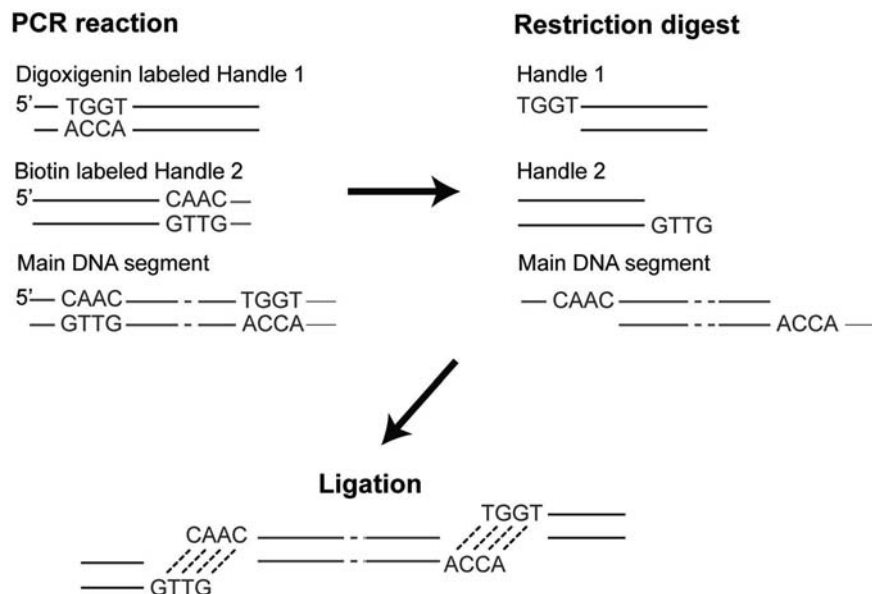


Fig. 1. Schematic of coilable DNA molecule assembly. Three DNA fragments are PCR amplified separately. To make the two DNA “handles” 40% of the dTTP in the PCR reaction is substituted with either biotinylated or digoxigeninylated dUTP to produce multiply labeled DNA. Next, BfuAI and BsaI restriction enzyme digestions generate complementary sticky ends, which are then ligated to form the final DNA product.

unlabeled DNA, whereas the two “handles” containing multiple biotin- or digoxigenin-labeled nucleotides are made by adding a small percentage of appropriately labeled dUTP to the PCR reaction of a ~500 bp template. The primers for the three PCR reactions are designed with unique nonpalindromic restriction sites such that after restriction digest and purification the two labeled DNA handles will ligate onto the unlabeled DNA in a unique orientation with no side products (Fig. 1) (see Note 1). This scheme improves the yield and specificity of the DNA assembly process (see Note 2).

3.1. Protocol for Creating Coilable DNA Molecules (Fig. 1)

1. Prepare the PCR reaction mixtures for generating digoxigenin or biotin-labeled DNA handles (500 bp) and the center DNA fragment (5 kb) (see Note 3).
2. The PCR reaction is as follows: initial melting ($T=98^{\circ}\text{C}$ for 1 min), 30 cycles of three steps: melting ($T=98^{\circ}\text{C}$ for 15 s); annealing ($T=60^{\circ}\text{C}$ for 30 s); and elongation (72°C for 5 min), final elongation ($T=72^{\circ}\text{C}$ for 15 min).
3. Purify DNA PCR product using PCR clean-up kit.
4. Quantify DNA (typical yield is 50 μl of ~200 ng/ μl).
5. Set up three different restriction digest reactions: one with BsaI and the digoxigenin labeled DNA handle, one with BfuAI

and the biotin-labeled DNA handle, and one with both enzymes for the 5 kb center DNA fragment.

6. Incubate the three reactions overnight at 50°C and purify DNA with a PCR clean-up kit.
7. Prepare the ligation reaction mixture and ligate the biotin- and digoxigenin-DNA handles to the main DNA segment at 16°C for 48 h.
8. Clean up DNA with a PCR clean up kit (optional).
9. Gel purify with gel extraction kit the ligated product (~6 kb) from 1% agarose gel (optional).
10. Quantify DNA (typical yield is 50 µl of ~20 ng/µl of final product).

3.2. Cover-Glass Cleaning

1. Place cover glass (#1½, 24 mm×60 mm) in a Teflon cover glass holder (see Note 4).
2. Prepare enough KOH–ethanol solution (15% w/v) to submerge cover glass holder in a 1-l glass beaker (~500 ml).
3. Place the glass beaker in the sonicator and sonicate the cover glass in KOH solution for 20 min.
4. Take out the holder and place it in a new 1 l glass beaker containing deionized water.
5. Sonicate for 20 min.
6. Repeat steps 4 and 5.
7. Take out the holder and rinse each cover glass two to three times with deionized water in a wash bottle to remove any residual KOH or small particles.
8. Squirt 95% ethanol over the cover glass so that water on the surface evaporates rapidly.
9. Dry the cover glass either by microwaving for a few minutes or baking for 15 min in an oven at 150°C.
10. Store the cover glass in an air-tight container. Clean cover-glass can be stored over 6 months.

3.3. Flow-Cell Assembly

1. Attach two strips of double-sided tape (5 mm×45 mm×80 µm) separated by ~5 mm to a #1½ coverslip (24 mm×60 mm) (Fig. 2).
2. Put a cover glass (22 mm×40 mm) over the two strips of double-sided tape on the bottom cover glass to form a ~10 µl volume sample chamber.
3. Put epoxy around the edge of the sample chamber to increase rigidity (optional).

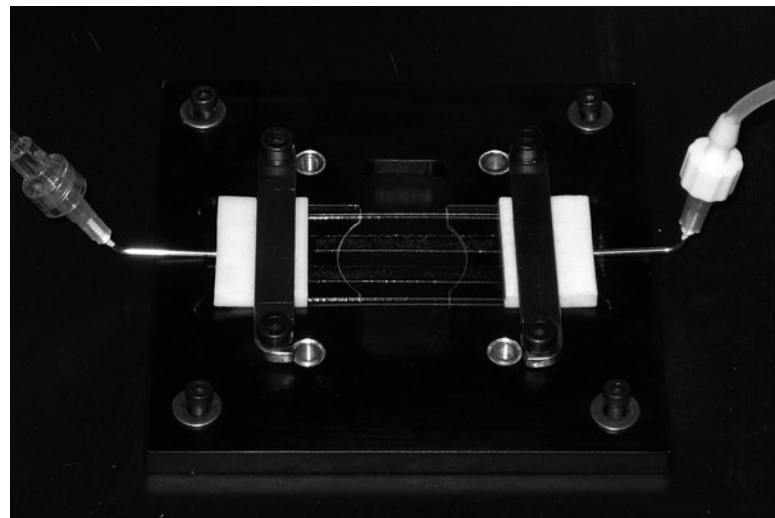


Fig. 2. Flow-cell assembly. Two flow-cell adaptors (*white block*) fastened to the sample-cell holder (*black stage*) with two clamps, enclose the open ends of the flow-cell. The buffer solution is introduced into the flow-cell through a needle (*left side*) and sucked out through the other needle (*right side*) by vacuum. The sample cell holder is mounted on the microscope stage.

3.4. Sticking Reference Beads to the Flow-Cell Surface (see Note 5)

1. Make 0.1% (w/v) polystyrene bead suspension in freshly prepared SB solution.
2. Place two flow-cells in a water-filled humidity chamber (see Note 6).
3. Flow 200 μ l of the bead suspension through the flow-cell and incubate for 30 min at room temperature.
4. Wash the flow-cell with 200 μ l of SBW buffer, close the lid of the humidity chamber, and incubate overnight at room temperature.
5. Wash the flow-cell with 200 μ l of water followed by ~100 μ l ethanol.
6. Remove ethanol immediately and completely dry flow-cells.
7. Bake flow-cells for 7 min on hot plate at ~150°C.
8. Wash with 2 ml of water. Completely remove water with a vacuum line and air dry.
9. Before use, bake flow-cells for 7 min on a hot plate at ~150°C.

3.5. Generation of Coilable DNA Tethers on the Surface with Super-Paramagnetic Beads

1. Prepare DNA incubation mixture in a 0.5-ml microcentrifuge tube (see Note 7).
2. Vortex the tube gently and spin down for 1–2 s. Place the tube in an microcentrifuge tube rack and incubate it for 15–20 min at room temperature to allow the anti-digoxigenin to bind the digoxigenin moieties on the DNA.

3. Pipette 15 μ l of the DNA solution into a flow-cell to overfill the chamber. Add any residual solution to both ends of the flow-cell.
4. Incubate the flow-cell overnight at 4°C or 1 h at RT in the humidity chamber.
5. Wash the flow-cell twice with 200 μ l of WB and incubate for 10 min.
6. While waiting, pipette 10 μ l of a 1% w/v 1 μ m diameter streptavidin magnetic particle suspension into a microcentrifuge tube.
7. Pull beads to the bottom of the tube by placing it on top of a permanent magnet.
8. Gently pipette out the supernatant.
9. Add 200 μ l of BWB buffer and vortex the tube quickly to mix.
10. Repeat steps 7–9 three times.
11. After the final wash, instead of adding BWB, add 100 μ l of WB and vortex quickly.
12. Sonicate the tube for 5 min to disperse any clustered beads.
13. Introduce 15 μ l of the bead solution into the flow-cell and incubate overnight to passivate the surface with BSA.
14. Before use, remove free beads by washing with 1 ml of WB through the flow-cell.
15. Put the flow cell on the sample holder platform (Fig. 2).
16. Put small amount of vacuum grease on the outer edges of the tape. Assemble the two flow-cell adapters onto the sample holder and hand-tighten the screws (Fig. 2).
17. Connect the outlet port of the flow-cell to a vacuum line attached to a waste flask.
18. This procedure typically yields 1 tether per ~300 μ m², roughly 60% of which are coilable.

3.6. Topoisomerase II α Relaxation Assay

1. Prepare enzyme stock, 100 mM ATP, DTT, buffers (WB; Topoisomerase II α dilution buffer; and 1× Topoisomerase II α reaction buffer) on ice. Put enzyme stock in a portable cooler that can hold 0°C for >2 h.
2. Turn on and initialize the instrument.
3. Set the force to ~0.5 pN and adjust the objective position to get a sharp image of a stuck bead.
4. Find a coilable DNA molecule (see Note 8) located within the region of interest where at least one stuck bead is available as a fiducial marker.
5. Exchange WB with the relaxation buffer by filling the reservoir with 1 ml of 1× topoisomerase relaxation buffer and open the vacuum line.

6. Dilute topoisomerase II α enzyme in Topoisomerase II α dilution buffer. Further dilute to make ~100 pM in 1 ml of 1 \times Topoisomerase II α reaction buffer and add 200 μ l to the reservoir (see Note 9).
7. Once almost all of the solution has flowed through the flow-cell, close the vacuum valve.
8. Move the magnet to a position where the desired force is applied to the DNA (<~0.4 pN for negative supercoil formation). Rotate the magnets (25 turns for 5 kb DNA) to generate a DNA plectoneme (Fig. 3).

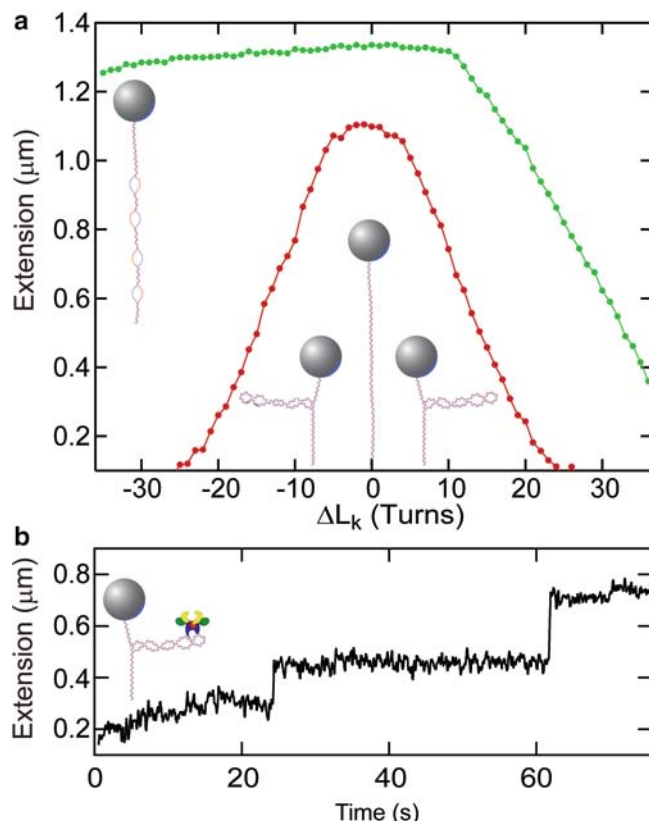


Fig. 3. DNA topology manipulation using magnetic tweezers and human topoisomerase II α relaxation assay. **(a)** DNA topological linking number changes (ΔL_k) due to magnet rotation result in DNA extension changes. At low force (~0.4 pN), DNA plectoneme formation (*inset cartoon*) and subsequent DNA extension changes are symmetric for positive and negative linking number changes (*closed circles*). On the other hand, at higher force (~1 pN), clockwise rotation of the magnets (*negative supercoiling*) leads to melting of the DNA (*upper left inset cartoon*) rather than the formation of plectonemes, thus, there is little change in DNA extension (*open circles*). In the positive direction, more magnet rotations are required for DNA plectoneme formation. These “hat-curves” provide the calibration between the DNA extension and its topological state, which allows the real-time measurement of topoisomerase activity. **(b)** Example data from DNA supercoil relaxation assay of topoisomerase II α . At $t = 0$, 20 positive turns were introduced, which decreased the extension of the DNA. The abrupt increase in DNA extension that occurred a few seconds later resulted from topoisomerase relaxation activity.

9. Supercoil relaxation by topoisomerase is measured from the DNA extension change, which can be calibrated prior to starting the experiment (Fig. 3).
10. When the supercoils are relaxed by a topoisomerase, the extension of the DNA increases (Fig. 3). The DNA molecule is automatically rewound when the extension of the DNA exceeds a preset threshold.

4. Notes

1. We designed primers to contain a nonpalindromic restriction enzyme recognition sequence to prevent ligation between handles or the center DNA fragments containing the same 5' overhang. Also, the nonpalindromic restriction endonucleases were specifically chosen to cut arbitrary sequences distal from their recognition sequences. The sequences at which the enzymes cut are designed to lack adenines since we assume that digoxigenin/biotin–uracil in the cutting sequence decreases the cutting efficiency.
2. The efficiency and specificity of the PCR reaction can be improved by linearizing the plasmid template.
3. The positional noise and temporal resolution of the measurement for a given force and bead size improve for shorter DNA molecules (18). In practice, we find that 3–5 kb DNA tethers offer a good balance between the number of supercoils that can be introduced (~12–25) and the spatial and temporal resolution.
4. A cover-glass holder was made by milling ten slots (~1.5 mm depth and 43 mm height) in a pair of precut Teflon blocks (10 mm thickness, 48 mm height, and 63 mm width) using a 0.033-in. diameter end mill (Fig. 4). The two Teflon blocks are held together by four Teflon rods (10 mm diameter, ~5 cm length) passing through four holes (10 mm diameter) in the corners of the blocks. The spacing between the two blocks can be adjusted to accommodate cover glass of different sizes.
5. To correct for drift of the flow-cell, we track a reference bead stuck to the surface. The position of the reference bead can be used to either actively stabilize the position of the surface, or make a differential measurement of the tethered bead position. Whereas nonspecifically stuck magnetic beads can be used as reference beads, we find that using a nonmagnetic polystyrene bead provides a more stable and reliable reference.
6. We make a simple humidity sample chamber for incubating slides from an empty 200 μ l pipette tip box with the tip holder

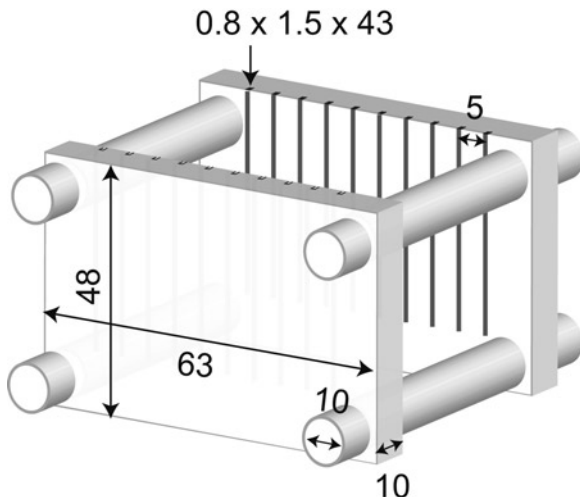


Fig. 4. Teflon cover glass holder. Dimensions are in mm. Slots on the two Teflon blocks were milled with a 0.033-in. diameter end mil. The Teflon blocks are held together by four Teflon rods, which allows adjustable spacing between the blocks to accommodate cover glass of different sizes.

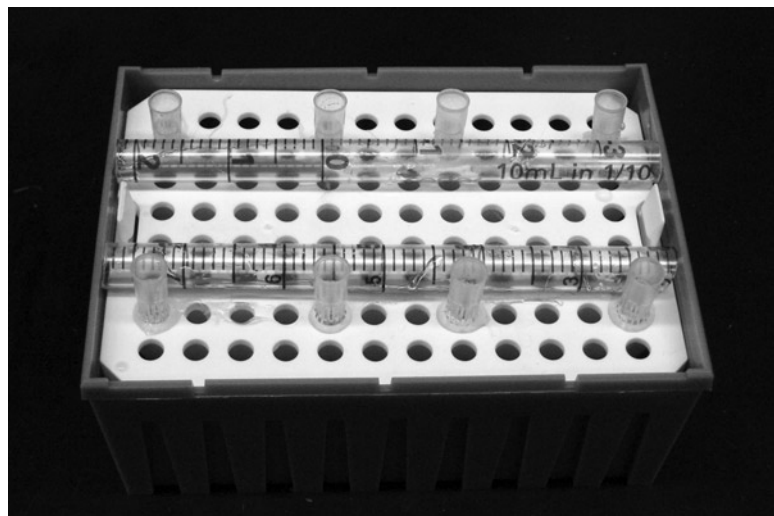


Fig. 5. Humidity chamber construction. Humidity chamber is used for storing flow-cells to prevent buffer evaporation during long incubations. It requires an empty pipette tip box, pipette tips, and a serological pipette, and epoxy. Epoxy should be applied to secure parts.

platform in place and a secure fitting lid (Fig. 5). Make two rows of 200 μ l pipette tips centered on the short axis of the pipette box separated by ~4 cm. The spacing of the tips along each row should be slightly larger than the width of the flow-cell (~3 cm). Secure the tips with epoxy. Cut two pieces of a 5-ml serological pipette to fit along the long axis of the pipette tip box. Place the cut pipette pieces along the long axis on the inside of the 200 μ l tips and secure with epoxy.

7. A single nick along the length of the DNA will render it torsionally unconstrained and unable to be supercoiled. To maximize the number of coilable molecules, the DNA should be handled and stored with a great deal of care. If the DNA fragment is gel purified, it should be done as quickly as possible and under the minimum amount of UV illumination. If nicking of the DNA is suspected, treatment with DNA ligase can improve the fraction of coilable molecules. For long-term storage, the DNA should be in a buffer containing 1 mM EDTA to inhibit nucleases. Repeated freezing and thawing of the DNA can also lead to the generation of nicks, and should be avoided. For much longer DNA substrates ($>\sim 10$ kb) shearing during sample handling such as pipetting can nick the DNA. For such long substrates, additional precautions such as using wider pipette tips should be taken.
8. To rapidly identify rotationally constrained DNA molecules, we impose enough clockwise, i.e., negative supercoiling, turns beyond the buckling transition, $N_B \approx L\sqrt{2Pk_BTF} / 2\pi C$, where L is the contour length of the DNA, $C \approx 90$ $k_B T$ is the torsional modulus, $P = 50$ nm is the persistence length of the DNA, and $k_B T$ is the thermal energy (7), so that at low force (<0.4 pN), the bead will be pulled to the surface of the flow-cell. At high forces (>0.5 pN), on the other hand, the DNA will locally denature and the bead will be pulled upward (7) (Fig. 3). By rapidly switching the force between high and low values the corresponding change in the height of the bead can be readily observed by eye.
9. The concentration of topoisomerase to achieve single-molecule activity is operationally determined when waiting times (the times between relaxation events) are significantly longer (~tenfold) than relaxation events (the time during which the topoisomerase is active). Under the assumption of independent binding, the probability of a second enzyme binding is negligible.

Acknowledgments

The authors would like to thank Marie-Paule Strub, Vincent Croquette, Jean-Francois Allemand, Timothée Lionnet, Omar Saleh, and David Bensimon for assistance and enlightening discussions and Grace Liou for critical reading of the manuscript. This research was supported by the Intramural Research Program of the National Heart, Lung, and Blood Institute, National Institutes of Health.

References

1. Bates, A. D., and Maxwell, A. (2005) *DNA Topology*, 2 ed., Oxford University Press, New York.
2. Wang, J. C. (2002) Cellular roles of DNA topoisomerases: a molecular perspective. *Nat. Rev. Mol. Cell Biol.* **3**, 430–440.
3. Travers, A., and Muskhelishvili, G. (2005) DNA supercoiling – a global transcriptional regulator for enterobacterial growth?, *Nat. Rev. Microbiol.* **3**, 157–169.
4. Espeli, O., and Marians, K. J. (2004) Untangling intracellular DNA topology. *Mol. Microbiol.* **52**, 925–931.
5. Schoeffler, A. J., and Berger, J. M. (2008) DNA topoisomerases: harnessing and constraining energy to govern chromosome topology. *Q Rev. Biophys.* **41**, 41–101.
6. Corbett, K. D., and Berger, J. M. (2004) Structure, molecular mechanisms, and evolutionary relationships in DNA topoisomerases. *Annu. Rev. Biophys. Biomol. Struct.* **33**, 95–118.
7. Champoux, J. J. (2001) DNA topoisomerases: structure, function, and mechanism. *Annu. Rev. Biochem.* **70**, 369–413.
8. Charvin, G., Strick, T. R., Bensimon, D., and Croquette, V. (2005) Tracking topoisomerase activity at the single-molecule level. *Annu. Rev. Biophys. Biomol. Struct.* **34**, 201–219.
9. Lipfert, J., Koster, D. A., Vilfan, I. D., Hage, S., and Dekker, N. H. (2009) Single-molecule magnetic tweezers studies of type IB topoisomerases. *Methods Mol. Biol.* **582**, 71–89.
10. Vilfan, I. D., Lipfert, J., Koster, D. A., Lemay, S. G., and Dekker, N. H. (2009) Magnetic Tweezers for Single-Molecule Experiments in *Handbook of Single-Molecule Biophysics* p 371, Springer.
11. Neuman, K. C., and Nagy, A. (2008) Single-molecule force spectroscopy: optical tweezers, magnetic tweezers and atomic force microscopy. *Nat. Meth.* **5**, 491–505.
12. Neuman, K. C., Lionnet, T., and Allemand, J. F. (2007) Single-molecule micromanipulation techniques. *Annual Review of Materials Research* **37**, 33–67.
13. Lionnet, T., Allemand, J.-F., Revyakin, A., Strick, T. R., Saleh, O. A., Bensimon, D., and Croquette, V. (2008) Single-Molecule Studies Using Magnetic Traps in *Single-Molecule Techniques: A Laboratory Manual*. (Selvin, P. R., and Ha, T., Eds.), Cold Spring Harbor Laboratory Press.
14. Neuman, K. C. (2010) Single-molecule measurements of DNA topology and topoisomerases. *J. Biol. Chem.* **285**, 18967–18971.
15. Gosse, C., and Croquette, V. (2002) Magnetic tweezers: micromanipulation and force measurement at the molecular level. *Biophys. J.* **82**, 3314–3329.
16. Charvin, G., Allemand, J. F., Strick, T. R., Bensimon, D., and Croquette, V. (2004) Twisting DNA: single molecule studies. *Contemporary Physics* **45**, 383–403.
17. Nollmann, M., Stone, M. D., Bryant, Z., Gore, J., Crisona, N. J., Hong, S. C., Mitelheiser, S., Maxwell, A., Bustamante, C., and Cozzarelli, N. R. (2007) Multiple modes of *Escherichia coli* DNA gyrase activity revealed by force and torque. *Nat. Struct. Mol. Biol.* **14**, 264–271.
18. Revyakin, A., Ebright, R. H., and Strick, T. R. (2005) Single-molecule DNA nanomanipulation: improved resolution through use of shorter DNA fragments. *Nat. Methods* **2**, 127–138.

Chapter 16

Assembly of Recombinant Nucleosomes on Nanofabricated DNA Curtains for Single-Molecule Imaging

Ja Yil Lee and Eric C. Greene

Abstract

Eukaryotic chromosomes are highly packed into chromatin, the basic unit of which is the nucleosome. The presence of nucleosomes and the resulting organization of the genome into higher-order chromatin structures has profound consequences for virtually all aspects of DNA metabolism, including DNA transcription, repair, and chromosome segregation. We have developed novel approaches for nanofabricating “DNA curtains” for high-throughput single-molecule imaging, and we have begun adapting these new research tools in an effort to begin studying chromatin biology at the single-molecule level. In this protocol, we describe procedures for assembly and real-time single-molecule visualization of DNA curtains bound by reconstituted nucleosomes made from recombinant histones.

Key words: DNA curtain, TIRF microscopy, Lipid bilayer, Nanofabrication, Nucleosomes, Chromatin

1. Introduction

In eukaryotic cells, genomic DNA is packed into chromatin. The primary building block of chromatin is a nucleosome, which is comprised of DNA and a histone octamer. In a canonical nucleosome, ~147 base pairs (bp) of DNA is wrapped in ~1.7 turns around an octamer containing two of each histone H2A, H2B, H3, and H4 (1, 2). Chromatin plays a major role in all aspects of DNA metabolism such as gene expression, replication, and repair because the proteins and enzymes associated with each of these biological pathways necessarily interact with nucleosomes to access any potential binding targets in the genome (1, 3–8).

We have established a new technology referred to as “DNA curtains,” which enables concurrent visualization of hundreds of individual DNA molecules and any associated proteins in real

time (9–13). This technique can be applied to the study of virtually any protein–DNA interactions and is based on a supported lipid bilayer, TIRFM (total internal reflection fluorescence microscopy), and nanofabricated barriers to lipid diffusion. The lipid bilayer coats the surface of a microfluidic sample chamber, and in the presence of buffer flow, DNA molecules linked by one end to the mobile lipids are pushed to the leading edges of the nanofabricated barriers. YOYO1-stained DNA molecules and fluorescently tagged proteins can then be imaged by TIRFM. This technique presents a rapid and direct high-throughput experimental platform to investigate the interactions between protein and DNA, and can be used for optical mapping of protein binding sites, visualizing assembly and disassembly of nucleoprotein complexes, and measuring protein movement along DNA in real time (11, 12, 14–17).

We have previously published protocols for making DNA curtains, including details of the electron-beam lithography for making nanofabricated barriers, along with procedures for flowcell construction and lipid bilayer deposition, and the use of quantum dots (QDs) as fluorescent protein labels for single-molecule imaging, and we refer the reader to previous publications for full details (11–14).

In this report, we focus on describing the full experimental procedures for expression and purification of recombinant yeast histones, assembly of nanofabricated DNA curtains bound by recombinant nucleosomes for single molecule imaging by TIRFM, and procedures for mapping the positions of QD-labeled nucleosomes on DNA (17). Once nucleosomes are assembled on the DNA, these substrates can be used as the starting point for a number of single molecule experiments on chromatin biology that one might envision.

2. Materials

2.1. Preparation of DNA with Nucleosomes

2.1.1. Expression and Purification of Histones

1. *E. coli* Rosetta strain or HMS174(DE3)pLysS (Stratagene) for protein expression and plasmids for histone expression (see Table 1). All plasmids are maintained and propagated in *E. coli* XL1 Blue.
2. LB broth supplemented with 34 µg/mL chloramphenicol and 1 µg/mL carbenicillin; 1 M IPTG (isopropyl β-D-1-thiogalactopyranoside).
3. Tris-sucrose buffer: 50 mM Tris-HCl (pH 8.0), 10% (w/v) sucrose, and 1 mM benzamidine.
4. TW buffer: 50 mM Tris-HCl (pH 7.5), 100 mM NaCl, 1 mM EDTA, 5 mM β-mercaptoethanol (βME), 1 mM benzamidine, and 1% (w/v) Triton X-100.

Table 1
Plasmids and *E. coli* strains for each type of histone

Histones	Wild-type	All HA-tags	Single FLAG-tags	Triple FLAG tags
Plasmid	pET11a	pET3a	pET3a	pET11a
Expression strain	Rosetta (DE3)pLysS	HMS174 (DE3)pLysS	Rosetta (DE3)pLysS	Rosetta (DE3)pLysS

5. Urea buffer: 10 mM Tris–HCl (pH 8.0), 7 M urea, 1 mM EDTA, 5 mM βME, and 100 mM NaCl for wt and HA-tagged H2A and H2B, 200 mM NaCl for wt and HA-tagged H3 and H4, or 100 mM for all FLAG. Deionize these buffers with 25 g/L AG 501-X8 resin (Cat. No. 142-6424, Bio Rad) for at least 30 min at RT or overnight at 4°C *before* adding NaCl. Use 1.0 µm Whatman paper to remove AG 501-X8 resin after deionization.
 6. Unfolding buffer: 20 mM Tris–HCl (pH 7.5), 7 M guanidinium-HCl, and 10 mM DTT.
 7. Buffer A: 10 mM Tris–HCl (pH 8.0), 7 M urea, 1 mM EDTA, and 1 mM DTT.
 8. Buffer B: 10 mM Tris–HCl (pH 8.0), 7 M urea, 1 mM EDTA, 1 mM DTT, and 1 M NaCl.
 9. Tris dialysis buffer: 10 mM Tris–HCl (pH 8.0) with and without 5 mM βME.
 10. Protein purification columns: 5 mL HiTrap Q and SP ion exchange columns, and Superdex 200 (16/60) gel filtration column, all purchased from GE Healthcare.
 11. Refolding buffer: 10 mM Tris–HCl (pH 8.0), 2 M NaCl, 1 mM EDTA, and 5 mM βME.
 12. 10,000 MWCO Centricon tube (GE Healthcare).
 13. Dialysis tubing: 3,500 MWCO, 7,000 MWCO and 10,000 MWCO dialysis buttons.
 14. Lyophilizer (Labconco).
 15. Microtip sonicator.
- 2.1.2. Nucleosome Reconstitution on λ-DNA Substrate**
1. Biotinylated λ-DNA (48,502 bp; purchased from NEB) (see Note 1).
 2. 1× TE (pH 8.0) with and without 1.5 M NaCl.
 3. Purified recombinant histones (see Subheadings 2.1.1 and 3.1).

2.2. DNA Curtains**2.2.1. Liposome Preparation**

1. Lipid buffer: 10 mM Tris–HCl (pH 8.0), and 100 mM NaCl. Filter this buffer using a 0.22-μm filter.
2. Lipids purchased from Avanti Polar Lipids: DOPC (1,2-dioleoyl-*sn*-glycero-3-phosphocholine) (Cat. No. 850375C), mPEG 550-POPE (1,2-dioleoyl-*sn*-glycero-3-phosphoethanolamine-*N*-[methoxy(polyethylene glycol)-550]) (Cat. No. 880530C), and Biotin-DPPE (1,2-dipalmitoyl-*sn*-glycero-3-phosphoethanolamine-*N*-(cap biotinyl)) (Cat. No. 870277X). Lipids can be stored at -20°C for several months.
3. 99% chloroform.
4. Microtip sonicator.
5. Hamilton syringes.

2.2.2. Flow Cell Preparation

1. Flowcell with nanofabricated barriers to lipid diffusion made using electron-beam lithography as described in the previous publications (11–13).
2. Biotinylated liposome solution (see Subheadings 2.2.1 and 3.2.1).
3. BSA buffer: 40 mM Tris–HCl (pH 7.8), 0.2 mg/mL bovine serum albumin (BSA), 50 mM NaCl, and 1 mM MgCl₂.
4. 0.25 mg/mL streptavidin in BSA buffer.
5. Biotinylated λ-DNA assembled with reconstituted nucleosomes (see Subheadings 2.1.2 and 3.1).
6. 300–500 nM anti-FLAG or anti-HA conjugated QDs (see Note 2).

2.2.3. TIRF Microscopy

1. Imaging buffer: 40 mM Tris–HCl (pH 7.8), 0.2 mg/mL BSA, 1 mM DTT, 0.8% (w/w) D-glucose, GLOXY (98 U/mL of glucose oxidase and 1,486 U/mL of catalase), and 0.1–0.3 nM YOYO1 (Cat. No. Y3601, Invitrogen).
2. Nikon TE-2000U microscope modified for prism-type TIRF illumination and equipped with a Nikon Plan Apo 60× (water-immersion, NA 1.2) or Plan Apo 100× (oil-immersion, NA 1.4), and a dual-view imaging system (Photometrics) equipped with a 630-nm dichroic mirror (necessary for two color imaging applications; see Note 3).
3. Flow system: syringe pump (KD Scientific), injection valve (Upchurch), and shut-off valve (Upchurch) (Fig. 1).
4. Temperature controller, which is homemade and used to control the temperature of the microfluidic sample chamber.

2.3. Data Acquisition and Analysis

1. NIS-elements imaging software (Nikon). This software is used for data acquisition.
2. ImageJ image processing software, which can be freely downloaded at <http://rsbweb.nih.gov/ij/> and plug-ins for data

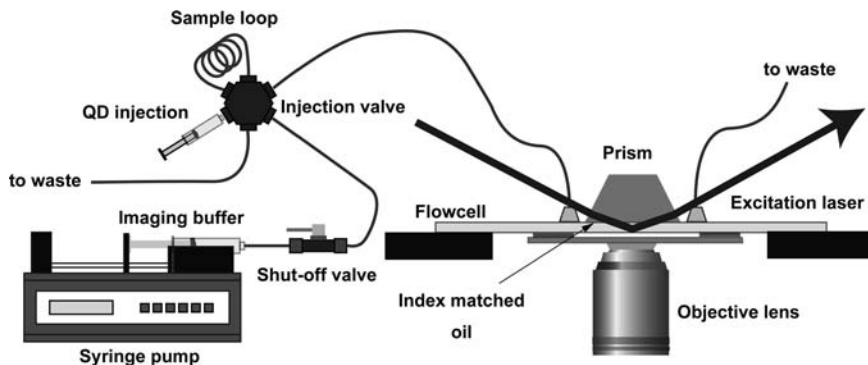


Fig. 1. Schematic of the fluorescence microscope setup and sample delivery system. Prism-type TIRF microscopy with 488 nm laser is used for fluorescence imaging. Index matching oil between prism and flowcell prevents the scattering of excitation laser. The flow system is comprised of syringe pump, shut-off valve, injection valve, and tubes. The syringe pump injects imaging buffer into a flowcell and forms DNA curtains. The flow can be momentarily stopped by a shut-off valve. The QDs are injected through an injection valve.

analysis: OI_cut_RGBmerge and Align RGB planes, which are freely downloaded from other websites.

3. Igor Pro software (WaveMetrics). This is used to obtain the positions of QDs based on 2D Gaussian fitting, and is programmed manually.

3. Methods

3.1. Preparation of DNA with Nucleosomes

The following protocol outlines full details for purifying recombinant *Saccharomyces cerevisiae* histones from *E. coli*, assembly of the histones into purified octamers, deposition of the octomers onto λ -DNA for DNA curtains (Fig. 2), and procedures for labeling the nucleosomes with QDs for single-molecule imaging. Purification and reconstitution of the nucleosomes is a 6-day procedure, and the following protocol is divided according to what should be done on each day.

3.1.1. Day 1: Expression of *S. cerevisiae* Histones

1. Histones are expressed from plasmids pET3A or pET11a, and grown in *E. coli* Rosetta cells (see Table 1).
2. Bacteria are grown at 37°C in LB broth with 34 µg/mL chloramphenicol and 1 µg/mL carbenicillin.
3. Induction is performed at OD₆₀₀=0.6–0.8 using 400 µL of 1 M IPTG per 1 L of culture, and growth is continued for 4 h at 37°C.
4. Cells are harvested by centrifugation at 3,000 rpm (2,691 × g) for 10 min at RT (Avanti J-HC, Beckman). Cell pellets are

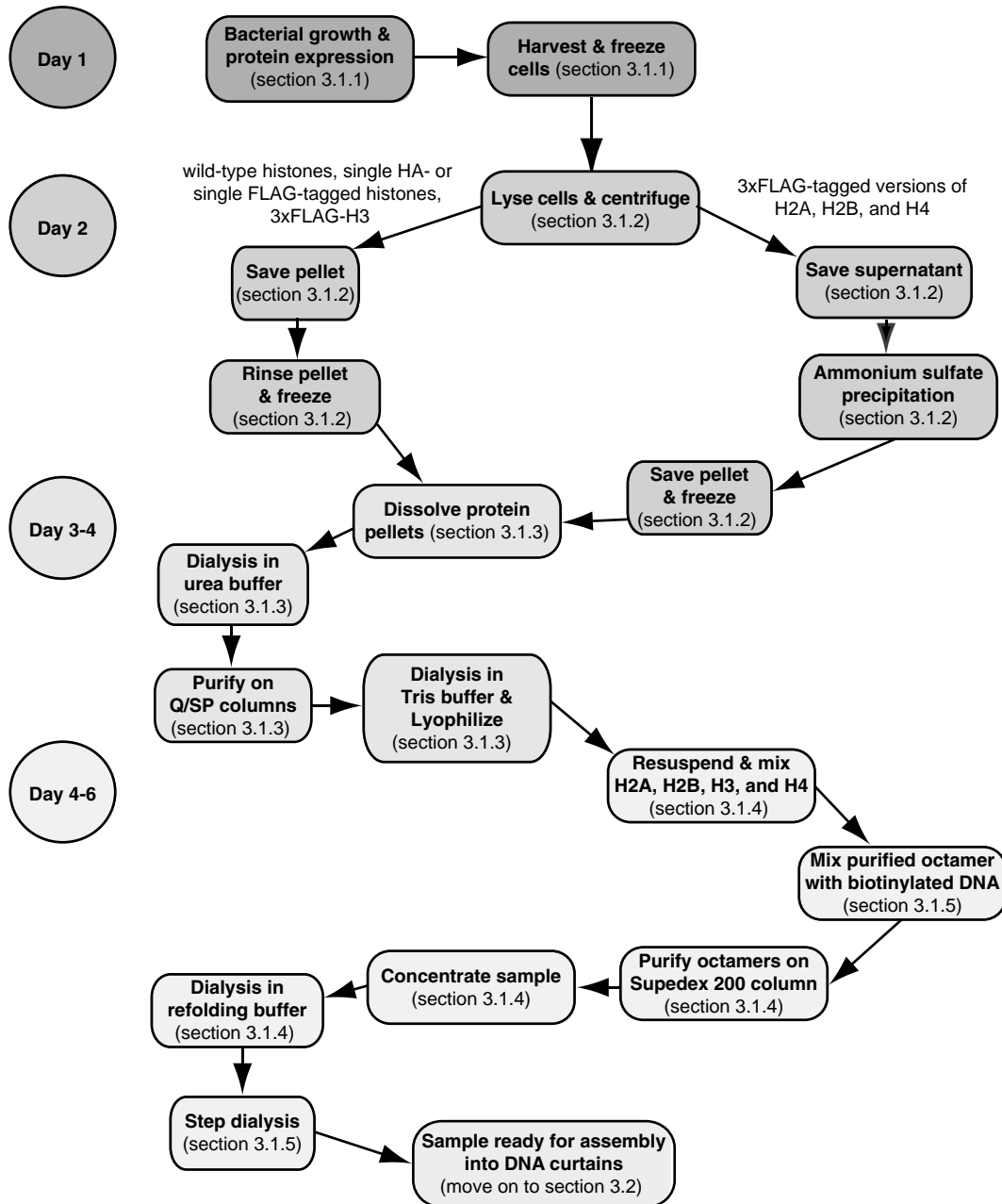


Fig. 2. Flow chart of histone purification and nucleosome reconstitution procedures. The flow chart shows an overview of the procedure of histone purification and nucleosome reconstitution.

resuspended in 10 mL Tris-sucrose buffer per 1 L culture and then frozen at -80°C.

5. Samples are analyzed by SDS-PAGE and Coomassie staining before proceeding to next step.

3.1.2. Day 2: Inclusion Body Purification

The following procedures pertain to wt histones, histones bearing a single FLAG or HA tag, and histone H3 bearing a 3xFLAG tag.

1. Add TW buffer to the cell suspensions up to 35–40 mL total volume and sonicate on ice for 2 min (10 s on and 50 s off) with 40% output.
2. Centrifuge at $20,000 \times g$ for 20 min at 4°C to harvest inclusion bodies.
3. Rinse the resulting protein pellets with TW buffer by resuspending as much as possible with aggressive agitation.
4. Repeat the spin-down and resuspension twice more using TW buffer without Triton X-100.
5. Freeze the protein pellets at –80°C.

The following procedures pertain to histones H2A, H2B, and H4 tagged with 3xFLAG.

1. Sonicate and spin down the cell suspensions as described above for wt histones, but this time keep the supernatant and discard the pellets.
2. Add 0.27 g of ammonium sulfate per mL of supernatant and stir at 4°C for 1 h.
3. Centrifuge at $20,000 \times g$ for 30 min at 4°C.
4. Freeze the protein pellets at –80°C.

3.1.3. Days 3–4: Histone Purification

1. Prepare deionized urea buffer as mentioned in Subheading 2.1.1.
2. Dissolve pellets in 6.5 mL unfolding buffer per 1 L culture and gently agitate for 1 h at RT (see Note 4).
3. Remove remaining cell debris by centrifugation at $20,000 \times g$ for 20 min at 4°C and save the supernatant.
4. Rinse the remaining pelleted material again with 1.5 mL unfolding buffer, spin down at $20,000 \times g$ for 20 min at 4°C, and combine the supernatants.
5. Dialyze the resulting histones against 1–2 L urea buffer using 7,000 MWCO with two buffer changes for several hours at RT or at 4°C if overnight. For each histone, appropriate urea buffer should be used as mentioned in Subheading 2.1.1.
6. Set up Q and SP ion exchange columns in tandem. The columns should be arranged so that the protein sample passes *through the Q column first*. Equilibrate the columns with 10% buffer B for H2A and H2B and all tagged histones, and 20% buffer B for wt H3 and H4.
7. Load dialyzed samples onto the Q/SP tandem columns at a flow rate of 0.5–1 mL/min with a superloop, wash with several column volumes, *remove the Q column* and elute over 20 column

volumes 10–40% buffer-B for H2A and H2B and all tagged histones; over 15 column volumes for 20–50% buffer-B for wt H3 and H4. Elute H4 slower than other histones with a flow rate no greater than 0.4 mL/min or 0.2 mL/min if eluted overnight.

8. Confirm peak fractions using SDS-PAGE and pool peak fractions.
9. Dialyze the histones over several hours against Tris dialysis buffer using 7,000 MWCO dialysis tubing with several times buffer changes at 4°C. Conduct the final two buffer changes without βME.
10. Lyophilize the dialyzed histones. This step can require up to 2 days. Store the lyophilized histones at -20°C.

3.1.4. Days 4–6: Octamer Reconstitution

1. Dissolve the lyophilized histones (~5 mg) in unfolding buffer with gentle agitation for 2–3 h at RT.
2. Mix histones in approximately equimolar ratios (use 10–15% more of H2A/H2B relative to H3/H4), and adjust concentration to 1 mg/mL (0.5 mg/mL for 3xFLAG-H3 containing reactions to reduce aggregation).
3. Dialyze the mixture against refolding buffer using 3,500 MWCO dialysis tubing with a total of four buffer changes over 48 h.
4. Centrifuge to remove any aggregates and concentrate to 1 mL using 10,000 MWCO Centricon tubes.
5. Spin sample in a microcentrifuge for 10 min at maximum speed (~16,000 ×*g*) to remove any remaining aggregates.
6. Resolve histone octomers from H2A/H2B dimers and H3/H4 tetramers on a Superdex 200 (16/60) column at 0.2 mL/min in refolding buffer and collect 1 mL fractions.
7. Analyze the fractions by SDS-PAGE, pool octamer peak, and concentrate it to at least 5 μM using 10,000 MWCO Centricon tubes.
8. Divide into small aliquots and freeze on liquid N₂, and store at -80°C until use.

3.1.5. Nucleosome Reconstitution on λ-DNA Substrate

1. Thaw the purified histone octamers on ice.
2. Mix biotinylated λ-DNA and the purified octamer in 1× TE (pH 8.0) with 1.5 M NaCl on ice. Add the *histone octamer last*. Typically, the reaction volume is 100 μL, where λ-DNA concentration is 0.02 mg/mL (see Note 5) and the molar ratio of DNA:octamer is 1:40, which should yield about five to ten fluorescent nucleosomes per DNA molecule. Different ratios can be used to vary the number of nucleosomes bound to the DNA.

3. Incubate the mixture for 30 min on ice and transfer the mixture to 10,000 MWCO dialysis buttons.
4. Gradually, reduce the NaCl concentration by step dialysis at 4°C for 2 h in 1× TE (pH 8.0) containing: 1 M NaCl; 0.8 M NaCl; 0.6 M NaCl; 0.4 M NaCl. Do a final dialysis step overnight in 1× TE (pH 8.0) with 0.2 M NaCl. Dialysis steps longer than 2 h are fine, but shorter dialysis times will lower reconstitution efficiency.
5. Transfer the λ-DNA with nucleosomes into a 1.5-mL tube, which can be stored at 4°C for several weeks.

3.2. DNA Curtains

3.2.1. Liposome Solution Preparation

1. 20 mg of DOPC, 1.6 mg of mPEG 550-DOPE, and 0.1 mg of Biotin-DPPE are mixed in a clean glass vial using Hamilton syringes that have been cleaned with 99% chloroform.
2. Evaporate all the chloroform from the mixture using ultrapure N₂ gas.
3. Keep the dried lipids in a vacuum chamber for >2 h. This step is essential to ensure *complete* evaporation of residual chloroform (see Note 6).
4. Resuspend the dried lipid mixture with 2 mL of fresh lipid buffer and allow it to hydrate for ≥2 h.
5. Vortex the hydrated lipid mixture for 2–3 min to form large multiple lamellar vesicles and transfer to a new 5 mL tube.
6. Sonicate the liposomes to form small unilamellar vesicles with a microtip sonicator: 1.5 min sonication with 20 W output power followed by a 2-min incubation on ice. Repeat sonication a total of three times.
7. Filter the resulting liposome solution using 0.22 μm filter into 1.5 mL tube. The liposome solution can be stored at 4°C for ~1 month. Do not freeze.

3.2.2. Curtain Assembly

1. Attach a syringe with 10 mL of deionized water to one end of the flowcell. Rinse the flowcell with deionized water, while tapping gently to flush out all air bubbles in the system. All subsequent syringes must be attached to the flowcell by making *drop-to-drop connections* to avoid air-bubble injection into a flowcell.
2. Wash the flowcell with 2–3 mL lipids buffer, contained in a 3-mL Luer lock syringe that is attached to the second nanoport. Alternating between two flowcell ports reduces the chance of injecting air bubbles into the tubing.
3. Dilute 40 μL of stock liposome solution with 960 μL of lipids buffer. Inject 1 mL of the diluted liposome solution into the flowcell as a series of three injections with a 5–10 min incubation time between injections.

4. Rinse the flowcell with 2–3 mL lipids buffer. Incubate for 30 min to promote vesicle fusion and bilayer growth along the silica surface.
5. Slowly inject 1 mL BSA buffer. Let stand 10 min to allow BSA to block remaining exposed surfaces.
6. Inject 1 mL of 0.25 mg/mL streptavidin in BSA buffer and let stand 10 min for streptavidin to bind biotinylated lipids.
7. Rinse flowcell with 2–3 mL BSA buffer to flush out free streptavidin.
8. Add 10 μ L of the λ -DNA with nucleosomes in 1 mL BSA buffer. Slowly inject the solution into the flowcell and incubate 5–10 min to allow for DNA binding to streptavidin on lipid bilayer surface. The amount of injected DNA may be adjusted to obtain the desired surface-DNA density.
9. The flowcell is transferred to the microscope syringe-pump system (Fig. 1). If necessary, use temperature controller to adjust the sample temperature at 37°C.
10. Apply imaging buffer into flowcell at 0.1–0.3 mL/min to align the nucleosome bound-DNA molecules into DNA curtains at the nanofabricated barriers to lipid diffusion (Fig. 3a; see Note 7).
11. Anti-FLAG conjugated QDs are diluted to 2–5 nM in imaging buffer. Inject 700 μ L of the diluted QDs into the flowcell at 0.15 mL/min and confirm the nucleosome labeling by visual inspection through the dual-view imaging system (Fig. 3b).

3.3. Data Acquisition and Analysis

3.3.1. Data Capture

1. YOYO1-stained DNA curtains bound with QDs tagged nucleosomes are visualized and imaged using NIS-Elements software (Fig. 3b).
2. Focus adjustments are made as necessary.
3. The exposure time is typically set as 100–200 ms in frame transfer mode.
4. The fluorescence intensity of DNA and QD can be optimized by controlling laser intensity, EM-CCD gain, and/or exposure time. DNA intensity can also be controlled by increasing or decreasing the YOYO1 concentration. QD intensity should be maximized as much as possible, but should not be over saturated.
5. Full-size images (512×512 pixels) are collected for 1–2 min (300–600 frames) using NIS-Elements software.
6. During the image collection, the flow should be transiently stopped once or twice using a shut-off valve (Fig. 1). This pause in buffer flow allows one to mechanically manipulate the DNA with hydrodynamic flow, and serves as an important control to confirm that any QD-nucleosomes under observation

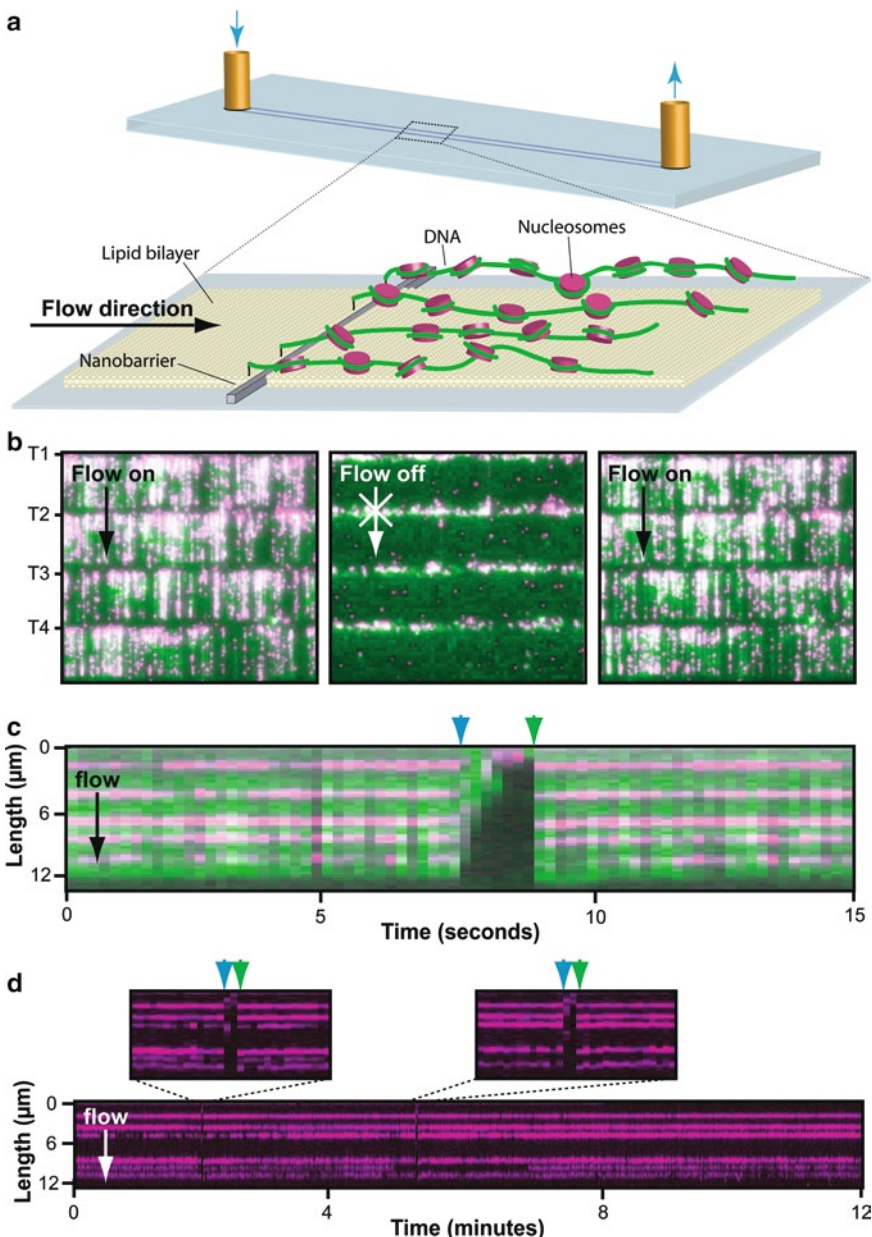


Fig. 3. DNA curtains with fluorescently tagged nucleosomes. Panel (a) depicts the experimental design; full details of the nanofabrication and DNA curtain assembly can be found in (11–13). YOYO1-stained DNA curtains bound by QD-tagged nucleosomes are shown in (b). The *tethered end of each curtain* is indicated as T1–T4, and arrows indicate the direction of flow. A kymogram illustrating five nucleosomes on one DNA molecule is shown in (c). All nucleosome reconstitution reactions were performed at 4°C, the samples were shifted to 37°C for a minimum of 15-min after injection into the microfluidic sample chamber, and all single molecule distribution measurements were made at 37°C. The nucleosomes disappear when flow is temporarily interrupted (*first arrowheads*), and reappear when flow is resumed (*second arrowheads*), verifying they are bound to the DNA and do not interact with the lipid bilayer. A longer kymogram collected without YOYO1 to avoid laser-induced photocleavage of the DNA is shown in (d). Insets highlight 30-s windows where flow was transiently paused. Other signal gaps result from QD blinking, which verify the absence of QD or protein aggregates. During a 25-min observation at 37°C 0.9% of the nucleosomes (5 of 580) moved and/or dissociated from the DNA, and the remaining 99.1% were stationary. Adapted with permission from Visnapuu and Greene (17).

are bound to the DNA and not simply stuck to the flow cell surface. The DNA molecule and any QD-tagged proteins bound to the DNA will diffuse out of the evanescent field and disappear from the field of view when buffer flow is paused (Fig. 3b–d). QDs that are nonspecifically stuck to the surface will not disappear from view when flow is paused.

3.3.2. Image Processing and Position Measurements

7. All images are stored in 16-bit TIFF format.
1. Open TIFF images in ImageJ.
2. The EM-CCD chip is monochromatic, and the image splitter divides the “red” and “green” channels onto two halves of the chip (Fig. 4). These images must be digitally separated and recombined into one image using the ImageJ plug-in “OI_cut_RGBmerge” to generate images containing the YOYO1-DNA (“green”) and QD-nucleosome (“red”) channels.
3. The two channels are aligned using an ImageJ plug-in “Align RGB planes.” The alignment is confirmed by matching common images in both channels, such as nanofabricated barriers, which are dark in both channels, and/or QD fluorescence, which leaks into the green channel.
4. The brightness and contrast of each channel are adjusted accordingly (Fig. 4).
5. Verify that the nucleosomes selected for analysis are bound to DNA by examining the image sequences where buffer flow was transiently terminated, and using only QDs that disappear when flow is paused (Fig. 3b–d).
6. Single QDs can be distinguished from QD aggregates by their blinking characteristics (18), and any data arising from QD or protein aggregates should be disregarded.
7. For the full-length λ -DNA, the y -coordinates (in pixels) of the tethered and free DNA ends (y_0 and y_D , respectively) are obtained from the YOYO1-stained DNA fluorescence signal using ImageJ as shown in Fig. 4. The DNA length can be calculated from the equation, $(y_D - y_0) \times \text{pixel size/magnification}$.
8. The y -coordinate (y_{QD}) of the QD-tagged nucleosomes is then obtained with 2D Gaussian fitting using Igor Pro where the peak of the Gaussian fit indicates the position of the nucleosome (Fig. 4). The position (in bp) of the QD is estimated from the equation, $48,502 \times (y_{QD} - y_0) / (y_D - y_0)$ for λ -DNA.
9. Histograms of nucleosome distributions on DNA can be built from thousands of the QD positions (Fig. 5) and compared to theoretically predicted distributions (19–22), as described (17).

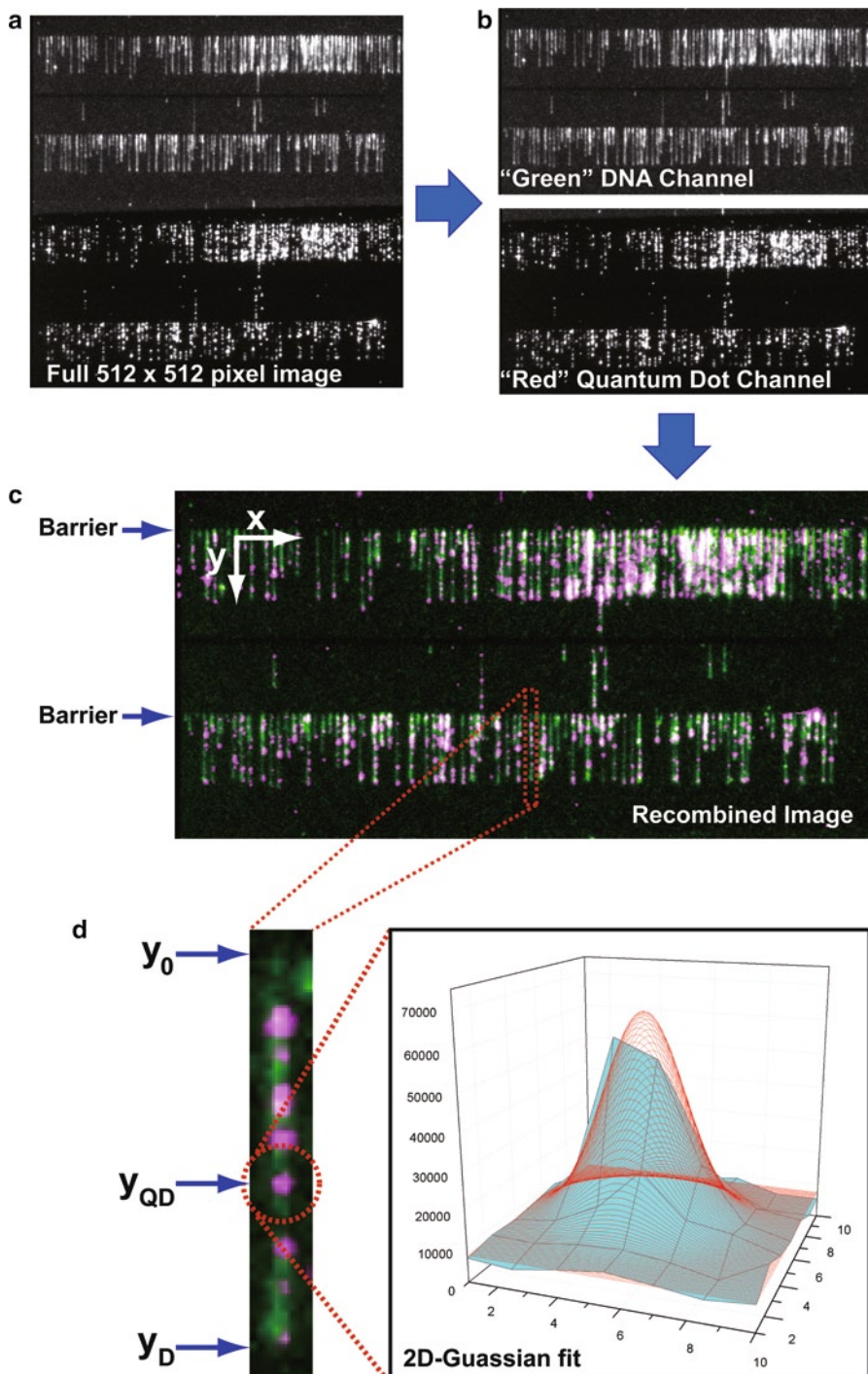


Fig. 4. Measurement of nucleosome position. Full frame images (512×512 pixels) are captured by TIRFM imaging using NIS Elements software (a). The DNA and QD channels are digitally segregated (b), and then aligned and merged to yield a two-color image (c) in ImageJ. The coordinates (y_0 and y_D) of tethered and free DNA ends are obtained from the DNA fluorescence signal, and the position of the QD-tagged nucleosomes (y_{QD}) are obtained from 2D Gaussian fitting in Igor Pro (d).

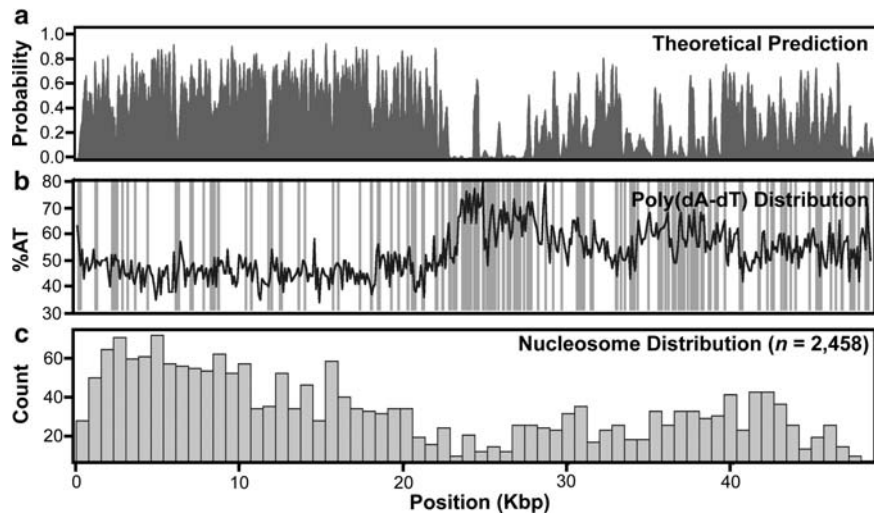


Fig. 5. Nucleosome distribution histogram. Theoretical nucleosome distributions as predicted by Field et al. (21) are shown in the *upper panel*. The theoretical data are shown at 1-bp resolution, and the observed data are compiled into 758-bp bins. The AT-content of the λ is shown (*black line*; calculated with a 100-bp window) superimposed with the distribution of poly(dA-dT) tracts ≥ 5 -mers (*gray bars*), which are asymmetrically distributed and comprise 3.2% of the phage genome (*middle panel*). The stiff DNA including poly(dA-dT) tracks exclude nucleosome binding. The observed nucleosome distribution measured by analysis of DNA curtains is shown in the *lower panel*. Adapted with permission from Visnapuu and Greene (17).

4. Notes

1. One end of λ -DNA is modified with a single biotin by ligation with 12-nt biotinylated oligomer containing a COS sequence, e.g., 5'-Phos-dAGGTGCGCCGCC-biotin-3'.
2. QDs are conjugated with anti-FLAG using Qdot® 705 antibody conjugation kit (Cat. No. Q22061MP, Invitrogen). The antibody-conjugated QDs are purified from free antibodies by using Superdex 200 gel filtration column (elution buffer: 1× PBS (pH 7.4)), which shows better performance than the gel filtration column provided with the kit.
3. The wavelength of dichroic mirror can be changed as necessary for use with fluorophores with different emission characteristics. The alignment of two channels in the dual-view imaging system should be done before image collection.
4. To dissolve wt histones, histones bearing a single FLAG or HA tag, and histone H3 bearing a 3xFLAG tag in unfolding buffer, 0.2 mL dimethyl sulfoxide (DMSO) per 1 L culture is added and the pellets are minced using a spatula *before unfolding buffer is added*.

5. Higher DNA concentrations provide more efficient reconstitution. The λ -DNA concentration should be greater than 0.01 mg/mL and we typically work at 0.02 mg/mL. If necessary, concentrate the biotinylated λ -DNA with isopropanol precipitation, but avoid any methods that might shear the DNA.
6. The removal of chloroform is critical for the mobility of lipid bilayer. If necessary, leave the dried lipids in a vacuum chamber overnight.
7. Gloxy slowly reduces the pH of the imaging buffer, and this is exacerbated with exposure to air. Add the Gloxy components immediately before use to minimize the effects of pH change, and keep the buffer capped and stored on ice.

Acknowledgments

We thank the many members of the Greene laboratory who have worked on developing the DNA curtain experimental platform, and we extend special thanks to Mari-Liis Visnapuu for establishing procedures for nucleosome purification and assembly. The Greene laboratory is supported by the Howard Hughes Medical Institute, the National Institutes of Health, and the National Science Foundation. J. Y. Lee was supported in part by the Korea Research Foundation Grant funded by the Korean Government (KRF-2008-357-C00048). We apologize to any colleagues whose work we were not able to cite due to length limitations.

References

1. Widom, J. (1998) Structure, dynamics, and function of chromatin in vitro. *Annu. Rev. Biophys. Biom.* **27**, 285–327.
2. Luger, K., Mader, A. W., Richmond, R. K., Sargent, D. F., and Richmond, T. J. (1997) Crystal structure of the nucleosome core particle at 2.8 angstrom resolution. *Nature* **389**, 251–260.
3. Rando, O. J., and Chang, H. Y. (2009) Genome-Wide Views of Chromatin Structure. *Annu. Rev. Biochem.* **78**, 245–271.
4. Rando, O. J., and Ahmad, K. (2007) Rules and regulation in the primary structure of chromatin. *Curr. Opin. Cell Biol.* **19**, 250–256.
5. Hager, G. L., McNally, J. G., and Misteli, T. (2009) Transcription Dynamics. *Mol. Cell* **35**, 741–753.
6. Hedges, C., Bintu, L., Lubkowska, L., Kashlev, M., and Bustamante, C. (2009) Nucleosomal Fluctuations Govern the Transcription Dynamics of RNA Polymerase II. *Science* **325**, 626–628.
7. Studitsky, V. M., Clark, D. J., and Felsenfeld, G. (1995) Overcoming a Nucleosomal Barrier to Transcription. *Cell* **83**, 19–27.
8. Groth, A., Rocha, W., Verreault, A., and Almouzni, G. (2007) Chromatin challenges during DNA replication and repair. *Cell* **128**, 721–733.
9. Graneli, A., Yeykal, C. C., Prasad, T. K., and Greene, E. C. (2006) Organized arrays of individual DIVA molecules tethered to supported lipid bilayers. *Langmuir* **22**, 292–299.
10. Visnapuu, M. L., Fazio, T., Wind, S., and Greene, E. C. (2008) Parallel arrays of geometric nanowells for assembling curtains of DNA with controlled lateral dispersion. *Langmuir* **24**, 11293–11299.

11. Fazio, T., Visnapuu, M. L., Wind, S., and Greene, E. C. (2008) DNA curtains and nanoscale curtain rods: High-throughput tools for single molecule imaging. *Langmuir* **24**, 10524–10531.
12. Greene, E. C., Wind, S., Fazio, T., Gorman, J., and Visnapuu, M. L. (2010) DNA Curtains for High-Throughput Single-Molecule Optical Imaging, *Methods in Enzymology, Vol 472: Single Molecule Tools, Pt A: Fluorescence Based Approaches* **472**, 293–315.
13. Finkelstein, I. J., and Greene, E. C. (in press) Supported lipid-bilayers and DNA curtains for high-throughput single molecule studies. *Methods in Molecular Biology*.
14. Gorman, J., Fazio, T., Wang, F., Wind, S., and Greene, E. C. (2010) Nanofabricated Racks of Aligned and Anchored DNA Substrates for Single-Molecule Imaging. *Langmuir* **26**, 1372–1379.
15. Prasad, T. K., Robertson, R. B., Visnapuu, M. L., Chi, P., Sung, P., and Greene, E. C. (2007) A DNA-translocating Snf2 molecular motor: *Saccharomyces cerevisiae* Rdh5,4 displays processive translocation and extrudes DNA loops. *J. Mol. Biol.* **369**, 940–953.
16. Robertson, R. B., Moses, D. N., Kwon, Y., Chan, P., Zhao, W. X., Chi, P., Klein, H., Sung, P., and Greene, E. C. (2009) Visualizing the Disassembly of *S. cerevisiae* Rad51 Nucleoprotein Filaments. *J. Mol. Biol.* **388**, 703–720.
17. Visnapuu, M. L., and Greene, E. C. (2009) Single-molecule imaging of DNA curtains reveals intrinsic energy landscapes for nucleosome deposition. *Nat. Struct. Mol. Biol.* **16**, 1056–U1075.
18. Smith, A. M., and Nie, S. (2010) Semiconductor Nanocrystals: Structure, Properties, and Band Gap Engineering. *Acc. Chem. Res.* **43**, 190–200.
19. Segal, E., Fondufe-Mittendorf, Y., Chen, L. Y., Thastrom, A., Field, Y., Moore, I. K., Wang, J. P. Z., and Widom, J. (2006) A genomic code for nucleosome positioning. *Nature* **442**, 772–778.
20. Kaplan, N., Moore, I. K., Fondufe-Mittendorf, Y., Gossett, A. J., Tillo, D., Field, Y., LeProust, E. M., Hughes, T. R., Lieb, J. D., Widom, J., and Segal, E. (2009) The DNA-encoded nucleosome organization of a eukaryotic genome. *Nature* **458**, 362–U129.
21. Field, Y., Kaplan, N., Fondufe-Mittendorf, Y., Moore, I. K., Sharon, E., Lubling, Y., Widom, J., and Segal, E. (2008) Distinct Modes of Regulation by Chromatin Encoded through Nucleosome Positioning Signals. *Plos Comput. Biol.* **4**, 25.
22. Tillo, D., and Hughes, T. R. (2009) G+C content dominates intrinsic nucleosome occupancy. *Bmc Bioinformatics* **10**, 442.

Chapter 17

Simultaneous Observation of Chemomechanical Coupling of a Molecular Motor

Takayuki Nishizaka, Yuh Hasimoto, and Tomoko Masaike

Abstract

F_1 -ATPase is the smallest rotary molecular motor ever found. Unidirectional rotation of the γ -shaft is driven by precisely coordinated sequential ATP hydrolysis reactions in three catalytic sites arranged 120° apart in the cylinder. Single-molecule observation allows us to directly watch the rotation of the shaft using micron-sized plastic beads. Additionally, an advanced version of “total internal reflection fluorescence microscope (TIRFM)” enables us to detect binding and release of energy currency through fluorescently labeled ATP. In this chapter, we describe how to set up the system for simultaneous observation of these two critical events. This specialized optical setup is applicable to a variety of research, not only molecular motors but also other single-molecule topics.

Key words: Molecular motor, F_1 -ATPase, TIRFM, Single-molecule observation, Cy3-ATP, Simultaneous observation, Chemomechanical coupling, Rotation assay

1. Introduction

Motor proteins are molecular machines that convert chemical energy into mechanical work. Progresses in single-molecule technique over the past two decades allow us to uncover mechanical steps of elaborate motors such as kinesin (1), myosin (2–4), dynein, and F_1 -ATPase (5, 6). To elucidate the coupling between the mechanical events and the chemical states in the catalytic site(s), what we have to do is directly correlate, or ideally, simultaneously visualize, these two events (e.g., Fig. 1). Various research groups have tried to achieve this, but to date, in our opinion, only four reports (7–10) have been published with technical tour de force.

In this chapter, we focus on the experimental setup and construction of an isotropic TIRFM (see Note 1). All devices, optical

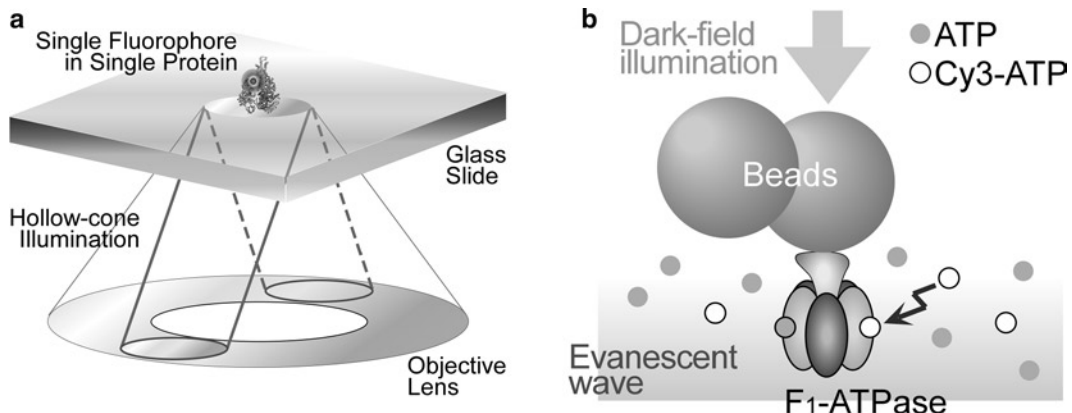


Fig. 1. Schematics to observe single molecules under TIRF illumination. (a) Nearly isotropic TIRFM. Unlike a conventional TIRFM, in which one-directed single laser beam reflects at the interface between glass and water, with isotropic TIRFM the laser beam comes from all directions as a hollow-cone of illumination. The resultant evanescent field has all polarization components along X-, Y-, and Z-direction, and therefore single fluorophores are efficiently excited even though each fluorophore orients in different direction. Sample proteins are immobilized to the glass surface. (b) Experimental system for simultaneous observation (not to scale). Single turnovers of ATP hydrolysis on catalytic sites in F₁-ATPase are visualized with fluorescently labeled ATP, which is excited by an evanescent field under isotropic TIRFM. Rotation of a bead duplex attached to the γ shaft simultaneously observed under dark-field illumination at a wavelength different from the emission of Cy3-ATP.

components, and filters required for the simultaneous observation are described in Subheadings 2.1–2.4, and step-by-step procedures for both alignment of a laser beam and adjustments of all components are reported in great detail in Subheadings 3.1–3.3. The following full description should enable “the researcher” to construct the whole observation system using mainly commercial products. This system will, in future, be applicable for not only studies of molecular motors, but also oligomer proteins having multiple catalytic sites and membrane proteins with complex subunit structures. Additionally, in Subheadings 2.5 and 3.4, preparation and rotation observation of F₁-ATPase, which is a major subject to understand how motor proteins as molecular machines work, are also described. A couple of research groups in Japan including us have studied this machine for more than 10 years, and are still further elucidating how rotation couples to the chemical reactions. Although its mechanism is understood in part, we still need a variety of approaches to unravel the mystery of this machine that directly converts the chemical energy into mechanical work, unlike man-made devices. It is hoped that motivated researchers will participate in this challenging subject and that this chapter will help them.

2. Materials

2.1. Microscope and Equipments

1. Inverted microscope: IX-71 (Olympus Co.) or TE-2000E (Nikon Co.).
2. Objective lenses: Apo 60×, NA 1.45 (Olympus) or Apo TIRF 100×, NA 1.49 (Nikon).
3. Cameras: EM-CCD cameras (iXon + DU 897 and Luca, Andor Technology plc.) (see Note 2 for details).
4. A hand-made optical system outside the camera port (see Note 3 for details).
5. Light source for fluorescence emitter: Diode-pumped solid-state laser with the wavelength of 532 nm (Compass 315 M, Coherent Inc.).
6. Light source for dark-field image: LED that emits 470 nm wavelength (pE-100, CoolLED Ltd.).

2.2. Alignment Tools

1. The halogen lamp designed for bright-field illumination of the microscope.
2. A ND filter that decreases the laser power to less than 20 mW (see Note 4 for this value).
3. A conventional 1/2 in. CCD camera (CS8420i, Toshiba Teli Co.) and a TV monitor to watch the illuminated image of fluorescent beads.
4. Carboxylated fluorescent beads 500 nm in diameter (see Note 5) to locate the beam center at the sample plane. Either red bead (FluoSpheres 585/605, Invitrogen Co.) or yellow-green bead (505/515, Invitrogen) is applicable.

2.3. Optical Components for Isotropic TIRFM

1. A diffractive diffuser (D074, Frankfurt Laser Company) fixed to a hollow rotary motor.
2. Three or more mirrors: M1, M2, and M3 in Fig. 3 (see Note 6).
3. Two lenses: L1 and L2 in Figs. 2 and 3, mounted in holders having XY-adjustment screws (see Note 7).
4. A concentric mask (customer-made, Photo Precision Co., Ltd.): CM in Figs. 2 and 3.
5. A polarizer (SPF-30C-32, Sigma Koki Co., Ltd.) and a quarter-wave plate (CVI Melles Griot): “Pol.” and “QWP” in Fig. 3, respectively, (see Note 8), which are mounted to separate holders with a rotation adjustment.

2.4. Filters

1. A dichroic beamsplitter that reflects 532 nm and transmits the emission of desired fluorophore (see Note 9). A customer-made one has been ordered from Chroma Technology Co. (550drlp-special, Chroma Technology Co.; DM1 in Fig. 3).

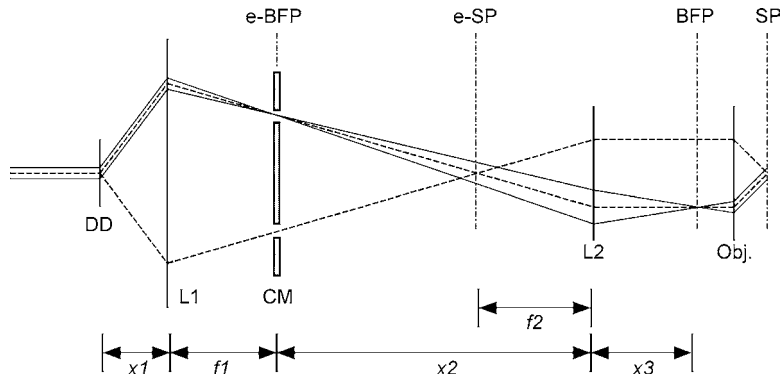


Fig. 2. Diagram of optical components to construct isotropic TIRFM. Hollow-cone laser beam from a diffractive diffuser (DD) is gathered by the lens (L1) to equivalent sample-plane (eSP) and parallelized by the other lens (L2) in front of the objective. Each component of light is focused to a concentric mask (CM) localized at equivalent back-focal-plane (eBFP) to cut zero-mode diffraction, and also focused to BFP inside the objective (Obj.). At the sample plane, the evanescent field emerged by the laser beam is coming from all directions.

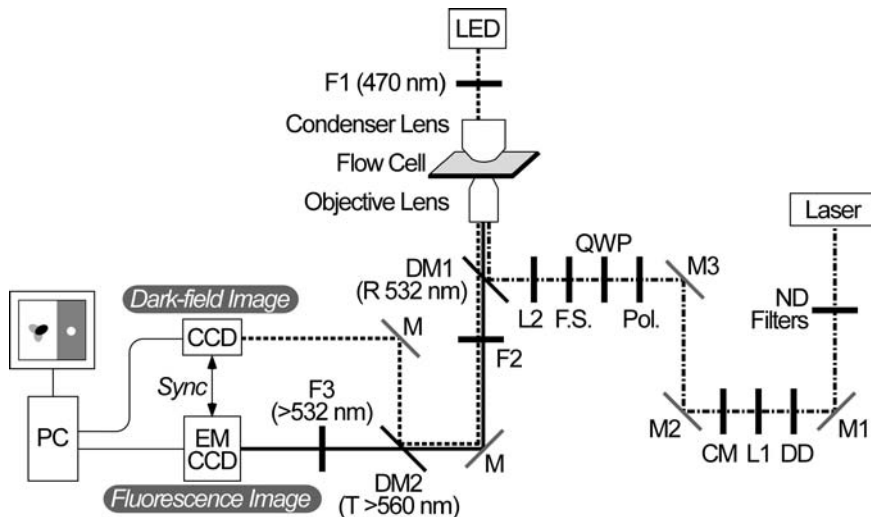


Fig. 3. Diagram of filters for simultaneous observation: dark-field image of beads; fluorescence image of single fluorescently labeled nucleotides. Blue light from a diode (dashed line) is used as a light source for dark-field microscopy to illuminate polystyrene beads. *Scattered light* from beads is passed through concentric mask (supplementary in ref. (12)) and visualized by a relatively low-sensitive EM-CCD camera. Red emission from Cy3 (thick line) excited by a green laser (dashed-dotted line) is visualized by iXon CCD camera. Two mirrors, M2 and M3, locate between a polarizer (Pol.) and CM in our real setup.

2. An optical filter that transmits a narrow wavelength of the illumination for dark-field image. As we use 470 nm LED for the illumination, the filter designed for this LED specificity was chosen (MaxDiode LD01-473/10, Semrock Inc.; F1 in Fig. 3).
3. Two filters to cut the laser line wavelength (NF03-532E and LP03-532RU, Semrock; F2 and F3, respectively, in Fig. 3). F2 transmits both blue and orange-red light, whereas F3 cuts blue.

**2.5. Materials
for Preparation
of F₁-ATPase Mutants
for Rotation Assay**

4. A dichroic mirror to split dark-field image and fluorescence image (FF560-Di01, Semrock; DM2 in Fig. 3).
1. The puc β plasmids: The *SacI-SmaI* fragment of F₁-ATPase containing the sequence of β subunit cloned into puc118 vector (11). Its derivative puc β -His-tag contains ten histidines at the N terminus of the β subunit (*EcoT22I* and *NdeI*) (see Note 10) (12).
2. A series of pkk $\alpha\gamma\beta$ plasmids for expression of $\alpha_3\beta_3\gamma$ subcomplex of F₁-ATPase. The pkk $\alpha\gamma\beta$ -CW-less plasmid contains no cysteines or tryptophans as mutations α C193S (*EcoRV*) and α W463F (*XbaI*) are introduced into the wild-type sequence (13). For rotation assay, further mutations were introduced into pkk $\alpha\gamma\beta$ -CW-less and named pkk $\alpha\gamma\beta$ HC5 (5): ten histidines at the N terminus of the β sequence (*EcoT22I* and *NdeI*) for immobilization of the stator $\alpha_3\beta_3$ on the glass surface, and γ S109C (*EcoT22I* and *SphI*) for biotinylation to attach avidinylated beads as a rotation probe. The pkk $\alpha\gamma\beta$ HC9 plasmid contains γ I212C (*XbaI*) mutation (14) instead of γ S109C. The pkk $\alpha\gamma\beta$ HC95 plasmid contains mutations contained in both HC5 and HC9 described above aiming for rigid attachment of beads via two cysteines (15). The pkk $\alpha\gamma\beta$ HCXP plasmid contains the same mutations as pkk $\alpha\gamma\beta$ HC95 except for further six histidines at the N terminus of the α subunit (*BamHI*) for more stable immobilization on the glass surface during manipulation of the γ subunit by magnetic tweezers (16).
3. Recochip (TaKaRa) for extraction of DNA fragments from agarose gel.
4. LB + ampicillin plate: 5 g bacto tryptone (DIFCO), 2.5 g bacto yeast extract (DIFCO), 5 g NaCl, and 7.5 g bottom agar are dissolved in 500 ml distilled water and autoclaved. After cooling down to 60°C, 100 µg/ml ampicillin is added and poured into plates.
5. 2× YT + ampicillin medium for preculture and glycerol stock of *E. coli*: 8 g bacto tryptone, 5 g bacto yeast extract, 2.5 g NaCl are dissolved in 500 ml distilled water and autoclaved. After cooling down below 60°C, 100 µg/ml ampicillin is added.
6. Plasmid Midi Kit (Qiagen) for plasmid purification.
7. Terrific broth + ampicillin medium for overexpression: 12 g bacto tryptone (DIFCO), 24 g bacto yeast extract (DIFCO), 2.31 g KH₂PO₄, 12.54 g K₂HPO₄, and 4 ml glycerol are dissolved in 1 l distilled water and autoclaved. After cooling down below 60°C, 100 µg/ml ampicillin is added.
8. TOYOPEARL phenyl 650 M or TOYOPEARL butyl 650 M (TOSOH) for partial purification.
9. Superdex 200 10/300 GL (GE Healthcare) for final purification.

10. Biotin-PEAC₅-maleimide (Dojindo) to biotinylate the γ subunit for attachment of avidin beads.
11. Commercially available avidinylated magnetic beads: Sera-Mag Magnetic Streptavidin Microparticles Surface Concentration – Level 4 (Thermoscientific).

3. Methods

In the experimental setup used to visualize fluorescent nucleotides developed by Yanagida's group (7, 17), TIRF illumination is realized with a single laser beam, and so the resultant evanescent field from this single beam will be highly polarized. If we define the incident plane as XZ , the p- and s-polarized light mainly produce Z - and Y -components, respectively, of the evanescent field. And therefore, the fluorophore in which its absorption transition moment directs X -axis is not excited efficiently. This effect makes the intensity histogram of single molecules broad and inaccurate. In the contribution we published in 2007 (18), the number of nucleotides binding the single rotary motor needed to be quantified, and so the above setup was not applicable to our theme. Instead, an isotropic TIRFM, in which the laser beam comes from all directions at the sample plane, was constructed.

The idea to use the hollow cone illumination for epi-illumination TIRF was originally proposed by Axelrod and coworkers (19). However, most of their ideas are not applicable to gain a uniform image, because each component of light is focused at the sample plane. They also proposed a conical lens, but such an optical arrangement is unworkable to illuminate a certain area. Only the center is illuminated from all direction and becomes extremely bright, while other areas are illuminated incoherently.

Here, we construct an isotropic TIRFM by using a diffractive diffuser (DD). The diffuser transfers the single beam into a profile of a single circle as a first degree image, which makes the beam run like a hollow cone shape. This optical component enables us to illuminate a ring-shaped profile by collimation without a large loss in laser power. Figure 2 shows a diagram of the optical components including DD. The circular pattern is focused through a lens (L1) and parallelized so as to be guided into the objective with an appropriate radius to realize TIRF illumination ($NA > 1.33$). Additionally, by rotating the DD faster than the time resolution of the camera, the interference pattern of the laser at the sample plane can be effectively canceled to acquire uniform fluorescence images.

In the following methods, step-by-step procedures to construct the isotropic TIRFM shown in Fig. 2 are described in Sub-headings 3.1 and 3.2. For simultaneous observation between

rotation of the bead attached to the shaft and chemical reaction through Cy3-ATP bound to catalytic sites, two cameras are set to a microscope as shown in Fig. 3. Tips and outline are described in Subheading 3.3. For preparation of F₁-ATPase motor, see Subheading 3.4. For 2'-Cy3-EDA-ATP preparation, refer to the contribution by Oiwa et al. (20).

3.1. Laser Alignment

1. Fix the mirrors for guiding the laser beam into the microscope to the optical bench with hex screws. In cases where the filter cube is below the objective adjustment screws for tilting DM1 (e.g., Nikon adjustable filter-cassette), height of M3 is set to the same height of DM1 using a scale.
2. The condenser lens for bright-field illumination is aligned for Köhler illumination using a standard procedure. A halogen lamp is used, instead of an LED light source, only for the laser alignment in steps 2 and 3.
3. Remove the objective and maximize the halogen light source, a green light reflected by DM1 should appear at the rear portion of the microscope. The green light is reflected by each mirror so the optical axis of the laser beam is virtually visible albeit in the reverse direction. And therefore, adjustments of position, height, and tilting of mirrors can be done by following the reflection. Adjustment of the DM1 tilting is also possible to set the reflection toward the center of M3.
4. Turn on the laser. If there is an allowance in the screw hole in the plate fixing the laser head, change the angle of the laser head before fixing so the beam follows the center of each mirror. This step is not a requirement but minimizes the following step adjustment (Subheading 3.2, step 6). An ND filter to decrease the power less than 20 mW is needed at this first step.
5. Set the objective and view a sample of 0.5 μm carboxylated fluorescent beads. Rapid Brownian motion of the bead is observed around the focus point at the sample plane. This image can be seen either through the eyepieces or by using a conventional CCD camera with the laser power of 0.3–0.003 mW. If the image is saturated, decrease the power with the combination of ND filters.
6. The beam can be adjusted so as to run the center of the objective by two procedures. First, tilt one mirror to move the illumination to the center of the sample field while watching the image acquired by the camera. Subsequently, tilt the other mirror to change the angle of the beam while watching the direction of the beam above the sample, e.g., 10–50 cm above. By repeating these steps vice versa, the beam is perfectly aligned along the optical axis of the objective. If there is not enough space above the sample, the condenser

lens is simply removed and then white paper is placed on the empty condenser-holder. The beam passing through both the objective and the sample is clearly seen on the paper.

7. A polarizer and a quarter-wave plate are fixed to the bench (see Note 11). Angles of these components are adjusted to make a circularly polarized light. Typically, deviation of polarization measured below the objective is within $\pm 2\%$.
1. Set L1 at the point estimated from the calculation. Alignment in the direction of the plane perpendicular to the optical axis can be done by watching the fluorescent beads through the camera.
2. Set L2 and adjust x and y by watching the fluorescent beads through the camera (for coordination, see Notes 12 and 13).
3. Fix the field diaphragm to the position being $f/2$ apart from L2. In our system, the optical tube holding L2 is connected with the diaphragm holder. The tube itself is moved with $X\bar{Y}Z$ -stage. Relative position of the diaphragm is adjusted through a translation stage (LINOS $x\text{-}y$ Precision translation stage, Qioptiq) against the position of the tube.
4. Set the diffractive diffuser. One beam is diverged into the hollow cone shape. Each component of light gathers by L1.
5. L1 is carefully adjusted along Z -direction so as to let the beam components gather at the position of the field diaphragm. This step assures that each beam component comes into the objective in parallel. This is the first requirement to realize isotropic TIRFM.
6. After the diffractive diffuser is removed, L2 is carefully shifted along the Z -direction. The divergence of the beam above the objective is obviously changed. Focusing at the back-focal-plane (BFP) is the second requirement. When the beam is focused to the BFP, the beam divergence above the objective is expected to become sharpest. $X\bar{Y}$ -position of L2 is also adjusted by setting the beam direction, so as to make the beam above the objective roughly perpendicular to the optical bench in an inverted microscope.
7. By repeating steps 4–7 several times, the positions of L1 and L2 are adjusted to the ideal point.
8. Set the diffractive diffuser and check the NA of the system. A semisphere prism is put on the objective instead of the bead sample. The beam passes through the prism without refraction, and therefore, the angle of the laser is directly quantified by measuring the angle of the circular light. $X\bar{Y}$ -position of L2 can also be refined in this step by watching the beam direction.

3.2. Adjustment of Optical Components

9. The concentric mask (CM in Figs. 2 and 3) is set at the equivalent BFP. Adjust the x , y , and z positions of the CM so that the beam profile after the mask becomes sharpest.

3.3. Filters and Cameras

1. Figure 3 shows the diagram of filter combination and cameras. DM1 and F2 are set in an empty filter holder, which is commercially available from microscope companies.
2. F1 locates above the condenser module. If the position or the size of F1 is inappropriate, the edge of the filter holder may cut the NA of the condenser lens.
3. DM2 and F3 are set outside the microscope using a hand-made optical system.
4. Between the microscope and cameras, two sets of two lenses are adjusted in order to focus the image at the camera planes.
5. Trigger output of one camera is connected to trigger input of the other camera. The software “SOLIS” is used to operate the iXon camera series and functions to capture multiple images from multiple cameras in sync.

3.4. Preparation of F_1 -ATPase Mutants for Rotation Assay

1. Design a mutation primer containing a unique restriction enzyme-cutting site as a “mutation marker,” and introduce the mutation by the mega-primer method using template plasmids of *pkkαγβ* or *pucβ* with histidine tags. Prepare a mutated fragment by cutting the resultant PCR product with restriction enzymes (*Eco*RI-*Bgl*II for α , *Bgl*II-*Nhe*I for γ , *Mlu*I-*Pst*I for β) and ligate it to the original template plasmid which lacks the corresponding fragment. Transform the ligated plasmid into *E. coli* strain JM109 and inoculate an LB + ampicillin plate. Incubate overnight at 37°C.
2. Pick several colonies of 1 and perform colony PCR. Check introduction of the mutation by restriction enzyme-cutting patterns of colony PCR products. Make glycerol stock of the *E. coli* containing successfully mutated plasmid.
3. Culture 2 with 50 ml of 2× YT + ampicillin and purify the plasmid using a Plasmid Midi Kit. Using DNA sequencing, confirm the entire DNA sequence of the region that originates from the PCR.
4. If the DNA sequence is correct, transform the purified plasmid into *E. coli* strain JM103ΔuncB-D, which lacks F_oF_1 genes. Make a glycerol stock.
5. Inoculate 4 into 3 ml of 2× YT + ampicillin medium for preculture.
6. Inoculate 1 ml of 5 into 1 l of terrific broth + ampicillin for overexpression at 37°C for 16 h.
7. Collect the cells by centrifugation and freeze using liquid nitrogen. Store at -80°C.

8. Thaw 7 and dissolve it in buffer containing 1 mM DTT (always contained until 10) to maintain cysteines in a reduced form. Disrupt the cells by sonication or a French press.
9. Incubate 8 at 60°C for 30 min. Skip this heat treatment step depending on stability of the mutant.
10. Partial purification of $\alpha_3\beta_3\gamma$ by hydrophobic interaction chromatography (phenyl toyopearl or butyl toyopearl) with linear gradient of ammonium sulfate concentration from 1 to 0 M at 25°C. Freeze it with liquid nitrogen and store at -80°C if the mutant is resistant to freezing.
11. Thaw 10. Final purification by gel filtration chromatography using superdex 200 10/300 GL at 25°C. Choice of buffers depends on the next step but should be without DTT for subsequent biotinylation and contain 50–100 mM KCl or NaCl for destabilization of $\alpha_3\beta_3$ without γ to prevent its contamination. Run HPLC at a flow rate of 0.5 ml/min, and collect the fraction containing $\alpha_3\beta_3\gamma$ which is eluted at around 20 min. Isolated β is eluted at around 30 min.
12. React the purified $\alpha_3\beta_3\gamma$ with biotin-PEAC₅-maleimide immediately after 11 at 25°C for 30 min. Note that the reaction of biotin should be 1:1 with cysteines. Therefore, concentration of biotin should be twice that of $\alpha\gamma\beta$ HC95 or $\alpha\gamma\beta$ HCXP. Quench the reaction by 1 mM DTT. Freeze it in small quantities (approximately 10 μ l) with liquid nitrogen and store at -80°C. Rotation assay without this freeze-and-thaw step is recommended for successful rotation assay of unstable mutants.
13. Prepare avidinylated polystyrene beads (21) or commercially available avidinylated magnetic beads and attach them to biotinylated γ of $\alpha_3\beta_3\gamma$ in the flow cell under the microscope.
14. Observe rotation of the γ subunit (21) simultaneously with binding and release of fluorescent ATP analog (Cy3-ATP) using the advanced version of total internal reflection fluorescence microscope (TIRFM) described in this chapter. Set L1 at the point estimated from the calculation. Alignment within the plane perpendicular to the optical axis can be done by watching the fluorescent beads through the camera.

4. Notes

1. We denote our advanced TIRFM as an isotropic TIRFM, because the resultant evanescent field has all the component of the electromagnetic field. Precisely speaking, the Z-component of the field is two times stronger than the XY-component as an

integration of γZ -polarized light to 360° rotation. Although this inhomogeneous property has not been checked, a single fluorophore should become, in theory, brighter in the case that its absorption transition moment becomes perpendicular to the sample plane.

2. For EM-CCD cameras, use a highly sensitive camera for fluorescent imaging of single fluorophores (iXon + DU 897) while for the other, can be a lower sensitivity with USB-connection (Luca). These two cameras capture each image in sync when one gives a TTL trigger to the other (as “Sync” in Fig. 3).
3. The first image plane at the port is refocused with a set of lenses with a hand-made optical system. DM2 located around the eBFP separates the image by the difference of the wavelength (Fig. 2).
4. As a rough guide, it is said that 20 mW is an upper limit not to damage conventional objectives.
5. Carboxylated fluorescent beads are dispersed and not attached to the glass surface. In contrast, amino-modified fluorescent beads of the same size tend to aggregate and are difficult to use.
6. At least two mirrors need to be mounted to holders having two accurate adjustment, which precisely tilt the mirror toward both latitude and longitude angles.
7. These focal lengths of L1 and L2 determine the whole size of the optical system. Key distances, x_1 , x_2 , and x_3 , are calculated by the standard lens equation, $1/a - 1/b = 1/f$, where a and b are coordinates of a source and a resultant image, respectively, as the lens position is zero, and f is a focal length of the lens. In the equation, coordination gives negative value when the source or the image position locates leftward from the lens.
8. The polarizer is used to refine the polarization ratio of the beam. The quarter-wave plate makes the beam into a circularly polarized one.
9. Because DM1 reflects the circularly polarized beam toward the objective, the phase shift of between s- and p-polarized light should be the same after reflection. Otherwise, circular polarization is transformed into ellipsoidal one, which makes an isotropic TIRF illumination incomplete.
10. In step 2 of Subheading 2.5, restriction enzymes used for confirmation of mutations are written in parentheses.
11. In Fig. 3, both the polarizer and a quarter-wave plate (QWP) are set between a dichroic mirror (DM1) and M3 to avoid the deformation of circular polarization of light by reflection of mirrors.
12. In this chapter, Z -axis is defined as the direction of the optical center-axis of the laser toward the objective lens. XY -plane is

defined as the plane that is perpendicular to Z -axis. In areas where the beam runs parallel to the optical bench, X and Y axes are parallel and perpendicular, respectively, to the bench.

13. Because the beam comes from all directions at the sample plane in the isotropic TIRF illumination, the incident plane cannot be defined.

Acknowledgments

Authors would like to thank Drs. Kazuhiro Oiwa, Kazuhiko Kinoshita Jr., Kengo Adachi, and Mitsuhiro Sugawa for their advice and encouragement, Ayako Tatsuguchi for technical assistance, and Junya Okawa and Takayuki Hirakawa for helping in the initial development of the advanced TIRFM. This work was supported in part by a Grant-in-Aid for Scientific Research on Priority Areas (No. 18074008) from the Ministry of Education, Culture, Sports, Science and Technology of Japan and a grant from the New Energy and Industrial Technology Development Organization to T.N.

References

1. Svoboda, K., Schmidt, C. F., Schnapp, B. J., and Block, S. M. (1993) Direct observation of kinesin stepping by optical trapping interferometry. *Nature* **365**, 721–727.
2. Miyata, H., Hakozaki, H., Yoshikawa, H., Suzuki, N., Kinoshita, K., Jr., Nishizaka, T., and Ishiwata, S. (1994) Stepwise motion of an actin filament over a small number of heavy meromyosin molecules is revealed in an *in vitro* motility assay. *J. Biochem.* **115**, 644–647.
3. Finer, J. T., Simmons, R. M., and Spudich, J. A. (1994) Single myosin molecule mechanics: piconewton forces and nanometre steps. *Nature* **368**, 113–119.
4. Mehta, A. D., Rock, R. S., Rief, M., Spudich, J. A., Mooseker, M. S., and Cheney, R. E. (1999) Myosin-V is a processive actin-based motor. *Nature* **400**, 590–593.
5. Noji, H., Yasuda, R., Yoshida, M., and Kinoshita, K., Jr. (1997) Direct observation of the rotation of F_1 -ATPase. *Nature* **386**, 299–302.
6. Yasuda, R., Noji, H., Kinoshita, K., Jr., and Yoshida, M. (1998) F_1 -ATPase is a highly efficient molecular motor that rotates with discrete 120° steps. *Cell* **93**, 1117–1124.
7. Ishijima, A., Kojima, H., Funatsu, T., Tokunaga, M., Higuchi, H., Tanaka, H., and Yanagida, T. (1998) Simultaneous observation of individual ATPase and mechanical events by a single myosin molecule during interaction with actin. *Cell* **92**, 161–171.
8. Nishizaka, T., Oiwa, K., Noji, H., Kimura, S., Muneyuki, E., Yoshida, M., and Kinoshita, K., Jr. (2004) Chemomechanical coupling in F_1 -ATPase revealed by simultaneous observation of nucleotide kinetics and rotation. *Nat. Struct. Mol. Biol.* **11**, 142–148.
9. Adachi, K., Kinoshita Jr, K., and Ando, T. (1999) Single-fluorophore imaging with an unmodified epifluorescence microscope and conventional video camera. *J. Microsc.* **195**, 125–132.
10. Sakamoto, T., Webb, M. R., Forgacs, E., White, H. D., and Sellers, J. R. (2008) Direct observation of the mechanochemical coupling in myosin Va during processive movement. *Nature* **455**, 128–132.
11. Ohtsubo, M., Yoshida, M., Ohta, S., Kagawa, Y., Yohda, M., and Date, T. (1987) In vitro mutated beta subunits from the F_1 -ATPase of the thermophilic bacterium, PS3, containing glutamine in place of glutamic acid in positions 190 or 201 assembles with the alpha and gamma subunits to produce inactive complexes. *Biochem. Biophys. Res. Commun.* **146**, 705–710.
12. Masaike, T., Koyama-Horibe, F., Oiwa, K., Yoshida, M., and Nishizaka, T. (2008) Cooperative

- three-step motions in catalytic subunits of F₁-ATPase correlate with 80° and 40° substep rotations. *Nat. Struct. Mol. Biol.* 15, 1326–1333.
13. Matsui, T. and Yoshida, M. (1995) Expression of the wild-type and the Cys-/Trp-less a₃b₃g complex of thermophilic F₁-ATPase in *Escherichia coli*. *Biochim. Biophys. Acta* 1231, 139–146.
14. Adachi, K., Yasuda, R., Noji, H., Itoh, H., Harada, Y., Yoshida, M., and Kinoshita, K., Jr. (2000) Stepping rotation of F₁-ATPase visualized through angle-resolved single-fluorophore imaging. *Proc. Natl. Acad. Sci. USA* 97, 7243–7247.
15. Yasuda, R., Noji, H., Yoshida, M., Kinoshita, K., Jr., and Itoh, H. (2001) Resolution of distinct rotational substeps by submillisecond kinetic analysis of F₁-ATPase. *Nature* 410, 898–904.
16. Rondelez, Y., Tresset, G., Nakashima, T., Kato-Yamada, Y., Fujita, H., Takeuchi, S., and Noji, H. (2005) Highly coupled ATP synthesis by F₁-ATPase single molecules. *Nature* 433, 773–777.
17. Funatsu, T., Harada, Y., Tokunaga, M., Saito, K., and Yanagida, T. (1995) Imaging of single fluorescent molecules and individual ATP turnovers by single myosin molecules in aqueous solution. *Nature* 374, 555–559.
18. Adachi, K., Oiwa, K., Nishizaka, T., Furuike, S., Noji, H., Itoh, H., Yoshida, M., and Kinoshita, K., Jr. (2007) Coupling of rotation and catalysis in F₁-ATPase revealed by single-molecule imaging and manipulation. *Cell* 130, 309–321.
19. Stout, A. L. and Axelrod, D. (1989) Evanescent field excitation of fluorescence by epi-illumination microscopy. *Appl. Opt.* 28, 5237–5242.
20. Oiwa, K., Eccleston, J. F., Anson, M., Kikumoto, M., Davis, C. T., Reid, G. P., Ferenczi, M. A., Corrie, J. E., Yamada, A., Nakayama, H., and Trentham, D. R. (2000) Comparative single-molecule and ensemble myosin enzymology: sulfoindocyanine ATP and ADP derivatives. *Biophys. J.* 78, 3048–3071.
21. Nishizaka, T., Mizutani, K., and Masaike, T. (2007) Single-Molecule Observation of Rotation of F₁-ATPase Through Microbeads. *Methods Mol. Biol.* 392, 171–182.

Chapter 18

Microsecond Resolution of Single-Molecule Rotation Catalyzed by Molecular Motors

Tassilo Hornung, James Martin, David Spetzler, Robert Ishmukhametov, and Wayne D. Frasch*

Abstract

Single-molecule measurements of rotation catalyzed by the F_1 -ATPase or the F_oF_1 ATP synthase have provided new insights into the molecular mechanisms of the F_1 and F_o molecular motors. We recently developed a method to record ATPase-driven rotation of F_1 or F_oF_1 in a manner that solves several technical limitations of earlier approaches that were significantly hampered by time and angular resolution, and restricted the duration of data collection. With our approach it is possible to collect data for hours and obtain statistically significant quantities of data on each molecule examined with a time resolution of up to 5 μ s at unprecedented signal-to-noise.

Key words: F_1 -ATPase, F_oF_1 ATP synthase, Nanodiscs, Gold nanorods, Plasmon resonance, Molecular motors, Dark field microscopy, Single molecule

1. Introduction

The F_oF_1 ATP synthase is composed of two opposed rotary molecular motors connected by a common axle of $\gamma\epsilon$ -subunits (1). The integral membrane F_o motor, which has a subunit stoichiometry of ab_2c_{10} in *E. coli* (2), uses the electrochemical potential-driven flux of protons across a membrane (proton-motive force or PMF) to drive clockwise rotation of the ring of ten c-subunits as viewed from the periplasm (3). The c-ring is docked to the $\gamma\epsilon$ -subunits that extend into the hexameric ring of α and β subunits in the F_1 peripheral membrane motor. Rotation of this axle drives conformational changes in each of the three catalytic $\alpha\beta$ heterodimers resulting in

*Author for correspondence, email: frasch@asu.edu

ATP synthesis (4). The F₁ motor can also hydrolyze ATP resulting in counterclockwise $\gamma\epsilon$ -subunit rotation and proton translocation via F_o (3). When solubilized away from F_o and the membrane, *E. coli* F₁-ATPase-driven rotation at saturating ATP concentrations occurs in three 120° power strokes (5–7), separated by 8.3 ms dwells comparable to the turnover time of the rate-limiting step of ATP hydrolysis (6, 8).

The sequential dwell positions of single molecules of F₁ or F_oF₁ can be tracked as a function of time through the use of single molecule FRET, or by attaching either micrometer-long actin filaments or nanoscale spheres to the rotor. However, these studies have been significantly hampered by the limited time and angular resolution of the measurements as well as the sampling duration. Consequently, the ability to obtain statistically significant measurements of rotational velocity and position has been severely limited. We recently developed a method to record ATPase-driven rotation of F₁ or F_oF₁ in a manner that solves these problems. With this approach it is possible to collect data for hours and obtain statistically significant quantities of data on each molecule examined with a time resolution of up to 5 μ s at unprecedented signal-to-noise.

This rotation assay exploits the optical properties of gold nanorods to make sensitive measurements of rotational position. When viewed using dark-field microscopy, a 75 \times 35 nm nanorod resonantly scatters red and green light from the long and short axis of the rod, respectively (9). Since the sample is illuminated at an oblique angle, only light scattered from the nanorod is observed. When viewed through a polarizing filter, the intensity of scattered light from a nanorod changes as a function of the relative angle between the nanorod axis and the polarizing filter (10). The intensity of scattered red light from a nanorod is maximal and minimal when the long and short axes of the rod are parallel and orthonormal to the plane of polarization, respectively, because the intensity of scattered light changes as a sinusoidal function relative to the orientation of the polarizer (Fig. 1).

The converse is true for the intensity of scattered green light such that a nanorod attached to the rotating shaft of the molecular motor appears to blink red and green when viewed through a polarizing filter.

Using this approach to measure rotation of *E. coli* F₁-ATPase, we determined that the velocity of the power stroke is \sim 0.5° μ s⁻¹ (6). We have also been able to resolve the formation of 50–200 μ s transient dwells that form as the result of an interaction of the F_o rotor and stator in F_oF₁, which had been incorporated into lipid nanodiscs for stabilization (11). The behavior of these transient dwells is consistent with a role in the F_o Brownian ratchet mechanism where c-ring rotation is limited to 36°.

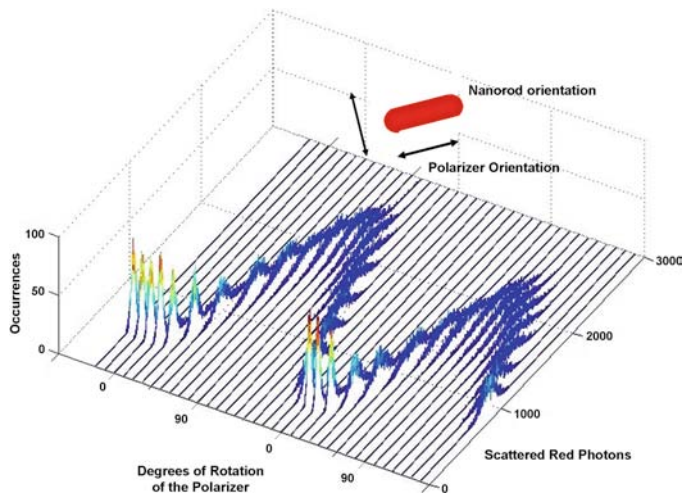


Fig. 1. Histograms of the intensity of red light scattered from a single nonrotating nanorod fixed to a slide as a function of the rotational position of the polarizer. Each histogram contains 3,520 measurements at each position of the polarizer obtained with the data acquisition speeds used to collect data points for c-ring rotation. The polarizer was then rotated counterclockwise by 10° and data collection was repeated.

2. Materials

2.1. Preparation of F_1 , and F_oF_1 -Nanodiscs ($n-F_oF_1$)

1. Buffer A: 100 mM KCl, 5 mM MgCl₂, 0.1 mM EDTA, 2.5% (v/v) glycerol, and 200 mM Tris-HCl, pH 8.0.
2. Buffer B: 5.0 mM TES, pH 7, 40 mM ε-amino-caproic acid, 1 mM EDTA, 1 mM DTT, 5.0% (v/v) glycerol.
3. Buffer C: 1 M KCl, 300 mM imidazole, 50 mM MgCl₂, and 0.5 M Tris-HCl, pH 8.0.
4. Buffer D: 100 mM KCl, 30 mM imidazole, 5 mM MgCl₂, 15% (v/v) glycerol, and 50 mM Tris-HCl, pH 8.0.
5. Buffer E: 100 mM NaCl, 40 mM ε-aminocaproic acid, 15 mM p-aminobenzamidine, 5 mM MgCl₂, 0.03% (w/v) phosphatidylcholine, 1.0% (w/v) octyl glucopyranoside, 0.5% (w/v) sodium deoxycholate, 0.5% (w/v) sodium cholate, 6% (v/v) glycerol, 30 mM imidazole, and 50 mM Tris-HCl, pH 8.0.
6. Buffer F: 100 mM NaCl, 4 mM 4-aminobenzamidine, 5 mM MgCl₂, 5% (v/v) glycerol, and 50 mM Tris-HCl, pH 8.0.
7. Ni-NTA column packing material.
8. Biotin maleimide for covalent modification of the target sulphydryl on F_1 and F_oF_1 .

9. Membrane scaffold protein construct MSP1E3D1. Prof. Steven Sligar at UIUC has made a strain available upon request that expresses MSP1E3D1 containing a cleavable his-tag (see Note 1).
10. TEV protease to cleave the his-tag from MSP1E3D1.

2.2. Preparation of Gold Nanorods

1. Gold nanorods are commercially available from Nanopartz (USA).
2. Cetyltrimethylammonium bromide (CTAB).
3. Neutravidin.
4. Modified bovine serum albumin (BSA-c).

2.3. Assembly of Components on a Microscope Slide and Single Molecule Assays

1. Assembly Buffer: 10 mM KCl and 50 mM Tris-HCl, pH 8.0.
2. Rotation Buffer: 1 mM MgCl₂ and 2 mM ATP, 10 mM KCl, and 50 mM Tris-HCl, pH 8.0 that sometimes contains a specified amount of PEG400.

2.4. Microscopy, Data Acquisition, and Analysis

1. Ni-NTA-coated glass microscope slides and glass cover slips.
2. An inverted dark-field microscope mounted on an optical bench. A Sutter LB-17 Xenon light with a custom Chroma cold mirror coupled with a series 2000 Lumatec light guide to deliver 400–925 nm, collimated light to the sample through the dark-field condenser.
3. An iris in the 63× variable aperture objective to block light not scattered by a gold nanorod. A digital color camera with a refresh rate of ~53 fps mounted to a port of the microscope that contains a polarizing filter to detect the fluctuation of red and green light scattered from the gold nanorods.
4. A motorized microscope stage with 0.002 μm/microstep resolution on which the slide is mounted.
5. A 100-μm pinhole mounted on an optical bench via an xyz translation stage at an alternate port from the microscope from that to which the color camera is mounted. Light passing through the pinhole is directed through a high-pass filter with a 600-nm cutoff as well as a polarizing filter mounted on a rotational stage, and is focused by a lens onto a single photon counting avalanche photodiode detector. The detector has a dark count of ~50 photons/s with a temporal resolution of 50 ns, equivalent to 20 million frames/s. The optics of the microscope are aligned so that the light from the sample that is incident upon the detector and the color camera are confocal. Output from the detector is fed directly into a counter/timer board in a computer with sufficient memory and processing speed to handle the large data files that are rapidly generated during data acquisition.

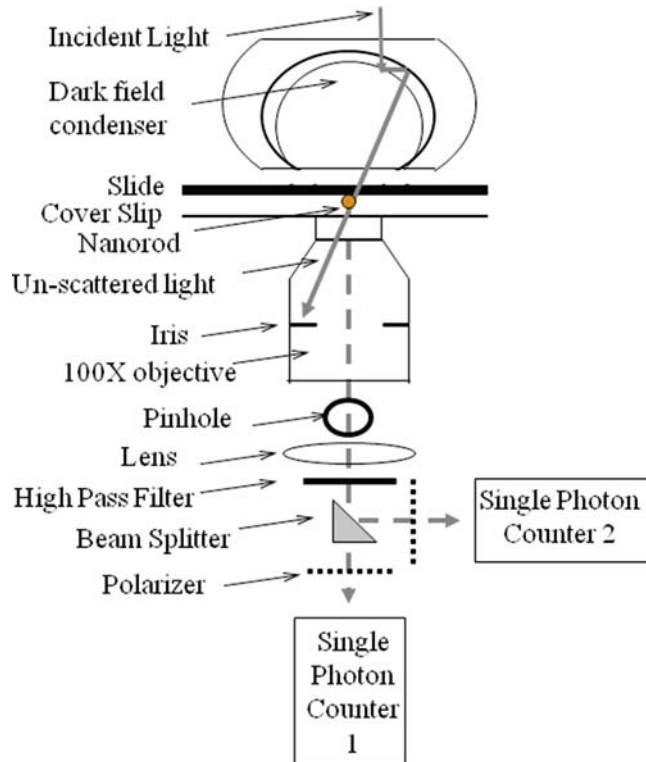


Fig. 2. Schematic of the dark-field microscope used to make the measurements. In this configuration, the scattered light from a single rotating gold nanorod (dashed line) passes through a beam splitter for measurement by two single photon counting avalanche photodiode detectors when the orientation of the polarizer for detector 1 is offset from that of detector 2.

6. In an optional configuration (Fig. 2), a nonpolarizing beam splitter is inserted between the high-pass filter and the polarizer. A second polarizer is mounted on a rotational stage between the split beam and a second single photon counter. The polarization angle of the second polarizer is offset by a known amount from the first polarizer.

3. Methods

3.1. Preparation of F_1 Protein

1. The F_1 -ATPase containing a His₆-tag on the N terminus of the β -subunit and γ S193C was expressed and purified from *E. coli* XL-10 strain (12, 13). Cells were grown with shaking at 37°C in 1 l of LB medium with 50 µg/ml of ampicillin. About 4–5 g wet weight of bacteria was harvested by centrifugation at 7,700 × g for 15 min at 4°C and stored as cell pellets at -80°C. Cell pellets, thawed at 25°C, were immediately resuspended in Buffer A, and the cells were broken using a French press at

16,000 psi. Unbroken cells were collected as a pellet at $7,700 \times g$ for 15 min at 4°C and discarded.

2. Membranes were resuspended in Buffer B, and centrifuged at $180,000 \times g$ for 1 h at 4°C. All subsequent steps were performed at 23°C. The supernatant was mixed with Buffer C at a 10:1 (v/v) ratio. Glycerol was added to 15% (v/v), and the mixture was put on a Ni-NTA column (0.8 cm diameter, 1.5 ml of resin) washed initially with water and equilibrated with Buffer D to bind F_1 -ATPase to the column, and the column was washed with 20 ml of Buffer D. An excess of biotin maleimide was dissolved in 3 ml of Buffer D, which was used to wash the Ni-NTA column containing bound F_1 -ATPase. After a wash with 10 ml of Buffer D, biotinylated F_1 -ATPase was eluted with 3 ml of Buffer D containing 180 mM imidazole, then stored at 0.1 mg/ml at -80°C prior to use.

3.2. Preparation of F_oF_1 , Protein Incorporated into Nanodiscs ($n\text{-}F_oF_1$)

1. Purified F_oF_1 that was cysteine-free except for the cysteine resulting from the c2Vc insertion was expressed and purified using the DK8 *unc* operon deletion strain of *E. coli* (14) containing the plasmid pNCcys. Cells were grown with shaking at 37°C in 6 l of LB medium with 50 µg/ml of ampicillin. About 25 g wet weight of bacteria was harvested by centrifugation at $7,700 \times g$ for 15 min at 4°C and stored as cell pellets at -80°C. Cell pellets thawed at 25°C were immediately resuspended in Buffer A, and the cells were broken using a French press at 16,000 psi. Unbroken cells were collected as a pellet at $7,700 \times g$ for 15 min at 4°C and discarded.
2. All subsequent steps were performed at 4°C. The supernatant fraction containing membrane vesicles was centrifuged at $184,000 \times g$ for 2–3 h. The pellet of membranes containing F_oF_1 was resuspended in Buffer E. About 5 ml of Buffer E was added to 1 g of membranes, which was shaken for 90 min at 4°C, then centrifuged at $184,000 \times g$ for 2 h. The supernatant was applied to a Ni-NTA column containing 1.5 ml of resin equilibrated with Buffer E. The resin containing bound F_oF_1 was washed with about 20 ml of Buffer E, and F_oF_1 was eluted with 3 ml of Buffer E containing 180 mM imidazole. After determination of protein concentration, the solubilized F_oF_1 was immediately incorporated into nanodiscs (11).
3. The His-tag of the purified membrane scaffold protein MSP-1E3D1 was cleaved by overnight incubation with TEV protease (at 25:1 ratio, w/w) at 25°C and passed through a Ni-NTA column. To assemble $n\text{-}F_oF_1$, MSP was mixed in Buffer F with 10% sodium cholate in Buffer F, and F_oF_1 in Buffer E to achieve a 1:5.3 molar ratio of F_oF_1 :MSP in 1% sodium cholate with a final volume not exceeding 1 ml, and adjusted with Buffer F.

To make biotinylated n-F₆F₁ a tenfold molar excess of biotin maleimide was added to this mixture. The mixture was incubated at 4°C for 15 min with gentle shaking, then passed through a 2-ml Sephadex G-50 column equilibrated with Buffer F from which 2.5 ml of effluent were collected. The effluent was diluted with Buffer F to 6.5 ml to decrease the imidazole concentration to <30 mM, and passed through a 1.5-ml Ni-NTA column. The column was washed with 15 ml of Buffer F and eluted with Buffer F, containing 150 mM imidazole (see Notes 1 and 2).

3.3. Gold Nanorod Preparation

1. Gold nanorods can be prepared by the reduction of HAuCl₄ to form 4-nm seeds (15), but are also commercially available from Nanopartz Inc.
2. Nanorods are coated with Neutravidin by exchanging the gold rod buffer (100 mM CTAB) with 1 mM CTAB. Neutravidin is added directly to the nanorod/CTAB solution to a final concentration of 40 µg/ml. The mixture is shaken at room temperature for 1 h and is best if prepared daily. Avidinated gold nanorods were further diluted in Assembly Buffer containing BSA-c (see Notes 3–5).
3. A variety of protocols are now available to make gold nanorods. These methods have primarily optimized factors that give rise to a high yield of nanorods with a narrow distribution of size and aspect ratio. However, to date, optimization of the dynamic range of polarized light scattering has not been a priority. Although the presence of Ag during the synthesis of the gold nanorods improves the yield and uniformity of the nanorods, it has been our experience that Ag decreases the dynamic range significantly.
4. Because the synthesis of nanorods is not precise, we routinely examine all Nanorod preparations that we make or purchase by electron microscopy to confirm size and shape before use in single molecule experiments. We have found that the drag on the motors can be determined precisely based on their dimensions, with the minor caveat that the drag is sensitive to the shape of the nanorods (16).

3.4. Assembly of Components on the Microscope Slide

1. Draw a small circle on the bottom surface of a clean Ni-NTA-coated glass microscope slide with a permanent marker in order to identify the location on which the enzyme and nanorods will be assembled. On the opposite side of the slide, apply 5 µl of 100 µg/ml of the ATPase enzyme within the circle to immobilize the enzyme on the surface via the His-tags. After 5 min wash the slide for 30 s with Assembly Buffer and wick excess liquid from the surface using the tip of a Kim wipe.

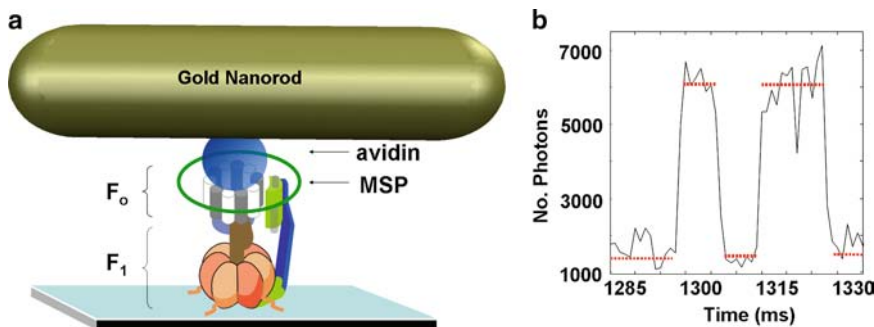


Fig. 3. (a) Assembly of F_0F_1 nanodiscs ($n-F_0F_1$) with a gold nanorod on a microscope slide for single molecule studies. Microscope slide bound $n-F_0F_1$ attached via β -subunit N terminus 6xHis tags attached to an avidin-coated 77 \times 39 nm nanorod via a biotinylated subunit-c cys that was inserted as the second residue in the sequence. Integral membrane protein subunits of F_0 are incorporated into a nanodisc comprised of the membrane scaffold protein (MSP) that forms a 13-nm diameter ring of α -helices around a bilayer of a few hundred phospholipid molecules, and has been shown to provide a good model for lipid bilayers. Rotation catalyzed by purified F_1 -ATPase is measured by assembling F_1 on the microscope slide in the same manner, but the Avidin-coated gold Nanorod is attached to a biotinylated cys on the γ -subunit (not shown). (b) Dwell duration and positions for ATPase-driven F_1 rotation using data acquired at 1 kHz. *Horizontal lines* indicate the catalytic dwells.

2. While the spot containing immobilized ATPase is still damp, apply 100 μ l of avidinated gold nanorods to the same spot and incubate for 5 min. Wash with Assembly Buffer for 30 s to remove unbound gold nanorods, and wick excess liquid from the surface as before. While the surface remains damp, add Rotation Buffer containing the desired amount of PEG400 and apply a glass cover slip (Fig. 3a) (see Note 6).
3. Silicone masks are commercially available that, when applied to a microscope slide, reversibly adhere and create wells. Assembly of the enzyme with the nanorods using these temporary wells eliminates the accumulation of a large amount of enzyme-bound nanorods that otherwise assemble on the slide at the edge of the droplet used to apply them to the surface. After assembly on the slide, the silicone mask is replaced by the cover slip.

3.5. Microscopy to Measure Rotation

1. As a control, apply the Avidin/BSA-c coated nanorods to a microscope slide that lacks the ATPase enzyme, incubate 5 min, and wash slide for 30 s with Assembly Buffer to remove unbound nanorods. If the nanorods are properly coated, very few (typically <10) nanorods/field of view will have become bound to the slide as observed by dark-field microscopy.
2. Mount a microscope slide on which the ATPase enzyme was assembled with the nanorods. Focus the microscope to view the light scattered from the gold nanorods bound to the surface of the slide with the color camera. Using the recommended concentration of protein (F_1 or F_0F_1) applied to the microscope slide, ~250 nanorods should be visible in an average field of view (see Note 7).

3. Examine the field of view to identify spots of scattered light emitted from the nanorods in which the intensity oscillates between red and green as an initial indication of ATPase-dependent rotation (see Note 8).
4. Use the stage to align a nanorod that appears to be flashing with the pinhole.
5. Adjust the data binning acquired from the single photon counter to obtain the desired speed of time resolution during data acquisition.
6. Divert the light from the color camera to the single photon detector, and monitor changes in the intensity of the scattered light as a function of time. Note that only one single photon counting avalanche photodiode detector is required for these measurements unless the objective is to determine the direction of rotation. The use of a single detector will increase the photons that reach the detector and thus the signal-to-noise of the measurements.
7. Maximize the dynamic range of the scattered light intensity at a data acquisition speed of 1 kHz by making minor adjustments to the position of the microscope stage and/or by rotating the polarizing filter by small increments. The scattered light intensity from a nanorod that is rotating will easily vary between maximum and minimum values of 2,500 and 500, resulting in a dynamic range of 3,000 photons. If the dynamic range of the nanorod examined meets or exceeds this value, collect data for a chosen interval. A data acquisition speed of 100–200 kHz provides a minimal time resolution of 20–10 μ s, respectively, which is sufficient to resolve the power stroke of ATPase-driven rotation. We typically collect data for a 50-s period, and monitor the intensity changes throughout to insure that the molecule rotated throughout the entire period examined (see Note 9).
8. Custom software written in LabView 7.1 simplifies pinhole alignment, and the ability to select options for data acquisition and storage. We also included a feature that shuts off power to the single photon counters should the photon flux on the camera exceed 10,000. Exceeding the allowable maximum light intensity incident upon these detectors can damage them irreversibly. Occasionally, a Nanorod preparation will have a dynamic range that approaches this flux at its maximum. In an application to observe catalytic dwells, which average 8 ms in duration, we collect data at 1 kHz. At this data acquisition speed the power strokes are not resolved, and the data appear to move from one dwell to the next as a discontinuous function (Fig. 3b), and under these conditions, it is easy to damage a photon counter.
9. The optional use of two photon counters to acquire rotation data (Fig. 2) provides the ability to determine the direction

of rotation. Once a nanorod is aligned with the pinhole, rotate the polarizer for detector 1 to give a minimum signal during one of the three catalytic dwells. Then rotate the polarizer for detector 2 so to be offset from that of the first detector by a known amount.

3.6. Data Analysis

1. For a nanorod immobilized directly to surface of the slide (Fig. 1), the distribution of scattered red light intensities as a function of the rotational position of the polarizing filter determines the variation in the intensity of scattered light from the immobile nanorod as detected by the single photon counter. Based on the data of Fig. 1, the standard error in the measurement varied between 0.02° and 0.12° as the scattered light intensity varied between minimum and maximum values (11).
2. Since minimum and maximum intensity values of red light scattered from the nanorod occur when the rod is perpendicular and parallel to the plane of polarization, respectively, these minimum and maximum intensity values provide the most sensitive measure of the rotation rate. Thus, the most sensitive measure of a 120° rotational power stroke driven by ATP hydrolysis at saturating Mg^{2+} -ATP will occur in the subset of data that includes the 90° of rotation between these maximum and minimum values. We refer to these 90° rotational events in the data set as transitions.
3. The single-molecule rotation data is analyzed to identify and measure transitions using custom software written in Mat Lab 6.5 (6). The program first establishes the minimum and maximum intensity values for each data set. Rotational events are then identified as a consecutive group of a minimum of three data points in which the intensity changes from within 5% of the minimum intensity of scattered light to $>95\%$ of the maximum or vice versa that also have a linear regression R^2 value of 0.95 or greater. Each group of data points in a transition are stored for use in determining the rotational velocity of each, and collated in a spread sheet. They can be accessed and plotted individually or as a group. The software allows the min/max intensity percentage cut-offs and R^2 values to be varied to examine the variation in the calculation of the rotational velocity. Information concerning the total number of rotational events, average velocity, and distribution of events in a given data acquisition is also tabulated (see Note 10).
4. A schematic of scattered light intensity during three consecutive power strokes (one complete revolution) is shown in Fig. 4 when the nanorod was initially aligned nearly, but not exactly, perpendicular to the polarizer. Since the stochastic nature of the enzyme results in a variation in the rotational position of each catalytic dwell (17), the alignment of the nanorod with

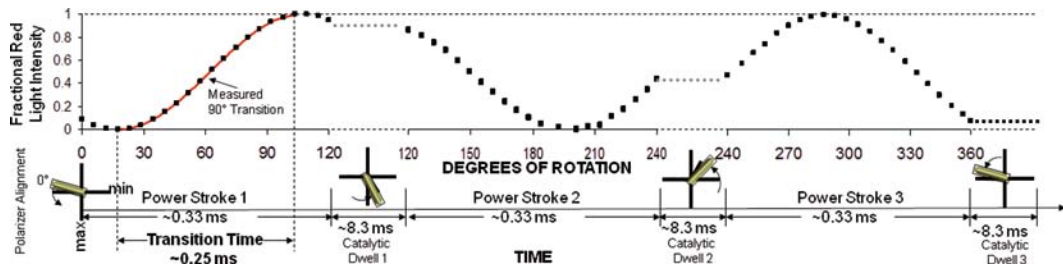


Fig. 4. Relationship between a 120° power stroke and a 90° measured rotational transition. Theoretical plot of the intensity of scattered red light from a nanorod during one complete revolution that involves three consecutive power strokes and three consecutive catalytic dwells separated by exactly 120°. The nanorod is initially positioned almost, but not exactly perpendicular to the orientation of the polarizer such that the scattered light intensity goes through a minimum than a maximum prior to catalytic dwell 1. A transition includes the data between the minimum and maximum intensities representing 90° of the 120° of rotation for analysis. When initial alignment of the nanorod is exactly at the minimum and each of the successive power strokes is exactly 120° the algorithm selects transitions for power strokes 1 (min to max) and 3 (max to min).

the polarizer will show small variations during the data collection period. If the nanorod is initially aligned perpendicular to the polarizer and the three consecutive power strokes are exactly 120° during a single revolution such that the nanorod is also perpendicular during catalytic dwell 3, the algorithm will analyze transitions from power strokes one and three. In practice, the number of consecutive power strokes analyzed is randomized by the stochastic nature of the molecular motor. Due to the randomization, there is an equal probability that the 90° increments of rotation measured as transitions represents the beginning, the middle, and the end of each 120° power stroke such that the entire power stroke is sampled in the course of the ~3,520 power stroke events monitored on average for each molecule during the 50 s of data acquisition at 100 kHz.

- Since the intensity of scattered light changes as a sinusoidal function of the rotational position of the nanorod, the degrees of rotation during a transition are derived from the arcsine of the fractional intensity of light scattered from the nanorod by Eq. 1:

$$\theta = (\arcsin I)180\pi^{-1} \quad (1)$$

where θ is degrees of rotation, and I is the fractional intensity of scattered light.

- Example transitions are shown in Fig. 5 (11). The ATPase-driven power strokes catalyzed by F₁ at saturating Mg-ATP appear as uninterrupted rotation throughout the 90° of data analyzed. Similar continuous power stroke events are also observed with ATPase-driven n-F_oF₁ rotation in the absence of PEG400. However, when the drag induced by the presence of PEG400 is sufficient to slow n-F_oF₁ rotation below a threshold,

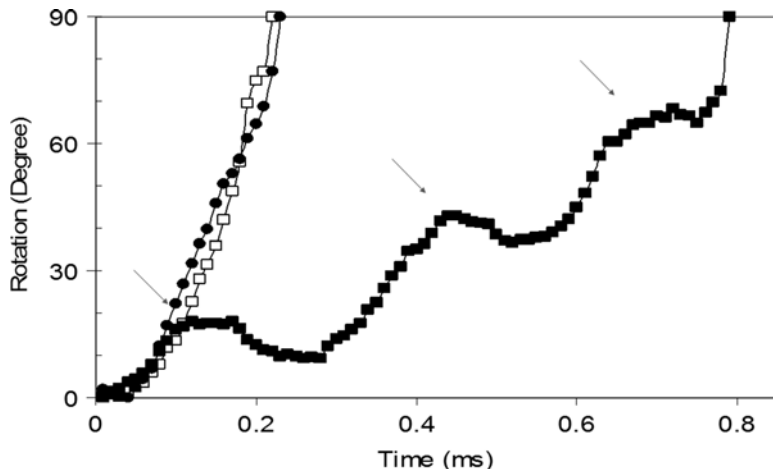


Fig. 5. Power stroke events with and without transient dwells due to ATPase-driven rotation of single molecules. Example transitions for F_1 (filled circle), as well as for $n\text{-}F_oF_1$ with (filled square) and without (open square) transient dwells. Arrows indicate transient dwells. Nanorod attachment occurred via the γ -subunit for F_1 or via the c-ring for $n\text{-}F_oF_1$. Data were acquired at 100 kHz in the presence of 15% PEG400 (v/v) and 1 mM MgATP, and were converted from scattered light intensity to degrees of rotation by Eq. 1.

transient dwells clearly resolved an average of every 36° . These transient dwells correspond to an interaction between the F_o stator and rotor subunits that can be measured to last from 200 to 50 μ s in the presence of 15 and 35% PEG400, respectively. The incorporation of F_oF_1 into nanodiscs provides a lipid environment that stabilizes the integral membrane protein interactions. The size of a nanodisc is ideal for use in single molecule experiments.

7. The load imposed on the motor can be varied by changing the size of the nanorod and/or by increasing the viscosity of the medium (Fig. 6). We vary the viscosity by the inclusion of PEG400 in the solution because we determined that PEG400 molecules behave as a Newtonian fluid (8). As such, they are too small to be pulled along by the rotating nanorod, and thus do not make secondary nonlinear contributions to the drag. The increased drag on the gold nanorod due to the viscosity of the PEG400 solution exerts a load on the motor that slows the power stroke velocity, which can be used to determine the torque (8). For a given size of nanorod, the angular velocity is determined by the rotational distance (arc distance) divided by time. In the absence of the transient dwell, the average angular velocity is calculated using the arc distance of the rod moving 90° divided by the transition time. In the presence of the transient dwell, the average angular velocity is the arc distance of the rod moving 36° divided by the average time between transient dwells.

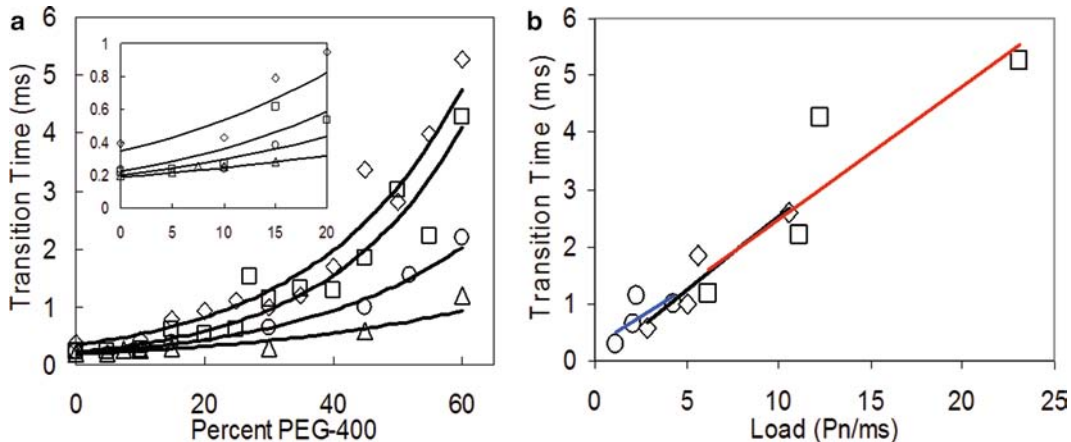


Fig. 6. Transition times of F_1 -dependent γ -subunit rotation as a function of PEG-400 concentration and nanorod size at 1 mM $MgCl_2$ and 2 mM ATP. (a) Average transition times as a function of PEG400 concentration measured using 75×35 nm (triangle), 87×36 nm (open circle), 90×46 nm (square) and 91×45 nm (diamond) nanorods. (Inset) Expansion of data between 0 and 20% PEG400 shows that the transition times for the three smallest nanorods converge to a single value of ~ 250 μ s. (b) Transition times plotted as a function of increasing nanorod size at fixed PEG400 concentrations. Lines are the linear best fit for 30, 45, and 60% PEG400.

Torque is calculated from the drag and the velocity by Eq. 2:

$$T = \Gamma \omega \quad (2)$$

where Γ is the drag force and ω is the angular velocity of the power stroke.

8. Comparison of direct measurements of the drag on the nanorod (8) showed that the propeller model provided a close approximation of the drag force as a function of PEG400 concentration (see Note 11). Based on this model, the drag force is approximated by Eq. 3:

$$\Gamma = \frac{4\pi\mu(L_1^3 + L_2^3)}{3\cosh^{-1}(h/r)} \quad (3)$$

where L_1 and L_2 are the lengths of the propeller extending from the rotational axis, r is the radius of the rod, μ is the viscosity of the medium, and h is the height of the cylinder axis relative to the surface. Values for the viscosity of a solution of PEG400 in the buffer used for these rotation measurements are provided in ref. 8. The drag generated by a 77×39 nm gold nanorod will vary depending on whether the axis of rotation is at the end or in the middle of the nanorod.

9. The optional use of two photon counters to acquire rotation data (Fig. 2) provides the ability to determine the direction of rotation. The exact number of degrees of offset between the two polarizers is not important, but it must be sufficient to distinguish the time that a power stroke is detected by the two single

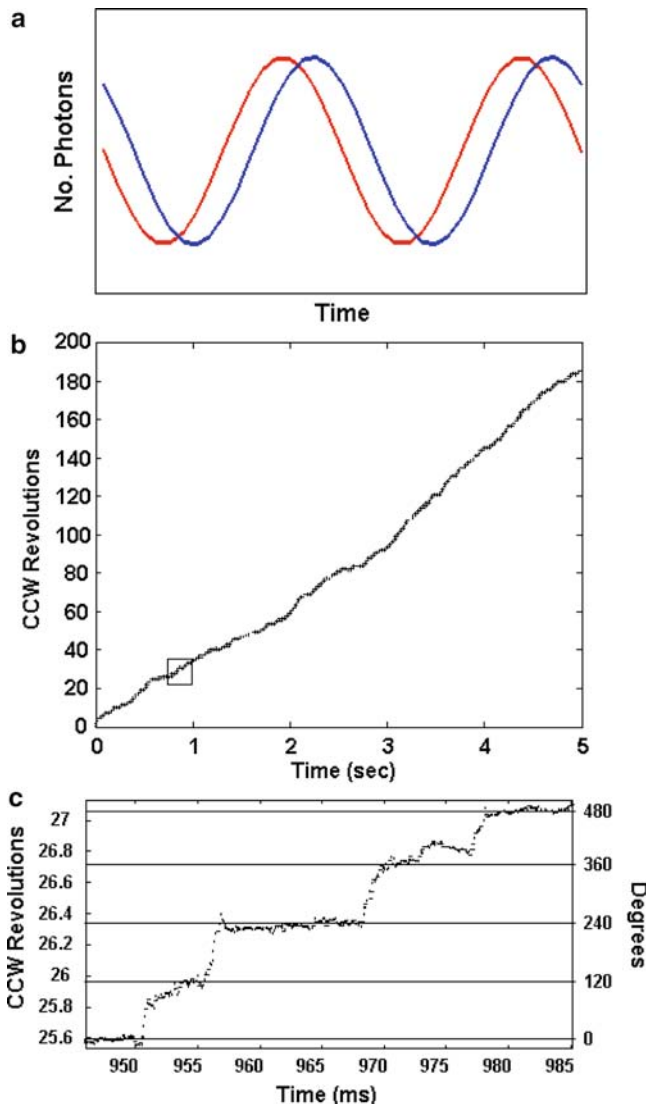


Fig. 7. (a) Theoretical plot of changes in intensity of red scattered light observed from two single rotating nanorod by two photon counters when the orientation of the polarizer for detector 1 is offset from that of detector 2. (b) Experimental time course of rotational position of the γ subunit in a single F_1 molecule determined from data acquired at 10 kHz with two photon counters in which the orientation of the polarizer for detector 1 was offset from that of detector 2. The substrate concentration was 1 mM $MgCl_2$ and 2 mM ATP. (c) Detail of the rotational stepping of the *boxed region* of (b). Horizontal lines indicate the 120° catalytic dwell positions.

photon counters (Fig. 7a). Simply, CCW rotation is indicated when photon counter 1 detects a power stroke before photon counter 2 and vice versa for CW rotation. By tracking the changes in intensity with a known polarization phase shift between the detectors, an algorithm can calculate the exact angular position of the Nanorod and the direction of rotation throughout during the entire data set. An example is shown in Fig. 7b and 7c.

4. Notes

1. The membrane scaffold protein construct MSP1E3D1 used is composed of scaffold protein that contains three 22-mer amphipathic helices and a cleavable his-tag as the result of an introduced TEV protease site to facilitate purification (18, 19). Nanodiscs formed from this construct contain a lipid bilayer that is about 13 nm in diameter surrounded by a double belt of the MSP helices.
2. The yield of n-F_oF₁ was ~60–70% of the amount of F_oF₁ starting material as measured with the BCA protein assay.
3. Removal of the CTAB is important since it was found to be a potent inhibitor of F₁ activity, though when the avidinated gold was mixed with the F₁ on the slide, there was no inhibition. The abundance of rotating molecules is also reduced if the bottles of Avidin and/or BSA-c have passed the expiration date on the bottles. This can sometimes cause the nanorods to clump on the slide, which is apparent as yellow spots by microscopy.
4. Coating the gold nanorods with avidin can be verified by spectrophotometry through a 4–10-nm red shift in the spectrum. This red shift is attributed to a change in the dielectric environment of the gold nanorod surface (20).
5. Coating with BSA-c decreased the nonspecific binding of the gold nanorods to the surface of the microscope slide.
6. Allowing the surface to dry completely causes a drastic reduction in the abundance of molecules that will be observed to rotate. The surface can dry out extremely quickly with some slides and/or some nanorod preparations.
7. The Mg–ATP concentration in the Rotation Buffer results in rates of ATP hydrolysis rates that approximate V_{max} , and this ratio of Mg to ATP in this buffer minimizes the occurrence of entrapped Mg–ADP in a catalytic site that results in extremely long catalytic dwells. Under these conditions, rotation is observed as discrete 120° events separated by the rate-limiting product release dwell.
8. Typically, about 30% of the rods in a given field of view will rotate on an average microscope slide, compared to less than 1% observed by Noji et al. (21). We have occasionally observed the abundance of rotating molecules to approach 85%, but as stated in notes above, several factors can adversely affect the abundance. The abundance also decreases in the presence of 35–40% PEG400, since the load exceeds the torque of the motor (see Note 11).

9. Single F_1 molecules can be observed to rotate for several hours using this method.
10. The average velocity of rotation measured using this method was about $0.5^\circ\mu\text{s}^{-1}$ (6). Minimal data acquisition speeds of ~50 kHz are required to obtain an accurate measure of the velocity of rotation.
11. The dependence of $n \cdot F_o F_1$ power stroke velocity on the PEG400 concentration is about the same as that of purified F_1 -ATPase, resulting in ~62 pN nm of torque when driven by ATP hydrolysis (8, 11).

Acknowledgments

This work was supported by grants from National Institutes of Health (GM50202), DARPA, and AFOSR (FA9550-05-1-0424) to W.D.F.

References

1. Stock, D., Leslie, A. G., and Walker, J. E. (1999) Molecular architecture of the rotary motor in ATP synthase. *Science* **286**, 1700–1705.
2. Jiang, W. P., Hermolin, J., and Fillingame, R. H. (2001) The preferred stoichiometry of c subunits in the rotary motor sector of *Escherichia coli* ATP synthase is 10. *Proc. Nat. Acad. Sci. USA* **98**, 4966–4971.
3. Börsch, M., Diez, M., Zimmermann, B., Reuter, R., and Gräber, P. (2002) Stepwise rotation of the gamma-subunit of $EF_o F_1$ -ATP synthase observed by intramolecular single-molecule fluorescence resonance energy transfer. *FEBS Lett.* **527**, 147–152.
4. Boyer, P. D. (1997) The ATP synthase—a splendid molecular machine. *Annu. Rev. Biochem.* **66**, 717–749.
5. Sabbert, D., Engelbrecht, S., and Junge, W. (1996) Intersubunit rotation in active F-ATPase. *Nature* **381**, 623–625.
6. Spetzler, D., York, J., Daniel, D., Fromme, R., Lowry, D., and Frasch, W. (2006) Microsecond Time Scale Rotation Measurements of Single F_1 -ATPase Molecules. *Biochemistry* **45**, 3117–3124.
7. Noji, H., Hasler, K., Junge, W., Kinoshita, K., Jr., Yoshida, M., and Engelbrecht, S. (1999) Rotation of *Escherichia coli* F_1 -ATPase. *Biochem. Biophys. Res. Commun.* **260**, 597–599.
8. Hornung, T., Ishmukhametov, R., Spetzler, D., Martin, J., and Frasch, W. D. (2008) Determination of torque generation from the power stroke of *Escherichia coli* F_1 -ATPase. *Biochim. Biophys. Acta* **1777**, 579–582.
9. Moskovits, M. (1985) Surface-Enhanced Spectroscopy. *Rev. Mod. Phys.* **57**, 783–826.
10. Sönnichsen, C., and Alivisatos, A. P. (2005) Gold nanorods as novel nonbleaching plasmon-based orientation sensors for polarized single-particle microscopy. *Nano Lett.* **5**, 301–304.
11. Ishmukhametov, R., Hornung, T., Spetzler, D., and Frasch, W. D. (2010) Direct Observation of Stepped proteolipid ring rotation in *E. coli* $F_o F_1$ ATP Synthase. *EMBO J.* **29**, 3911–3923.
12. York, J., Spetzler, D., Hornung, T., Ishmukhametov, R., Martin, J., and Frasch, W. D. (2007) Abundance of *Escherichia coli* F_1 -ATPase molecules observed to rotate via single-molecule microscopy with gold nanorod probes. *J. Bioenerg. Biomembr.* **39**, 435–439.
13. Greene, M. D. and Frasch, W. D. (2003) Interactions among gamma R268, gamma Q269, and the beta subunit catch loop of *Escherichia coli* F_1 -ATPase are important for catalytic activity. *J. Biol. Chem.* **278**, 51594–51598.
14. Klionsky, D. J., Brusilow, W. S., and Simoni, R. D. (1984) *In vivo* evidence for the role of the epsilon subunit as an inhibitor of the proton-translocating ATPase of *Escherichia coli*. *J. Bacteriol.* **160**, 1055–1060.

15. Jana, N. R., Gearheart, L., and Murphy, C. J. (2001) Wet Chemical Synthesis of high aspect ratio cylindrical gold nanorods. *Phys. Chem.* **105**, 4065–4067.
16. Spetzler, D., Ishmukhametov, R., Hornung, T., Day, L. J., Martin, J., and Frasch, W. D. (2009) Single molecule measurements of F₁-ATPase reveal an interdependence between the power stroke and the dwell duration. *Biochemistry* **48**, 7979–7985.
17. Yasuda, R., Noji, H., Yoshida, M., Kinoshita, K., and Itoh, H. (2001) Resolution of distinct rotational substeps by submillisecond kinetic analysis of F₁-ATPase. *Nature* **410**, 898–904.
18. Bayburt, T. H., Leitz, A. J., Xie, G., Oprian, D. D., and Sligar, S. G. (2007) Transducin activation by nanoscale lipid bilayers containing one and two rhodopsins. *J. Biol. Chem.* **282**, 14875–14881.
19. Denisov, I. G., Grinkova, Y. V., Lazarides, A. A., and Sligar, S. G. (2004) Directed self-assembly of monodisperse phospholipid bilayer Nanodiscs with controlled size. *J. Am. Chem. Soc.* **126**, 3477–3487.
20. Raschke, G., Kowarik, S., Franzl, T., Sönnichsen, C., Klar, T. A., Feldmann, J., Nichtl, A., and Kurzinger, K. (2003) Biomolecular recognition based on single gold nanoparticle light scattering. *Nano Lett.* **3**, 935–938.
21. Noji, H., Yasuda, R., Yoshida, M., and Kinoshita, K., Jr. (1997) Direct observation of the rotation of F₁-ATPase. *Nature* **386**, 299–302.

INDEX

A

- Actin..... 14, 37, 53, 99, 100, 104–108, 112–118, 123, 124, 139, 143, 146, 151–153, 155, 158, 162, 274
Actomyosin interactions 143
Affinity purification 46
Agarose gel electrophoresis 178, 183, 184, 209, 226
Airy function 34
Alexa dyes 50
Aminosilane 38, 44, 52, 199, 200
Anisotropy 162
Anti-digoxigenin 189
Atomic Force Microscopy (AFM) 180, 232, 235
ATPase cycle 58, 98, 106
ATP hydrolysis 20, 37, 143, 144, 155, 157, 158, 161, 274, 282, 287, 288
ATP regeneration system 23, 26, 99, 197, 207
Autocorrelation 7, 27, 29, 30
Autofluorescence 49, 112, 217
Avalanche photodiode 2, 20, 23, 146, 276, 281

B

- Background fluorescence 27, 35, 36, 43, 55, 90, 126, 141, 156, 158, 162, 199, 203, 207, 209, 211
Beam expanders 38, 42, 126
Binding stoichiometry 198
Biotin 12, 17
Biotin-streptavidin 73
Biotinylated antibodies 13, 17
Boltzman coefficient 148
Borosilicate glass 181
Bright-field illumination 53, 54, 179, 187, 261, 265
Brownian motion 102, 105, 265
Bulk measurements 195, 208, 210

C

- Calibrating the four-quadrant detectors 102
Cantilever 71–73, 75–76, 78–82, 85, 87–92
Carboxylated fluorescent beads 261, 265, 269
Cleaning cover-slips 26
Colony PCR 267

- Confocal fluorescence microscope 20
Conservation of momentum 97
Co-sedimentation assay 58, 59, 61, 62
Critical angle 36, 128, 155
Cross-linking chemistry 73
Cryo-electron microscopy 57, 65, 85
Cy3 38, 50, 146, 154, 158, 164–168, 171, 172, 216, 220, 221, 224, 225, 262
Cyanine dyes 50, 164
Cytoskeleton 22, 58, 74, 112, 124

D

- Dark current 36
Dark field microscopy 262, 274, 276, 277
Dichroic beamsplitter 261
Dichroic mirror 21, 23, 38, 41, 53, 221, 246, 256, 263, 269
Differential-interference-contrast (DIC) microscopy 13
Diffraction limited spots 33, 35, 124
Diode pumped solid state laser 261
DISH criteria 132
DNA curtains 243–257
DNA helicases 170, 193–213
DNA metabolism 194, 210, 243
DNA repair 193
DNA tethers 176, 177, 180, 186–188, 232, 235, 238
DNA topology 229, 230, 237
DNA transcription 175–190
3D reconstructions 58, 64

E

- Elastic properties 187
Electron-multiplying charge-coupled device (EMCCD) 36, 37, 42, 47, 126, 129, 140, 197
Emission filter 23, 38, 41, 53, 113, 118, 128, 221
Emission spectra 51, 53, 111, 140
End-labeled DNA 182–184, 186, 189
Endothelial cells 135–139
Ensemble analysis 98
Epi-fluorescence 187

Evanescence field 36, 124, 133, 155, 252, 260, 262, 264, 268
Extinction coefficient 163, 164, 168, 170, 210, 222

F

F1-ATPase 259, 260, 263–265, 267–268, 274, 277, 278, 280, 288
Feedback loop 72, 91
Foetal calf serum (FCS) 125, 126
Fibroblasts 119, 137, 138
Field diaphragm 266
FIONA. *See* Fluorescence Imaging with One Nanometer Accuracy (FIONA)
FLAG 113, 245, 249, 250, 256
Flow cells 99, 101, 125, 203
Fluorescence Imaging with One Nanometer Accuracy (FIONA) 34–37, 42, 47–50, 55
Fluorescence polarization 20
Fluorescence spectrophotometer 31, 166, 167, 196
Fluorescent nucleotides 161–173, 264
Force feedback circuit 98
Force vs distance curves 74, 76
Förster resonance energy transfer (FRET) 19–31, 73, 162, 274
Fourier transformation 78, 81
French press 222, 268, 277, 278

G

Gaussian function 27, 34, 35, 47, 48, 105
Glass surface 13, 26, 43, 46, 54, 77, 92, 117, 130, 132, 136, 152, 154, 157, 199, 200, 216, 217, 260, 263, 269
Gliding assay 13, 14, 16, 17, 54
Gold nanorods 274, 276, 279, 280, 287
Green fluorescent protein (GFP) 11–17, 38, 49, 111, 113, 116, 125, 126, 129–131, 141, 215–227

H

Harmonic potential well 20, 105
Hidden Markov Models 37
High resolution tracking 118
Histone purification 248, 249
Humidity chamber 235, 236, 239
Hydrodynamic flow 252
Hydrophobic coating 77
Hypertonic 115, 119
Hypotonic 115, 119, 120

I

Image acquisition rate 86, 87
ImageJ 40, 47, 206, 246, 254, 255
Image processing software 118, 206, 246

Imaging chamber 125–127, 140
Immersion oil 55, 128
In Vivo Motility Assay 115, 118–119
Isotropic TIRFM 259–262, 264, 266, 268

K

Kinesin 11, 19–31, 37, 46, 48, 50, 51, 57–70, 75, 76, 86–88, 143, 161, 259
Kip3p 12, 14, 16

L

LabView 23, 30, 76, 86, 281
Laser 2, 7, 21, 23, 27, 34, 36, 37, 41, 42, 46, 47, 49, 51, 53–55, 71, 72, 78, 81, 82, 91, 97, 98, 102–104, 113, 124, 126–129, 132, 133, 135, 140, 143–146, 149, 155, 157, 187–189, 197, 206, 210, 221, 224, 247, 252, 253, 260–262, 264–266, 269
Laser traps. *See* Optical tweezers
LED-illuminated 13, 15
Ligand–receptor bonds 74
Linear regression 178, 282
Lineweaver–Burk 107
Liposome 74, 246, 251
Load-dependent 175

M

Magnetic tweezers 229–240, 263
Maxwell–Boltzmann distribution 137
Mean squared displacement 102, 137
Mechanical coupling 176
Metal-affinity chromatography 185, 190
Mica 76
Michaelis–Menten 8, 20, 30, 107
Microinjection 50, 125
Microneedles 143–158
Microspheres 12–17, 20, 98, 99, 101, 176–181, 184–190, 221
Microtubules 11–16, 19, 20, 53, 57–70, 72–76, 84–88, 90
Multi-colour TIRF 128
Myosin 6, 7, 37, 97–108, 112–114, 116, 117, 120, 123–141, 143–146, 149, 151–158, 161, 162, 165, 169–171, 259
Myosin-6 126, 132, 137–140

N

Nanodiscs 274, 275, 278–280, 284, 287
Nanofabrication 253
Negative stain electron microscopy 58, 59, 62
NEM-myosin 100, 101, 108, 114, 117
N-ethylmaleimide (NEM) 99, 114
Nonpolarizing beam splitter 277

- Non-specific binding 36, 43, 54, 116, 117, 130, 164, 165, 199, 287
 Non-specific interactions 186
 Nucleoside triphosphate 161–173
 Nucleosomes 76, 87, 243–257
 Numerical aperture 23, 33, 38, 40, 98

O

- Optical table 30, 37, 38
 Optical tweezers 2, 6, 8, 97–108, 175–190
 Optics 38, 42, 55, 145, 155, 276
 Osmotic shock 118, 121
 Oxygen scavenger solutions 107, 114, 119, 197, 206, 207, 210

P

- Particle density 90
 Passive adsorption 16, 189
 PCR 183, 189, 196, 197, 204–206, 209–211, 213, 219, 221, 226, 231–234, 238, 267
 PcrA helicase 170
 PEGylation 38–39, 43–45, 54, 200–203, 210
 Peltier 220
 Peristaltic pumps 140
 Phase contrast 126
 Phosphate binding protein 167
 Photobleaching 49, 50, 55, 119, 131–136, 141, 152, 154, 158, 162, 164, 198, 210
 Photodiodes 2, 150, 151
 Photon noise 35
 Photostability 130, 131, 164, 165, 209
 Piezo 73, 82, 146, 150, 179
 Piezo stage 24, 103, 187
 Pixel size 34, 35, 37, 42, 48, 254
 Plasma Cleaning 51, 90, 199–200
 Plasma membrane 124, 132–140
 Plasmid DNA 223, 226
 Pleckstrin homology (PH) domains 132, 138
 Point-spread function 47, 118
 Polarizing filter 274, 276, 281, 282
 Polymerisation and fluorescent labelling of actin 99
 Power spectrum 78, 80, 81, 149
 Power-stroke 105
 Processivity 175, 195, 197, 198, 208, 230
 Protein A 179, 184, 185, 189
 Protein-coated surfaces 11
 Protein data bank 85
 Protein folding 73, 215
 Protein synthesis 215–227
 Proton-motive force or PMF 273
 PURE (Protein synthesis Using Recombinant Elements) 217, 220, 222, 223, 226

Q

- Quadrant photodiode (4QD) 88, 98, 102, 104, 105, 146, 176, 179, 189
 Quantum dot 46, 50, 111–121, 164, 244
 Quantum yield 163–165, 209

R

- Random walk 137, 138, 141
 Rate constant 107, 135, 136, 172
 Rate-limiting 7, 8, 178, 274, 287
 Real-time 175–190, 215–227, 237
 Refractive index 124, 128, 140
 Resonance 19–31, 73, 78–82, 87, 91, 92, 162
 Restriction endonuclease 179, 183, 238, 812
 Ribosome 215–227
 Ribosome stalling 217
 RNA polymerase (RNAP) 175–180, 182, 185, 188–190
 Rotation assay 263–264, 267–268, 274
 rRNA 216, 220

S

- Sample chamber 26, 36, 38–40, 42–48, 52, 55, 90, 234, 238, 244, 246, 253
 SDS-PAGE 25, 59, 61, 185, 190, 248, 250
 Second order rate constant 107, 136
 Secretion Monitor (SecM) 216–219
 Semiconductor nanocrystals 111
 Series compliance 108
 Signal-to-noise ratio 6, 27, 36, 49, 50, 54, 112, 113, 127, 128, 133, 162, 224
 Silanization 13, 76–78
 Single exponential decay 107
 Single-molecule transcription assay (SMTA) 176, 177, 180, 185, 188, 190
 Single-particle 65, 69, 111, 136, 162
 Single-particle tracking 111, 136
 Single-stranded DNA-binding protein (SSB) 194–199, 205, 206, 209–213
 Sonication water bath 189
 Spatial resolutions 74, 115, 125, 129, 130, 143
 Spherical aberrations 42
 Spin-coating 13
 Spring constant 73, 74, 78–82, 88, 91, 144
 Stiffness of the optical tweezers: equipartition principle 102, 103
 Stiffness of the optical tweezers: stokes calibration 103–104
 Streptavidin 16, 73, 113, 115–116, 118, 180, 194, 196, 199, 203, 206–211, 216, 221, 224, 232, 246, 252, 264
 Streptavidin coated microspheres 12, 16
 Student's t-test 37, 40, 48, 53

- Sub-nanometer precision..... 71
Super-paramagnetic beads..... 235–236
Super-resolution techniques..... 34
Surface-blocking buffer..... 178
Surface-immobilize 176, 185, 189, 190, 225
Syringe-pump flow system 247, 252
- T**
- T7 RNA polymerase 176–178, 180, 182, 185, 188, 190
Tapping mode 72, 82, 88
Temporal resolution..... 79, 162, 207, 238, 276
Tensile strength 152
Tetramethyl-Rhodamine-Iso-Thiocyanate 99
Thermal noise..... 73, 78, 80, 81, 91, 103
Three bead geometry..... 98–100, 104, 105, 177, 179, 180
Time-lapse 133, 134
Topographical profiles 84
Topoisomerases 229, 230, 232
Torque 284, 285, 287, 288
Total internal reflection fluorescence microscopy
 (TIRF) 6–7, 17, 37, 41, 113, 118, 124–128, 131, 133, 138, 155, 162, 194, 195, 197, 200, 203–206, 244, 246, 247, 255, 259–261, 264, 266, 268–270
- Transcription initiation..... 176, 177, 180, 188
Transfection..... 125, 126, 130
Transient transfection..... 125, 130
tRNA 226
Tubulin 12, 15, 22, 25, 26, 31, 58, 60, 61, 63, 65, 67, 68, 75, 85, 87
- U**
- Unconventional myosin 124
UV spectrophotometer 196
- V**
- Video microscopy 111
 V_{\max} 107, 171, 287
- W**
- Wide-field illumination 27
- Y**
- Yellow fluorescence protein (YFP) 113
Young's modulus 79, 156